School of Physical Sciences

SOME TECHNIQUES FOR THE ENHANCEMENT OF ELECTROMAGNETIC DATA FOR MINERAL EXPLORATION

Michael Paul Sykes

This thesis is presented as part of the requirements
for the award of the degree of
Doctor of Philosophy of the Curtin University of Technology

March 2000

ACKNOWLEDGMENTS

My sincere gratitude is extended to my supervisor, Associate Professor Umesh Das, for the original ideas that form the basis of this work and his ceaseless optimism and encouragement. I am also grateful for the support and encouragement offered by Professor Norm. Uren who acted as replacement supervisor toward the end of this work.

I would like to thank the staff of the Department of Exploration Geophysics, Curtin University for their friendship during this time. Special thanks to my fellow PhD student Brett Harris.

Most importantly I thank my wife Lyn for her tremendous support throughout this time.

I am thankful for the scholarship provided by the cooperative research centre for Australian minerals exploration technology (CRCAMET). Additional funding from AMIRA project P481 for field tests is also acknowledged.

ABSTRACT

The usefulness of electromagnetic (EM) methods for mineral exploration is severely restricted by the presence of a conductive overburden. Approximately 80% of the Australian continent is covered by regolith that contains some of the most conductive clays on Earth. As a result, frequency-domain methods are only effective for near-surface investigations and time-domain methods, that are capable of deeper exploration, require the measurement of very small, late-time signals. Both methods suffer from the fact that the currents in the conductive Earth layers contribute a large portion of the total measured signal that may mask the signal from a conductive target. In the search for non-layered structures, this form of geological noise is the greatest impediment to the success of EM surveys in conductive terrains. Over the years a range of data acquisition and processing techniques have been used in an effort to enhance the response of the non-layered target and thereby increase the likelihood of its detection.

The combined use of a variety of survey configurations to assist exploration and interpretation is not new and is practiced regularly. The active nature of EM exploration means that the measured response is determined to a large degree by the way in which the Earth is energised. Geological structures produce different responses to different stimuli. In this work, two new methods of data combination are used to transform the measured data into a residual quantity that enhances the signature of non-layered geological structures. Based on the concept of data redundancy and tested using the results of numerical modelling, the new combinations greatly increase the signal to noise ratio for targets located in a conductive environment by reducing the layered Earth contribution. The data combinations have application to frequency-domain and time-domain EM surveys and simple interpretive rules can be applied to the residuals to extract geological parameters useful in exploration. The new methods make use of inductive loop sources and can therefore also be applied to airborne surveys.

Airborne surveys present special difficulties due to the data acquisition procedures commonly used. Flight-line related artefacts such as herringbones detract from the appearance of maps and make boundary definition more difficult. A new procedure, based on the Radon transform, is used to remove herringbones from airborne EM maps and locate the conductive boundaries correctly, making interpretation more reliable and easier. In addition, selective filtering of the Radon transform data enables the enhancement or attenuation of specific linear features shown in the map to emphasise features of interest. Comparison of the Radon transform procedures with the more conventional Fourier transform methods shows the Radon transform processing to be more versatile and less prone to distortion of the features in a map.

The procedures developed in this work are applied to field data with good results.

TABLE OF CONTENTS

CHAPTER 1

CHAPTER 2

CHAPTER 3

CHAPTER 4

CHAPTER 5

CHAPTER 6

CHAPTER 7

LIST OF FIGURES

CHAPTER 7

CONCLUSIONS AND RECOMMENDATIONS

New techniques have been developed for the enhancement of electromagnetic data for mineral exploration. Exploration for conductive mineral deposits using EM methods is made more difficult in conductive environments due to the small signals from target bodies being masked by the currents flowing in conductive Earth strata. In Australia, which has some of the most conductive clays in the world, the conductive regolith acts as a barrier to deeper exploration using EM methods since the response from targets beneath the regolith is often too small to be observed above the large response from the regolith itself. Time domain EM systems that measure the decay of currents after the transmitter current is switched off provide the best option for detecting targets buried beneath the regolith, but to date have only been successful in areas of relatively thin cover.

Enhancement of a signal is only possible if the information sought is contained in the data at the time of measurement and the task is then one of selective enhancement. All measurements of physical quantities have some error or noise associated with them so it is important to be able to enhance the relevant information to obtain the maximum benefit. Much of the signal that is measured in an EM survey is due to the layered Earth and often provides relatively little information about the presence of three-dimensional conductive targets. Also, in the case of airborne surveys, flight related artefacts are regarded as noise since they may have a significant negative effect on the quality of the measured data. Enhancement of the signal is tantamount to increasing the signal to noise ratio by either increasing the signal of interest or by reducing the noise. With a limited ability to increase the signal, the most effective way to enhance the data is to reduce the noise component.

Enhancement of the EM data in this thesis has been developed along two related approaches: data acquisition and data processing.

7.1 Data Acquisition

Two new multi-system acquisition methods that make use of data redundancy have been developed, tested on synthetic data and trialed in the field. To achieve this, a sound theoretical basis was required. Both techniques were devised using the integral equation method of 3-D EM modelling that describes the total measured response as being comprised of a portion due to the currents flowing in the Earth layers (noise) and a portion due to the currents flowing in the non-layered structures i.e. the target body (signal). Relationships between the purely layered Earth responses using different field measurement systems were developed theoretically. These relationships were then used to combine the measured data in a particular way that generates a residual which is zero over a purely layered Earth. The residual is non-zero when 3-D anomalous bodies are present, while the dominant effect of layered structures is minimised. The residual signature produced by such a combination is therefore principally due to the effects of the non-layered structures.

To test the validity of these theoretical techniques of residual generation, forward 3-D numerical modelling in both the frequency and time domains was performed using a range of simple geological models. This required the development of new modelling programs to accurately compute the EM field components that would be measured on or above the Earth's surface as part of a geophysical survey. Part of this development included a new method for computing EM fields without using digital filters. The new method, which replaces Hankel transform integrals with derivatives of modified Bessel functions, was shown to compute the field components more accurately than common methods using digital filters and faster, using much less CPU time.

7.1.1 Small loop sources

The EM responses measured (or computed) using the HCP, VCP and VCA loop configurations were transformed into a residual quantity based on the relationship between their layered Earth responses. Reducing the layered Earth component from the data has been shown to greatly enhance the appearance of anomalous (non-layered) signals in profile curves. Being a combination of three different survey configurations, the signature of a target (mineral deposit) displayed by the residual contains more information than the signature displayed by the individual configurations. The multi-system approach results in a more complete measure of the geological response which translates into a more complete knowledge of the sub-surface structure. However, the residual often displays a more complicated signature to interpret, particularly when there are a number of non-layered structures in the survey area. The data combination technique reduces the layered Earth response but does not discriminate between anomalous signals. *All* non-layered responses are therefore enhanced. For simple situations some interpretative 'rules of thumb' have been developed that can be applied to provide a ‘first guess’ interpretation of field data.

The small-loop field example presented in the thesis provides evidence that the method is effective on 'real' data. Despite being taken in quite a hilly and resistive environment the field measurements were noticeably enhanced by the SLR - particularly at high frequencies. The in-phase residual appeared to be more responsive to topography than the sub-surface conductivity whereas the quadrature SLR provided an enhanced signature of the conductive zone. The method is expected to be more effective in flat, conductive terrains where the layered Earth component is larger, and the signal from the target is less apparent in the individual measurements.

7.1.2 Large loop sources

Large loop sources are limited to the horizontal orientation which restricts the use of redundant magnetic field measurements. However, a relationship between the magnetic field response and the *electric* field response was found that can be used to reduce the layered Earth part of the measured data. The relationship was used to derive a residual that has application to in-loop, separated loop and fixed-loop configurations. The results of numerical modelling show the technique to be very useful in reducing the layered Earth response in both frequency and time domain surveys. Like the small loop method, the large loop residual data more clearly displays the presence of a target than the data from measurements of one component only.

Forward modelling of the responses from large loop sources is a more difficult task than those due to dipole sources because of the need to compute Hankel transforms of Bessel functions. The numerical simulation produces model results that are not as accurate as one would wish in some cases, but still verify the usefulness of the technique to reduce the layered Earth response. The numerical examples shown in Chapter 3 verify the usefulness of the residual procedure.

Accurate measurement of electric fields in a practical setting is a difficult task that may place some limits on the usefulness of the LLR technique. The effect of conductivity variations near the electrodes may introduce an extra source of noise into the measurements that could be enhanced in the LLR. This was not found to be a problem in the field tests that have been conducted so far. The fixed-loop field test presented in this thesis demonstrates the ability of the residual to present a more complete picture of the sub-surface than either of the separate components from which it was derived. The residual profile emphasises the non-layered structures that are not so evident in the individual field measurements. The early-time features in the residual provide information about the changing overburden thickness while the existence of later time anomalies suggests the presence of a deeper conductive zone. Interpretation of the residual is a more complex matter than the interpretation based a single field component because the residual contains more information about the total EM field. Simple 'rules of thumb' have been developed for the large loop residual as a first guess interpretation of the field data. Time domain decay curve analysis also assists in the interpretation as the decay of the residual is greatly influenced by the presence of a conductive body.

The moving loop surveys also demonstrated that the combination of the magnetic and electric field responses could be used to reduce the layered Earth response. In addition to more clearly indicating the presence of conductive zones, the residual signature was evident earlier in time than the dB_z/dt signature. An advantage of observing a signature in the early time channels is that the need to measure very small signals late in time is not so necessary. This will lead to more efficient data acquisition and ultimately reduce the cost of EM surveys.

7.2 Data processing

The small loop residual concept also has application to airborne methods making it a versatile technique. The problem of flight-line related herringbones caused by alternately directed flight lines has been addressed and a new data processing technique based on the Radon transform has been developed. The Radon transform method of herringbone removal has been shown to remove herringbones from data maps more effectively than other procedures, while preserving the information content of the original measurements. By transforming the measured data to the Radon domain, it is possible to isolate and remove the herringbone artefacts by filtering the affected regions only.

The numerical forward and inverse Radon transforms are not exact, which results in an inability to recover the amplitudes exactly. This does not detract from the procedure since exact EM amplitudes in a map are not absolutely necessary for useful interpretation to be made.

Application of the Radon method to time domain airborne EM data measured with a fixed-wing system was shown to greatly improve the quality of a map by removing the unwanted herringbones and producing a more coherent and accurate map of the boundaries of conductive zones.

The Radon transform was also used to enhance linear events of interest by the application of selective scaling to portions of the transform domain data. The lineament enhancement method developed in this work was used to both enhance and attenuate selected linear features in geophysical maps. Although the bulk of the work in this thesis is directed at electromagnetic methods, the Radon domain processing was also applied to radiometric measurements with equal success.

7.3 Recommendations for further work

This work has introduced new methods and techniques for EM data enhancement. There are a number of improvements that might expand the usefulness of the techniques developed in this thesis. The measurement of the transient electric field is presently considered to be somewhat unreliable due to the influence of near surface inhomogeneities that may dominate the measured responses. Consequently, it is very rarely measured in current field preactice. Neglecting the electric field responses means that half of the useful information is being ignored. Further work needs to done to enable accurate and meaningful measurement of the transient electric field. This would benefit the LLR concept.

Improvements to instrument design and noise reduction techniques will inevitably result in better EM survey data quality generally. There would be a corresponding benefit to multi-system techniques. Along with the increased data quality will come a need to improve the interpretative aspects of the multi-system Residual concepts developed in this work. Computer assisted interpretation should be developed to accommodate the use of multi-system measurements and integral equation modelling needs to be developed further to enable more realistic models to be used. The analytical computational procedure developed in this work may be useful in this regard and should be extended to include large loop sources so that rapid modelling routines can be developed to assist the interpretation.

The field trials of the multi-system methods presented in this thesis showed the practical potential of the Residual concept. Other similar residuals, which are zero in the absence of anomalous 3-D bodies might also be developed and tested on field data.

The Radon transform has been shown to be more versatile than Fourier methods in enhancing geophysical maps and could be more widely used. The Radon method for removal of specific linear features in maps could be applied to magnetic data to remove fence-line, pipe-line and power-line anomalies.

CHAPTER 1

INTRODUCTION

1.1 Importance of the mineral industry to Australia

In 1996 Australia was the world's largest exporter of iron ore, bauxite and diamonds, the second largest exporter of alumina and the third largest exporter of aluminium and gold. Exports such as these contributed $16.5B to the Australian economy and represented approximately 22% of the total export earnings. Approximately $2B was spent on mineral exploration in Australia during 1997. These figures alone suggest that the mineral industry plays a major role in the economic well-being of Australia.

Here, like most other parts of the world, the evidence of modern society's reliance on mining and mining products is indisputable. It would not be possible for many of us to imagine life without the everyday products manufactured from materials extracted from the Earth at one of the thousands of operational mine sites around the world. Since the industrial revolution of the nineteenth century, technological advances in materials science have led to the development of new products and an ever increasing demand for raw materials such as aluminium, nickel, lead, titanium, tin, silver, silicon, uranium, antimony, zircon etc. It is now generally accepted in the mineral industry that almost all of the major, readily available surface and near-surface mineral deposits have been found. Future discoveries of economically viable mineral reserves will require a greater emphasis on the techniques of exploration geophysics to explore beneath surface cover such as regolith or water. Seismic methods have been very successful in probing deeper into the Earth in the search for oil and gas but the logistical difficulties associated with deep mining has restricted mineral exploration and mining to the upper-most 500 m or so. In order to sustain the ever-increasing demand for raw materials it is necessary to extend the reach of our exploration and mining technology.

1.2 Geophysics and resource exploration

Implicit in the term 'exploration' is an element of uncertainty. In order to determine the geological composition of the sub-surface it is necessary to acquire information from which models can be constructed. The role of the geophysicist is to provide the appropriate information to the geologist to enable a model of the structure and composition of the sub-surface to be produced. Such models are of great importance in terms of the overall exploration effort. In order to produce an accurate model of the sub-surface it is useful to have as much information of the physical properties of the Earth materials as possible. Some of the physical characteristics of Earth materials which are of interest to the geophysicist include properties such as density, porosity, magnetic susceptibility and electrical conductivity, whereas structural characteristics such as the location of faults, dykes, synclines, sedimentary contacts etc. are also very useful in developing a geological model.

A fundamental problem in geophysical exploration is that the quantities of interest cannot usually be measured directly because of the physical separation between the subject and the observer. The cost associated with routine large scale drilling and sampling of the sub-surface rocks to obtain a direct measure of the properties is prohibitive. Therefore, in order to deduce the sub-surface characteristics, measurements of physical quantities at (or above) the surface of the Earth must be interpreted and then related back to the characteristic being sought. For example, the density of sub-surface rocks can be deduced from measurements of the gravitational acceleration g at the Earth's surface. Variations in g can then be used to make inferences regarding the sub-surface distribution of rock density and hence the geological structure.

Successful geophysical exploration for mineral deposits has traditionally relied very heavily on magnetic and gravimetric surveys since they require simple instrumentation for measurements to be made and the data are relatively simple to interpret. However, like all geophysical methods, these methods are restricted in their application to situations where a sufficient contrast in the particular property exists. For the many instances where a significant magnetic or density contrast is not present, other methods based on the measurement of other physical properties must be used.

1.3 Electrical methods in mineral exploration

Electrical methods, such as direct-current (DC) resistivity, induced polarisation (IP), magnetotellurics (MT) and electromagnetic methods (EM) have been successfully used in the search for conductive mineral deposits, petroleum, ground-water, geothermal energy sources as well as general mapping of the sub-surface conductivity distribution (Mooney, 1980; Eadie et al., 1985; Vozoff, 1991; Spies and Frischknecht, 1991; Brescianini et al., 1992; Frohlich et al., 1994; Vogelsang, 1995). Electrical conductivity is the most widely varying of all the physical properties and so when using electrical methods for geophysical exploration it is anticipated that widely varying results will be obtained. The amount of current flowing through a material is related to its resistivity. Figure 1.1 shows the typical resistivities of some common Earth materials spanning seven orders of magnitude which gives some idea of the enormous variability likely to be encountered using electrical methods.

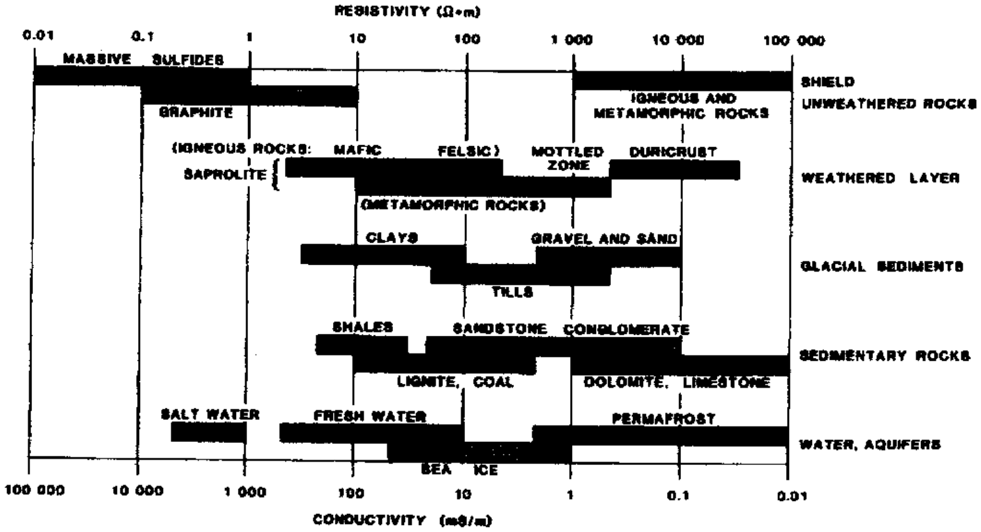

Figure 1.1 Resistivity of common Earth materials showing a variation of more than seven orders of magnitude. (After Palacky, 1991)

Common to all of the electrical methods is the need to measure electrical voltage or potential difference. The electric potential provides a measure of the electromagnetic field from which inferences about the flow of current (and subsequently the conductivity distribution) in the Earth can be made.

Unlike the passive techniques of magnetic and gravity surveys that require the measurement of a static potential field that is independent of the method of measurement, the electrical methods are more complicated and may involve a variety of source and receiver configurations. The measured electrical response is greatly influenced by the manner in which the Earth is energised and which component of the EM field is being measured.

In the direct current DC methods, an electric current is injected into the ground via a pair of electrodes connected to a direct current source. As the current flows through the Earth, two closely spaced sensors are used to measure the potential difference between them at the surface. Analysis of the potential difference measurements allows the conductivity of the Earth layers to be determined. DC methods are particularly useful for ground-water, salinity and pollution monitoring applications (Mooney, 1980; Frohlich et al., 1994; Vogelsang, 1995).

The electromagnetic methods differ from the DC methods by making use of a changing source current. The source current can either be injected into the ground via a pair of electrodes, or confined to a transmitter loop. In the latter case, the current loop acts as a magnetic source and the currents in the Earth are purely inductive. This method does not require direct contact with the ground and can, therefore, also be used for airborne surveys. Several modes of operation are currently in use both on land and in the air for a range of applications. The flow of current through the Earth produces a measurable response that is related to the conductivity structure of the underlying rocks. Changes in the electrical conductivity distribution can be significant pointers in the search for mineralisation.

1.3.1 Frequency domain electromagnetic surveys

In a frequency domain inductive EM (FEM) survey an alternating current with a particular frequency is passed around a transmitter loop. As the current in the transmitter loop is continuously changing, the magnetic field associated with the transmitter current is also changing. This causes an electrical current to be induced in the Earth materials directly below the transmitter. The magnitude of the induced current is dependent on the conductivity of the local geological structures. Measurement of the magnetic and electric fields on the Earth's surface or in a bore hole can provide information about the flow of current in the Earth and thereby lead to inferences being made about the electrical structures below the surface. The depth of investigation of a frequency domain survey is related to the transmitter frequency. A high frequency transmitter current will, due to attenuation in the conductive Earth media, only yield information about the near surface. Lower transmitter frequencies will enable the EM field to penetrate deeper into the Earth and provide information about greater depths. However, associated with the lower frequency is a reduced ability to induce currents in the conductive materials and therefore a smaller signal will be observed. It is usual practice to transmit a range of frequencies at each location in order to acquire information about the conductivity variations with depth. Modern equipment is capable of measuring several frequencies simultaneously which increases the efficiency of data collection and consequently helps to reduce the cost of the survey.

A commonly touted criticism of frequency domain surveys is the fact that the transmitter current is always switched on and the measurement of the Earth response must be made in the presence of the large primary field from the transmitter. This reduces the sensitivity of frequency domain surveys to small signals from deeply buried targets. This criticism has been addressed to a large degree by modern survey equipment that adequately compensates for the primary field component at the time of measurement and is sensitive enough to detect very small changes in the measured voltage. However, the unwanted response from the superficial Earth layers remains a major portion of the measured voltage that limits the sensitivity of FEM surveys to resolve small signals from deep targets. A thorough overview of frequency domain equipment and applications is given in Frischknecht et al. (1991).

1.3.2 Time domain electromagnetic surveys

In Australia the preferred EM method among geophysicists is the time domain or transient (TEM) method because of its ability to measure the response from conductive targets after the current in the regolith has decayed away. Utilising a variety of survey configurations and measurement parameters, the common methodology is the rapid switching of the transmitter current. The sudden change of magnetic field associated with the turning on or turning off of the current in the transmitting loop induces transient (eddy) currents directly below the transmitter loop that diffuse downward and outwards through the Earth. As the eddy currents diffuse away, they energise the Earth materials and measurement of the EM field components at the receiver at different time intervals allows the decay of the transient to be measured. The rate of decay, quantified by the use of a time constant τ, is related to the conductivity distribution in the Earth. In the search for massive sulfide mineralisation large decay time constants (i.e. slow decay rates) are of prime importance as they indicate the presence of conductive materials.

There has been a long-standing debate among geophysicists about the relative merits of frequency and time domain exploration methods with both sides being unable to convince the other of their point of view. A comparison of frequency and time domain surveys is given by Kaufman (1978a, 1989), McCracken et al. (1986a), and Gomez-Trevino (1987). In their study of noise limitations in EM methods, McCracken et al. (1986b) claim the only advantage to be gained by using a time domain instrument is associated with the large transmitter loops which tend to be fashionable. There is no intrinsic difference in relation to the physics of the induction process between frequency and time domain EM systems and a diplomatic agreement that each method has its relative advantages in particular applications has been adopted. What is not debated however is that *both* methods have their limitations when it comes to exploration beneath conductive overburden. A comprehensive overview of the range of EM applications is given by Spies and Frischknecht (1991).

1.3.3 What do electromagnetic surveys give us?

Whether dealing with frequency or time domain EM surveys, the desired outcome is an increased knowledge of the conductivity distribution below the Earth's surface. Regions of conductivity contrast are important in mineral exploration as they may be indicators of magmatic intrusion or fracturing, around which may be an increased likelihood of mineralisation. The EM response of a rock (from which its conductivity is estimated) is a complex characteristic that is more closely linked to the texture and moisture content of the rock than its mineral content (Keller, 1991). This is particularly so in regions of saline ground-water. Since it is impossible to identify the minerals present in a rock based on the measured EM response alone, a successful EM survey for mineral exploration will only provide an indication of areas that may warrant further investigation. At best, we can produce an *estimate* of the location, orientation, size and conductivity of an anomalous zone based on comparisons made with the responses computed using simple geological models.

1.4 The need for this work

In parts of the world where the Earth is sufficiently resistive to the flow of charge, attenuation of the energising eddy current is small and the EM inductive methods have proven to be very useful for mineral exploration. In Australia a wide range of EM techniques is routinely used for near surface investigations for ground-water and salinity applications as well as borehole methods for delineation of ore bodies in existing mines. Although EM methods have played a part in a few mineral deposit discoveries in Australia (Eadie et al., 1985; Brescianini et al., 1992), the method has not been as successful as it has been in other parts of the world. The main obstacle to successful EM surveys in Australia is the regolith (conductive overburden). The highly conductive and highly variable layer of weathered material covering about 80% of the continent severely restricts the transmission of energy to conductive ore bodies below it. Consequently the EM response of a conductive ore body, when measured on or above the surface, is often very small in comparison to the EM response of the regolith itself (Ward et al., 1974; Lajoie and West, 1976). It would be of great advantage to the mineral exploration industry in Australia if EM methods could be used to greater effect in regolith dominated terrains. This would enable much more of the continent to be thoroughly explored and would undoubtedly lead to more mineral deposits being found. The physics of EM induction in conductive terrains places limits on the ability of both frequency and time domain EM surveys to resolve sub-surface structures. Attenuation and broadening of target responses (Smith and West, 1987; West and Macnae, 1991) by the regolith are beyond the control of any survey design, except in the case of a borehole that extends below the regolith. If the effect of the regolith could be removed or at least *significantly reduced by data processing*, the small signals from target bodies would be more easily observed.

The vast expanse of the Australian continent means that mineral exploration in Australia is more suited to the use of airborne methods than ground methods. Airborne electromagnetic (AEM) surveys that are capable of mapping large areas of land in a very short period of time are used primarily for reconnaissance purposes, i.e. to locate conductive zones that may warrant further investigation. AEM systems have the same intrinsic limitations as ground surveys in regolith dominated regions and in addition, the data often contain flight related artefacts (Palacky and West, 1991) that can distort the signal and lead to a disjointed amplitude map being produced. Despite this, AEM technology has progressed to such a level that modern AEM systems are capable of producing conductivity maps that rival those obtained from surface measurements. It is expected that AEM will soon be used to direct the drilling programs of exploration companies without the use of follow-up land surveys. It is evident that airborne EM is set to become a very important tool in mineral exploration in Australia and other parts of the world so any developments that result in a better quality map from which more accurate information can be extracted will be of great benefit to the exploration industry.

1.5 Enhancement of EM signals

The complex diffusive nature of EM fields makes the task of data interpretation a difficult proposition in many geological settings. In the presence of a conductive regolith, which by its very nature is highly variable, the task becomes even more difficult. The signal from a conductive target may be overshadowed or masked by the response from the regolith, especially if the target is very deep or the overburden is very conductive. If the signal from the target could be enhanced in some way, these small anomalous signals would become more detectable by explorers.

The Macquarie dictionary defines enhancement as: raise to a higher degree; intensify; magnify.

On a very simplistic level an enhancement could be achieved by resetting the gain on the instrument, or by using a larger transmitter moment. In this way, the signal being measured is amplified, but the noise component would also be amplified. For the purposes of this work a more useful definition of the term enhancement is "any change to the measured data that results in an increase in the signal to noise ratio or to an improved representation of the true geological structure”

In the past there have been a number of techniques developed which aim to enhance the response of various targets. West et al. (1984) use continuous normalisation in fixed transmitter surveys to enhance the small signals measured at large distances from the transmitter loop. Kaufman (1978b) and Olm (1981) used slightly different redundancy methods involving the difference between responses measured at two frequencies to enhance the response from a target body below conductive cover. Doll et al. (1984) made use of the responses obtained using different coil separations to subtract the half-space response from the data. Asten (1992) used forward modelling to compute a time-domain half-space response which was then subtracted from field measurements to highlight the response of a target. The combination of data from different measurement systems can also be used to enhance the signal of interest to aid interpretation. For example, Fraser (1979) combined the responses obtained by different coil configurations to reduce the overburden effect in helicopter EM surveys. Buselli et al. (1990) used a combination of time domain EM and DC resistivity to delineate sub-surface contamination near a waste disposal site and Benson et al. (1997) made use of a combination of DC resistivity and very low frequency (VLF) EM measurements to map ground-water contamination. Raiche et al. (1985) made use of a combination of coincident loop EM and Schlumberger resistivity soundings to resolve layered structures.

The signal to noise ratio (SNR) is the most fundamental quantity of interest when measuring small responses from conductive targets. The variation in signal due to the presence of the target must be observable in the presence of other signals. Measurement of the EM signals usually involves a measurement of electrical voltage. This can be in the form of the electric potential between two points or the voltage induced in a receiver coil. In EM prospecting there are many sources of noise that can adversely affect the quality of the recorded data (e.g. Zonge and Hughes, 1991) that must be taken into account. These include electrode self-potential, transmitter drift, receiver mis-alignment, electronic response characteristics of the receiver, interference signals such as spherics, wind noise, topographical variation, cultural sources and geological noise. Pre-processing operations such as stacking and filtering of the measured voltages can greatly improve the quality of the data prior to inversion and interpretation (Macnae et al., 1984; Strack et al., 1989; Stephan and Strack, 1991). Numerical inversion routines can produce inaccurate results when working on noisy input data, so it is important to always acquire the highest quality data. In this work I limit the problem to one of geological noise and leave the other problems for further work on instrument design by other researchers.

1.6 Geological noise

Geological noise is that part of the measured response that arises from geological structures other than those of interest to the exploration objectives (Spies and

Frischnecht, 1991). Overburden response is a common example of geological noise associated with mineral exploration. In conductive environments such as those found in Australia, EM target signals are often very small and difficult to detect. Random noise in the measurements can be reduced by repeating the measurements many times and stacking the data. Coherent noise is enhanced by this procedure and therefore needs to be reduced by the use of appropriate filtering methods. Geological noise is a more difficult problem to address since it is created by the same induction and conduction processes that the survey is utilising to energise and detect the real target. Geological noise is not so much a problem of measurement, it is more a question of interpretation because it represents a real signal, just not the right one. Geological noise can only be identified and managed by careful interpretation. Multi-component and multi-system data provide a useful guide to identifying and explaining geological noise. If the aim of the survey were to map the lithological boundaries, then geological noise could refer to the small discrete packets of conductive (or resistive) but un-economic material that produce an anomalous response. In the search for conductive ore bodies, where the signal from discrete packets of conductive material is the target, geological noise is that part of the signal due to currents flowing in the 'normal' Earth layers i.e. the layered Earth response. The notion of geological noise is contentious since all geological responses are 'real' signals that have real value in helping to produce an accurate picture of the sub-surface. The task facing the geophysicist is to reorganise the measured responses in order to enhance the signal that will produce the most accurate and useful information of particular interest to the exploration objective.

For an EM survey to be successful in a particular application, the most important aspect is the appropriate choice of survey parameters. *The measured response is as* *much a function of how the measurements are made as it is of the electrical properties of the Earth.* Once the survey is completed the task then is to organise the data into an interpretable form. The information that can be extracted from any particular set of observations is limited by the quality of the observations, so it is not possible to extract more information from the data than was recorded during measurement. It is possible, however, to reorganise the data to more clearly display the relevant information. Appropriate processing techniques can enhance the signal of interest.

1.7 Composition of the thesis

In view of the above discussion this thesis will deal with the development of processing techniques to enhance the EM signal from conductive targets located in a conductive host environment. The processing techniques will be developed from two philosophical standpoints. The first being a novel and innovative approach to data *acquisition* and subsequent processing and the second being a more conventional *signal processing* approach based on data transformation and filtering. Although different in their methodology, the two approaches are linked by their common outcome: enhancement of EM signals.

In the first approach, the combined use of multiple acquisition systems as a means of reducing the layered Earth response will be investigated. The concept of data redundancy will be examined and applied to frequency and time domain EM systems to develop a residual quantity that contains a reduced layered Earth component and is therefore more sensitive to the presence of anomalous signals from a target body. The concept of signal enhancement by the reduction of the layered Earth response will be investigated through the results of 3-D numerical modelling. The results of field trials will also be presented.

The second approach is based on the more conventional method of signal processing by data transformation. The Radon transform is a well-known method of data processing that is used in many areas of science including geophysics. The Radon transform has the ability to decompose a 2-D image or map into 1-D, direction-specific components. Since the most common mode of EM data presentation is in the form of 2-D maps produced from 1-D measurements the Radon transform may have a role in the enhancement of the maps. To assist interpretation, it is often desirable that specific linear features of interest be enhanced for a clearer display. Also, features displayed in the map that relate to the specific method of measurement (acquisition artefacts) can make interpretation more difficult and should be removed by appropriate processing. The Radon transform has been successfully used for processing seismic data and its potential for use on other geophysical data needs investigation. The application of the Radon transform for the purpose of signal enhancement will be investigated using synthetic maps as well as real data from airborne EM and radiometric surveys.

In Chapter 2, the mathematical expressions for the electromagnetic fields on or above the surface of a layered Earth due to a current loop source are derived in terms of the magnetic Hertz potential. The integral equation method is used to compute the responses of a 3-D body located in a conductive layered Earth environment. As part of the mathematical development, a new analytical method of field computation that has application to a uniform half-space is presented and tested.

In Chapter 3 the mathematical relationships between selected EM field components are used to develop a procedure for reducing the layered Earth contribution to the measured data. The new processing technique, that combines the data measured using different survey configurations, is investigated using the results of numerical modelling obtained for a variety of simple geological models.

Chapter 4 examines the effect of the data combinations on the residual signature and provides some simple interpretative rules for determination of dip, strike direction and depth of the target.

In Chapter 5 the Radon transform is examined for use in a processing technique to improve the quality of geophysical maps. A new procedure is presented for the removal of 'herringbones' from airborne EM data maps together with a new procedure to selectively enhance the appearance of linear features in the maps.

Field examples that demonstrate the usefulness of the techniques developed in the thesis to enhance EM signals are presented in Chapter 6. The results of experimental field tests of the multi-system method are presented together with some examples of the Radon transform methods. The results of conventional acquisition and processing are included for the purpose of comparison. Also included is an example of the Radon transform method applied to radiometric data to demonstrate the versatility of the procedure.

CHAPTER 2

3-D ELECTROMAGNETIC NUMERICAL MODELLING

In this chapter, Maxwell's equations are used as the basis for computing the EM response of a 3-dimensional body embedded in a layered Earth. The theory presented here is not new and can be found in a number of geophysical papers (Raiche, 1974; Weidelt, 1975; Hohmann, 1975) and textbooks (Harrington, 1961; Ward and Hohmann, 1991; Kaufman and Keller, 1983) in one form or another. The variety of approaches used in the literature may lead to some confusion so a brief overview of the derivations useful for the remainder of the thesis is presented. The complexity of the derivations is limited by considering a 3-D body located in the lower part of a two-layered Earth although the method is applicable to Earth models having any number of layers. The integral equation approach to numerical modelling is used to compute the EM response of an arbitrarily shaped 3-dimensional body. The results of numerical modelling will be used to test the enhancement procedures developed in later chapters.

2.1 Maxwell's Equations

Maxwell's equations are the result of the classic discoveries made in the nineteenth century by Ampere, Faraday, Coulomb and Biot. Although simple in their individual meaning, the equations are used to describe all of the complex behaviours of electromagnetic fields. Employing the differential vector notation, Maxwell's equations can be written as:

$$\nabla\times H = J + \frac{\partial D}{\partial t}; \tag{2.1}$$

$$\nabla\times E = \frac{-\partial B}{\partial t}; \tag{2.2}$$

$$\nabla \cdot D = q; \tag{2.3}$$

and

$$\nabla \cdot B = 0, \tag{2.4}$$

where, using the SI system of units, H is the magnetic field intensity (A/m), D is the electric displacement (C/m^2), E is the electric field intensity (V/m), B is the magnetic induction (Wb/m^2), q is the electric charge density (C/m^3) and J is the current density (A/m^2).

These equations are applicable in any medium and are invariant under coordinate transformations. For simplicity the Cartesian coordinate system shown in Figure 2.1 is used throughout this thesis. In this coordinate system the vector differential operator del ∇ has the following form

$$\nabla = \frac{\partial}{\partial x}\hat{x} + \frac{\partial}{\partial y}\hat{y} + \frac{\partial}{\partial z}\hat{z}, \tag{2.5}$$

where $\hat{x}, \hat{y}$ and $\hat{z}$ represent the unit vectors in the x, y and z directions respectively.

2.1.1 Constitutive relations

The electromagnetic vector functions B, D, E, H and J are related by the relations

$$D = \tilde{\varepsilon} \cdot E, \tag{2.6}$$

$$B = \tilde{\mu} \cdot H, \tag{2.7}$$

and

$$J = \tilde{\sigma} \cdot E. \tag{2.8}$$

In the most general sense the quantities $\tilde{\varepsilon}, \tilde{\mu}$ and $\tilde{\sigma}$ are complex tensors that describe the electrical permittivity, the magnetic permeability and electrical conductivity of the medium in question.

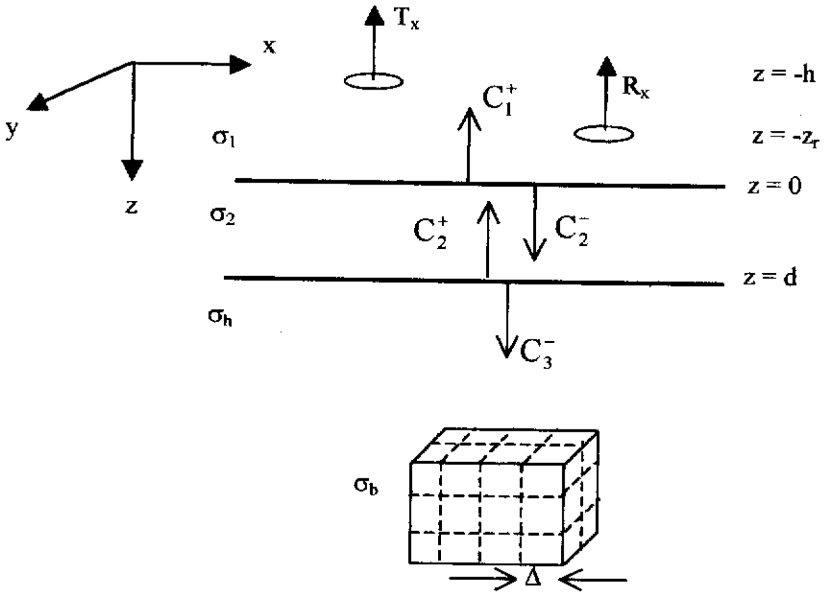

Figure 2.1 An arbitrarily shaped 3-D body located in the lower level of a two-layered Earth used for EM modelling. The transmitter and receiver are both located in region 1. The constants represent the spectral Hertz potential amplitudes at each interface.

In order to simplify the analysis, the electromagnetic properties of the media are assumed to be linear, isotropic, homogeneous and independent of time, temperature and pressure. In this thesis, low frequency ($< 10^5$ Hz) inductive EM methods are examined and the analysis can be further simplified by the assumption of free-space values for the permittivity and permeability of the Earth materials i.e. $\varepsilon = \varepsilon_0$ and $\mu = \mu_0$.

Using the relationships given in Maxwell's equations it can be shown (Wangsness, 1979; Ward and Hohmann, 1991) that

$$(\nabla^2 + k^2)H = 0, \tag{2.9}$$

where $k^2 = \omega^2 \mu_0 \varepsilon_0 - i\omega\mu_0\sigma$ is the wave number.

Equation (2.9) is known the magnetic Helmholtz equation for a source-free region. This equation holds true for all source-free regions regardless of their complexity. Alternatively, a similar equation can be derived for the electric field,

$$(\nabla^2 + k^2)E = 0. \tag{2.10}$$

In electromagnetic methods of geophysical exploration an external electromagnetic source is used to energise the Earth. The mathematical equation that governs the behaviour of the fields must therefore be modified to reflect the presence and nature of the source. In a region that contains an electric dipole source located at coordinate (x_s, y_s, z_s) equation (2.10) becomes

$$(\nabla^2 + k^2)E = \sigma' I \delta(x - x_s)\delta(y - y_s)\delta(z - z_s)\partial l, \tag{2.11}$$

where σ' is the complex conductivity $\sigma' = \sigma + i\omega\varepsilon_0$ of the medium, I is the current in the dipole and ∂l is the dipole length. The dirac delta functions δ are used to indicate that the source is only present at the location (x_s, y_s, z_s).

The equivalent equation for the case of a magnetic dipole source located at (x_s,y_s,z_s) is

$$(\nabla^2 + k^2)H = \frac{I}{2\pi}\delta(x - x_s)\delta(y - y_s)\delta(z - z_s)\partial A \qquad (2.12)$$

where ∂A is the effective area of the dipole loop.

For the purpose of further analysis and to avoid duplication of effort, it is convenient to replace the magnetic and electric field vectors in equations (2.11) and (2.12) with the Hertz potential π (Stoyer, 1977) which is related to the electric and magnetic fields by

$$E = k^2\pi^E + \nabla\nabla\cdot\pi^E - i\omega\mu_0\nabla\times\pi^M \qquad (2.13)$$

and

$$H = k^2\pi^M + \nabla\nabla\cdot\pi^M + \sigma'\nabla\times\pi^E, \qquad (2.14)$$

where the superscripts M (magnetic) and E (electric) indicate the nature of the source of the potential being used. By doing so, the electric and magnetic fields can be considered together in one equation without the need to repeat an almost identical procedure. The electromagnetic field resulting from an external source is fully described by

$$(\nabla^2 + k^2)\pi = S\delta(x - x_s)\delta(y - y_s)\delta(z - z_s)\partial s \qquad (2.15)$$

where the source terms S and ∂s will vary according to the nature of the source.

The solution of the above inhomogeneous equation depends on the nature of the particular environment being considered. For the case of a uniform whole space, Wait (1982) provides the solution as

$$\pi = \frac{S}{2\pi}\int_0^\infty \frac{\lambda}{p} e^{-pz} J_0(\rho\lambda)\partial\lambda, \qquad (2.16)$$

where $p^2 = \lambda^2 - k^2$, ρ is the horizontal displacement vector, J_0 is the Bessel function of the first kind of order zero and λ is the integration variable.

Equation (2.16) can be integrated analytically (Erdelyi, 1954) to give

$$\pi = S\frac{e^{-ikr}}{r}, \tag{2.17}$$

where r is the displacement vector given by $r^2 = \rho^2 + z^2$.

The field components H_x, H_y, H_z, E_x, E_y, E_z, are readily obtained from the Hertz potential using equations (2.13) and (2.14).

2.2 Layered Earth computation

In order to compute the magnetic and electric fields for the case of a layered Earth environment the effects of the layer boundaries must be taken into account. Using the simple two layered Earth model shown in Figure 2.1, and following normal procedures for the solution of inhomogeneous equations (Rainville and Bedient, 1974; Spiegel, 1968) the total solution of equations (2.11) and (2.12) can be written as the sum of the homogeneous solution and the particular solution.

To facilitate solution of the homogeneous equation, use is made of the two dimensional Fourier transform

$$F\ \{A(x,y)\} = \hat{A}(k_x,k_y) = \iint A(x,y)e^{-i(k_x x+k_y y)}\partial x\partial y, \tag{2.18}$$

and the derivative property of the Fourier transform

$$F\ \{\tfrac{\partial}{\partial x}A(x)\} = -ik_x\hat{A}(k_x). \tag{2.19}$$

In equations (2.18) and (2.19) $F\{\}$ represents the Fourier transform operator, A(x,y) is an arbitrary two dimensional vector, $\hat{A}(k_x,k_y)$ is the corresponding spectral domain vector and k_x is the spectral wavenumber corresponding to the spatial domain x direction.

Since the Earth layers are considered to be infinite in their horizontal extent, application of equations (2.18) and (2.19) allows the space domain differential equation in three dimensions shown in equation (2.15) to be recast as an equivalent spectral domain differential equation in one dimension i.e.

$$\frac{\partial^2}{\partial z^2}\hat{\pi} - (k_x^2 + k_y^2 - k^2)\hat{\pi} = 0, \tag{2.20}$$

where $\hat{\pi}$ is the spectral domain Hertz potential. The partial differential equation of equation (2.20) is a second order ordinary differential equation of one variable in the Fourier domain that has solutions of the form of upward and downward propagating waves i.e.

$$\hat{\pi}_i = C_i^+ e^{-p_i z} + C_i^- e^{p_i z}. \tag{2.21}$$

C_i^+ and C_i^- represent the amplitude of the upward and downward waves in layer i respectively and are constants to be determined by the application of the appropriate boundary conditions. To this end I adopt the propagator matrix formulation (Patra and Mallick, 1980; Wait, 1982; Kaufman and Keller, 1983) and write the potential within each layer in terms of the potential at each interface,

$$\hat{\pi}_1 = C_1^+ e^{-p_1 z} + C_1^- e^{p_1 z}, \tag{2.22}$$

$$\hat{\pi}_2 = C_2^+ e^{-p_2 z} + C_2^- e^{p_2 z}, \tag{2.23}$$

$$\hat{\pi}_3 = C_3^+ e^{-p_3 z} + C_3^- e^{p_3 z}. \tag{2.24}$$

Since layer 1 is the uppermost layer, there cannot be a downward decaying wave so the constant C_1^- can be set to zero. A similar line of reasoning leads to C_3^+ being set to zero leading to

$$\hat{\pi}_1 = C_1^+ e^{-p_1 z} \tag{2.25}$$

and

$$\hat{\pi}_3 = C_3^- e^{p_3 z}. \tag{2.26}$$

To evaluate the constants C_1^+, C_2^+, C_2^- and C_3^- in equations (2.22) to (2.24), the particular solution is added to the expression for the layer containing the source (layer 1) and the boundary conditions at each interface are applied.

2.2.1 Boundary conditions

The behaviour of the EM field at an interface between two different media requires special attention due to the different properties of the media on opposite sides of the interface. Boundary conditions can be derived directly from the integral representation of Maxwell's equations (Stratton, 1941; Ward and Hohmann, 1991) but are simply stated here.

At the boundary between medium i and medium i + 1, the normal component of magnetic flux intensity, B^n is continuous i.e.

$$B_i^n = B_{i+1}^n. \tag{2.27}$$

The tangential component of the magnetic field intensity H^t is continuous if there is no surface current i.e.

$$H_i^t = H_{i+1}^t. \tag{2.28}$$

The tangential component of the electric field intensity E^t is continuous i.e.

$$E_i^t = E_{i+1}^t, \tag{2.29}$$

whereas the normal component of the electric displacement D^n is discontinuous due to the accumulation of electric charge at the interface i.e.

$$D_i^n - D_{i+1}^n = q_s. \tag{2.30}$$

2.2.2 Evaluation of the spectral constants

2.2.2.1 Vertical magnetic dipole

When considering magnetic dipole sources, application of the boundary conditions to the spectral domain Hertz potential for evaluation of the spectral constants begins with consideration of equation (2.28) which states that

$$k_i^2\hat{\pi}_i + \nabla\nabla\cdot\hat{\pi}_i = k_{i+1}^2\hat{\pi}_{i+1} + \nabla\nabla\cdot\hat{\pi}_{i+1}. \tag{2.31}$$

Equation (2.29) states that

$$-i\omega\mu_0\nabla\times\hat{\pi}_i = -i\omega\mu_0\nabla\times\hat{\pi}_{i+1}. \tag{2.32}$$

For the particular case of a vertical magnetic dipole on or above a horizontally layered Earth, the tangential fields are those in the x and y direction, and only the vertical component $\hat{\pi}^z$ of the Hertz potential exists. So, by expanding the vector operators in equations (2.31) and (2.32) the x component of the magnetic field intensity H_i^x and electric field E_i^x in the i'th layer can be written as

$$\hat{H}_i^x = \tfrac{\partial}{\partial x}\tfrac{\partial}{\partial z}\hat{\pi}_i^z, \tag{2.33}$$

and

$$\hat{E}_i^x = -i\omega\mu_0\tfrac{\partial}{\partial y}\hat{\pi}_i^z. \tag{2.34}$$

Now, due to the infinite extent of the uniform, isotropic layers in the x and y directions on either side of the boundary, the derivatives with respect to those directions in each layer must be equal. Equations (2.33) and (2.34) can therefore be integrated with respect to x and y, respectively, to yield the boundary conditions that must be satisfied by the spectral Hertz potential i.e.

$$\tfrac{\partial}{\partial z}\hat{\pi}_i^z = \tfrac{\partial}{\partial z}\hat{\pi}_{i+1}^z \tag{2.35}$$

and

$$\hat{\pi}_i^z = \hat{\pi}_{i+1}^z . \tag{2.36}$$

The same conditions can be derived by consideration of the y directed field components $\hat{H}_i^y$ and $\hat{E}_i^y$. Application of the boundary conditions leads to the spectral constant C_3^- being evaluated as

$$C_3^- = \left[\frac{2S\lambda(p_2 + p_3)e^{p_1 h - p_2 d}}{(p_3 - p_2)(p_2 - p_1)e^{-p_2 d} + (p_3 + p_2)(p_2 + p_1)e^{p_2 d}} \right], \tag{2.37}$$

from which the other constants C_1^+, C_2^+, C_2^- can be determined via the propagator matrix. The spectral potential on or above the surface of the Earth is found using equation (2.25).

2.2.2.2 Horizontal magnetic dipole

In the case of an x-directed magnetic dipole, there exists two components of the spectral Hertz potential. One, $\hat{\pi}_i^x$, is in the direction of the source and the other, $\hat{\pi}_i^{zx}$, is perpendicular to the boundaries (Patra and Mallick, 1980; Ward and Hohmann, 1991). The perpendicular component is created by the build-up of electric charge at the boundaries between the layers.

In this case $\hat{H}_i^x$ and $\hat{E}_i^x$ in any layer are given by

$$\hat{H}_i^x = k_i^2 \hat{\pi}_i^x + \frac{\partial^2}{\partial x^2} \hat{\pi}_i^x + \frac{\partial^2}{\partial x \partial z} \hat{\pi}_i^{zx} \tag{2.38}$$

and

$$\hat{E}_i^x = -i\omega\mu_0 \frac{\partial}{\partial y} \hat{\pi}_i^{zx} , \tag{2.39}$$

whereas H_i^y and E_i^y are given by

$$\hat{H}_i^y = \frac{\partial^2}{\partial y \partial x} \hat{\pi}_i^x + \frac{\partial^2}{\partial y \partial z} \hat{\pi}_i^{zx} \tag{2.40}$$

and

$$\hat{E}_i^y = i\omega\mu_0(\tfrac{\partial}{\partial z}\hat{\pi}_i^x - \tfrac{\partial}{\partial x}\hat{\pi}_i^{zx}). \tag{2.41}$$

The superscript zx represents the z-directed potential due to an x-directed source. Consideration of these four equations at the boundaries between layers leads to the conditions required to evaluate the spectral constants.

i.e.

$$\hat{\pi}_i^{zx} = \hat{\pi}_{i+1}^{zx}, \tag{2.42}$$

$$\tfrac{\partial}{\partial z}\hat{\pi}_i^{zx} = \tfrac{\partial}{\partial z}\hat{\pi}_{i+1}^{zx}, \tag{2.43}$$

$$k_i^2\hat{\pi}_i^x = k_{i+1}^2\hat{\pi}_{i+1}^x, \tag{2.44}$$

$$\tfrac{\partial}{\partial x}\hat{\pi}_i^x + \tfrac{\partial}{\partial z}\hat{\pi}_i^{zx} = \tfrac{\partial}{\partial x}\hat{\pi}_{i+1}^x + \tfrac{\partial}{\partial z}\hat{\pi}_{i+1}^{zx}. \tag{2.45}$$

A similar set of equations can be derived for the case of a y-directed magnetic dipole. Application of these four equations for the evaluation of the spectral domain constants requires a significant amount of algebraic manipulation and is not presented here. The spectral Hertz potential constant C_1^+ that applies to the upward decaying potential in the direction of the source moment, is found to be

$$C_1^+ = \frac{S\lambda}{p_1}e^{2p_1h}\left[\frac{r(1+q)e^{-2p_2d}+(1-q)}{r(1-q)e^{-2p_2d}+(1+q)}\right], \tag{2.46}$$

$$\text{where } q = \frac{k_1^2p_2}{k_2^2p_1} \text{ and } r = \left(\frac{k_3^2p_2-k_2^2p_3}{k_3^2p_2+k_2^2p_3}\right). \tag{2.47}$$

A constant $C_1^{+\prime}$ applies to the potential that is perpendicular to the source moment (eg. $\hat{\pi}_i^{zx}$) and is written in terms of the other constants as

$$C_1^{+\prime} = \frac{\lambda\left[T(e^{-p_2h}-1)\right]}{(p_2-p_1)(2e^{-p_2h}-1)}, \tag{2.48}$$

where

$$T = C_2^+ e^{(p_1 - 2p_2)h} + C_2^- e^{p_1 h} - C_1^+ e^{-2p_2 h} - \tfrac{S\lambda}{p_1} e^{(2p_1 - p_2)h} . \tag{2.49}$$

Having evaluated the spectral domain Hertz potential constants, it is then possible to return to the space domain by making use of the 2-D inverse Fourier transform

$$F^{-1}\left\{\hat{A}(k_x, k_y)\right\} = A(x, y) = \iint \hat{A}(k_x, k_y) e^{(k_x x + k_y y)} \partial k_x \partial k_y . \tag{2.50}$$

The cylindrical symmetry associated with the layered Earth model allows the double integral in equation (2.50) to be written as a Hankel transform integral (Banos, 1966) of the form

$$\int_{-\infty}^{\infty}\int_{-\infty}^{\infty} \hat{A}(k_x, k_y) e^{(k_x x + k_y y)} \partial k_x \partial k_y = 2\pi \int_0^{\infty} \hat{A}(\lambda) \lambda J_0(\rho\lambda) \partial\lambda , \tag{2.51}$$

where

$$\lambda^2 = k_x^2 + k_y^2 \tag{2.52}$$

and

$$\rho^2 = x^2 + y^2 . \tag{2.53}$$

Using equation (2.51) the Hertz potential on the surface of the Earth can be written as

$$\pi_1 = \int_0^{\infty} (C_1^+ + C_1^{+\prime}) e^{-p_1 z} \lambda J_0(\rho\lambda) \partial\lambda \tag{2.54}$$

to which the vector differential operations of equations (2.31) and (2.32) are applied to obtain the desired magnetic and electric field components.

2.3 Integral equation approach to 3-D modelling

Computation of the EM response of a 3-D target body can be achieved using Maxwell's equations in differential form or integral form. The differential methods of finite elements (Coggon, 1971; Pridmore et al., 1981) or finite difference (Oristaglio and Hohmann, 1984; Wang and Hohmann, 1993) require the EM fields to be computed everywhere that is close enough to have an influence on the target body. Despite being very accurate and versatile, the differential equation (DE) methods require the construction of extensive mathematical grids or networks and the solution of a very large system of linear equations. DE methods are very expensive in terms of computer time and memory. The integral equation (IE) approach to 3-D modelling (Raiche, 1974; Hohmann, 1975; Weidelt, 1975; Meyer, 1976; Wannamaker et al., 1984) has the advantage that the fields inside the 3-D body can be computed by a volume integration that is restricted to the 3-D body itself. The IE method drastically reduces the computational requirements but is limited in its ability to model complex geological structures. The IE method requires the use of a simple layered Earth model. Hybrid schemes (Scheen, 1978; Lee et al., 1981; Best et al., 1985) have also been successful in 3-D EM modelling. In these methods an integral equation approach is used for computing the fields at the outer boundary of the 3-D body and a finite difference approach for the fields inside the 3-D body. Hybrid methods also require the use of a simple layered Earth model.

To develop the mathematical procedure for computing the EM response of a geological target, consider the simple geological model shown in Figure 2.1 of an arbitrarily shaped 3-dimensional body located in the lower layer (host region) of a two-layered Earth model. Above the surface is the region that represents the atmosphere characterised by zero conductivity and infinite upward vertical extent. The upper Earth layer is characterised by a conductivity of σ_1 and thickness d and represents a uniform overburden layer. The lower Earth layer, the host layer, has conductivity σ_h and is infinite in its downward vertical extent. A transmitter (a horizontal loop of current in this case) is situated above the surface with its centre at the location (x_s,y_s,z_s) separated from a receiver centred at the location (x_r,y_r,z_r).

The electromagnetic response at the receiver location resulting from a harmonic transmitter current $I_o e^{i\omega t}$ can be calculated using the integral equation

$$E^T_{(r)} = E^L_{(r)} + \int_V G(r,r')J_{(r')}dV. \qquad (2.55)$$

In equation (2.55) $E^T_{(r)}$ is the total field at the receiver location (r), $E^L_{(r)}$ is the field at the receiver due solely to the layered Earth response, $G(r,r')$ is the tensor Green's function that relates the electric field at location r to that at r′ and $J_{(r')}$ is the scattering current density located inside the 3-D body at the location r′. The integration over the volume of the 3-D body represents the extra response observed at the receiver due to the scattering currents within the body.

The layered Earth response is computed as described in the previous section. To compute the effect of the 3-D body I follow the methods of Raiche, (1974), Hohmann, (1975), and Weidelt, (1975) and divide the 3-D body into a number of cubic elements. Each element can be considered as a separate source of scattering current that influences the current flowing in all of the other elements. The mutual interaction between the currents in the elements requires the solution of a system of equations to determine the electric fields within each element.

2.3.1 Electric fields inside the 3-D body

The most important aspect of 3-D modelling is the determination of the scattering currents inside the body. The current flowing in one part of the body affects the current flowing in all other parts and cannot therefore be determined without consideration of the body as a whole. The electric field E_m at the centre of an arbitrary element m is given by Hohmann (1975) as

$$E_m^T = E_m^L + \frac{(\sigma_b - \sigma_h)}{\sigma_h} * \sum_{n=1}^{N} \Gamma_{mn} E_n , \tag{2.56}$$

where E_n is the electric field at the centre of element n and Γ_{mn} is the integrated Green's dyadic that relates the field at the centre of element m to the volume integral of the current flowing in element n. Details of the volume integration can be found in Wannamaker et al., (1984) and Hohmann, (1975). Equation (2.56) can be re-written as

$$\left(\sum_{n=1}^{N} \frac{(\sigma_b - \sigma_h)}{\sigma_h} \Gamma_{mn} - \delta_{mn} \right) E_n = -E_m^L , \tag{2.57}$$

where δ_{mn} is the Kronecker delta to account for the case when n = m. This can be recast as a partitioned matrix equation

$$|K| \cdot |E| = -|E^L| , \tag{2.58}$$

in which the elements of $|K|$ are the 3x3 Green's dyadic for each of the N body elements. Solution of this matrix equation for the electric fields at the centre of each element E_i is achieved using matrix inversion methods i.e.

$$|E| = -|K|^{-1} \cdot |E^L| . \tag{2.59}$$

To evaluate the $|K|^{-1}$ matrix any recognised method can be used, including LU decomposition, singular value decomposition and the method of conjugate gradients.

Once the fields inside the elements have been determined, the EM fields at the receiver location are determined using equation (2.55).

2.3.2 Computational accuracy

The issue of accuracy in 3-D computation is a problem that has many facets, not the least of which is the programmer's ability to avoid numerical instabilities. The level of discretization of the 3-D body is very important to the accuracy of the computed response (Raiche, 1978) and will depend on the model in question. It is not possible to prescribe an optimum element side length Δ but a generally accepted rule of thumb is $\Delta < {}^{\delta}\!/_{2}$, where δ is the skin depth of the electric field inside the body. Due to the complicated nature of the computations it is not surprising that the results obtained with one modelling program do not always match those obtained using another. In some cases, the results will only be of the same order of magnitude and exhibit the same general trends in terms of frequency and spatial dependency. The most difficult aspect of the computation is the evaluation of the Hankel transform integrals associated with the various EM field components.

2.3.3 Hankel transforms using digital filters

The evaluation of the Hankel transform integrals necessary to compute the EM Hertz potential can be achieved using digital convolution filters (Ghosh, 1971; Koefoed, 1972). The speed, versatility and simplicity of use of digital filters have led to their widespread acceptance and use in many forward modelling and inversion applications (Kumar, 1974; Das and Verma, 1982). As a result, a range of filters has been produced with the aim of improving the accuracy and robustness of the computation (Anderson, 1979; Johansen and Sorensen, 1979; Christensen, 1990; Mohsen and Hashish, 1994; Guptasarma and Singh, 1997). However, in some cases, the filters fail to produce a convergent result, which must therefore introduce some doubt about their accuracy. Also, by virtue of their finite length and digital nature, even when convergence is achieved, they produce only an approximation to the correct result (albeit usually a very good one). Accuracy can be improved by increasing the range and density of sample points used by the filter. Doing so, however, increases the number of computations (and consequently the time) required to evaluate each integral. It is usual to balance the need for greater accuracy against the extra computational time associated with the use of very long filters. In 3-D EM modelling, where the Hankel transforms are computed many times depending on the number of discretised elements being used, the computation can become extremely slow. Also, the accumulated error associated with the repeated approximation implicit in the use of digital filters may have a significant impact on the accuracy of the final result.

Accurate filters are designed for use with a particular type of input function. In most EM modelling programs the Hankel transforms required to compute different EM components are evaluated using the same J_0 and J_1 filters regardless of the complexity of the input function. It is unrealistic to expect that a filter that has been designed for use with a particular type of input function, will be as accurate when used for a different type. Consequently, the digital filters do not always produce accurate results. As an indication of this, Table 2.1 lists the analytical values of some common Hankel type integrals with the corresponding values I obtained using three different convolution filters. While the majority of results are very accurate, it is seen in some cases that the digital filters have failed to produce an accurate result. The most recently produced filters (Guptasarma and Singh, 1997) are seen to produce the most accurate results.

Function	Analytical value	Koefoed	Christensen	Guptasarma and Singh
$\int_0^\infty \lambda J_0 d\lambda$	0	-1.23072×10^{-5}	7.72832×10^{-8}	4.76286×10^{-13}
$\int_0^\infty \lambda^2 J_0 d\lambda$	-1.0×10^{-6}	-1.53178×10^{-6}	-1.00125×10^{-6}	-9.99999×10^{-7}
$\int_0^\infty \lambda^3 J_0 d\lambda$	0	-1.80273×10^{-3}	-6.05820×10^{-9}	5.23473×10^{-11}
$\int_0^\infty \lambda J_1 d\lambda$	1.0×10^{-4}	1.00047×10^{-4}	9.99050×10^{-5}	9.99999×10^{-5}
$\int_0^\infty \lambda^2 J_1 d\lambda$	0	-3.58959×10^{-7}	3.31268×10^{-8}	-6.09364×10^{-11}
$\int_0^\infty \lambda^3 J_1 d\lambda$	-1.0×10^{-8}	-4.28875×10^{-6}	-3.68692×10^{-8}	-7.40156×10^{-8}
$\int_0^\infty e^{-\lambda z} J_0 d\lambda$	9.95037×10^{-3}	9.95125×10^{-3}	9.94991×10^{-3}	9.95037×10^{-3}
$\int_0^\infty \frac{\lambda e^{-pz}}{p} J_0 d\lambda$	4.27138×10^{-3}	4.27136×10^{-3}	4.27114×10^{-3}	4.27138×10^{-3}
$\int_0^\infty J_0 d\lambda$	1.0×10^{-2}	9.99995×10^{-3}	1.0×10^{-2}	1.0×10^{-2}
$\int_0^\infty J_1 d\lambda$	1.0×10^{-2}	9.99996×10^{-3}	9.99952×10^{-3}	9.99999×10^{-3}

Table 2.1 Comparison of numerical filters for evaluating common Hankel type integrals. The filters occasionally do not produce accurate results.

2.4 Analytical computation of EM field components

A number of authors (Fuller and Wait, 1976; Slob and Van den Berg, 1995) have published mathematical descriptions of the analytical computation of electromagnetic fields in the frequency and time domains. The whole-space problem is relatively straight-forward. In the case of a half-space, it is a commonly held view (Frishknecht et al., 1991; Ward and Hohmann, 1991) that analytical expressions for the Hankel transform integrals shown in equation (2.54) are available only for the case of both the transmitter and receiver being located on the surface of the Earth (i.e. z = 0). In the case of a vertical magnetic dipole source, Spies and Frischknecht (1991) write the electric and magnetic field components as

$$H_x = \frac{-mk^2}{4\pi}[I_1K_1 - I_2K_2], \tag{2.60}$$

$$E_y = \frac{-m}{2\pi\sigma\rho^4}[3-(3+3ik\rho-k^2\rho^2)e^{-ik\rho}], \tag{2.61}$$

$$H_z = \frac{-m}{2\pi k^2\rho^5}[(9+9ik\rho-4k^2\rho^2-ik^3\rho^3)e^{-ik\rho}-9]. \tag{2.62}$$

In equations (2.60) to (2.62), m represents the transmitter moment. In equation (2.60) I_1 and I_2 are the modified Bessel functions of the first kind of order 1 and 2 respectively and K_1 and K_2 are the modified Bessel functions of the second kind of order 1 and 2 respectively. All four of these modified Bessel functions have the argument ½ ikρ.

Raiche and Coggon (1975) derived analytical expressions for the electric tensor Green's functions for the scattering current sources inside an anomalous target zone located in a half-space. In the case of a layered Earth, the complexity of the input functions prevents an analytical solution being obtained, unless simplifying approximations are made. Mahmoud et al. (1979) present an analytical solution for the EM fields *on the surface* of a two-layered Earth but, presently, there appears to be no published analytical solutions for the fields *within* the Earth, even for a half-space.

2.4.1 Analytical computation of EM fields within a half-space

I now extend the work of Raiche and Coggon (1975) to derive analytical expressions for the field components below the surface of a uniform half-space due to a vertical magnetic dipole source on the surface. Using equations (2.25) and (2.37) I write the vector potential within the half-space at offset ρ and depth z as

$$\pi^M = \frac{m}{2\pi}\int_0^\infty \frac{\lambda e^{-p_2 z}}{p_1 + p_2} J_0(\rho\lambda)\partial\lambda . \qquad (2.63)$$

This is equivalent to the expressions given by Patra and Mallick (1980) and Ward and Hohmann, (1991). Using equations (2.13) and (2.14) the EM field components can be written as

$$H_x = \frac{mx}{2\pi k^2 \rho}\int_0^\infty p_2 \lambda^2 (p_1 - p_2) e^{-p_2 z} J_1 d\lambda . \qquad (2.64)$$

$$E_y = \frac{mx}{2\pi\sigma\rho}\int_0^\infty \lambda^2 (p_1 - p_2) e^{-p_2 z} J_1 d\lambda , \qquad (2.65)$$

and

$$H_z = \frac{m}{2\pi}\int_0^\infty \lambda (p_1 - p_2) e^{-p_2 z} J_0 d\lambda - \frac{m}{2\pi k^2}\int_0^\infty p_2^2 \lambda (p_1 - p_2) e^{-p_2 z} J_0 d\lambda . \qquad (2.66)$$

The integrals in equations (2.64) to (2.66) can be written in closed form by making use of the quasi-static approximation (by setting $p_1 = \lambda$) and introducing the Foster integral F, and Sommerfeld integral S, and their analytical equivalents

$$F = \int_0^\infty \frac{e^{-p_2 z}}{p_2} J_0(\rho\lambda)d\lambda = I_0[\tfrac{ik}{2}(r - z)].K_0[\tfrac{ik}{2}(r + z)], \qquad (2.67)$$

$$S = \int_0^\infty \frac{\lambda}{p_2} e^{-p_2 z} J_0(\rho\lambda)d\lambda = \frac{e^{-ikr}}{r}. \qquad (2.68)$$

In Equation (2.67) I_0 is the modified Bessel function of the first kind of order 0 and K_0 is the modified Bessel function of the second kind of order 0. The displacement vector r is given by $r^2 = \rho^2 + z^2$.

I show in Appendix A that the expressions in equations (2.64) to (2.66) can be replaced by a combination of the derivatives of the Sommerfeld and Foster integrals, i.e.

$$H_x = \tfrac{x}{2\pi k^2 \rho}(F_{\rho\rho\rho zz} + \tfrac{1}{\rho}F_{\rho\rho zz} - \tfrac{1}{\rho^2}F_{\rho zz} - S_{\rho zzz}), \qquad (2.69)$$

$$E_y = \tfrac{x}{2\pi\sigma\rho}(-F_{\rho\rho\rho z} - \tfrac{1}{\rho}F_{\rho\rho z} + \tfrac{1}{\rho^2}F_{\rho z} + S_{\rho zz}), \qquad (2.70)$$

$$H_z = \tfrac{1}{2\pi}(F_{\rho\rho z} + \tfrac{1}{\rho}F_{\rho z} - S_{zz}) + \tfrac{1}{2\pi k^2}(F_{\rho\rho zzz} + \tfrac{1}{\rho}F_{\rho zzz} - S_{zzzz}), \qquad (2.71)$$

where the subscripts of the right members of equations (2.69) to (2.71) indicate differentiation with respect to that variable. Each term inside the brackets in equations (2.69) to (2.71) can be replaced by its analytical equivalent derived using equations (2.67) and (2.68). I provide selected examples of these expressions in Appendix B. Note that for the surface EM fields where z = 0, equations (2.69) to (2.71) are equivalent to equations (2.60) to (2.62).

2.4.2 Examples of the Bessel function computation

A FORTRAN 77 routine (referred to as BESSEL) was written to compute the EM field components of equations (2.69) to (2.71) using a series expansion (Spiegel, 1968) to evaluate the modified Bessel functions. The values of the Bessel functions were compared with those obtained using the Maple computing package and the number of terms used in the series expansion was selected so that agreement to 15 decimal places was obtained. The number of terms required to achieve such accuracy varied from 5 to 35 depending on the value of the argument. The divergent nature of the modified Bessel functions I_o and I_1 for small arguments and K_o and K_1 for large arguments may create numerical difficulties and should be avoided if possible. For the range of parameters encountered in EM computations where the quasistatic approximation remains valid, the modified Bessel functions are well-behaved and do not present numerical problems. However, difficulties may arise in the case of very small or very large separations. Asymptotic expressions and polynomial approximations are available for the modified Bessel functions (Abramowitz and Stegun, 1970) which would further assist in dealing with extreme arguments and also increase computational speed. In addition, the complicated nature of the algebra and the many terms involved in evaluation of the higher order derivatives may also create numerical problems. Careful organisation of the order in which each term is computed is required so that satisfactory results are obtained. It is necessary to first combine terms of similar magnitude to reduce the effect of round-off errors.

Using a 100 Ω.m half-space as the Earth model and a vertical magnetic dipole source on the surface operating at a range of frequencies from 0.01 Hz to 10000 Hz, the BESSEL routine was used to compute the vertical (z direction) and radial (x direction) magnetic fields and the transverse (y direction) electric field at a point on the surface 200 m away from the transmitter loop (along the x axis). For comparison, the same three field components were also computed using the analytical expressions in equations (2.60) to (2.62) and using three other modelling programs: EM3D; EM1DSH and MARCO. EM3D is an integral equation program that uses a 61 point filter for the J_o Hankel transform and a 47 point filter for the J_1.

EM1DSH is a thin-sheet program that uses the Anderson (1979) filters and MARCO uses filters derived from Johansen and Sorensen (1979). To ensure the quasi-static approximation remains valid only the results obtained using frequencies up to 1000 Hz are presented. At this upper frequency, the inclusion of displacement currents in the computation alters the computed field values by less than 1 ppm in all three components. In order to present the results in a meaningful way, the assumption is made that the analytical expressions of equations (2.60) to (2.62) provide the most accurate results and are therefore used as the basis for comparison. The accuracy of a result is determined by comparison with the results obtained using these expressions.

Figure 2.2 shows the relative error in the in-phase (R) and quadrature (Q) fields for the H_x, E_y and H_z components on the surface of a 100 Ω.m half-space using frequencies ranging from 0.01-1000 Hz. The relative error is expressed in ppm of the analytical result. Figure 2.3 shows the corresponding results using a 10 Ω.m half-space. In all cases the field values computed using these programs are in very close agreement with each other.

Differences of a few ppm are considered insignificant for most applications and the computed field values would ordinarily be considered equal. However, for the sake of this discussion 1ppm is considered a significant computational error, since the quasi-static assumption at the lower frequencies produces errors of less than 0.001 ppm.

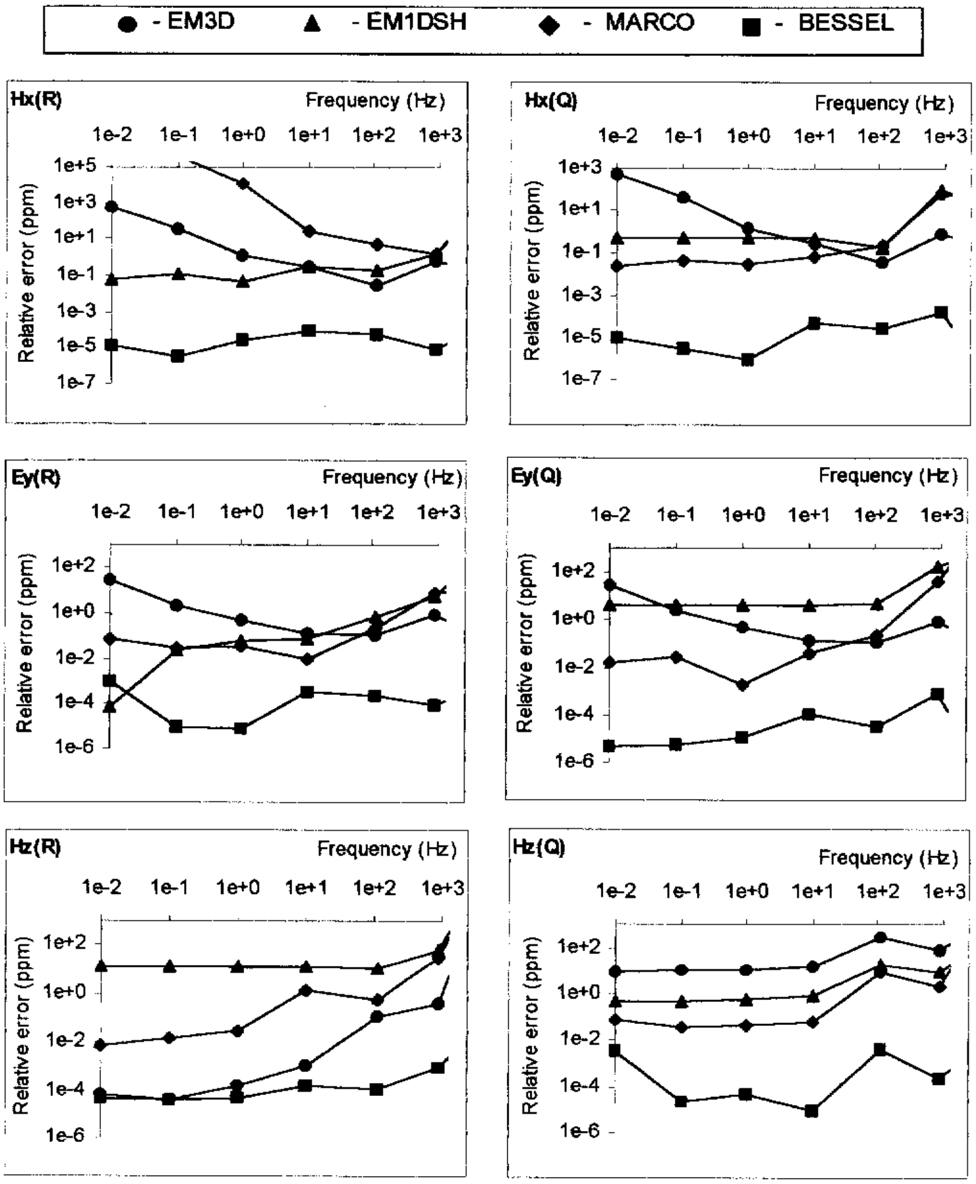

Figure 2.2 Frequency variation of the relative error (in ppm of the analytical solution) in the computed field components on the surface of a 10 Ω.m half-space. (R) represents the in-phase component and (Q) the quadrature component. ρ = 200 m. The BESSEL results are consistently more accurate than the others.

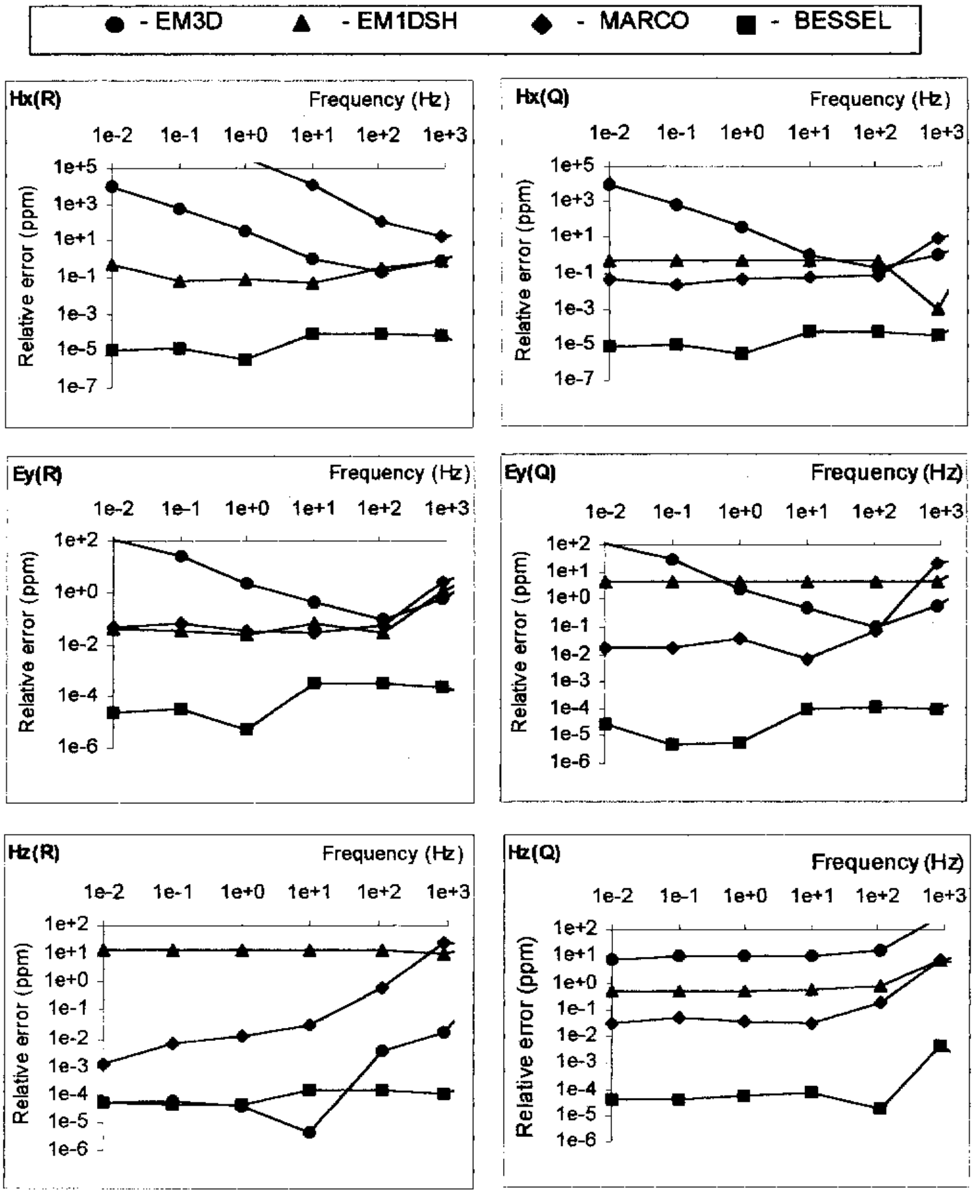

Figure 2.3 Frequency variation of the relative error (in ppm of the analytical solution) in the computed field components on the surface of a 100 Ω.m half-space. (R) represents the in-phase component and (Q) the quadrature component. ρ = 200 m. The BESSEL results are consistently more accurate than the others.

It is seen from Figures 2.2 and 2.3 that the field values computed using my BESSEL routine are consistently between two and three orders of magnitude more accurate than the 'best' results obtained using the digital filter programs. In some cases, the BESSEL results are greater than four orders of magnitude more accurate. Also, it should be noted that the numerical programs are very accurate in some cases and less accurate in others. This is particularly noticeable in the H_x component. The consistent results produced by the BESSEL routine provide confidence that the Bessel function expressions will also produce results of a similar accuracy for field points below the Earth's surface.

Figure 2.4 shows the results obtained for the EM field components at a point 50 m below the surface ($\rho = 200$ m, $z = 50$ m) of a 100 Ω.m half-space at 1 Hz; 110 Hz and 880 Hz. In this case, there are no simple analytical expressions to use as a basis for comparison so the relative variation with respect to the BESSEL results is used. This choice does not imply that the BESSEL results are the most accurate, it simply provides a basis for comparison. Figure 2.5 shows the corresponding results for a 10 Ω.m half-space. It can be seen in Figures 2.4 and 2.5 that in most cases the computed field components are in good agreement.

Only a few results are significantly different from the rest. It is therefore reasonable to suggest that the BESSEL function expressions can also be used with confidence to compute the field components below the surface.

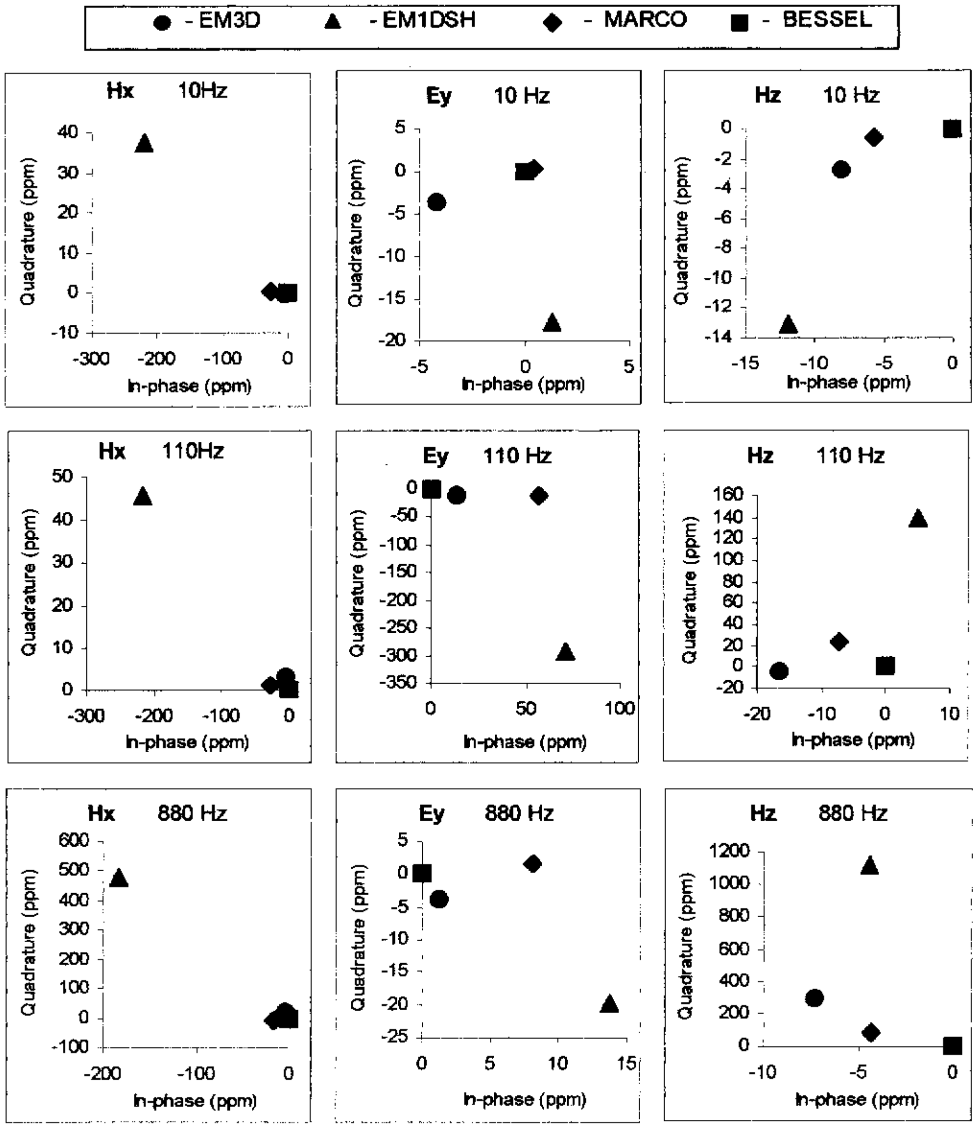

Figure 2.4 Relative error in the computed field components for a point located 50m below the surface of a **100 Ω.m** half-space. Note that the variation in agreement necessitates the use of different scales for each plot. ρ = 200 m.

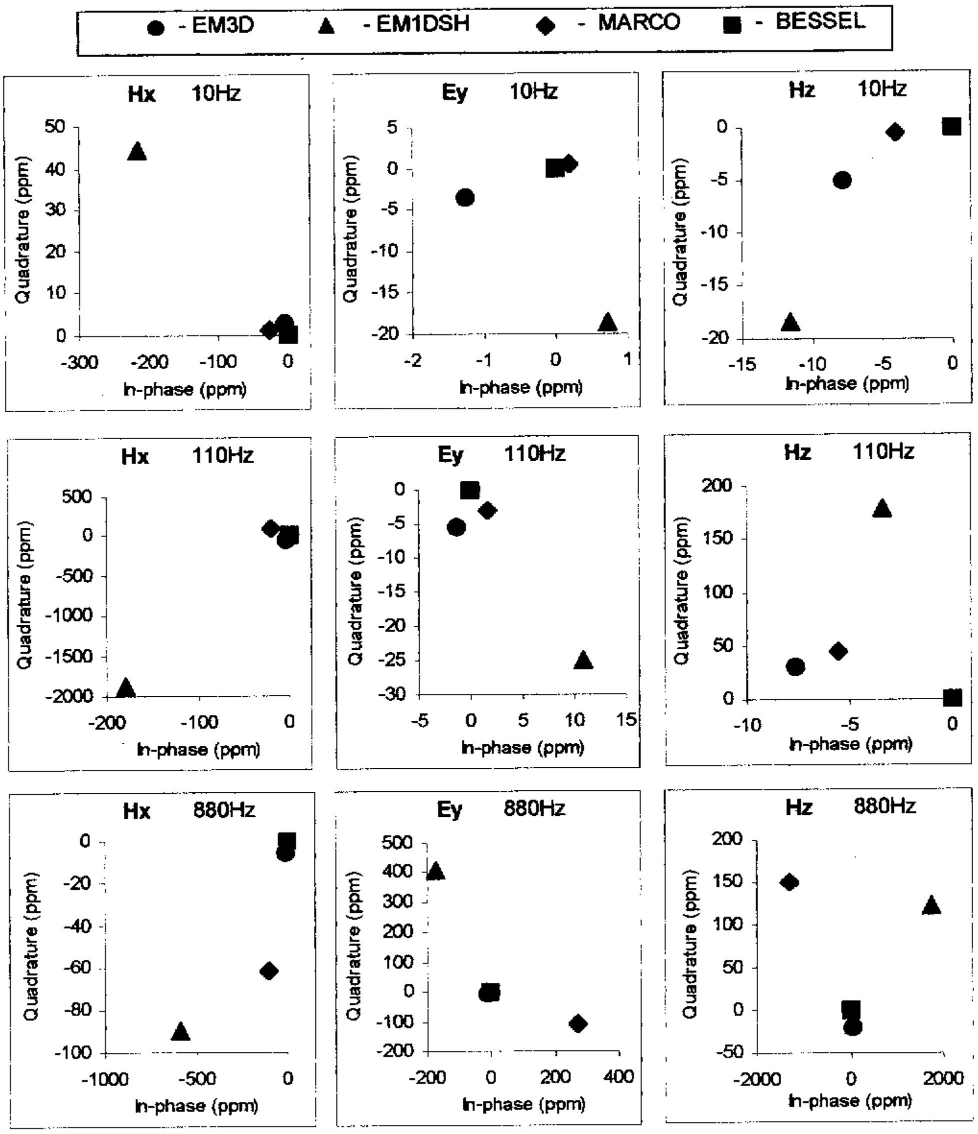

Figure 2.5 Relative error in the computed field components for a point located 50m below the surface of a **10 Ω.m** half-space. Note that the variation in agreement necessitates the use of different scales for each plot. ρ = 200 m.

2.4.3 Computational speed

As an indication of the relative computational speed of the analytic expressions in BESSEL compared to the digital filter methods, the EM fields were computed at a number of sub-surface locations (field points) using the same frequency range mentioned earlier. Program EM1DSH could not be used in a valid comparison of computational speed since it does not compute the half-space fields separately from the fields due to a conductive plate. The EM3D and MARCO programs allow for the layered Earth (half-space in this case) fields to be computed separately, i.e. without the 3-D body being present. Table 2.2 lists the CPU times for the three programs using 50, 100, 200, 500 1000 and 5000 field points in a 100 Ω.m half-space. EM3D uses very short filters (61 points for J_o and 47 points for J_1) and is consequently very fast. MARCO is comparatively slow but becomes more efficient as the number of field points increases. My analytical BESSEL program was able to compute the field components in less time than the digital filter programs in all cases. The plot of CPU time against the number of field points shown in Figure 2.6 indicates that the BESSEL routine is most advantageous when the number of field locations is large. It should be noted that at low frequencies, the number of terms used in the Bessel function series expansion (twenty in this example) can be reduced without affecting the accuracy of the results. This would further reduce the CPU time required for large computations.

	CPU time used for computation (seconds)					
Program	50 points	100 points	200 points	500 points	1000 points	5000 points
MARCO	6.11	6.49	7.25	8.16	11.08	23.92
EM3D	0.53	0.96	1.87	4.07	7.80	39.16
BESSEL	0.44	0.58	1.11	2.28	4.75	15.46

Table 2.2. CPU time used for field computation at various numbers of points in the half-space. Each component was computed at ten frequencies at each field point. The BESSEL routine was consistently faster than the two routines that use digital filters.

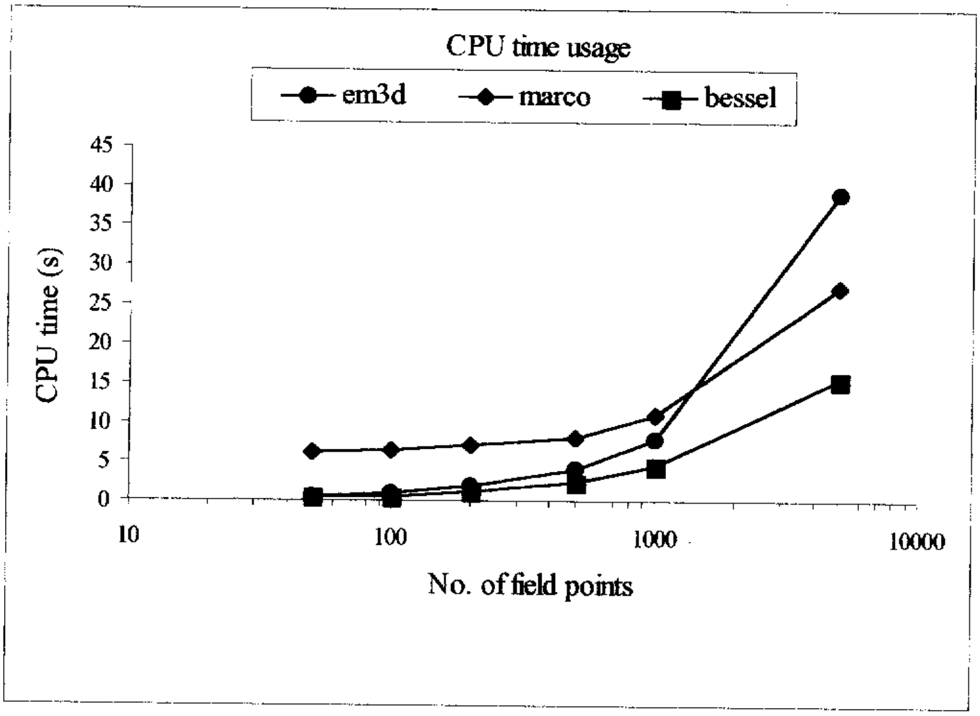

Figure 2.6 Plot of the CPU time used for field computation using different programs. Field components were computed at 10 frequencies for various numbers of points in the half-space using EM3D, MARCO and BESSEL routines. Note that MARCO becomes more efficient as the number of field points increases, but memory limitations prevented a larger number of field points being used. The BESSEL routine used less CPU time for all computations.

As an example, using only ten terms in the series expansion reduces the CPU time from 15.46 to 8.03 s for the 5000 point computation, making the BESSEL routine much faster than the other programs. Presently, no attempt has been made to optimise the performance of the BESSEL routine. Doing so may further increase its appeal in terms of computational speed.

2.5 Concluding remarks

This chapter has presented an overview of the theory of 3-D EM modelling using the integral equation approach and has addressed the issue of computational accuracy using digital filters. A new method of computing EM field components *without* the use of digital filters has been developed and tested. The new method has been shown to be faster, and produce more accurate results, than similar computations using digital filters.

CHAPTER 3

DEVELOPMENT OF THE ELECTROMAGNETIC RESIDUAL CONCEPT

The wide range of EM equipment and survey methods available for use has not come about by accident. The electromagnetic response of a particular geological environment will vary according to the type of survey being conducted and the choice of survey parameters being used. Unfortunately, the best choice of survey parameters for one case may be completely useless for another. An appropriate choice of survey type and parameters can only be made with knowledge of the local geology and the target. For example, if the target is a conductive body within a resistive host, an inductive EM method may be used, whereas if the target is a more resistive layer in a conductive environment, DC methods may be preferred instead.

Although various acquisition systems will produce different results, they all respond to the flow of current within the Earth and must therefore be related to each other. The use of multi-system measurements has been shown to have advantages over single system measurements for a variety of applications (Buselli et al., 1990; Raiche et al., 1985).

In this chapter, two signal enhancement techniques based on the use of multi-system measurements are developed and tested using 3-D numerical modelling. The enhancement schemes are based on the idea of data redundancy, which is useful for measurements that contain similar information and are related in some way.

3.1 Small loop (dipole) frequency domain surveys

In order to develop and test the signal enhancement techniques, a computer program, based on the mathematical procedures presented in Chapter 2, was developed. The program required the versatility to simulate slingram surveys utilising vertical and horizontal dipole sources as well as large loop transmitters. The results obtained from the program were verified by comparison with those from similar models found in the literature (eg. Newman et al., 1986; Spies and Frischknecht, 1991; Avdeev et al., 1998). As part of the verification, the half-space responses for the case of a ground survey were checked against analytical solutions and the layered Earth responses were checked for convergence to the corresponding half-space response. This was achieved by selecting a very thin (< 1m) top layer or a very small contrast between the conductivities of the Earth layers. The notion of reciprocity was also used as a check on the computations. Reciprocity refers to the invariance of the measured response when the transmitter and receiver are interchanged, i.e. the H_z response at location (x_r,y_r,z_r) due to an x-directed transmitter moment at location (x_s,y_s,z_s) is the same as the H_x response at (x_s,y_s,z_s) due to a z-directed transmitter moment at (x_r,y_r,z_r). Reciprocity is independent of geological structure.

After validation of the program, a few simple models were used to demonstrate the complex behaviour of EM fields. Some of these are presented in the following section.

3.1.1 EM response of 3-D targets

It is a well accepted notion among geophysicists that a conductive geological setting is a difficult environment for EM prospecting. In the absence of a suitable alternative we are often forced to make best the use of a limited exploration tool. To demonstrate the difficulties of prospecting in a conductive environment I present a few simple cases using the results of 3-D modelling.

Figure 3.1(a) shows a regularly shaped prismatic body of 1 Ω.m resistivity embedded at a depth of 50 m in a uniform half-space having a resistivity of 1000 Ω.m. The body is centred on x = 0 m, has dimensions of 40 x 200 x 40 m and represents a small but significant deposit that may be of interest to a mining company. A small horizontal coplanar (HCP) loop configuration with a loop separation of 100 m was used. Following common practice, Figure 3.1(b) shows the ratio (expressed as a percentage) of the 3-D anomalous response H^A to the layered Earth response H^L computed at the receiver location for the in-phase and quadrature signals at six frequencies. The anomalous response H^A is the *change* in the field measured at the receiver due to the presence of the body (see section 3.1.3). The ratio H^A/H^L is often called the detection ratio (Morrison et al., 1998). The ordinate on the plots is the mid-point of the transmitter-receiver array. The anomalous in-phase and quadrature responses contribute approximately 25% to 30% of the total response and represent a readily detectable target in the absence of noise. The Earth model is modified in Figure 3.2(a) to include an overburden layer of resistivity 10 Ω.m and thickness 20 m. The effect of the overburden layer, displayed in Figure 3.2(b), is to greatly reduce the H^A/H^L ratio. The in-phase ratio is reduced to less than 5% whereas the quadrature ratio is reduced to approximately 10%. Also of note in Figure 3.2(b) is the strong frequency dependence of the quadrature response compared to the half-space case. The greater frequency dependence is due to the increased attenuation of the higher frequencies by the conductive overburden.

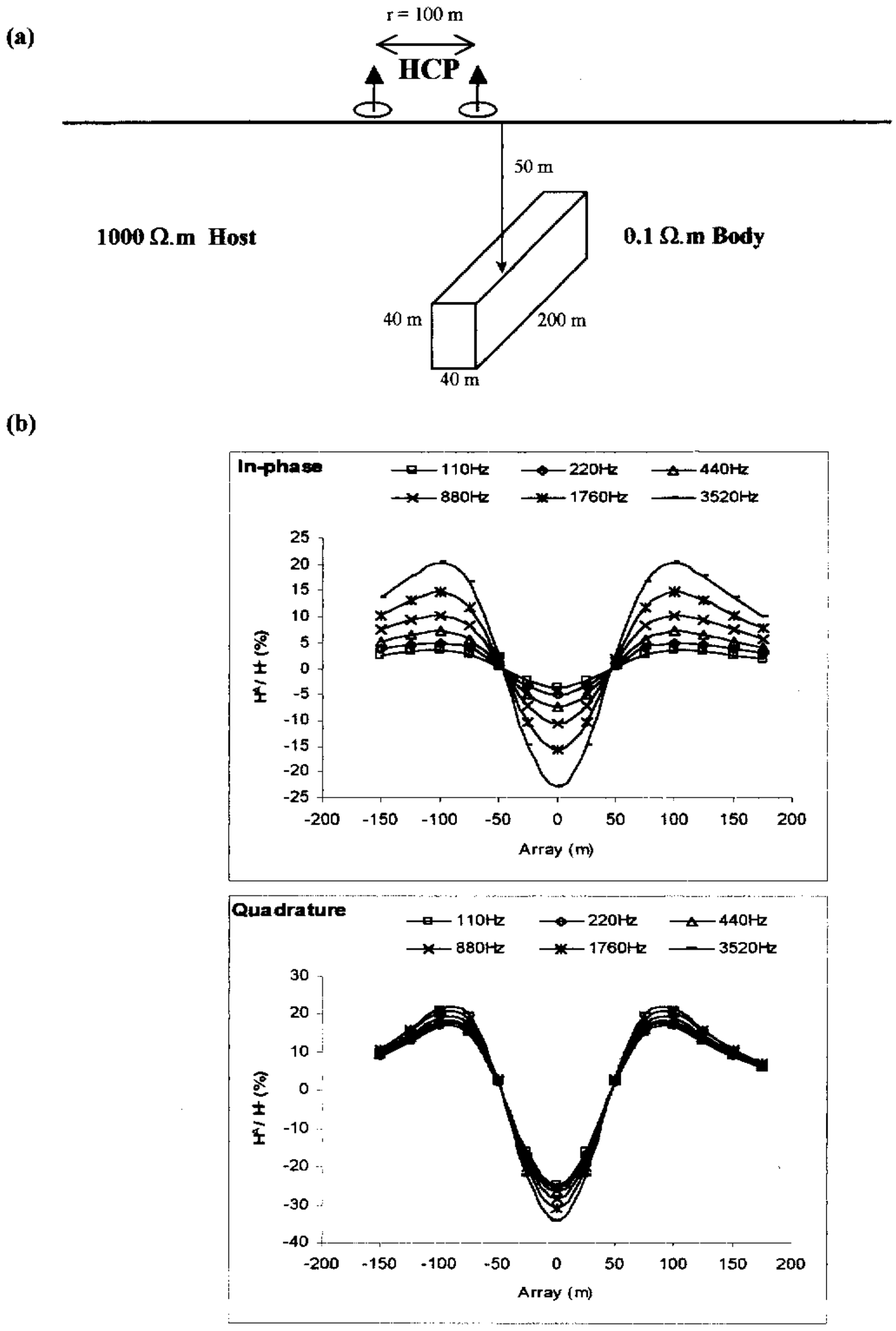

Figure 3.1 Ratio of anomalous H^A signal to layered Earth H^L signal for the HCP configuration on a resistive half-space. **(a)** Resistive half-space model including a conductive 3-D body. **(b)** Ratio of anomalous H^A signal to layered Earth H^L signal for the HCP configuration. In-phase and quadrature profile responses are given. Note that the quadrature response is nearly frequency independent.

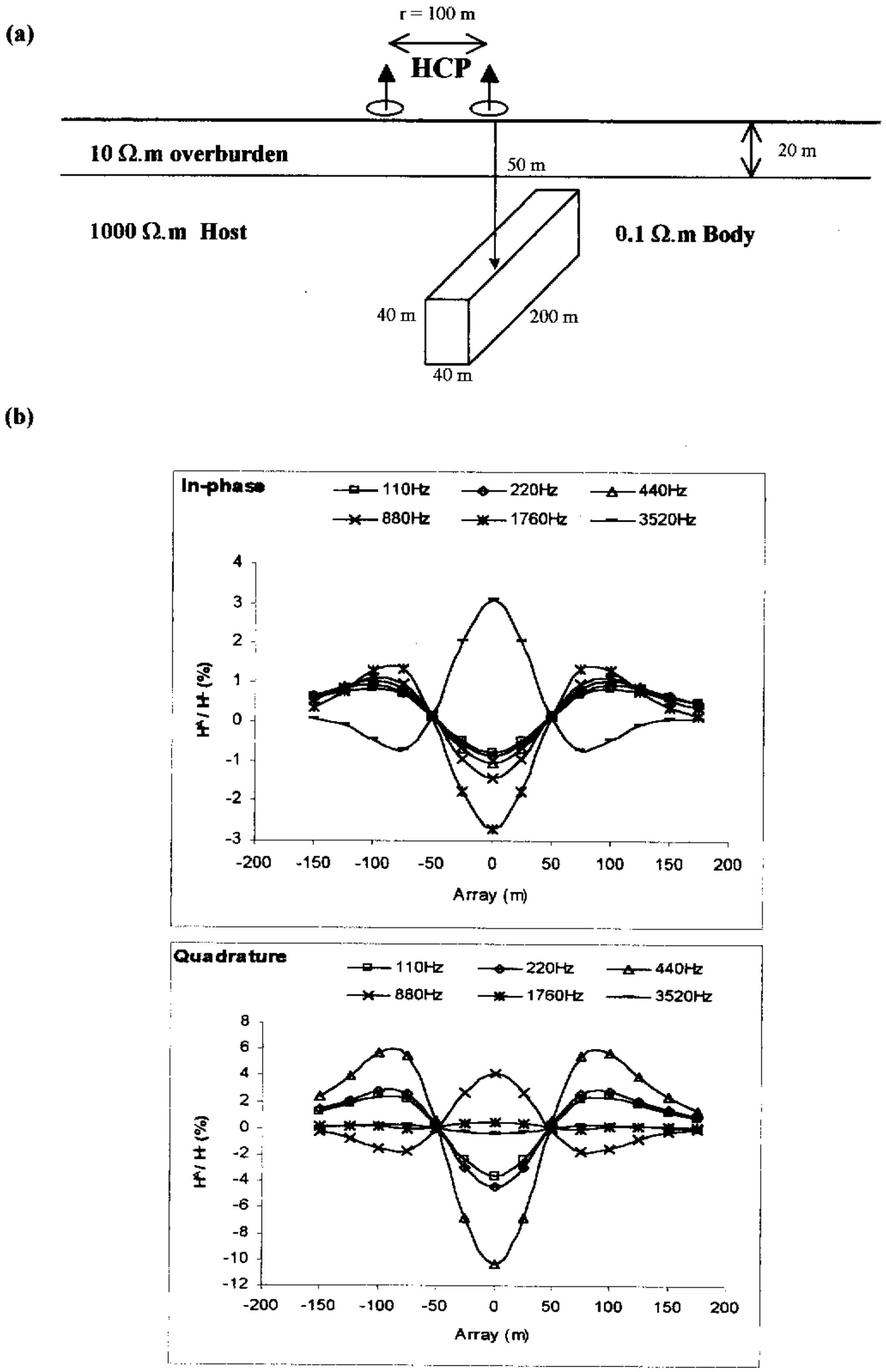

Figure 3.2 Ratio of anomalous H^A signal to layered Earth H^L signal for the HCP configuration on a resistive half-space with overburden. **(a)** Resistive half-space below conductive overburden including a conductive 3-D body. **(b)** Ratio of anomalous H^A signal to layered Earth H^L signal for the HCP configuration. In-phase and quadrature profile responses are given. Note that the resistive host prevents current channelling, resulting in a very small signal from the target.

The reduction in the target response due to the presence of a conductive overburden is well documented (Smith and West, 1987; Nabighian and Macnae, 1991; West and Macnae, 1991) and may result in such a target remaining undetected in practice. The severe restriction imposed by the presence of the conductive overburden may give the appearance that EM methods have no hope of success in conductive environments. Fortunately, the effect of a conductive overburden can be partially offset if the host layer is also conductive. A conductive host medium is able to channel currents into the 3-D body and augment its contribution to the measured response. The effects of current channelling are described by Palacky (1975), Ferneyhough (1985), and West and Macnae (1991). As an example of this, Figure 3.3(a) shows the same 3-D target embedded in a host medium having a resistivity of 100 Ω.m below a more conductive overburden. The H^A/H^L ratios shown in Figure 3.3(b) indicate that much of the signal, which was removed by the insertion of the overburden layer, has been replaced by the contribution of current channelling through the conductive host. This is particularly noticeable in the quadrature response.

It is apparent from this simple analysis that the conductivity of the Earth layers plays a very important role in the amount of current flowing in a target and the consequent response measured at the receiver.

3.1.2 Detectability of a target response

In a typical EM survey for mineral exploration most interest often lies in finding areas of increased conductivity that may be associated with the presence of sulfide ores. In order for a target to be detected its contribution to the total measured response must be sufficiently large that a measurable change is recorded at the receiver.

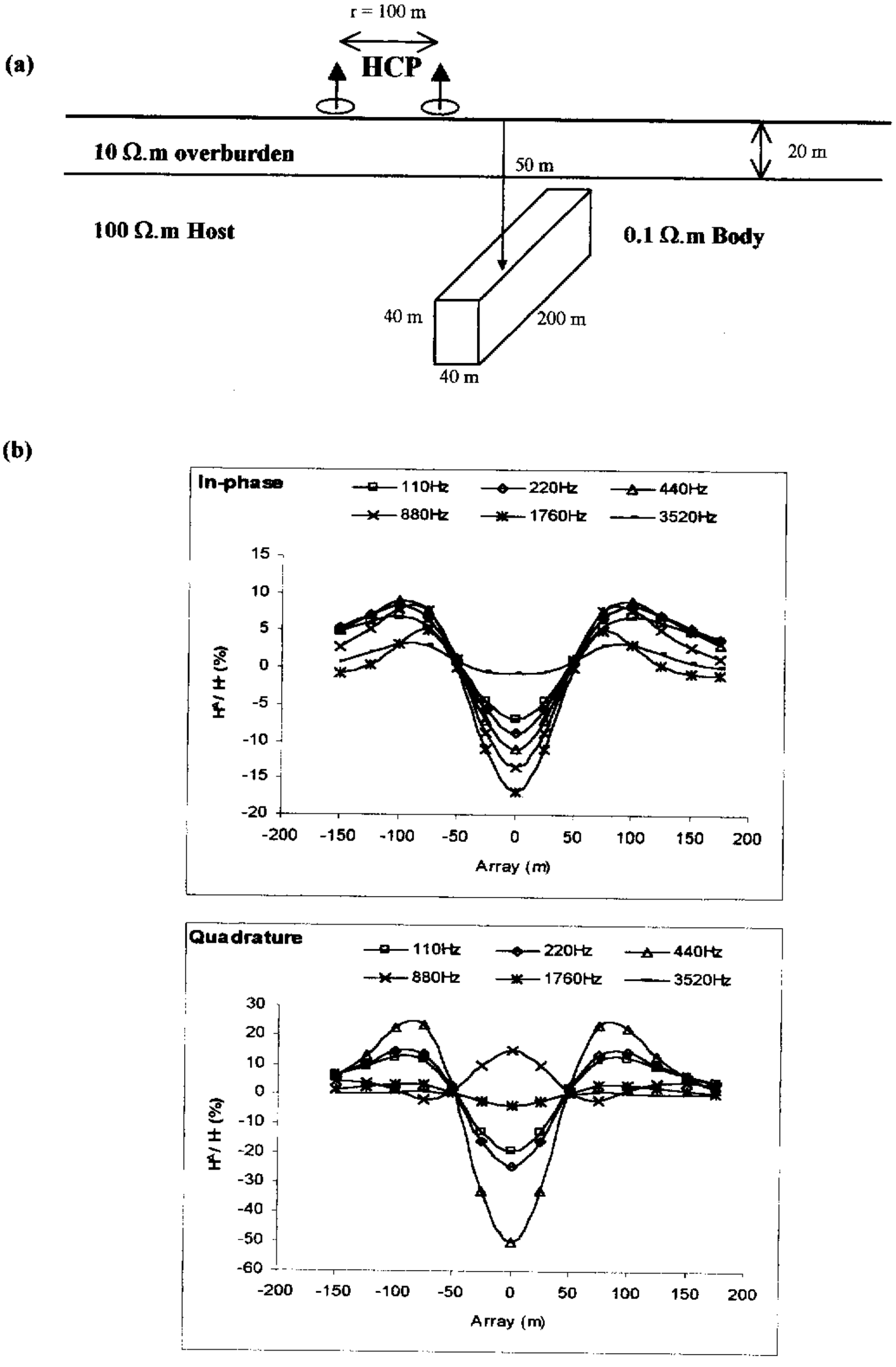

Figure 3.3 Effect of a conductive host medium on the H^A to H^L ratio. **(a)** Conductive half-space below conductive overburden including a conductive 3-D body. **(b)** Ratio of anomalous H^A signal to layered Earth H^L signal for the HCP configuration. In-phase and quadrature profile responses at the range of frequencies listed. Note the strong frequency dependency in the quadrature response. All ratios are larger than those in Figure 3.2 but are reduced compared to those in Figure 3.1 (except the 440 Hz quadrature).

How large that change must be cannot be determined without consideration of the nature of the survey environment, the noise level and the sensitivity of the measuring system. The H^A/H^L ratio is a commonly used measure of the detectability of a target although it does not take noise into account.

Spies (1980) recommends that the H^A/H^L ratio should be at least 3, Morrison et al., (1998) agree that a ratio of 3:1 guarantees the target will be detected whereas McCracken et al. (1986a) say it should be 5:1. Peltoniemi (1998) in his analysis of the penetration depth of airborne EM surveys, takes a more general view by saying the anomalous response should be four times greater than the average noise level of the system. Eaton and Hohmann (1987) are the least committed to the use of a simple numerical value and assert that the limit of detectability ultimately comes down to the experience of the interpreter.

Regardless of the criterion used to determine whether a response is detectable or not, in a conductive environment, the largest unwanted contribution to the measured signal comes from the half-space or layered Earth response. As noted by Morrison et al. (1998) the layered Earth HCP quadrature response has a sign reversal at a frequency related to the half-space and overburden conductivities. In Figure 3.3(b) the unusually large detection ratio noticed in the 440 Hz quadrature response is due to the near-zero layered Earth response at that frequency. Herein lies the thrust of the signal enhancement technique developed in the next section. If a way could be found to reduce the layered Earth response, by data processing or other means, the detection ratio could be greatly increased and the target would therefore be more likely to be detected.

3.1.3 Reduction of the layered Earth response

As seen in Chapter 2, the integral equation method of EM modelling (Raiche, 1974; Weidelt, 1975; Hohmann, 1975) allows the total measured field H^T to be expressed in two parts

$$H^T(\omega,r) = H^L(\omega,r) + \int_V \mathbf{G}(r,r')J_S(\omega,r')dV \qquad (3.1)$$

For convenience I re-write the integral equation of (3.1) in the more simple form

$$H^T = H^L + H^A. \qquad (3.2)$$

The first term H^L on the right of equation (3.2) represents the magnetic field that would be measured at the receiver if the 3-D body were not present i.e. the layered Earth response. In very resistive environments this term is relatively small but in conductive environments it may be very large and dominate the total response. The second term H^A represents a change in the field measured at the receiver as a result of the perturbation of the field (and currents) by the presence of a 3-D body. This perturbation is often referred to as the scattering of the EM field and the currents flowing inside the 3-D body are referred to as the scattering, secondary or anomalous currents. The change in measured response due to the presence of the 3-D body is referred to as the scattered, secondary or anomalous response.

It is important to note that the apparent simplicity of equation (3.2) does not imply that the responses of anomalous zones are additive, nor does the H^A term represent the free-space response of the body.

The notion of superposition does not hold in EM prospecting due to the mutual interaction between conductive bodies and their conductive host rocks. The volume integral in equation (3.1) encompasses all anomalous regions and the tensor Green's functions account for their interaction with each other and with the host rock.

Equation (3.2) is a general equation that applies to all survey configurations. If it were possible to find a relationship between the layered Earth responses obtained using different survey configurations it may be possible to combine the measurements so that the layered Earth response H^L is cancelled. This notion can be described as data redundancy. I investigate this idea by making use of commonly used small-loop survey configurations: vertical co-axial VCA; vertical co-planar VCP; and horizontal co-planar HCP and examining the mathematical expression of the appropriate magnetic field components for a layered Earth model. Using the techniques described in the previous chapter, the magnetic field on the surface of the Earth for each configuration can be written (Ward and Hohmann, 1991) as

$$H^{VCA} = \tfrac{m}{4\pi\rho}\int_0^\infty (1-R)\lambda J_1(\rho\lambda)d\lambda - \tfrac{m}{4\pi}\int_0^\infty (1-R)\lambda^2 J_o(\rho\lambda)d\lambda . \qquad (3.3)$$

$$H^{VCP} = \tfrac{-m}{4\pi\rho}\int_0^\infty (1-R)\lambda J_1(\rho\lambda)d\lambda , \qquad (3.4)$$

$$H^{HCP} = \tfrac{m}{4\pi}\int_0^\infty (1+R)\lambda^2 J_o(\rho\lambda)d\lambda . \qquad (3.5)$$

In equations (3.3) to (3.5) the function R represents the spectral constants derived in Chapter 2 and is related to the entire sequence of Earth layers. The superscript ^{L} has been omitted for convenience. The horizontal displacement vector ρ represents the separation of the loop centres. Now, assuming that the same transmitter-receiver separation, frequency and dipole moment is used in each configuration, the terms in these equations suggest that there may be a simple relationship that links them together. So, adding equation (3.3) to equation (3.4) yields

$$H^{VCP} + H^{VCA} = \tfrac{-m}{4\pi}\int_0^\infty (1-R)\lambda^2 J_o(\rho\lambda)d\lambda \qquad (3.6)$$

which, using equation (3.5) can be written as

$$H^{VCP} + H^{VCA} = H^{HCP} - 2\tfrac{m}{4\pi}\int_{0}^{\infty} \lambda^2 J_o(\rho\lambda)d\lambda\,. \qquad (3.7)$$

The integral in equation (3.7) is a standard integral having an analytical value of $-1/\rho^3$ hence,

$$H^{HCP} - H^{VCP} - H^{VCA} = -2\tfrac{m}{4\pi\rho^3}\,. \qquad (3.8)$$

The right hand side of equation (3.8) is recognised as two times the free space (primary) field H_o of a coplanar system. Since most frequency domain survey equipment (eg. MaxMin, Dighem, EM-34 etc.) record data normalised to the primary field, I normalise equation (3.8) with the primary field of a coplanar system to obtain

$${}^{Z}\!/_{Z_o}{}^{HCP} - {}^{Z}\!/_{Z_o}{}^{VCP} + 2\,{}^{Z}\!/_{Z_o}{}^{VCA} = 2\,, \qquad (3.9)$$

where ${}^{Z}\!/_{Z_o}$ represents the mutual coupling ratio (equivalent to ${}^{H}\!/_{H_o}$) of the indicated configuration. The VCA configuration has a primary field double that of the coplanar systems and opposite in sign, hence the VCA mutual coupling ratio is multiplied by negative two. Equation (3.9) forms the basis of the residual concept as it clearly shows that for a uniformly layered Earth there is a very simple relationship between the field measurements obtained using these three configurations.

I therefore define the Small Loop Residual (SLR) as

$$SLR = {}^{Z}\!/_{Z_o}{}^{HCP} - {}^{Z}\!/_{Z_o}{}^{VCP} + 2\,{}^{Z}\!/_{Z_o}{}^{VCA} - 2\,, \qquad (3.10)$$

which for a uniformly layered Earth (or half-space) will have a value of zero. In the presence of some inhomogeneity such as a conductive mineral deposit, the SLR will be non-zero and its magnitude will represent a combination of the scattered responses measured using the different configurations.

The magnitude of the residual is determined by a complicated relationship that depends on the size, shape and conductivity of the 3-D body, depth of burial, transmitter-receiver separation and location relative to the body, source frequency and the *layered Earth conductivity*. Although the layered Earth response H^L does not form part of the residual, the scattering currents cannot be separated from the influence of the host rock and will therefore still be dependent on the layered Earth environment. It could be argued, therefore, that the layered Earth response is not totally removed from the measurements, just significantly reduced by the removal of the H^L response (remembering that H^L refers to the response that would be observed if the inhomogeneity were not present). If two or more 3-D bodies are present, the residual will be complicated even further by their mutual interaction and interpretation will become more difficult.

The SLR concept is not restricted by the number of Earth layers and may also be applied to airborne acquisition systems, provided the transmitter and receiver are at the same elevation (eg. helicopter EM surveys).

3.1.4 Model data

Although very simple in concept, the SLR involves the combination of three measurements at each receiver location. This may be unattractive to contractors in terms of field time and the quantity of data to process, so it must be shown to have some real benefit to the exploration program if it is going to be used routinely.

3.1.4.1 Uniform half-space

To examine the potential of the SLR concept as a valid processing technique I again consider the model in Figure 3.1(a) and compute the corresponding VCA and VCP profile responses. To be consistent with usual field practice the responses are expressed as mutual coupling ratios (Z/Z_o). Figure 3.4(a) shows the in-phase responses obtained for the three configurations for the case where the *3-D body is not present* (i.e. the layered Earth responses only).

(a)

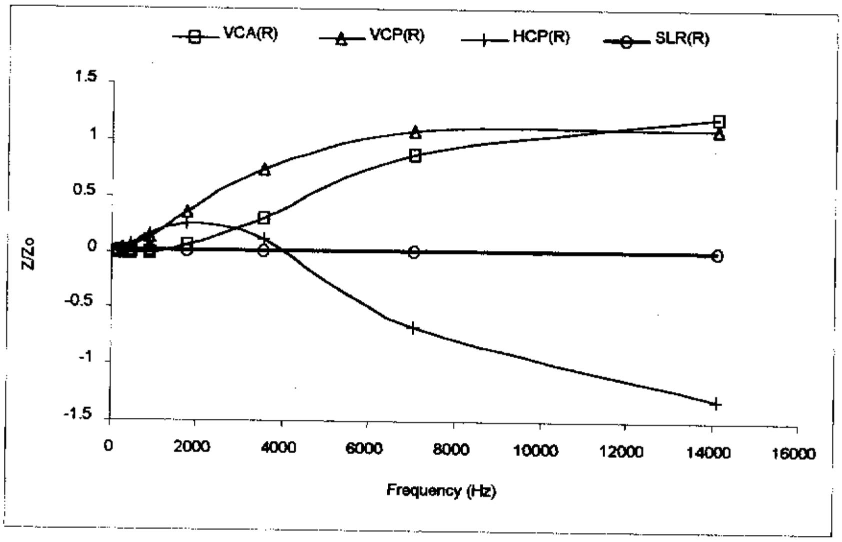

(b)

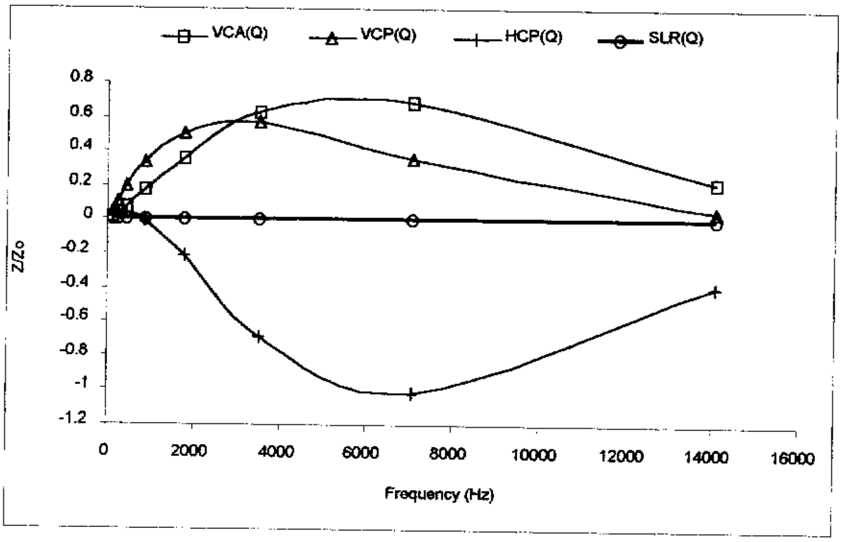

Figure 3.4 Frequency variation of the VCA, VCP, HCP and SLR responses for a two-layered Earth. **(a)** in-phase responses for the model in Figure 3.3(a) WITHOUT the 3-D body. **(b)** the corresponding quadrature responses. The SLR produces a null response at *all* frequencies over a layered Earth.

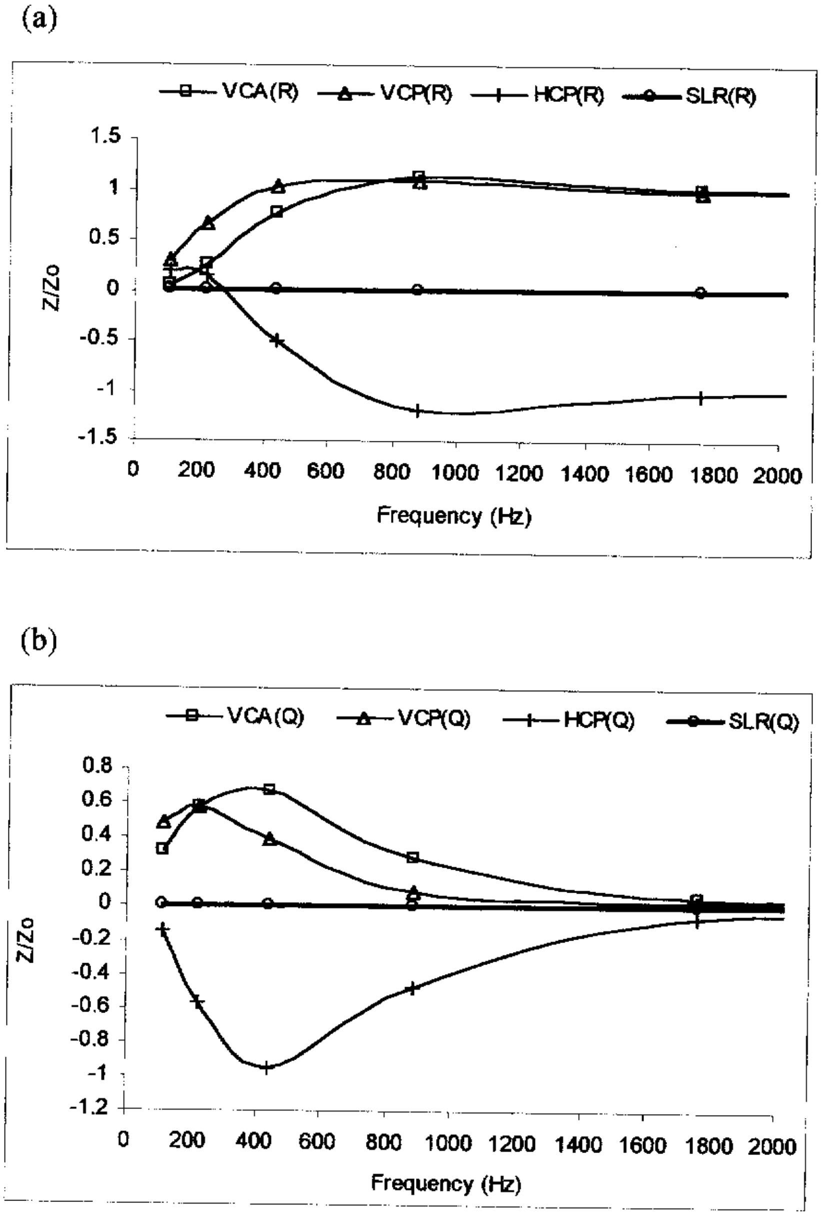

Figure 3.5 Frequency variation of the VCA, VCP, HCP and SLR responses for a two-layered Earth with an overburden resistivity of 1 Ω.m. **(a)** in-phase responses for the model in Figure 3.3(a) WITHOUT the 3-D body and with an overburden resistivity of 1 Ω.m. **(b)** the corresponding quadrature responses. The SLR produces a null response at all frequencies over a layered Earth.

Also included in Figure 3.4(a) is the SLR computed from these responses. Figure 3.4(b) shows the corresponding quadrature response. Figure 3.5 shows the responses for the case where the overburden resistivity is reduced to 1 Ω.m.

It is evident in these figures that the computed SLR has a value very close to zero at all frequencies and is therefore very effective in reducing the Earth response in the measured data. The fact that the SLR is not exactly zero in this case is due to numerical inaccuracies associated with the computation of the field responses using digital filters. Table 3.1 presents a comparison of the in-phase and quadrature HCP, VCA and VCP responses for a 1000 Ω.m half-space at three frequencies computed using digital filters and the analytic expressions. The residuals derived from the analytical results are many orders of magnitude smaller than the corresponding residual derived from the responses computed using digital filters. Table 3.2 contains a similar comparison for a 10 Ω.m half-space.

For the case where the 3-D body is present in the host layer, the HCP, VCP and VCA profile responses computed at the same frequencies and separations are shown in Figures 3.6 and 3.7. Each profile response is characterised by a spatially constant but frequency dependent layered Earth response upon which is superimposed a characteristic signal from the target body. The signal from the target in this example is readily discernible in the HCP and VCA configuration responses but cannot be seen at all in the VCP profiles. In the case of the SLR however, the Earth response has been greatly reduced. Consequently, the variations along the profile line due to the target responses are centred on the zero line and are much more evident, even when all frequencies are displayed together. This makes the SLR a much more useful quantity for display than the measured field responses.

1000 Ω.m half-space		**In-phase (Z/Zo) -1**		**Quadrature (Z/Zo)**	
freq.	config.	**analytical**	**numerical**	**analytical**	**Numerical**
	VCA	-3.51E-5	-3.50E-5	3.81E-5	3.82E-5
110 Hz	**VCP**	7.32E-5	7.32E-5	2.10E-3	2.10E-3
	HCP	1.43E-4	1.43E-4	2.02E-3	2.02E-3
	RESIDUAL	**-2.84E-14**	**1.34E-7**	**-2.88E-13**	**1.11E-9**
	VCA	-2.57E-4	-2.56E-4	3.03E-4	3.04E-4
440 Hz	**VCP**	5.62E-4	5.61E-4	8.08E-3	8.08E-3
	HCP	1,08E-3	1.08E-3	7.47E-3	7.47E-3
	RESIDUAL	**-3.33E-15**	**2.17E-6**	**8.76E-14**	**3.37E-8**
	VCA	-4.10E-3	-4.04E-3	6.56E-3	6.57E-3
3520 Hz	**VCP**	1.09E-2	1.08E-2	5.59E-2	5.59E-2
	HCP	1.91E-2	1.90E-2	4.28E-2	4.28E-2
	RESIDUAL	**4.44E-15**	**1.43E-4**	**-2.47E-14**	**4.17E-6**

Table 3.1 Comparison of VCA, VCP, HCP and SLR computed using digital filters with the analytical expressions. Loop separation of 100 m on a **1000 Ω.m** half-space.

10 Ωm half-space		**In-phase (Z/Zo) -1**		**Quadrature (Z/Zo)**	
freq.	config.	**analytical**	**numerical**	**analytical**	**numerical**
	VCA	-1.36E-2	-1.36E-2	3.30E-2	3.31E-2
110 Hz	VCP	4.95E-2	4.95E-2	1.45E-1	1.45E-1
	HCP	7.67E-2	7.67E-2	7.84E-2	7.84E-2
	RESIDUAL	**4.44E-16**	**1.44E-7**	**-4.43E-15**	**6.89E-9**
	VCA	-5.63E-3	-5.62E-3	1.89E-1	1.89E-1
440 Hz	VCP	2.49E-1	2.49E-1	3.51E-1	3.51E-1
	HCP	2.60E-1	2.60E-1	-2.73E-2	-2.74E-2
	RESIDUAL	**0.00E+0**	**2.43E-6**	**1.67E-15**	**1.23E-7**
	VCA	7.70E-1	7.71E-1	5.35E-1	5.36E-1
3520 Hz	VCP	9.57E-1	9.57E-1	2.74E-1	2.74E-1
	HCP	-5.84E-1	-5.84E-1	-7.97E-1	-7.98E-1
	RESIDUAL	**-2.22E-16**	**1.63E-4**	**0.00E+0**	**1.37E-6**

Table 3.2 Comparison of VCA, VCP, HCP and SLR computed using digital filters with the analytical expressions. Loop separation of 100 m on a **10 Ω.m** half-space.

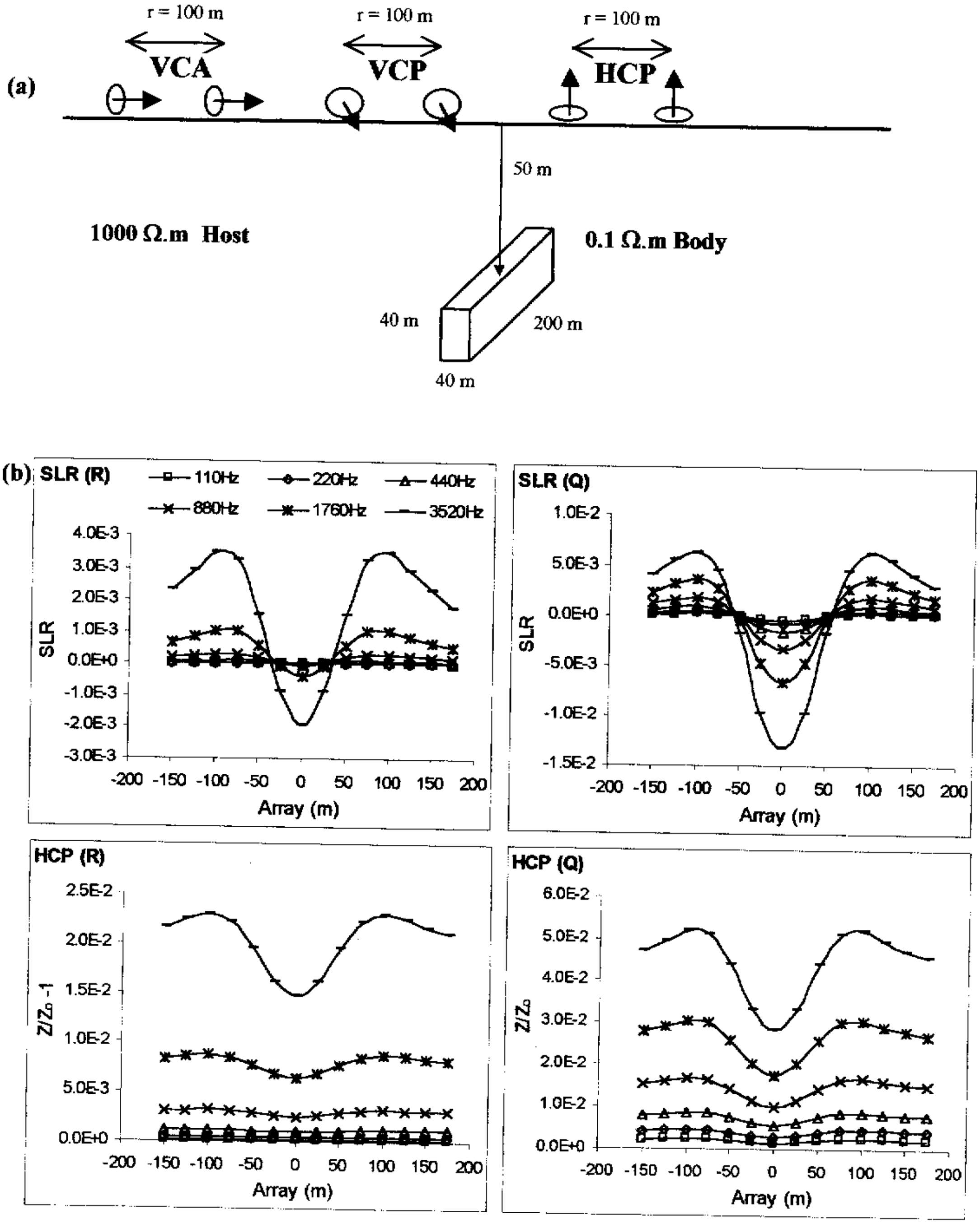

Figure 3.6 SLR and HCP responses for a 3-D body in a homogeneous half-space. **(a)** Homogeneous half-space Earth model including a conductive 3-D body. **(b)** In-phase (R) and quadrature (Q) profile responses at the range of frequencies listed in the first plot. Note that the SLR signature is centred on zero whereas HCP profiles retain the layered Earth background signal.

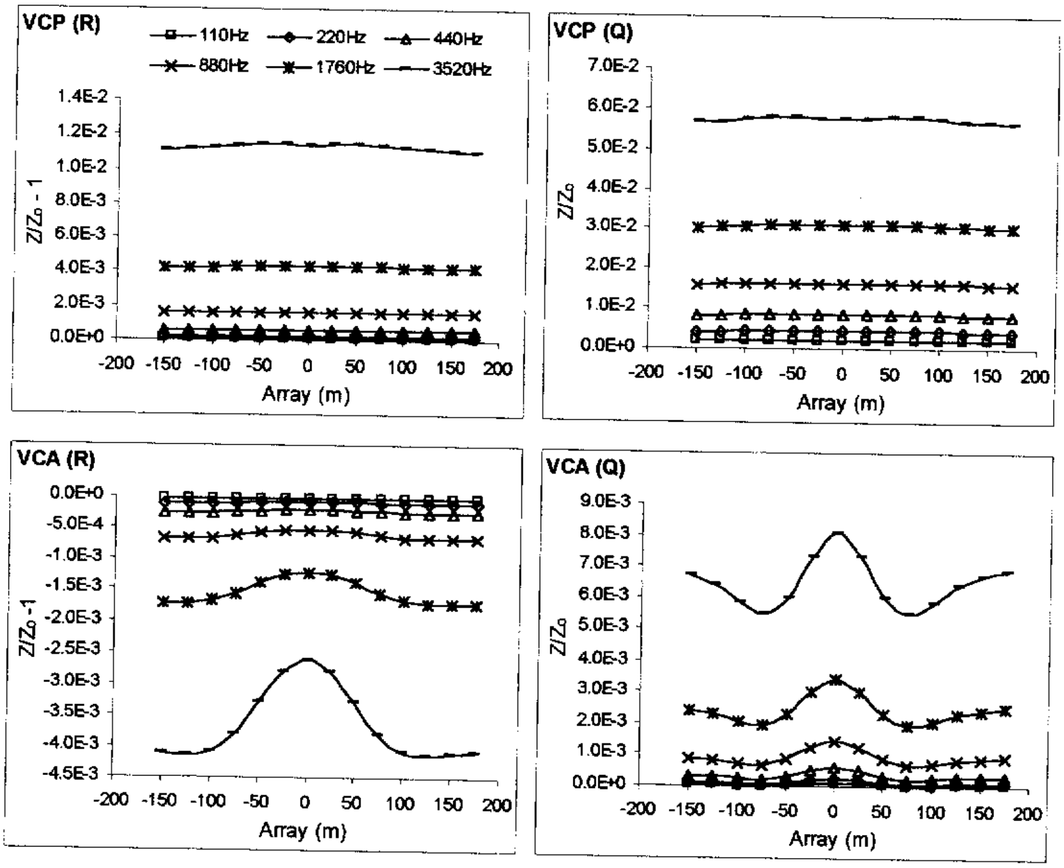

Figure 3.7 VCP and VCA responses for a 3-D body in a homogeneous half-space. In-phase (R) and quadrature (Q) profile responses at the frequencies shown in the first plot for the model shown in Fig. 3.6(a). Note the inability of the VCP configuration to detect the target whereas the VCA configuration clearly indicates the target response. Note also the frequency dependent Earth response in each plot.

In this example the 3-D body is located in a resistive environment and represents a readily detectable target that would be adequately resolved using a conventional survey configuration alone. The following examples involve more challenging exploration targets.

3.1.4.2 Effect of overburden

It is well known that a conductive overburden poses a difficult obstacle to inductive EM prospecting. Frequency domain surveys are particularly affected by the large currents that are induced in the overburden and which produce a very large response at the receiver coil. A conductive overburden also acts as a filter that attenuates and broadens the response from a target (Ward et al., 1974; Lajoie and West, 1976) that can only be avoided by drilling below it and conducting a down-hole survey. Even then, the overburden may influence the measurements but will not attenuate the signal from the target. Down-hole surveys are very expensive and not usually an option for initial surveys.

The effect of a conductive overburden on the anomalous HCP response has been seen in Figure 3.2(b) to drastically reduce the detection ratio. Increasing the thickness or the conductivity of the overburden will have the effect of further reducing the target response and increasing the Earth response. The effect of a conductive overburden on the HCP and SLR profiles is seen in Figure 3.8(b). The HCP profiles do not indicate the presence of the target because the large response from the overburden masks its signal. However, in the SLR profiles computed from the three configuration responses, the layered Earth (including overburden) response has been significantly reduced and the small signal form the target is clearly revealed.

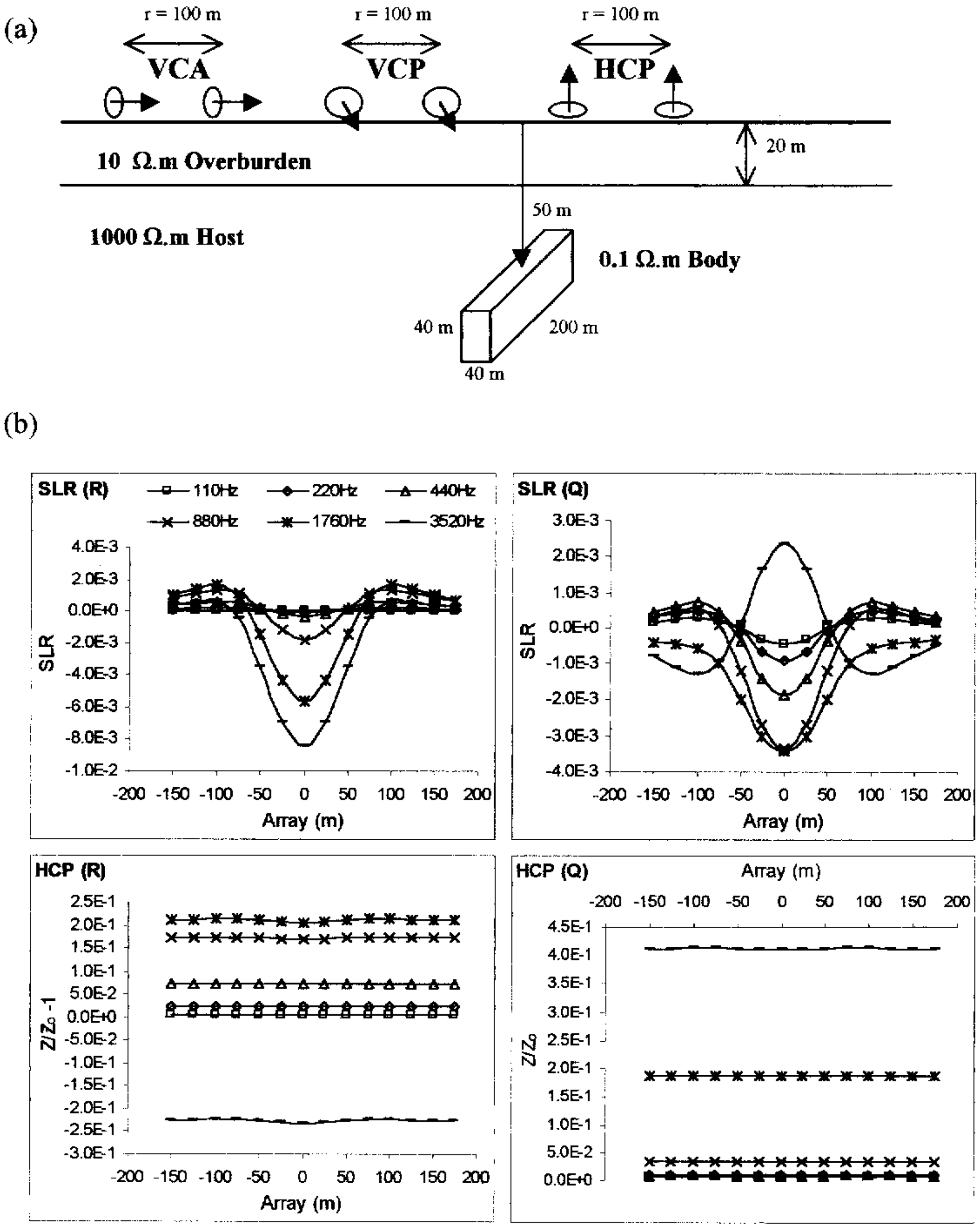

Figure 3.8 SLR and HCP responses for a 3-D body in a homogeneous half-space below conductive overburden. **(a)** Homogeneous half-space below conductive overburden Earth model including a conductive 3-D body. **(b)** In-phase (R) and quadrature (Q) profile responses at the range of frequencies listed in the first plot. Note that the large HCP layered Earth response due to the conductive overburden prevents the signal from the body from being adequately resolved.

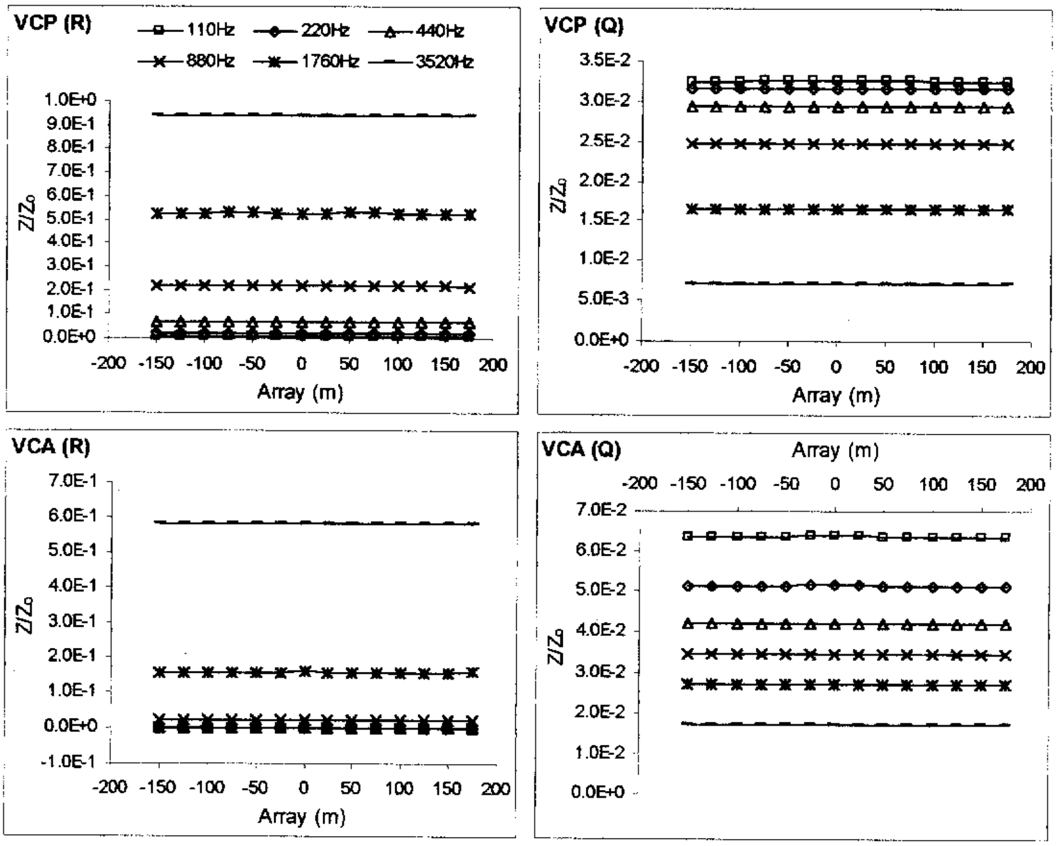

Figure 3.9 VCP and VCA responses for a 3-D body in a homogeneous half-space below conductive overburden. In-phase (R) and quadrature (Q) profile responses for the model in Figure 3.8(a) at the range of frequencies listed in the first plot. Note that the large Earth response in both configurations due to the conductive overburden prevents the signal from the body from being observed.

It is interesting that the SLR in-phase signal is actually larger when the overburden is present when compared to the half-space case. This apparent contradiction is a result of the SLR being a combination of measurements and not a direct measurement of the EM fields. The VCA and VCP profiles are shown in Figure 3.9 to be dominated by the overburden response and do not indicate the presence of the body.

It must be emphasised that the SLR transformation is a data processing technique and as such it is limited by the quality of the measured data input. If the survey equipment is not sufficiently sensitive to respond to the target signals at the time of measurement then the target will not be detected. Also, if one system is particularly noisy, it will reduce the effectiveness of the transform. The only limitation imposed on the ability of the SLR transformation to enhance the signal from a target appears to be related to the sensitivity of the measuring system.

3.1.4.3 Displaced bodies

It is very likely that in an initial survey the profile lines will not pass directly over the centre of a symmetric body necessary to produce the responses presented in the previous section. It is more likely to be the case that the target body is laterally displaced from the profile line direction by some distance. Using the model shown in Figure 3.10(a), the profile responses were computed for the case where the profile line is perpendicular to the strike of the target but is displaced by 150 m to one side of the centre of the target body. In Figures 3.10(b) and 3.11, the profile responses for the individual configurations are shown together with the SLR derived from them. In this case only the VCA profile responses indicate the presence of the body. The HCP and VCP responses are dominated by the layered Earth response and the target response cannot be readily observed.

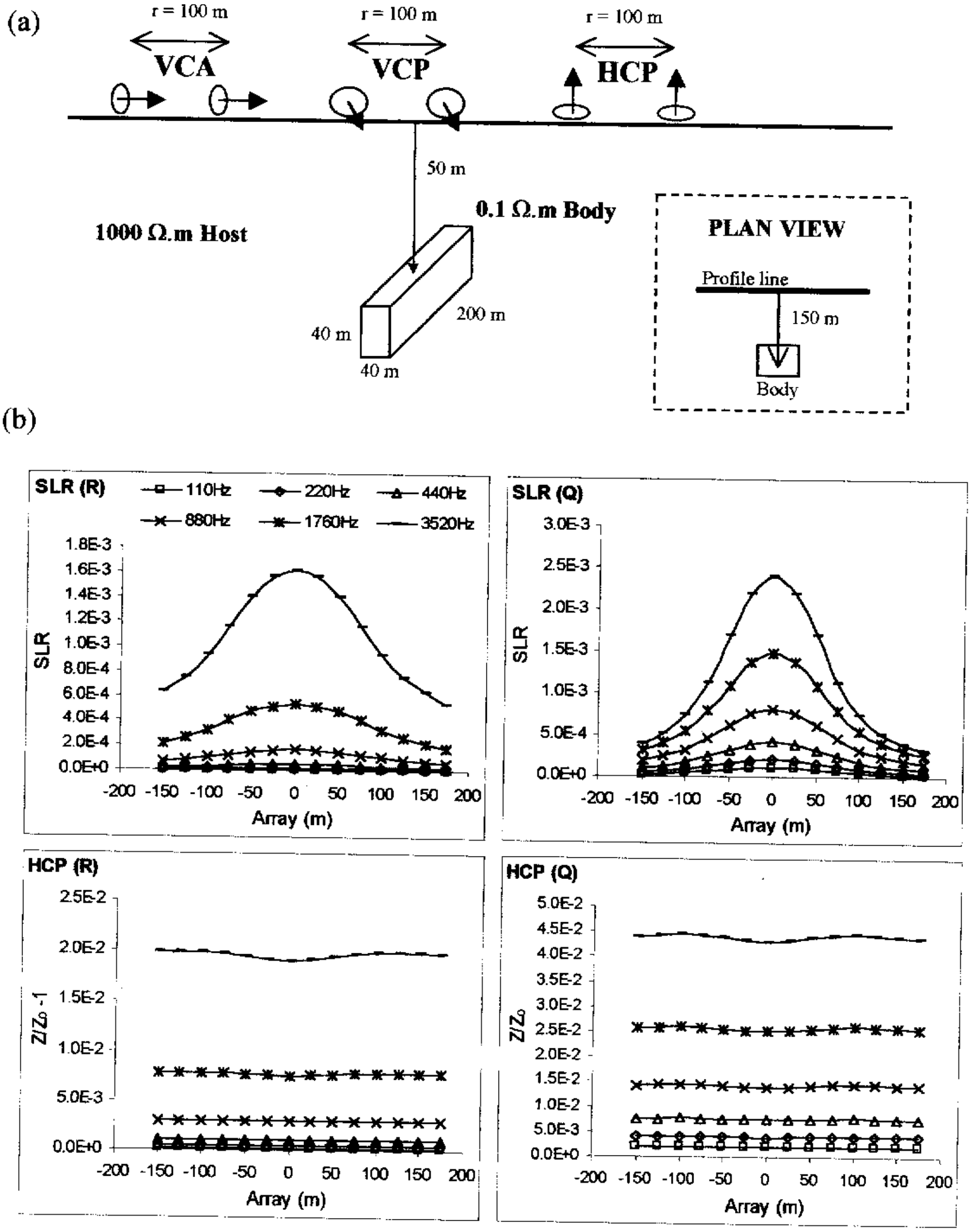

Figure 3.10 SLR and HCP responses for a homogeneous half-space Earth model including a conductive 3-D body displaced 150m off profile. **(a)** Earth model including a conductive 3-D body displaced 150m off profile. **(b)** In-phase (R) and quadrature (Q) profile responses at the range of frequencies listed in the first plot. HCP is not sensitive to off-profile body and is dominated by the layered Earth response. The SLR profile clearly indicates the presence of the body and is a different shape compared with Figure 3.6. In this case the VCA response is the main contributor to the SLR anomaly.

(a)

(b)

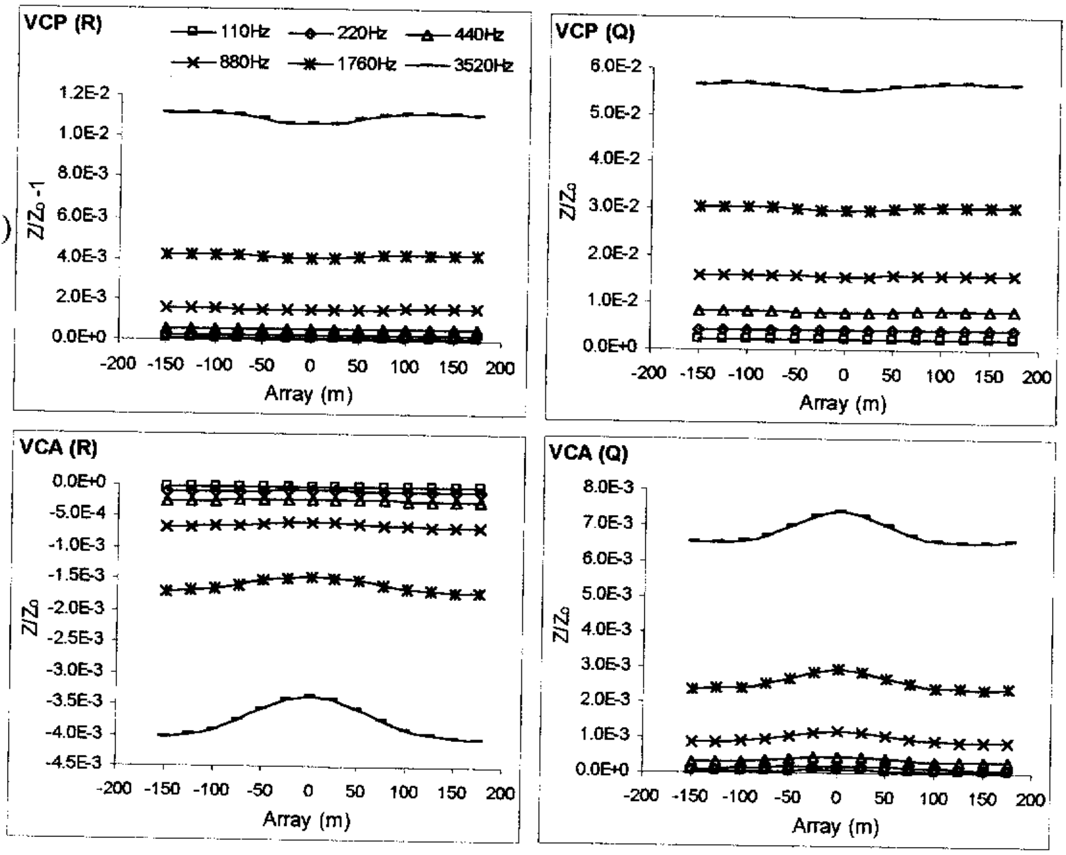

Figure 3.11 SLR and HCP responses for a homogeneous half-space Earth model including a conductive 3-D body displaced 150m off profile. **(a)** Earth model including a conductive 3-D body displaced 150m off profile. **(b)** In-phase (R) and quadrature (Q) profile responses at the range of frequencies listed in the first plot. HCP is not sensitive to off-profile body and is dominated by the layered Earth response. The SLR profile clearly indicates the presence of the body and is a different shape compared with Figure 3.6. In this case the VCA response is the main contributor to the SLR anomaly.

The SLR profiles, being a combination of the three configuration responses, exhibit a greater sensitivity to displaced bodies than the HCP and give a very noticeable indication of the target. Note, however that the shape of the SLR is very different to the shape in Figure 3.6(b). This is due to the VCA configuration being the main contributor to the SLR in this case. The SLR resembles a typical VCA anomaly.

3.1.4.4 Resistive bodies

EM inductive methods are used primarily in the search for conductive target bodies embedded in more resistive host rocks because the increased magnetic field observed near a conductive body is created by the extra current flow induced in or channelled through the body. Resistive bodies do not allow current to flow through them as readily as the conductive host rock and so the effect of a resistive body in a conductive host medium is a deflection of the current around the resistive body. A consequence of the deflection of currents around the resistive body is a change in the measured magnetic field at the surface. However, the lack of current flow in the resistive body produces less effect than the extra currents flowing in a conductive body and is consequently more difficult to detect. Unless the resistive body is very extensive or close to the surface, the change in magnetic field due to the presence of a resistive body is not usually noticeable in the presence of the large response from the more conductive Earth layers. The idea can be cast in the form of a simple analogy with a number of candles illuminating a dark room. If one of the candles is extinguished or burns less brightly than the others, its effect is not readily noticed due to the light coming from the other candles. However, the extinguishment or reduced luminance of a single candle becomes very significant and is readily noticed if it is the only source of light in the room. Based on this simple analogy the SLR concept extinguishes the 'other candles' and enables the weaker response of a resistive body to be observed.

The concept of exploring for resistive targets with an inductive technique may be viewed with scepticism by some geophysicists but it can be achieved using the SLR technique. To demonstrate the potential of the SLR to locate resistive targets in a more conductive host, the resistivity of the body shown in Figure 3.12(a) is changed to 500 Ω.m and the half-space resistivity changed to 100 Ω.m. The HCP and SLR profile responses are shown in Figure 3.12(b) and the VCA and VCP profiles are shown in Figure 3.13. The presence of the resistive body is not evident in the profile responses of the VCP and VCA configurations, other than small variations in the VCA in-phase response at 3520 Hz, and is only indicated in the HCP quadrature profile by very subtle variations. Upon transforming the data to the SLR, the presence of the target is unambiguously shown. It is also an interesting (and not totally unexpected) feature of the SLR that a resistive target body produces an amplitude peak over the body whereas a conductive target produces a trough over the body. This feature of the SLR provides a simple and clear indication of the nature of the conductivity contrast responsible for the anomalous signals and assists in the interpretation of the SLR.

3.1.4.5 Multiple bodies

The signal from a conductive target can not be considered in isolation due to the coupling between it, the conductive host medium and other conductive structures nearby. In many applications the signal from the target body is difficult to resolve due to interference from the signals from other conductive units in close proximity. In particular, small, shallow, conductive structures can very easily produce a response that overshadows the responses coming from deeper targets.

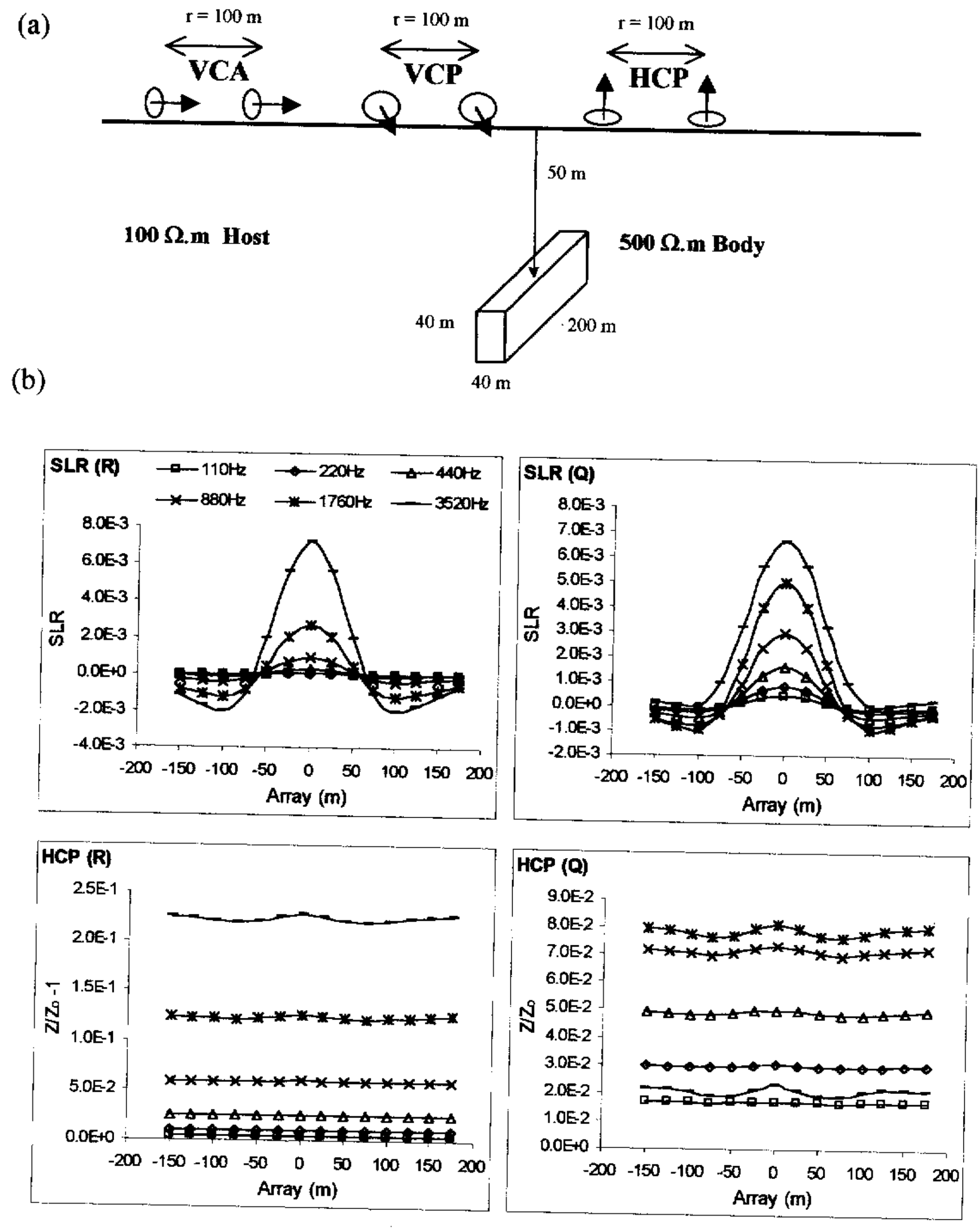

Figure 3.12 SLR and HCP responses for a homogeneous half-space Earth model including a ***resistive*** 3-D body. **(a)** Earth model including a ***resistive*** 3-D body. **(b)** SLR and HCP in-phase (R) and quadrature (Q) profile responses at the range of frequencies listed in the first plot. Note that the HCP response is very small and the SLR responses are reversed in sign compared with Figure 3.6.

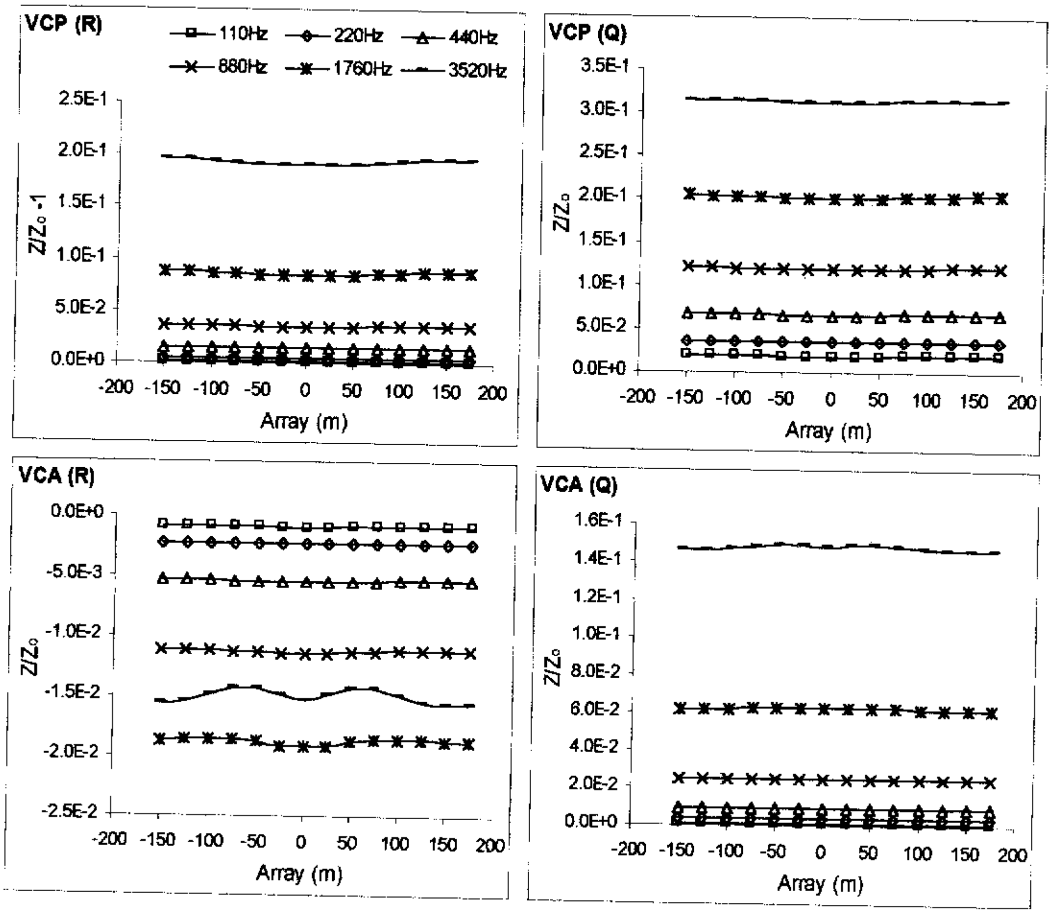

Figure 3.13 VCP and VCA responses for a homogeneous half-space Earth model including a ***resistive*** 3-D body. In-phase (R) and quadrature (Q) profile responses at the range of frequencies listed in the first plot. Note that the in-phase VCA response at 3520 Hz displays a small but observable signal from the target.

The SLR transformation has been seen to enhance the responses from off-profile structures (see Figure 3.10) which may result in deleterious effects on the profile response in terms of interference from unwanted 'targets'. To demonstrate the effect of multiple bodies, the model in Figure 3.14(a) was used. In this model the target body is located at x = 0 m at a depth of 50 m. Two smaller bodies are included in close proximity, one along the profile at x = -100 m and depth 20 m, the other at x = 0 m but displaced from the profile by 150 m and at a depth of 30 m. All bodies have the same resistivity (0.1 Ω.m) and their dimensions are given in the figure. The HCP and SLR profile responses are shown in Figure 3.14(b). It is noted in this figure that the HCP profiles are dominated by the layered Earth response whereas the SLR provides a more definite signature of the target. The presence of the two smaller bodies has distorted the shape of the SLR signature, especially at 3520 Hz. The SLR is not capable of discriminating between useful and unwanted signals so it is very important that the survey is designed to produce the maximum response from the target being sought.

3.1.4.6 Non uniform overburden

Prospecting in regolith affected areas is a difficult proposition due not only to the problem of transmitting enough energy to the target beneath the overburden but also due to the variable nature of the overburden. Changes in overburden depth and conductivity will affect the current flow in the Earth and produce a measurable change in the fields at the surface. It is often difficult to distinguish the responses caused by overburden variations from those of possible targets (Scott and Fraser, 1973; Villigas-Garcia and West, 1983; Nabighian and Macnae, 1991).

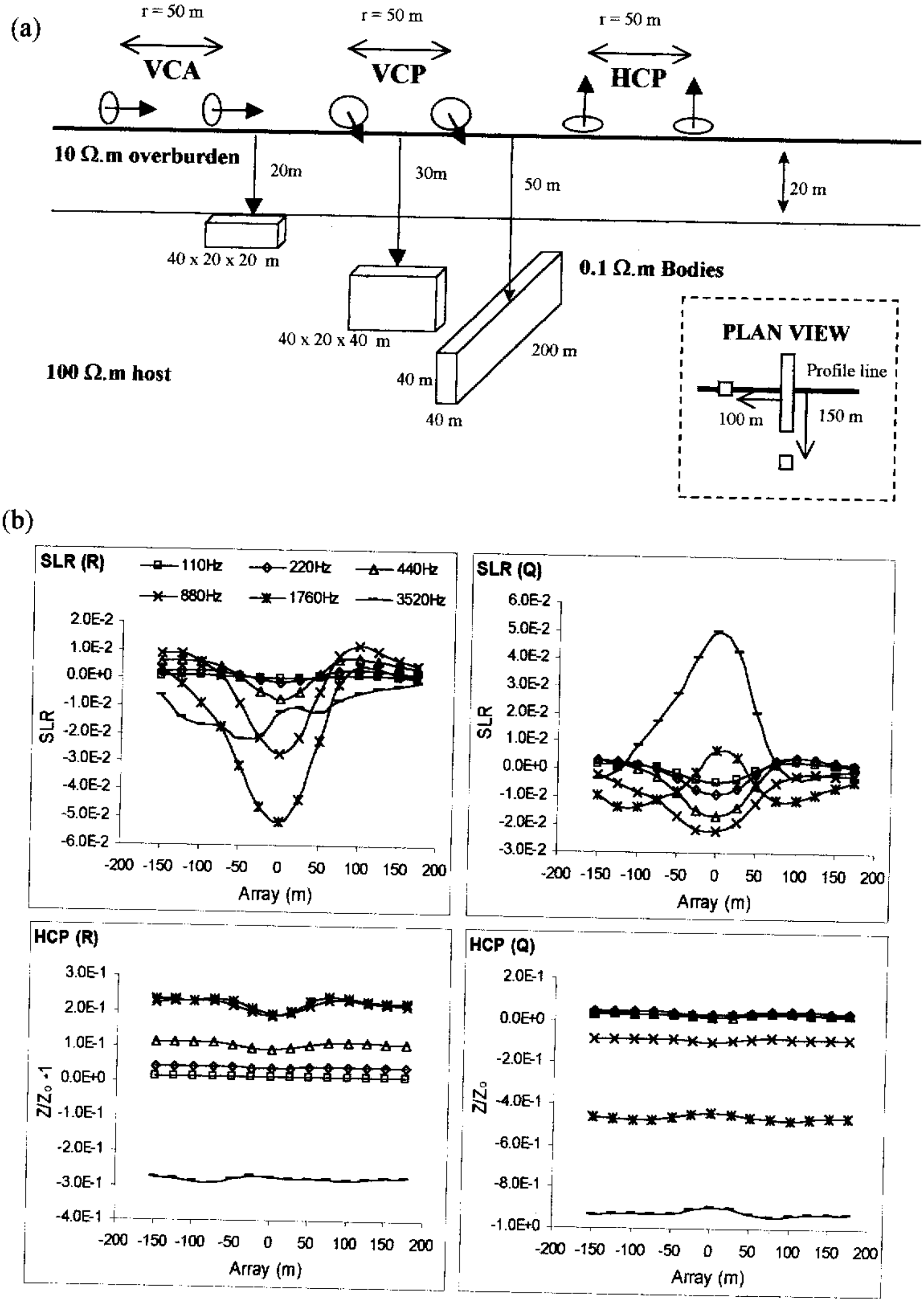

Figure 3.14 SLR and HCP responses for a homogeneous half-space below conductive overburden Earth model including 3 conductive bodies of equal resisitivity at different depths. **(a)** Earth model including 3 conductive bodies of equal resistivity at different depths. **(b)** In-phase (R) and quadrature (Q) profile responses at the range of frequencies listed in the first plot. The SLR has been distorted by the shallow bodies particularly at the higher frequencies.

Modelling a varying overburden using integral equation methods requires the use of a large number of elements to define an overburden area that is sufficiently large that edge effects are not apparent. Because of this, I limit modelling the range of overburden variations to a step like change in thickness. Finite element and thin sheet integral equation programs may be more useful in this regard but were not pursued since the main purpose of this section is purely to demonstrate the usefulness of the SLR concept and not necessarily produce intricate models.

A simple model to represent a step-like change in overburden thickness is shown in Figure 3.15(a). The overburden has a conductivity of 10 Ω.m and has a 20 m change in depth at x = 0 m. The HCP, VCP and VCA profiles across this step all provide some indication that the overburden is not uniform. The HCP configuration again produces the largest variation whereas the VCP and VCA responses are much more subtle. The SLR transformation removes a large part of the signal and emphasises the subtle variations in the individual profiles. This results in a very noticeable change in the profile response in the vicinity of the overburden step.

In Figure 3.16(a) the model is changed to include a target body beneath the overburden irregularity. This represents a common exploration scenario. The profiles shown in Figure 3.16(b) show that the SLR response is dominated by the overburden irregularity causing the small signal from the target to be undetected. This illustrates a limitation of the SLR technique, that *all* anomalies are enhanced, regardless of their cause. In this geological scenario, the target may be observed where the overburden is less conductive or the target body is larger or more conductive.

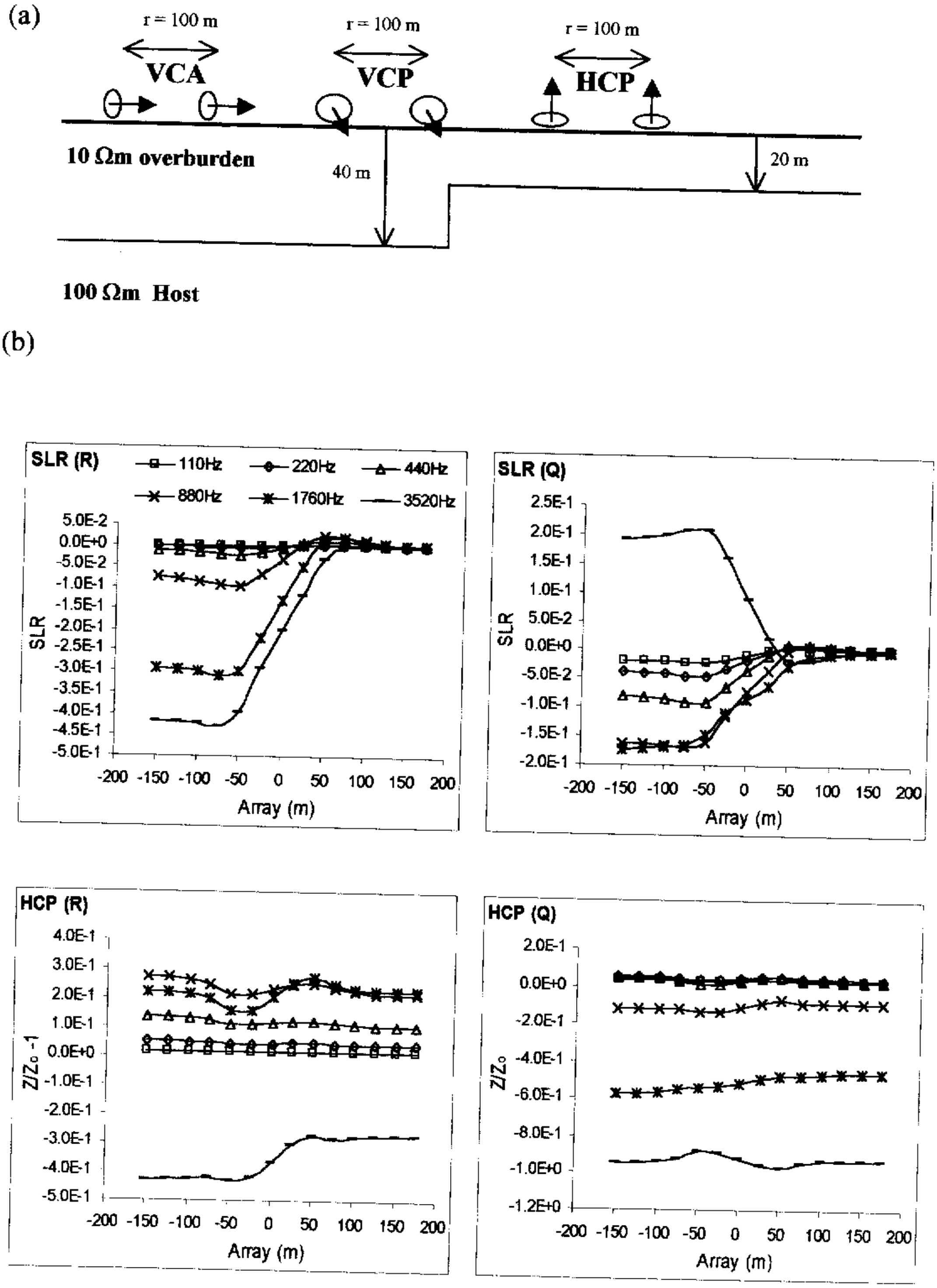

Figure 3.15 SLR and HCP responses near a step change in overburden thickness. **(a)** Earth model showing a step change in overburden thickness at location x = 0 m above a homogeneous half-space, no target body present. **(b)** SLR and HCP in-phase (R) and quadrature (Q) profile responses at the range of frequencies listed in the first plot. Note that the SLR signature enhances the effect of the overburden non-uniformity.

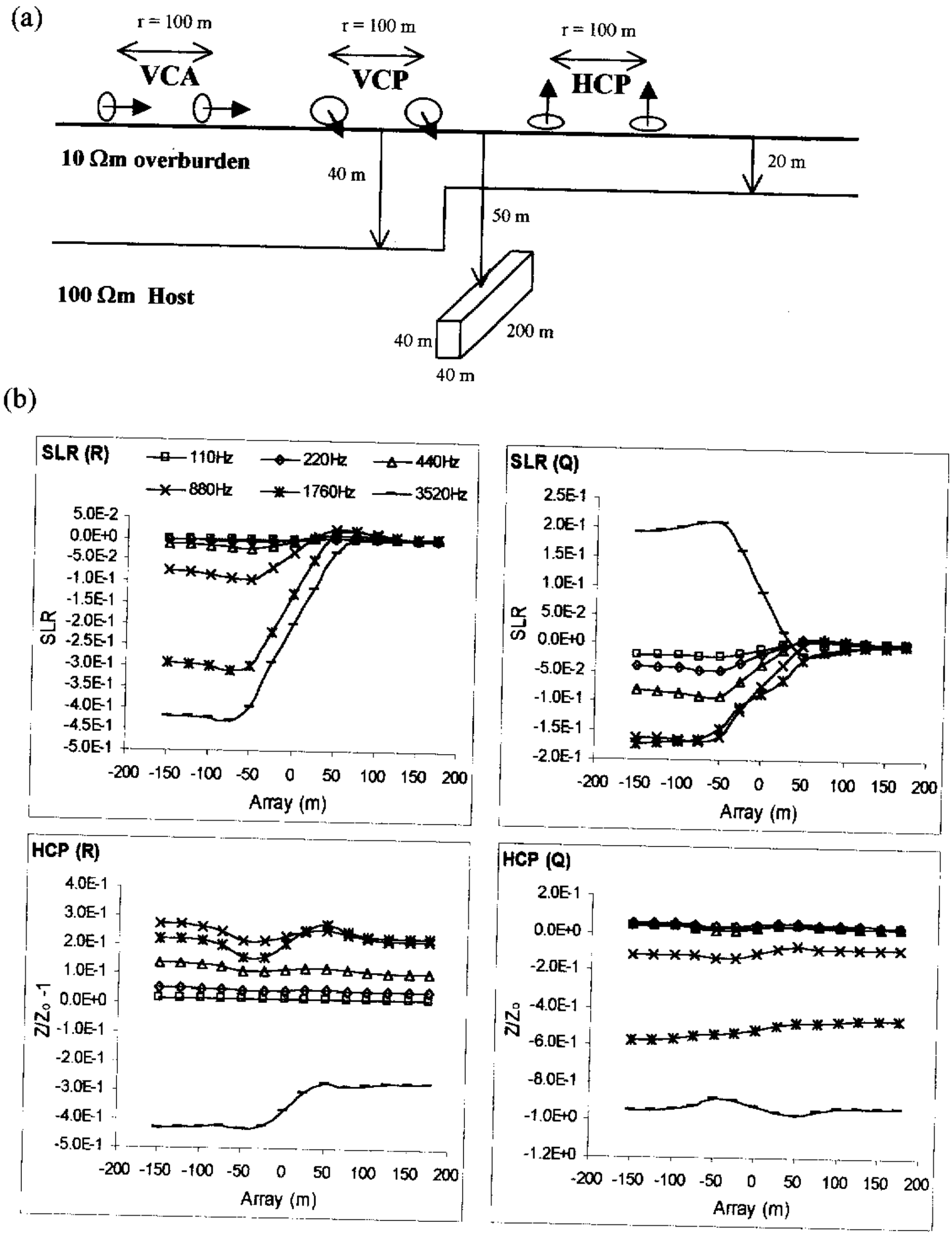

Figure 3.16 SLR and HCP responses near a step change in overburden with a conductive 3-D target located adjacent to the step. **(a)** Earth model showing a step change in overburden thickness at location x = 0 above a homogeneous half-space with conductive 3-D target located adjacent to the step. **(b)** SLR and HCP in-phase (R) and quadrature (Q) profile responses at the range of frequencies listed in the first plot. The responses are dominated by the overburden non-uniformity. The SLR enhances *all* anomalies.

3.1.4.7 Airborne surveys

One advantage of inductive EM methods when compared with galvanic methods (CSAMT, MMR) is that the transmitter need not be in contact with the ground. This makes inductive EM methods very useful for airborne surveys that provide the opportunity to explore large areas of relatively inaccessible regions in a short period of time. This is of particular interest to Australian exploration where vast areas of land in very remote regions need to be explored. Airborne systems have the added disadvantage of being affected by other sources of noise due to altitude variations, wind noise, aircraft navigation error and bird swing (Palacky and West, 1991; Buselli et al., 1998; Green, 1998). The SLR concept has application to helicopter EM surveys in which a rigid boom is used to hold the transmitter and receiver at the same altitude. However, there are currently no airborne systems that are equipped to record the three configuration responses necessary for the SLR transformation to be applied. In the case of fixed-wing airborne surveys the receiver is often towed behind the aircraft in a 'bird' that flies below the transmitter altitude, so the relationship between the different configurations does not hold. Some fixed-wing AEM systems (Fountain, 1998) use horizontal dipole sources, but in most cases the fixed wing transmitter loop is strung around the tips of the aircraft horizontally to produce a vertical magnetic dipole source.

As an indication of the application of the SLR to helicopter surveys, the two-layered Earth model of Figure 3.17(a) was used with the transmitter and receiver elevated 30 m above the Earth's surface. In this case a transmitter-receiver separation of 10 m was used.

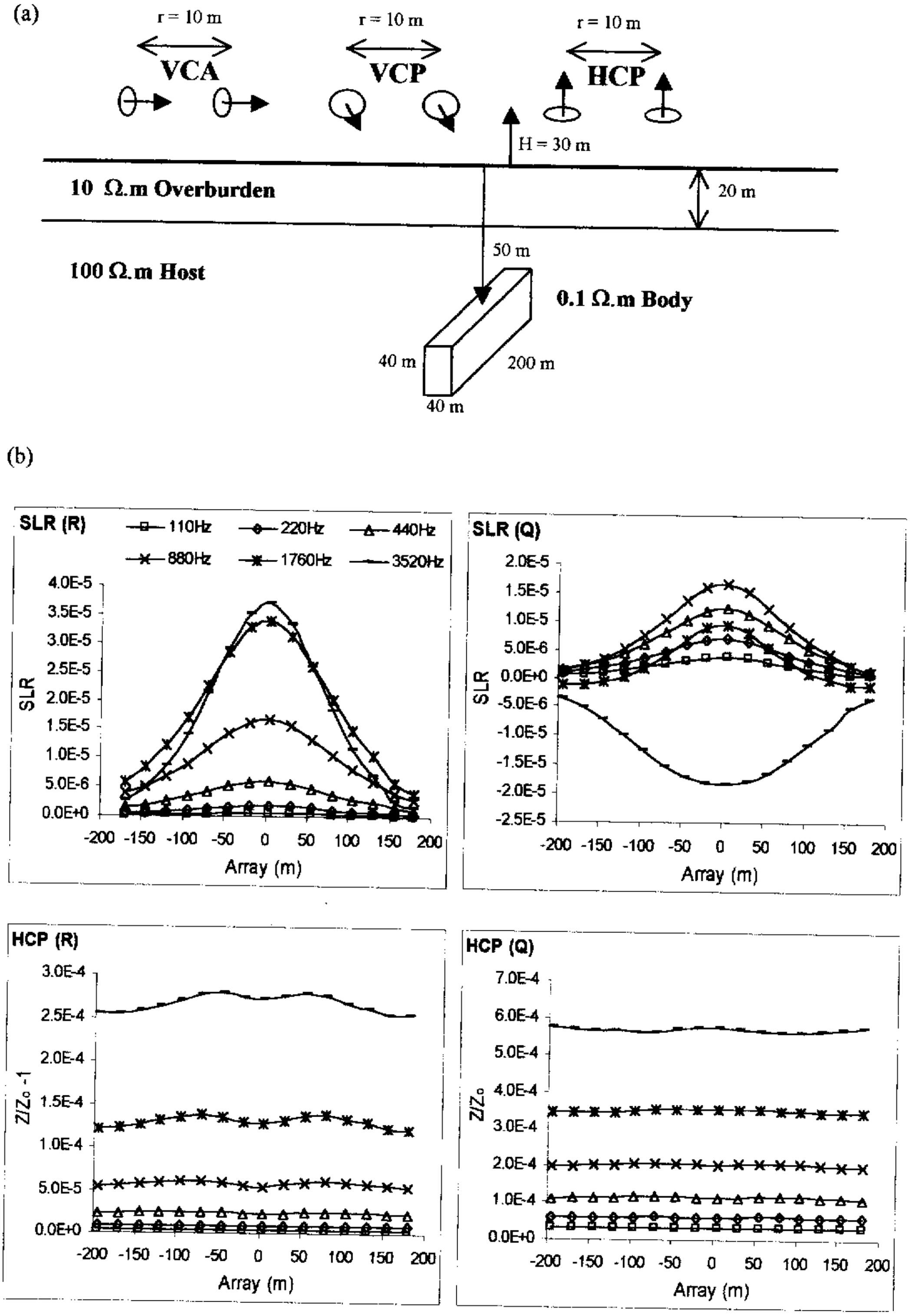

Figure 3.17 SLR concept applied to helicopter EM. **(a)** Homogeneous half-space below conductive overburden Earth model including a conductive 3-D body. Note the configurations at a height of 30 m to simulate a helicopter AEM survey. **(b)** SLR and HCP in-phase (R) and quadrature (Q) profile responses at the range of frequencies listed in the first plot. Note the very small and broad response due to the elevation above the ground.

(c)

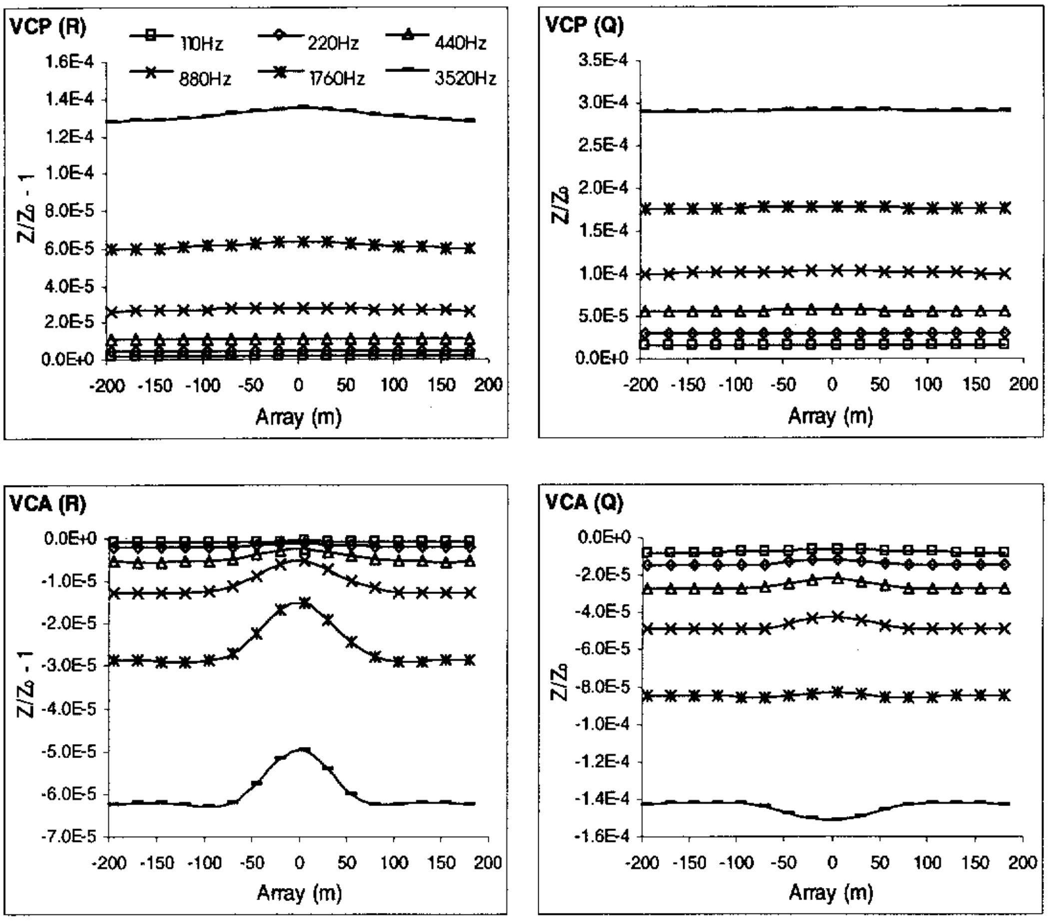

Figure 3.17 *continued* **(c)** VCP and VCA in-phase (R) and quadrature (Q) profile responses for the model in Figure 3.17(a) at the range of frequencies listed in the first plot. Note that the large Earth response in both configurations due to the conductive overburden prevents the signal from the body from being observed.

The profile responses shown in Figure 3.17(b) and 3.17(c) are dominated by the Earth response with the exception of the SLR which presents a very obvious signature of the target. In this case, due to the elevation above the surface and the small Tx-Rx separation, the measured ${}^{Z}\!/_{Z_0}$ amplitudes are much smaller than the ground survey amplitudes and the target signature is very broad.

3.2 Large loop transmitters

In areas dominated by conductive regolith it is very important that enough energy is transmitted into the Earth to induce a sufficiently large response from the target. The transmitter moment (and consequently the energy output) is proportional to the area of the transmitter loop, so doubling the radius of the loop produces a four-fold increase in the transmitter moment. In Australia it is common to use square or rectangular transmitting loops ranging from 50 m to 200 m on a side for moving loop profiles using up to 20 Amperes of current. Larger loops are often used for follow up fixed-loop surveys where more a priori information regarding the location of the target is available. There is a range of configurations commonly used in large loop EM prospecting, including coincident loop, in-loop and separated loop geometries that differ only in the position and nature of the receiver. Like the small loop systems, the fields measured by the receiver consist of a portion due to the currents in the Earth layers and a portion due to the scattering currents inside the target. Clearly, with large loops it is impractical to consider using vertical loops as done in the previous section. I therefore examine the field equations and seek some other means of data redundancy to reduce the Earth response and enhance the target response.

For a circular loop of radius 'a' metre on the surface of a uniformly layered Earth the surface EM field equations in cylindrical coordinates are given by Ward and Hohmann (1991) as

$$E_{\phi} = \tfrac{i\omega\mu_0 Ia}{2}\int_0^{\infty}(1+R)J_1(\lambda a)J_1(\lambda\rho)d\lambda\,, \tag{3.11}$$

$$H_z = \tfrac{Ia}{2}\int_0^{\infty}(1+R)\lambda J_1(\lambda a)J_0(\lambda\rho)d\lambda\,, \tag{3.12}$$

$$H_{\rho} = \tfrac{Ia}{2}\int_0^{\infty}(1-R)J_1(\lambda a)J_1(\lambda\rho)d\lambda\,. \tag{3.13}$$

It should be noted that when profiling, the displacement vector ρ corresponds to the profile direction (Cartesian x direction) and the transverse vector ϕ corresponds to the cross-profile direction (Cartesian y direction). Taking the derivative of equation (3.11) with respect to ρ yields

$$\tfrac{\partial}{\partial\rho}E_{\phi} = \tfrac{i\omega\mu_0 Ia}{2}\int_0^{\infty}(1+R)J_1(\lambda a)[\lambda J_0(\lambda\rho) - \tfrac{1}{\rho}J_1(\lambda\rho)]d\lambda \tag{3.14}$$

which can be written as

$$\tfrac{\partial}{\partial\rho}E_{\phi} = \tfrac{i\omega\mu_0 Ia}{2}\int_0^{\infty}(1+R)\lambda J_1(\lambda a)J_0(\lambda\rho)d\lambda - \tfrac{i\omega\mu_0 Ia}{2\rho}\int_0^{\infty}(1+R)J_1(\lambda a)J_1(\lambda\rho)d\lambda\,. \tag{3.15}$$

Comparison of equation (3.15) with equations (3.11) and (3.12) allows me to write equation (3.15) as

$$\tfrac{\partial}{\partial\rho}E_{\phi} = i\omega\mu_o H_z - \tfrac{1}{\rho}E_{\phi}\,. \tag{3.16}$$

Recognising the first term of the right hand side of equation (3.16) as the time derivative of the vertical magnetic field intensity $\frac{\partial B_z}{\partial t}$, which is the quantity most readily measured in the field, I define the Large Loop Residual LLR as

$$LLR = \tfrac{\partial}{\partial\rho}E_{\phi} + \tfrac{1}{\rho}E_{\phi} - \tfrac{\partial}{\partial t}B_z \tag{3.17}$$

Like its small-loop counterpart, the LLR has a value of zero when the measurements are made on the surface of a uniform half-space or layered Earth. In the presence of an inhomogeneity such as a conductive mineral deposit, or some other non-layered structure, the LLR will have a non-zero value. Since the LLR is a combination of the electric and magnetic field measurements, a non-zero residual will represent a combination of the electric and magnetic field responses of an inhomogeneity.

3.2.1 Survey configurations

The LLR definition has application to any large loop survey configuration that allows measurements to be made at a number of locations along the profile for each transmitter position. The most likely geometries in which the LLR will find application are the fixed loop, in-loop and the separated loop (slingram) configurations. It may also have application to the coincident loop configuration that utilises the transmitter loop as the magnetic field receiver, but this has not been pursued in this work.

A difficulty arises when dealing with the in-loop configuration since this involves measuring the EM field components (most commonly $\partial B_z/\partial t$) at the centre of the transmitting loop. The LLR has a singularity at the centre of the transmitter loop i.e. where $\rho = 0$ by virtue of the E_ϕ/ρ term. To overcome this, the field measurements must be assumed to be made at a short distance (< 5 m) away from the centre of the loop and the LLR computed in the usual way. This small mathematical difficulty should not detract form the basic philosophy of the LLR approach which is to transform the measured data into a quantity that does not include the layered Earth response H^L.

The LLR concept may be considered unnecessary for the in-loop configuration since the layered Earth response at the centre of the transmitter is zero for both the transverse electric and horizontal magnetic field components. Any variation in these components at the centre of the transmitter loop is therefore attributable to non-horizontal structures within the Earth. Despite this, the component of choice in most surveys is the vertical magnetic field $\partial B_z/\partial t$ since the horizontal components are more vunerable to interference from spherics and other sources of noise (West et al., 1984; McCracken et al., 1986b). Survey configurations that measure the EM field components away from the centre of the transmitter loop (fixed loop and separated loop), will record data that contain a layered Earth response in all components. In many cases the layered Earth response may be larger than the response from the target and will require processing to enhance the target response. It is these surveys that should benefit most from the LLR concept.

3.2.2 Spatial derivative of the transverse electric field

The LLR is more difficult to compute than the SLR due to the presence of the $\frac{\partial}{\partial \rho} E_\phi$ term. In order to produce an accurate estimate of its spatial derivative it is necessary to make at least two measurements of the transverse electric field near each receiver station. The rate at which the field varies between the two locations approximates the spatial derivative if the distance between the two measurements is sufficiently small. There are a variety of methods of numerical differentiation that can be used for determining the derivative of a quantity from a set of measurements. I compare three very simple techniques below.

3.2.2.1 Difference method

The difference method involves the approximation of a derivative by a difference between closely spaced measurements. In this case the average of the derivatives calculated in the forward and reverse directions using the field measurements at the stations immediately to either side of the station in question are used. i.e. the spatial derivative of the transverse electric field at the i'th receiver location $\partial E_\phi^i / \partial \rho$ is found using

$$\frac{\partial E_\phi^i}{\partial \rho} = \frac{1}{2}\left[\frac{E_\phi^i - E_\phi^{i-1}}{\rho^i - \rho^{i-1}} + \frac{E_\phi^{i+1} - E_\phi^i}{\rho^{i+1} - \rho^i}\right]. \tag{3.18}$$

In effect this method assumes a linear trend between data points which is very simplistic but gives good results if the receiver interval is sufficiently small near the transmitter or the field is being measured at large distances from the transmitter. When dealing with more rapidly varying functions the simple approach used here becomes less reliable and more rigorous methods must be used.

3.2.2.2 Newton's method

An alternative method of estimating the value of the spatial derivative is described by Press et al., (1992) as

$$\frac{\partial E_\phi^i}{\partial \rho} = \left[\frac{(2\rho^i - \rho^{i+1} - \rho^{i+2})E_\phi^i}{(\rho^i - \rho^{i+1})(\rho^i - \rho^{i+2})} + \frac{(\rho^i - \rho^{i+2})E_\phi^{i+1}}{(\rho^{i+1} - \rho^i)(\rho^{i+1} - \rho^{i+2})} + \frac{(\rho^i - \rho^{i+1})E_\phi^{i+2}}{(\rho^{i+2} - \rho^i)(\rho^{i+2} - \rho^{i+1})}\right] \tag{3.19}$$

This method differs from the previous one in that it computes the derivative at location i by using the next two locations i+1 and i+2, and not by using the nearest points on either side. As an improvement to the method, I again take the average of the forward and reverse derivatives to obtain a closer estimate of the derivative at the station.

3.2.2.3 Polynomial curve fitting

The third method of estimation involves approximating the spatial function with an appropriate polynomial function. This is achieved using the best fitting curve, determined using a least squares criterion, over the specified range of data points. The derivative can then be computed analytically from the estimated polynomial.

Computer routines are readily available (Press et al., 1992) to perform such tasks but need to be used with consideration of the type of polynomial curve being used. The derivative obtained using a quadratic fit may be significantly different from that obtained if a cubic (or higher) polynomial fit were used. In this work the routine DDPOLY (Press et al., 1992) is used.

3.2.2.4 Comparison of the methods

Examination of the frequency domain electric field amplitudes shown in Figure 3.18 as a function of distance from a circular transmitter of radius 56m on the surface of a uniform half-space of resistivity 100 Ω.m, reveals that the in-phase part varies as a cubic function of position whereas the quadrature part varies as a power-law. The equations that describe the variations are shown in Figure 3.18.

As an indication of the usefulness of the methods of gradient computation, each was used in turn to evaluate the gradient of the quadrature E_ϕ power-law function at each receiver location. The function has a derivative that is readily calculated analytically and provides a reliable check on the performance of the different methods of derivative estimation. Figure 3.19 compares the error associated with the gradient estimation obtained using the three methods described above, including a three point and five point polynomial fit. The error is expressed as a percentage of the analytical value. It is clear from Figure 3.19 that the five point polynomial fit provides the best estimate of the derivative in this example. It should be noted however, that the other methods may be sufficiently accurate for use in the computation of the LLR.

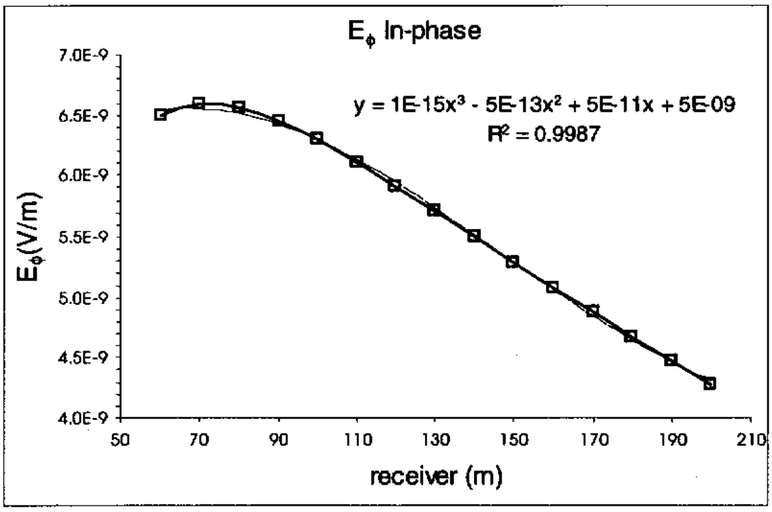

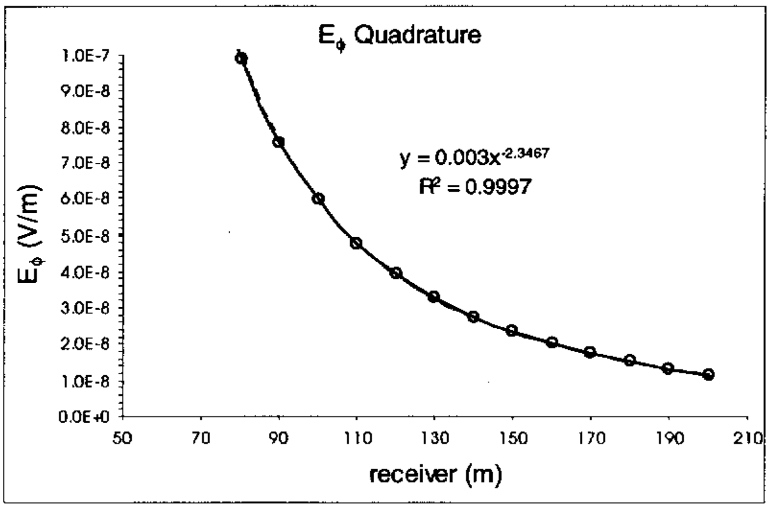

Figure 3.18 Spatial variation of the in-phase and quadrature E_ϕ component on the surface of a uniform Earth outside a circular loop transmitter at 880 Hz. The transmitter wire is located at x = 56 m. The smoothness of the cubic and power law functions should enable an accurate estimate of the gradient to be obtained.

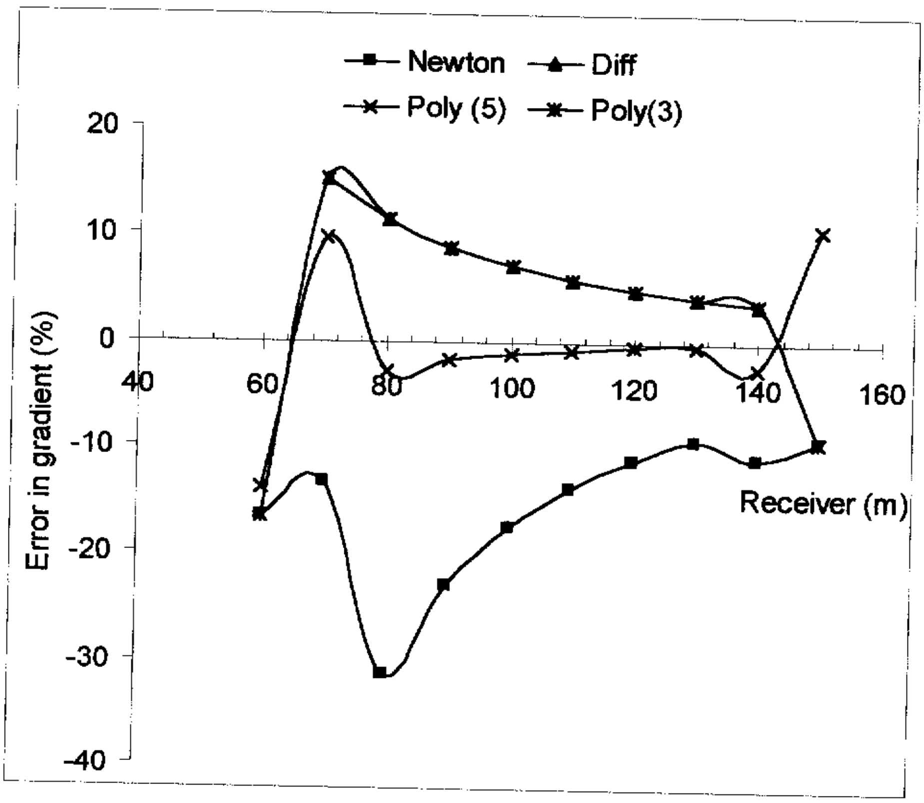

Figure 3.19 Percentage error in the gradient of analytical functions calculated by different methods. The 5 point polynomial fit produces the best estimate of the gradient.

3.2.3 Sensitivity of the LLR to the spatial derivative

In Figure 3.20 I present the quadrature part of the vertical magnetic field component computed for a fixed loop transmitter of radius 56 m, on the surface of a uniform half-space of resistivity 100 Ω.m. The field responses are computed at 880 Hz at 10 m intervals and combined to produce the LLR according to equation (3.17). Also in Figure 3.20 are the LLR values computed using the different methods of gradient calculation described above. It is apparent in this figure that the LLR is relatively insensitive to the method of gradient calculation. The residuals are all very closely matched but exhibit some variation due to the different methods of gradient calculation. The variations in the LLR are more than two orders of magnitude smaller than the dB_z/dt responses i.e. less than 1% difference, but are exaggerated by the logarithmic plot. It is not likely that the small errors introduced in the calculation of the gradient will detract from the LLR concept which is to remove as much of the layered Earth response from the profile response as possible.

3.3 Application to square loops

The mathematical expressions used to define the LLR transformation are derived from the equations for the EM field components associated with a circular loop transmitter. The logistical difficulties associated with laying out a circular loop mean that it is very rarely done in practice. Most large loop transmitters are square or rectangular due to the relative ease of laying out wires in straight lines. At the centre of the transmitter loop the field responses obtained using a square loop are approximately equal to those obtained using a circular loop. Also, at large distances (> 2a) from the centre, a square loop adequately resembles a circular loop. It is only in the vicinity of the transmitter wire that there is a significant difference in the fields due to a circular transmitter and those due to a rectangular transmitter.

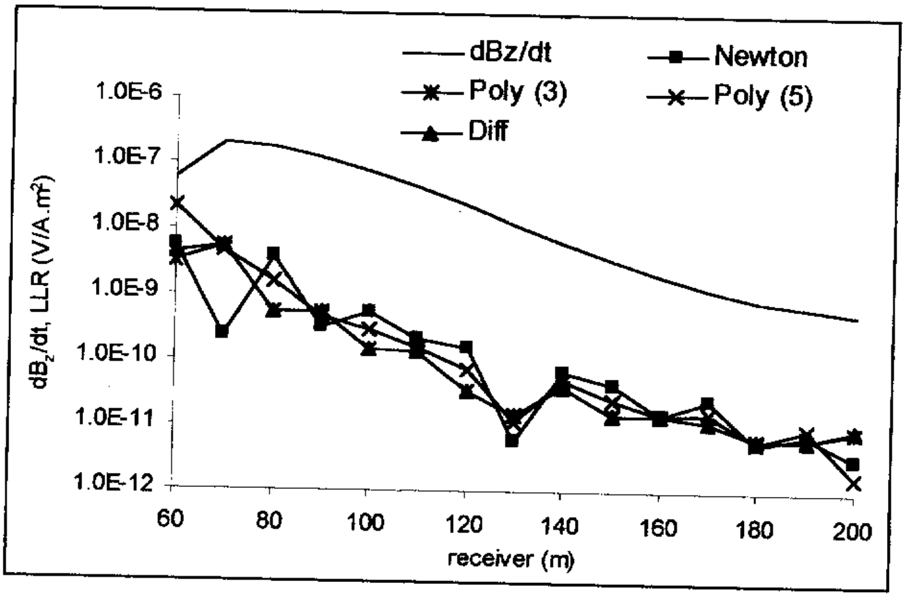

Figure 3.20 The LLR computed using different methods of gradient calculation compared to the dB$_z$/dt response. The LLR values show some variation but are 2 to 3 orders of magnitude smaller than the dBz/dt responses (i.e. less than 1% difference). The method of gradient calculation is *not* a critical part of the LLR concept.

The LLR concept does not suffer from this difference since the *relationship* between the fields is not dependent on the source geometry.

As a means of comparison, the layered Earth fields were computed using a circular loop of radius 56 m and square loop of 100 m length such that the area of the loops were equal. The vertical magnetic H_z and transverse electric E_ϕ fields were computed at 10 m increments from the centre of the loops. The layered Earth responses in these two components along the profile for a transmitter frequency 880 Hz is shown in Figure 3.21. It is evident that there is very little difference in the field responses due to a square loop compared to those of a circular loop (of equivalent area) for distances greater than 2a from the centre. Although not shown here, the fields at the centre of the loops are also very closely matched. It should be emphasised that the differences between these field values may be due not only to the different transmitter shapes, but also to the method of computation of those fields.

Computation of fields from a large transmitter is more difficult to accomplish than the fields from a dipole. The circular loop computation requires the evaluation of Hankel transforms in which the function to be integrated contains a first order Bessel function [see equation (3.11)] whereas the square loop computation involves the integration of Hankel transforms over the entire length of the transmitter wire (Poddar, 1982). Both methods are prone to significant numerical error.

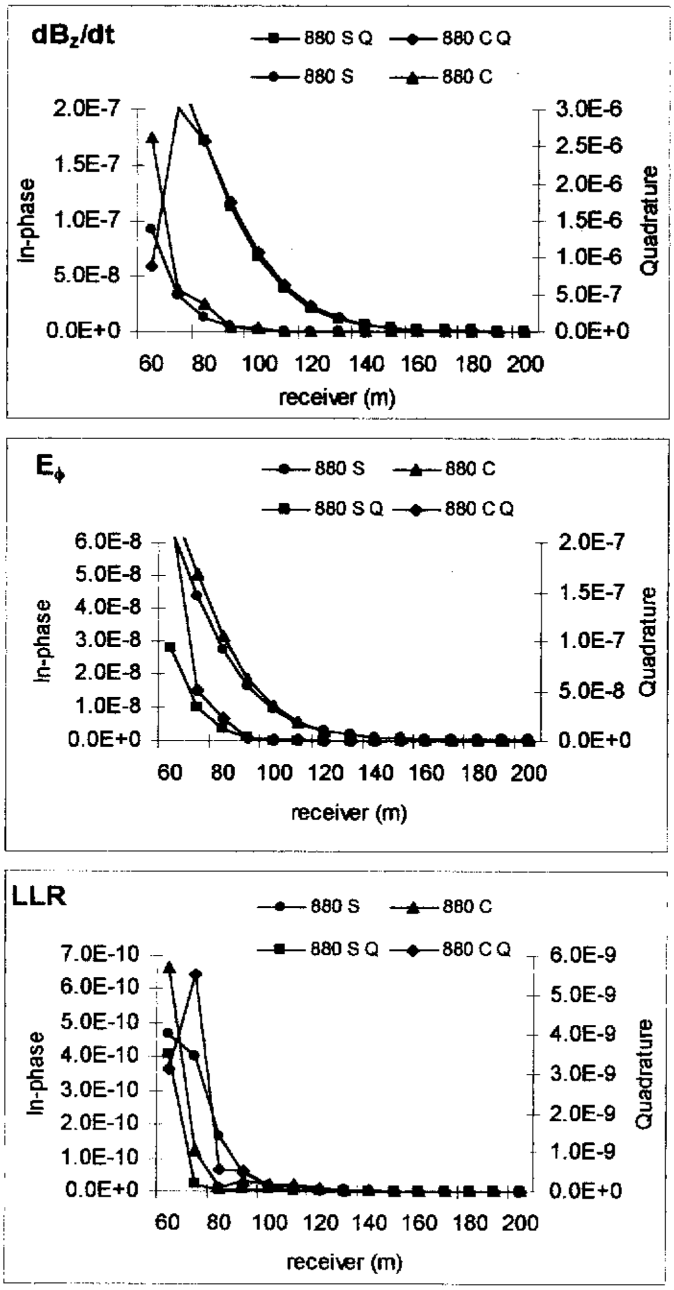

Figure 3.21 Comparison of the in-phase and quadrature (Q) field components and LLR using a square (S) and circular (C) transmitter. The field values show some variation close to the wire but are very similar beyond 50 m from the wire. The LLR is 2 to 3 orders of magnitude smaller than the E fields close to the wire and 4 to 5 orders smaller at distances beyond 50 m. Small differences in the LLR are probably due to computational inaccuracies.

The field responses computed for square and circular transmitters were used to compute the LLR using a five point polynomial fit of the E_ϕ data for calculating its spatial derivative $\frac{\partial}{\partial\rho}E_\phi$. The LLR values along the profile are shown in Figure 3.21 to be 2 to 3 orders of magnitude smaller than the field components and are very closely matched. This indicates that the shape of the transmitter is not critical to the success of the LLR concept. If the computations were exact, the LLR would be zero at all points along the profile. The relatively large values of the residual close to the transmitter wire are due to the differences in the field components at those locations. Small changes in the field components are enhanced by the LLR. The residual concept is not capable of discriminating between useful and non-useful signals and so careful interpretation is required.

3.4 Time domain Residuals

Modern frequency domain EM systems compensate for the primary field using a reference cable that links the transmitter to a bucking coil in the receiver. The bucking coil produces a magnetic field that negates the primary field from the transmitter and enables the receiver to measure only the signal from the currents induced in the Earth. In a resistive environment the EM field diffuses quickly and with little energy loss so that a large current can be induced in the conductive target. In a conductive environment much of the energy supplied by the transmitter is 'used up' by driving currents through the conductive Earth. This results in very much less energy being available to drive the currents in the conductive target and consequently its response is smaller than it would be if it were embedded in a resistive environment. Frequency domain EM methods are less successful in conductive environments due also to the shielding effect of the large signal produced by electric currents flowing in the Earth. The advantage of using a time-domain or transient system lies in the fact that the measurements are made in the absence of the primary field from the transmitter. As the transient currents in the Earth decay, the currents induced in the more conductive regions decay at a slower rate and may become detectable at late times. Late time channels usually measure the responses from conductive bodies after the Earth response has decayed away. However, the amplitude of the signal is much smaller in the late time channels and may be difficult to resolve. In order to resolve small signals late in time, many repeated measurements must be made and stacked together. This slows down acquisition and increases the cost of a survey. If the Earth response were reduced, the target response might be detectable earlier in time when its signal is larger. If this were possible, it would make target definition easier and also increase the production rate of EM surveys since the data would not have to be stacked for so long.

So far, in this chapter, the concept of data redundancy and the SLR and LLR transformations have been restricted to frequency domain surveys. This is primarily due to the fact that most time domain EM modelling is performed in the frequency domain and then converted to an equivalent time domain survey using a data transform such as the Fourier (Newman et al., 1986) or Laplace (Knight and Raiche, 1982) transform. In section 3.4 the ideas presented in section 3.1 are extended to include the time domain case. The concept is once again demonstrated on synthetic data. To avoid unnecessary repetition of the theoretical development of the residuals only a brief overview of the frequency to time transform, followed by some results of computer modelling is presented.

In time domain EM surveys for mineral exploration one of the most important indicators of the presence of a conductive deposit is a slow decay of the transient EM fields. It is only within a finite time window that the response of a target body will be large enough to be observed above the layered Earth response. The exponential decay of the fields associated with a confined current can be seen on log-log decay plots as a convex curvature impressed on an otherwise linear decline. The notion of data redundancy and the removal of the layered Earth response described in the previous sections apply equally well to time domain measurements.

3.4.1 The Fourier transform

The Fourier transform F(ω) of a function f(t) is defined by the integral

$$F(\omega)=\int_{-\infty}^{\infty} f(t)e^{-i\omega t}dt \tag{3.20}$$

and the corresponding inverse transform by the integral

$$f(t)=\frac{1}{2\pi}\int_{-\infty}^{\infty} F(\omega)e^{i\omega t}d\omega\,. \tag{3.21}$$

The fast Fourier transform (FFT) has found application in many areas of data processing and signal enhancement and numerical routines for its implementation are well developed. In order to adequately sample the frequency domain data to ensure a reliable transformation to the time domain, a large number of frequency domain data may be required. In EM 3-D modelling the requirement of a large number of computed frequency domain samples is often prohibitive in terms of computational time, particularly when using detailed models having a large number of elements. It is therefore necessary to compute the frequency domain responses at a number of sparsely sampled frequencies and then transform the data to the time domain. The accurate interpolation of complex numbers in the frequency domain is impossible (Uren and Leiss, 1989) and will create inaccuracies in the transformation (Lamontagne, 1975; Hohmann, 1983). Consequently, the FFT is not usually a preferred option for frequency to time transformations. Since the time domain response has a value of zero until the transmitter current changes, the transform shown in equation (3.21) can be modified to represent a causative step turn-off by use of the semi-infinite cosine transform (Newman et al., 1986)

$$B(t) = -\tfrac{2\mu_0}{\pi}\int_0^{\infty}\frac{\mathrm{Im}[H(\omega)]}{\omega}\cos(\omega t)d\omega, \qquad (3.22)$$

where B(t) represents the time varying magnetic field intensity and Im[H(ω)] the imaginary (quadrature) part of the frequency domain response computed at the angular frequency ω.

The quantity most readily measured in the field (by way of the voltage induced in a receiver coil) is the time derivative of magnetic field intensity dB/dt, which can be obtained directly from the frequency domain results using the Fourier sine transform

$$\frac{\partial B(t)}{\partial t} = \tfrac{2\mu_0}{\pi}\int_0^{\infty}\mathrm{Im}[H(\omega)]\sin(\omega t)d\omega. \qquad (3.23)$$

The integrations required for the transformation can be achieved by lagged convolution using digital filters (Anderson, 1975) and may require only 30 to 50 frequency domain computations, depending on the time interval being modelled.

3.4.2 Time domain modelling

In the following sections the LLR concept is applied in the time domain to three common survey configurations: fixed-loop; in-loop; and separated-loop (slingram), using some of the Earth models used in the previous section. In each case, the LLR is presented together with the conventional dB_z/dt response for comparison.

3.4.2.1 *Fixed loop survey*

A fixed loop survey was simulated using a 400 m x 400 m loop centred at x = -300 m on the surface of a two layered Earth and computing the EM field components along a profile line that extends from the loop and over the target. In this case, the target is a thin sheet of conductance [conductivity-thickness product (σ.t)] 400 S. Figure 3.22(a) shows the Earth model and Figure 3.22(b) the dB_z/dt profile responses for a number of time channels ranging from 2 ms to 15 ms. The profiles compare the responses obtained for the case where the target is not present i.e. the layered Earth response only, with the case where the target is present. The effect of the target is quite apparent. Also in Figure 3.22(b) are the LLR profiles for the same time channels with and without the target. The LLR profiles for the layered Earth case show very small amplitude variations caused by computational inaccuracies. The effect of the target body on the LLR profiles provides a much more definite indication of the presence of the target than the dB_z/dt profiles. The signature displayed in the LLR profiles is centred on the target location.

In addition to the information presented in the profile plots, time domain surveys also provide information about the rate of decay of the EM fields. The decay curves for selected receiver locations are shown in Figure 3.22(c) for the dB_z/dt component and Figure 3.22(d) for the LLR. Again, a comparison is made between the purely layered Earth case and the response when the target is present.

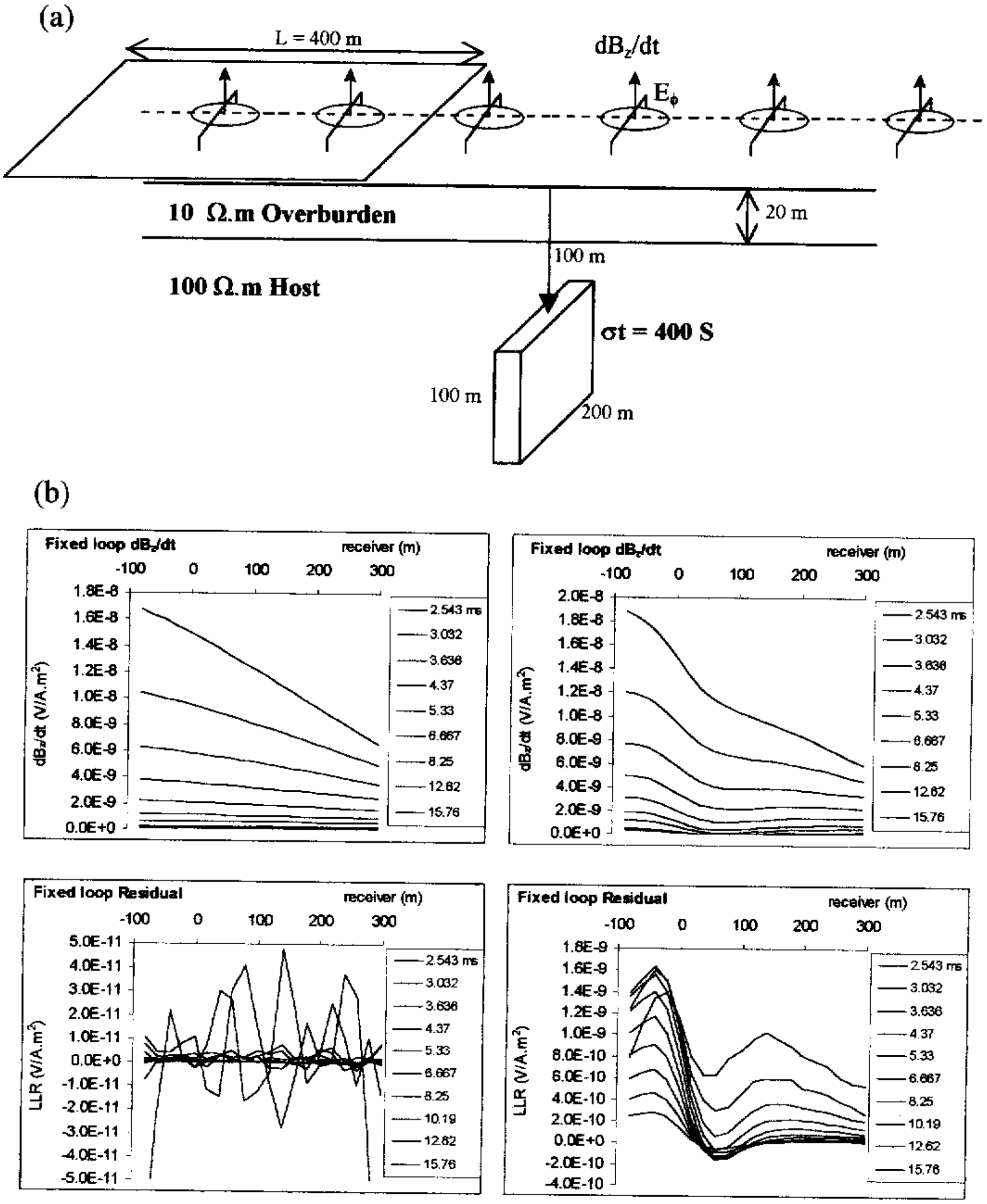

WITHOUT BODY **WITH BODY**

Figure 3.22 dB$_z$/dt and LLR responses for a fixed-loop survey over a conductive plate. **(a)** Thin sheet conductive target located a x = 0m in a 2 layered Earth model depicting a 400 m fixed-loop survey. **(b)** *upper*: dB$_z$/dt responses for the layered Earth compared with those when the target is present. *lower:* LLR responses for the layered Earth compared with those when the target is present. Note that the layered Earth residual is again 2 to 3 orders of magnitude smaller that the dB$_z$/dt response and has no signature over a layered Earth, making it very sensitive to small variations caused by non-layered structures.

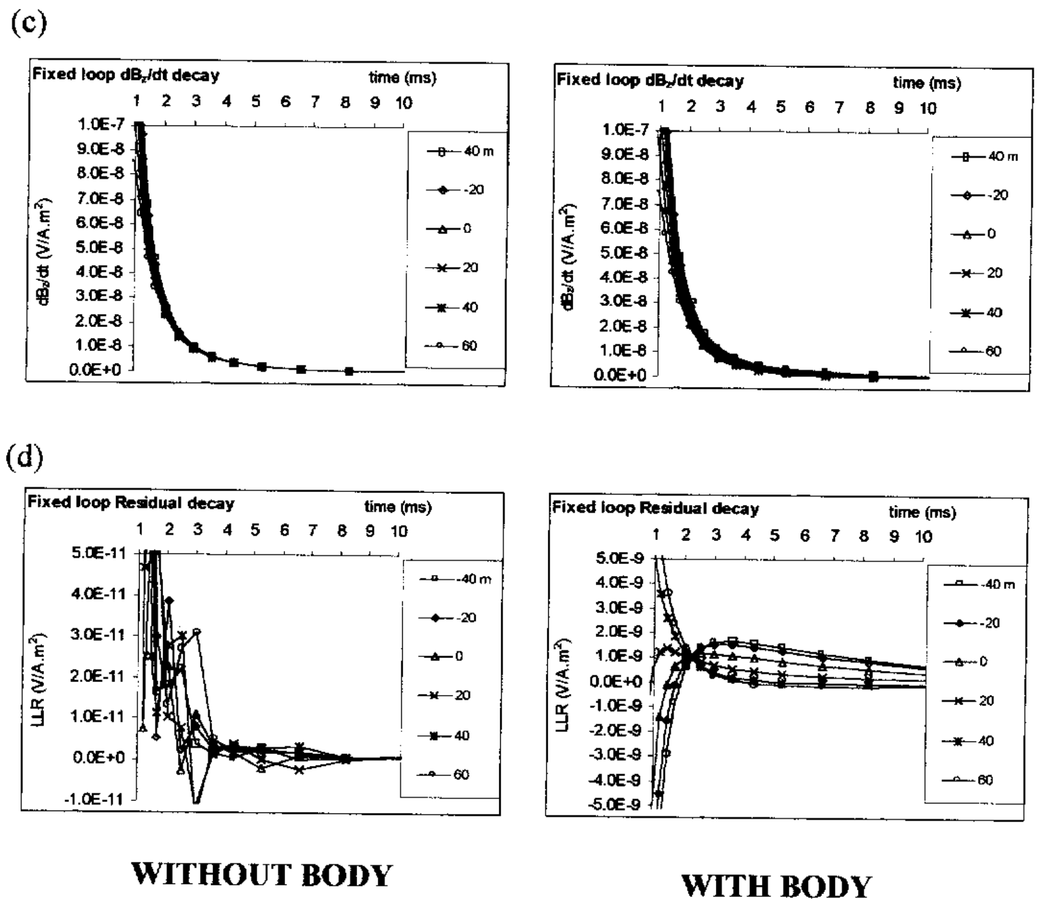

Figure 3.22 *continued* **(c)** Fixed loop decay curves for the dB$_Z$/dt component for the model in (a). The presence of the target has little effect on the shape of the decay. **(d)** decay curves for the LLR exhibit a vastly different character when the target is present compared to the layered Earth response.

The dB_z/dt decay curves are very similar for all of the stations in this time interval and do not provide evidence of the target being present. The LLR decays do not contain any signature for the purely layered Earth, but a definite signature is seen when the target is present.

The LLR decays are vastly different for the receiver stations close to the target body compared to those that are some distance from the target. The change in decay characteristics shown in the LLR provides extra evidence of the presence of a conductive target. An interesting feature of the decay curves shown in Figure 3.22(d) is that they all have a common amplitude at some point in time. The time at which all the decay curves intersect varies according to the depth of burial of the target.

3.4.2.2 In-loop

Using the Earth model shown in Figure 3.23(a), an in-loop survey is simulated using a 100 m x 100 m transmitter loop with 50 m move-ups. Figure 3.23(b) shows the in-loop dB_z/dt and LLR responses for the 1.5 to 10 ms time channels. The signal of the target is easily seen in the dB_z/dt profiles but is greatly enhanced in the LLR profiles. Notice that the LLR is centred on the zero line as the background layered Earth response has been greatly reduced by the processing. The corresponding decay curves for selected stations in the vicinity of the target are shown in Figure 3.23(c). The dB_z/dt decay curves are identical at early times (< 2 ms) due to the response being dominated by the conductive overburden. At later times (> 3 ms) there is a slight but noticable difference in the decay curves as the target response begins to have an effect. In contrast, the LLR decays are markedly different in the vicinity of the target, especially at early times because the target response is larger at early times and the overburden response has been reduced. The residual only displays the non-layered aspects of the measured response.

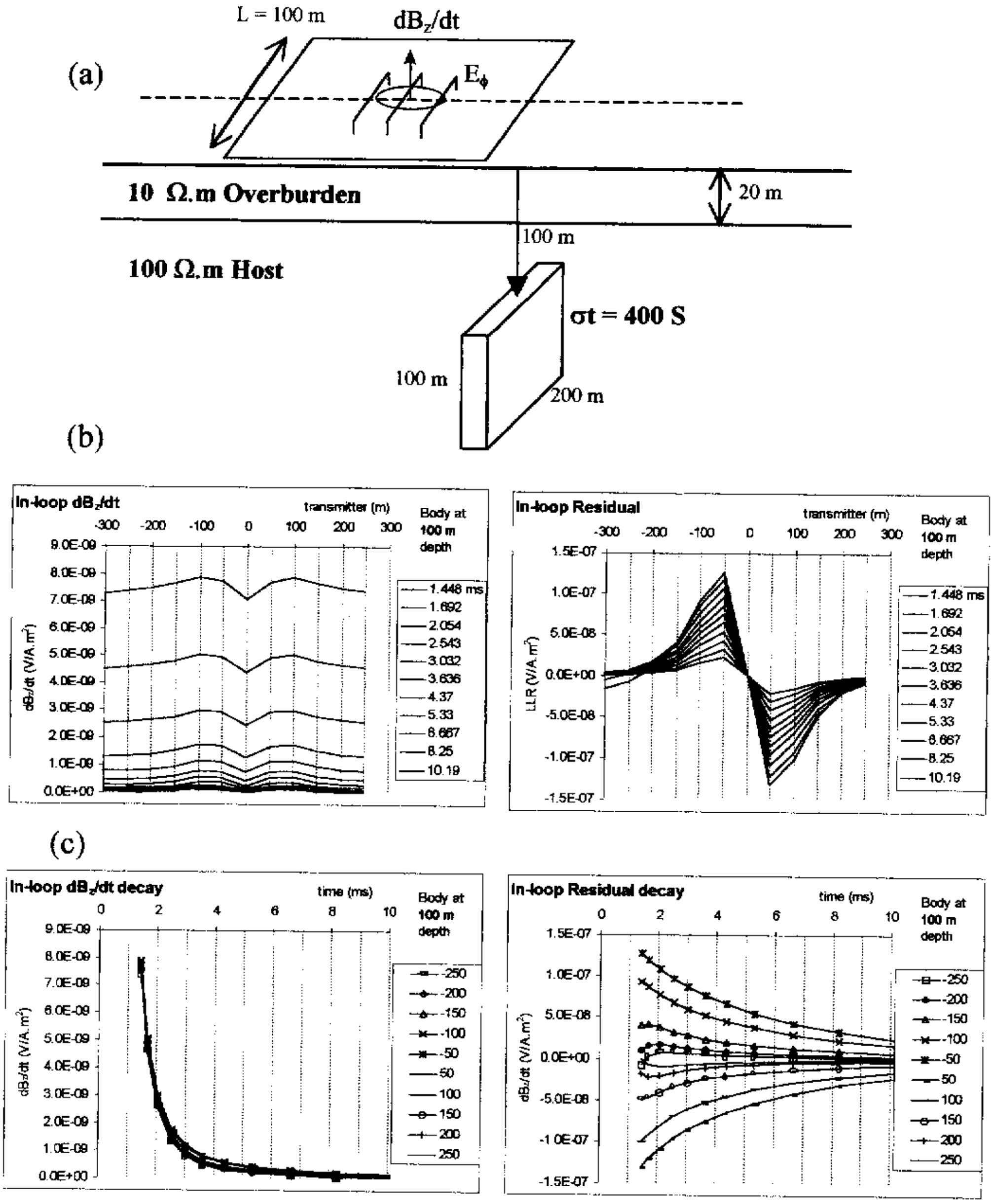

Figure 3.23 dB$_z$/dt and LLR responses for an in-loop survey over a conductive plate. **(a)** In-loop survey configuration on the surface of a two layered Earth model with a conductive target at x = 0 m. **(b)** dB$_z$/dt and LLR profiles for times between 1 and 10 ms indicating the presence of the target. **(c)** comparison of the decay curves at selected stations near the target. The LLR provides an enhanced signature of the target in both the profile and decay curves.

3.4.2.3 Slingram surveys

In some cases the measurement of EM fields inside the transmitter loop is undesirable due to induced polarisation of the surface materials in the vicinity of the transmitter wire. IP effects can be identified as a very slowly decaying negative signal at late times and may reduce the detectability of a conductive target. IP effects are not such a problem if the receiver and transmitter are separated by some distance. Figure 3.24(b) presents the profile response for a slingram configuration over the model in Figure 3.24(a), the transmitter-receiver separation being 100 m. The dB_z/dt profiles are again seen to contain a signature from the target imposed on a background response from the conductive Earth. The variations in the LLR profiles for the same time channels are much more emphatic. It is again seen that the LLR signature from the target is very much centred on the zero line and decreases to zero at large distances from the body. There is virtually no layered Earth signal being displayed by the residual. The decay curves the dB_z/dt and LLR for selected stations are shown in Figure 3.24(c). Again, there is no difference between the dB_z/dt decays at early times and there are only small differences at later times. The decays near the target are slower than those away from the target but they do not provide an obvious indication of the conductive target. In contrast, the LLR decay curves vary dramatically between receiver stations as the survey approaches the target, even in the very early time channels.

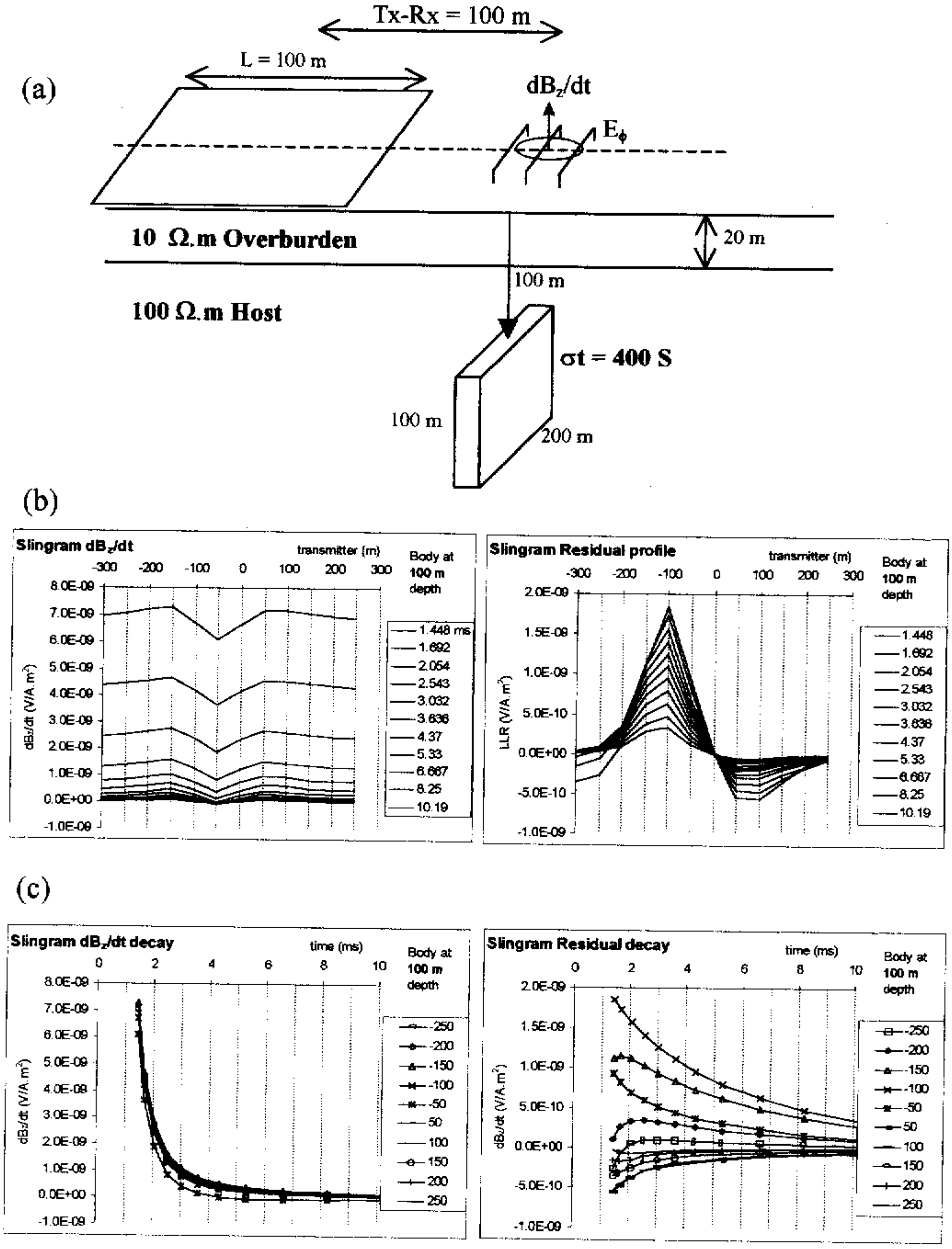

Figure 3.24 dB$_z$/dt and LLR responses for a slingram survey over a conductive plate. **(a)** Slingram survey configuration on the surface of a two layered Earth model with a conductive target at x = 0 m. **(b)** dB$_z$/dt and LLR profiles for times between 1 and 10 ms indicating the presence of the target. **(c)** comparison of the decay curves at selected stations near the target. The LLR provides an enhanced signature of the target in both the profile and decay curves.

3.4.2.4 Multiple bodies

The presence of a number of conductive targets has been shown in an earlier section to affect the shape of the profile response and make interpretation of the residual more complicated. In time domain surveys, the interaction of two or more bodies also creates interpretational difficulties. Using the model of Figure 3.25(a) an in-loop survey was simulated and the dB_z/dt profile response is shown in Figure 3.25(b). The corresponding residual profile response is shown in Figure 3.25(c). The residual profile responses indicate the presence of both bodies much more clearly than the dB_z/dt profiles.

3.4.3 Noisy data and the LLR

The difficulties associated with accurate measurement of the electric field are well documented (Macnae, 1981) and may cause problems when performing the LLR transformation on field data. Sampling and stacking the data many times during acquisition helps to reduce the effect of random noise on the measurements but does not reduce the unwanted geological effects of topographical variations or small scale changes in surface conductivity. Subtracting the measurements obtained at different locations for the purpose of estimating the spatial derivative has the effect of enhancing the small differences between them. If the differences are due to localised variations in surface conditions rather than the effects of the regional conductivity they will be enhanced and may appear in the LLR as false anomalies. To assess the sensitivity of the LLR to random noise in the measurements, the model data of Figure 3.23 were corrupted with 5% random noise in the dB_z/dt measurements and 20% in the electric field measurements prior to transformation to the LLR.

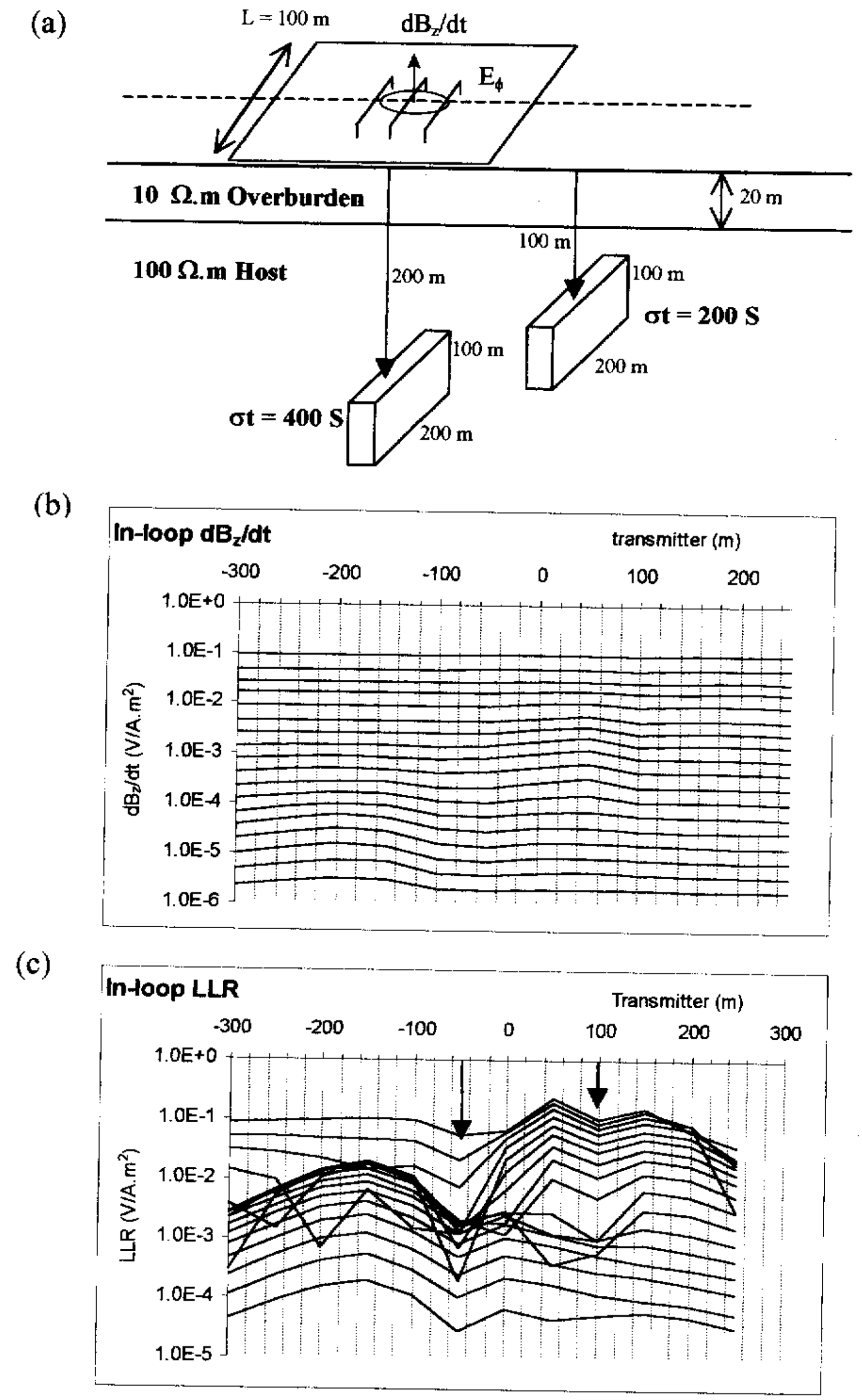

Figure 3.25 dB$_z$ /dt and LLR responses for an in-loop survey over two conductive of different conductances and depth of burial. **(a)** Two-layered Earth model containing two bodies (at x = -50 m and x = 100 m) of equal dimensions but different conductances and depth of burial. **(b)** In-loop dB$_z$/dt profile responses for time channels from 1 to 30 ms. **(c)** LLR profiles for the same time channels showing a greatly enhanced signature of the two bodies (arrowed).

The larger noise level in the electric field was selected to reflect common experience with electric field measurements (Macnae, 1981). The presence of the random noise in the field components can be seen in Figure 3.26. The effect of 5% noise in the dB_z/dt measurement is seen in Figure 3.26(a) to have very little effect on the profile response in the LLR. However, in Figure 3.26(b) the noisy electric field component has caused the LLR profile to become very distorted. Even though the signature is distorted, the profile response still provides a clear indication of an anomalous conductive zone. The effect of noise in both measurements is seen in Figure 3.26(c). The LLR transform has again successfully reduced the unwanted layered Earth response from the data but the noise in the data has caused the LLR profile shape to be less interpretable than noise free data. Interpretation of the LLR will be considered in Chapter 4.

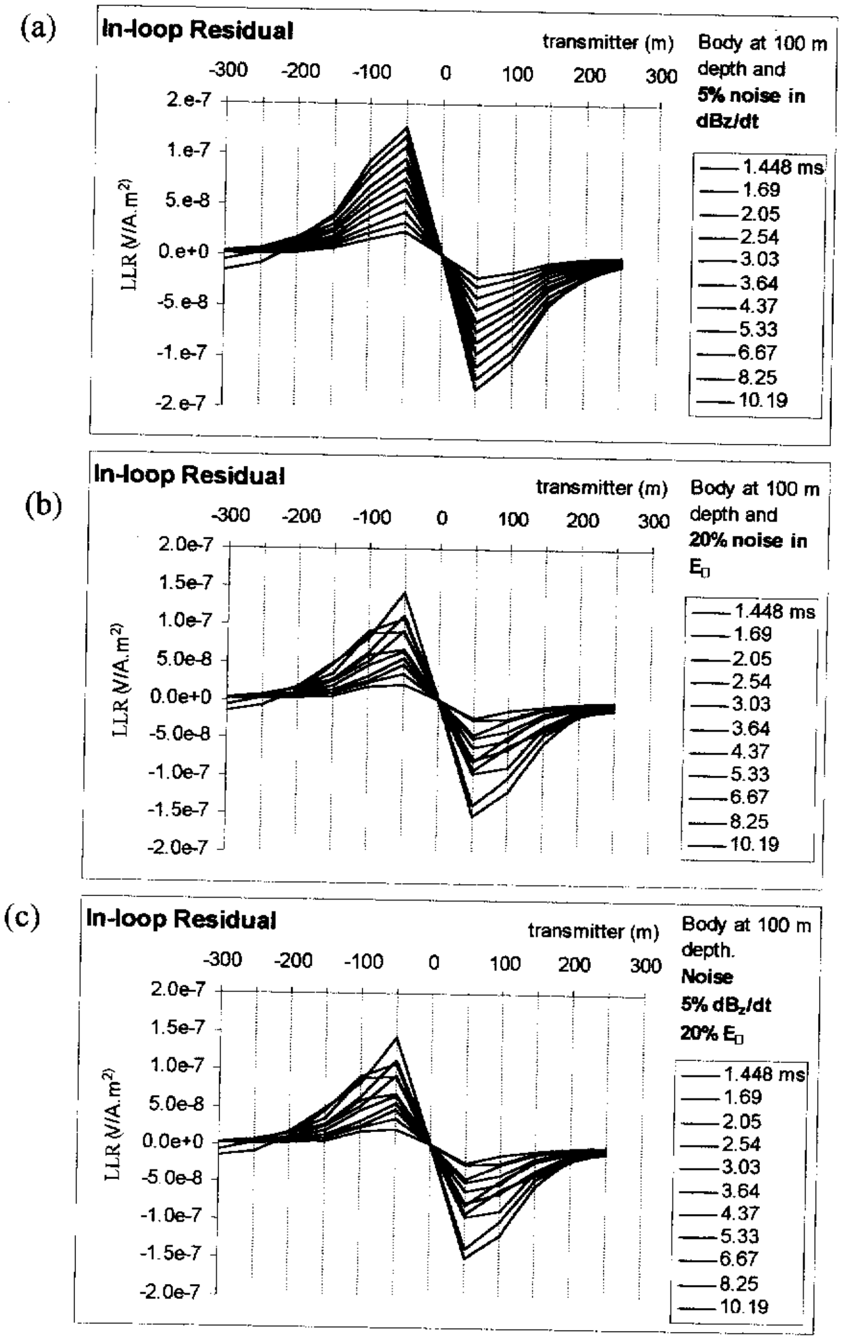

Figure 3.26 The effect of random noise on the LLR. **(a)** dB$_z$/dt measurement contains 5% random noise, **(b)** E$_\phi$ contains 20% random noise, **(c)** noise in both components. The LLR provides a very clear signal of the target even in noisy data.

CHAPTER 4 INTERPRETATION OF THE RESIDUALS

In Chapter 3 the SLR and LLR have been shown to be effective in reducing the layered Earth contribution from the recorded EM responses and thereby enhancing the appearance of the target response. In all of the numerical examples presented so far, the residuals provide a very clear signature of the 3-D target. It is desirable, however, to be able to obtain more information from a survey than simply identifying an anomalous signal. Currently, a successful EM survey will also produce an estimate of the depth and orientation of a target body. Computer modelling may also enable an estimate of target conductivity to be made.

In this chapter, some interpretative aspects of the SLR and LLR profiles are investigated using further numerical modelling. Simple 'rules of thumb' are developed to assist interpretation.

4.1 Apparent resistivity / conductivity

Interpretation of geophysical data can be assisted by transforming the measured data to some other quantity that may emphasise a particular feature of the geology. For example, the analytical signal (Nabighian, 1972) and vertical derivatives obtained from magnetic profile data, or the extraction of attributes such as instantaneous phase and instantaneous frequency (Taner et al., 1979) in seismic trace analysis, greatly assist interpretation. The most commonly used method of interpretation of EM signals involves the transformation of the measured voltage into an apparent resistivity ρ_a or apparent conductivity σ_a value. The two quantities are inversely related i.e. $\sigma_a=1/\rho_a$ and either may be used as an interpretative quantity. Apparent resistivity is defined as the resistivity of a homogeneous half-space that would produce the same response as measured over the real Earth using the same acquisition parameters (Spies and Eggars, 1986). The apparent resistivity estimated from frequency domain EM measurements is a function of transmitter loop dimensions, Earth resistivity and frequency which allows an estimate of the variation of resistivity with depth to be made. The depth associated with a particular frequency is related to the skin-depth δ_{FD} given by

$$\delta_{FD} = \left(\frac{2\rho_a}{\mu_o\omega}\right)^{1/2}. \tag{4.1}$$

The skin depth represents the depth at which the EM field amplitude is reduced by a factor of *e* (base of natural logarithms) relative to the surface field.

In the case of time domain surveys, the diffusion depth δ_{TD} given by Raiche and Gallagher (1985) is

$$\delta_{TD} = \left(\frac{2\rho_a t}{\mu_o}\right)^{1/2}. \tag{4.2}$$

It represents the depth of the electric field maximum at time t.

The relationship of the skin/diffusion depth to the actual depth of investigation depends on a number of factors including the sensitivity of the measuring instrument, the complexity of the geological section as well as the ambient noise levels (Spies, 1989). A variety of relationships have been used to relate the depth of investigation to the skin/diffusion depth (Bostick, 1977; Sinha, 1979; Wilt and Stark, 1982; Mundry and Blohm, 1987). Despite the lack of consistency, 2-D pseudo-sections that display the apparent resistivity-depth correspondence at each station along a profile, are widely used for EM data presentation and interpretation.

It must be emphasised that the apparent resistivity is simply an *interpretative convenience*, the function of which is to provide some tangible quantity for display and comparison of results. It has little physical significance (Spies and Eggers, 1986) to the actual resistivity of the Earth materials nor does it enable any assessment of mineral content of the rocks to be made. It simply helps to identify and delineate regions of conductivity contrast.

For a given geological setting, the measured EM profile response will vary depending on the type of configuration being used. For low frequency applications, Spies and Frischknecht (1991) give the formula for computing the apparent resistivity value directly from the HCP quadrature measurement $(\frac{Z}{Z_o})^Q$ as

$$\rho_a^{HCP} = \frac{\mu_0 \omega r^2}{4(\frac{Z}{Z_o})^Q}, \tag{4.3}$$

where r is the transmitter-receiver separation. It should be noted that r in this case is equivalent to the cylindrical coordinate variable ρ used earlier since $z_r = z_s$ for these configurations. The coordinate variable ρ is not used here due to the possible confusion with ρ_a.

Likewise, the apparent resistivity can be determined from the VCP configuration measurements using

$$\rho_a^{VCP} = \frac{\mu_0 \omega r^2}{4(\frac{Z}{Z_o})^Q} \tag{4.4}$$

and the VCA configuration using

$$\rho_a^{VCA} = \frac{\mu_0 \omega r^2}{[15(\frac{Z}{Z_o})^Q]^{2/3}}. \tag{4.5}$$

It is evident from equations (4.3) and (4.4) that the quadrature responses measured using HCP and VCP should be the same if they are to produce the same value of apparent resistivity. Even for the most simple models that are not one-dimensional, this is not the case. For models that include a 3-D target body, for example, the measured fields will be altered in the vicinity of the target due to the scattering currents inside the body, and these will affect the HCP and VCP apparent resistivity values differently. Thus, the apparent resistivity concept that is based on a 1-dimensional Earth model cannot be applied universally with any certainty to non-layered Earth models. Despite this, it is worth examining the effect of the SLR combination on the apparent resistivity values to see if the SLR provides any additional quantitative measure of resistivity variations.

4.2 A modified apparent resistivity

Using the equations (4.4) to (4.6) I write the quadrature responses of the three configurations as

$$\left(\frac{Z^{\mathrm{HCP}}}{Z_0}\right)^{Q} = \frac{\mu_0 \omega r^2}{4\rho_a}, \tag{4.6}$$

$$\left(\frac{Z^{\mathrm{VCP}}}{Z_0}\right)^{Q} = \frac{\mu_0 \omega r^2}{4\rho_a} \tag{4.7}$$

and

$$\left(\frac{Z^{\mathrm{VCA}}}{Z_0}\right)^{Q} = \frac{1}{15}\left[\frac{\mu_0 \omega r^2}{\rho_a}\right]^{3/2}. \tag{4.8}$$

Combining equations (4.5) to (4.7) with equation (3.64) leads to

$$\mathrm{SLR} = \frac{2}{15}\left[\frac{\mu_0 \omega r^2}{\rho_a}\right]^{3/2}, \tag{4.9}$$

which can be inverted to obtain an apparent resistivity determined from the SLR,

$$\rho_a^{\mathrm{SLR}} = \frac{\mu_0 \omega r^2}{(7\cdot 5 \mathrm{SLR})^{2/3}}, \tag{4.10}$$

where the superscript SLR is used to distinguish this modified apparent resistivity quantity from conventional apparent resistivity.

It is immediately noticed that on a layered Earth, the modified apparent resistivity has no meaning since the SLR is (theoretically) zero. This form of apparent resistivity only has application to non-layered Earth models. In view of this, it may be prudent to make use of the apparent conductivity

$$\sigma_a^{\mathrm{SLR}} = \frac{(7 \cdot 5.\mathrm{SLR})^{2/3}}{\mu_0 \omega r^2} \qquad (4.11)$$

as an interpretative quantity so the range of values is finite.

The SLR data presented in Figure 3.7 were transformed to a modified apparent resistivity value using equation (4.10). The modified apparent resistivity profile is shown in Figure 4.1(b) together with the apparent resistivity obtained from the HCP quadrature response [using equation (4.3)]. It is seen in Figure 4.1(b) that the HCP profiles give an apparent resistivity value of approximately 10 Ω.m for the higher frequencies which matches the overburden resistivity. The lower frequencies yield apparent resistivity values increasing from 80 Ω.m up to 140 Ω.m. The HCP apparent resistivity profile does not indicate the presence of the target very well. The modified apparent resistivity values derived from the SLR do not provide any additional information about the Earth resistivity but do provide an enhanced indication of the conductive target. In the higher frequencies, the target is characterised by high values of the modified apparent resistivity.

The HCP apparent conductivity values shown in Figure 4.1(c) indicate a high conductivity for the higher frequencies that corresponds to the overburden and lower conductivities for the lower frequencies corresponding to the host rock. In contrast however, it is the lower frequencies that produce a greatly enhanced indication of the target body in the SLR apparent conductivity profiles. In this case, the target is characterised as a high conductivity anomaly. For this reason it is preferable to display the SLR data in terms of its apparent conductivity rather than the apparent resistivity. However, it appears as though there is little to be gained by transforming the SLR into a modified form of apparent resistivity or conductivity.

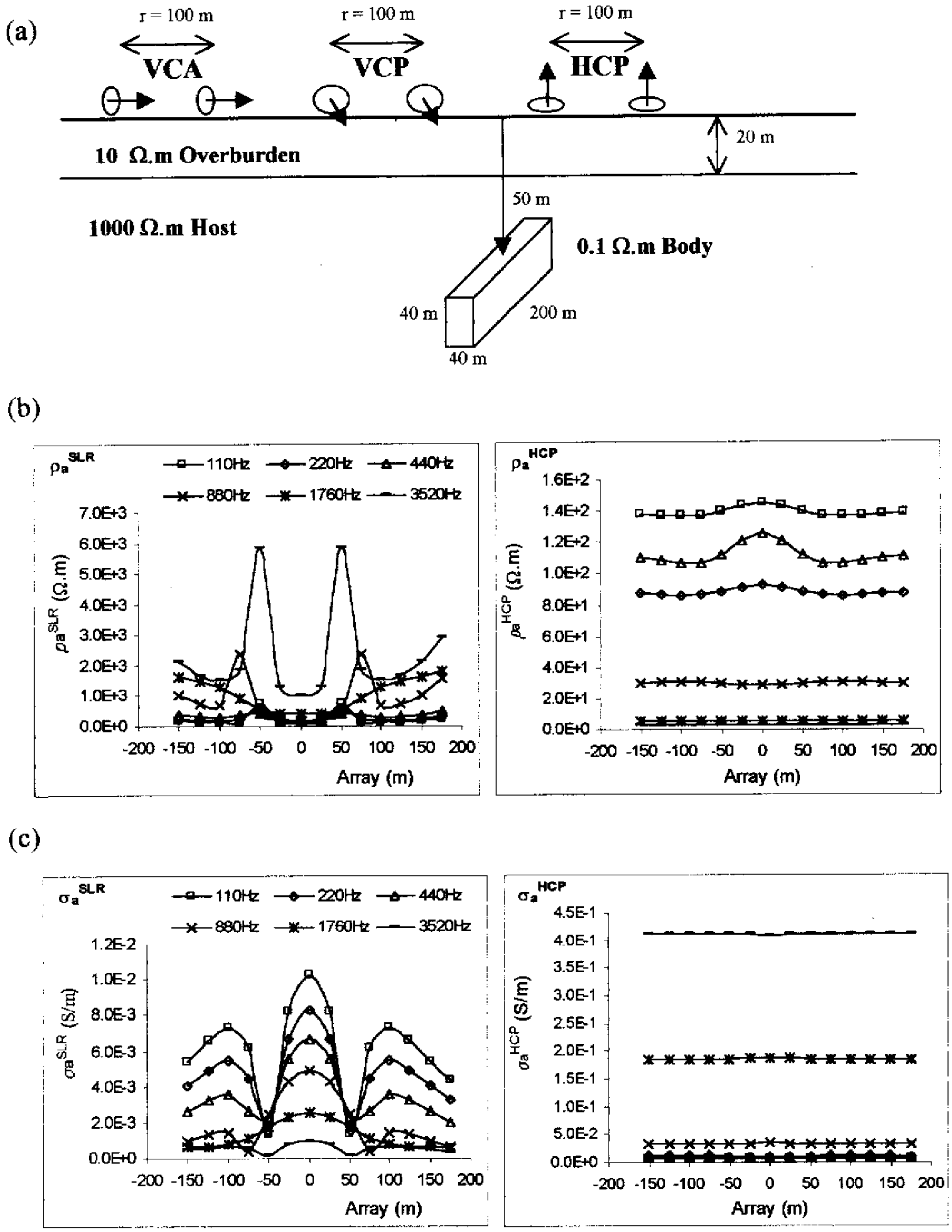

Figure 4.1 The SLR and HCP apparent resistivity profiles. **(a)** Conductive target beneath conductive overburden model. **(b)** The SLR and HCP apparent resistivity profiles for the model shown in (a). **(c)** the corresponding apparent conductivity profiles. The HCP profiles more closely reflect the layered Earth structure whereas the SLR emphasises the presence of the target

The main purpose of the SLR is to enhance the response of the conductive target by reducing the Earth strata response. The traditional concepts of apparent resistivity and conductivity have no meaning with regard to the SLR and LLR because the residuals do not provide enough information about the layered Earth. Transforming the SLR to a *modified* apparent resistivity or conductivity may lead to some confusion.

Like apparent resistivity, the SLR and LLR are contrived quantities. They represent the combination of measured responses and as such, they have more complicated signatures than the individual responses that comprise them. Complicated signatures that contain information related to different aspects of geology are more difficult to interpret than simple signatures so care must be taken when attempting to interpret the residuals. However, the shape of the profile response may enable a limited interpretation of depth and dip of the target to be made. To assist the interpretation, numerical modelling of the effects of a conductive, thin plate of 200 m strike length and 100 m depth extent in a uniform half-space of 100 Ω.m resistivity was performed. The depth of burial, dip, strike direction and conductance of the plate were varied and the effects on the SLR responses examined.

4.3 Frequency domain SLR

4.3.1 Depth of the target

For a vertical, rectangular plate-like body in a uniform half-space the residual profiles provide a very useful indication of the burial depth. Like the HCP responses, the shape of the residual profile depends on the source frequency and conductivity contrast between the target and the host. In cases where the residual profile response contains a dual peak, the depth of burial of the target is related to the peak to peak separation. Using a conductive plate with a conductance of 100 S, a plot of the SLR peak to peak distance versus depth of burial is shown in Figure 4.2 for a few selected frequencies. The selected frequencies represent a skin depth to loop separation ratio δ/r of 5.0, 2.5 and 1.0 respectively. To provide a direct measure of the depth of burial, the Tx-Rx separation (100 m in this case) must be subtracted from the peak to peak distance. Figure 4.2 shows that a very reliable estimate of depth can be obtained from both the in-phase and quadrature SLR profile responses for a body buried up to 1.5 times the loop separation if δ/r is greater than 5. The depth estimate is less reliable for targets deeper than $r/2$ for small δ/r but remains very reliable for bodies buried shallower than $r/2$. For the higher frequencies (> 3500 Hz) that correspond to a $\delta/r < 0.5$, the peak to peak width displayed on the SLR profile responses does not vary and therefore does not provide any information about the depth of the body. For the case of a flat lying conductor, the shape of the residual profile response does not provide enough information for an estimate of depth to be made. Numerical modelling would provide a more useful method of interpretation in this case.

4.3.2 Dip of the target

Although vertical targets are sometimes encountered, it is more common in mineral exploration that the target will be non-vertical. In an exploration program it is important that some knowledge of the dip of a target body is obtained so that drill holes can be correctly oriented to maximise the probability of intersecting the target body. A vertical, tabular body produces a symmetric response using the VCA, VCP and HCP configurations.

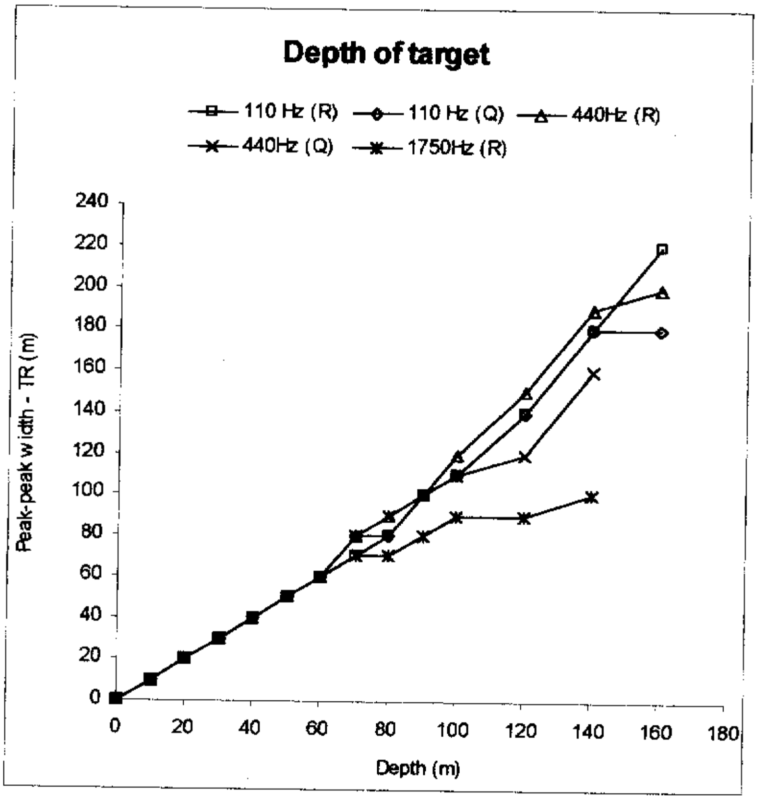

Figure 4.2 Interpretation of depth of burial from the SLR profiles. Variation of the SLR peak to peak distance with depth of burial for selected frequencies. The linearity of the relationship in the in-phase (R) and quadrature (Q) parts for burial depths less than 0.5 T-R provides an accurate measure of the depth of a target but becomes less accurate for deeper targets.

Dipping targets produce an asymmetric profile response due to the different coupling of the transmitter and the body on opposite sides of the body. The shape of the profile response is therefore dependent on the steepness of the dip and the direction of the survey traverse.

Figure 4.3 shows SLR profile responses obtained from numerical models using a thin conductive plate of conductance 100 S, located at a depth of 100 m in a 100 Ω.m half-space, for a range of dip angles when using a 440 Hz transmitter signal. The dip angle is measured in an anti-clockwise sense from the horizontal. Most of the profile responses (in-phase and quadrature) have a similar shape, i.e. two peaks separated by a trough. There is a gradual change in the shape of the profile as the dip angle changes that enables an estimate of dip to be made. The in-phase part produces a more noticeable change in profile shape than the quadrature. Note that a dip greater than 90° produces an identical response to its complementary dip when the direction of the profile traverse is reversed. Figure 4.4(a) shows a plot of the ratio of the amplitude of the first peak to the amplitude of the second peak for the in-phase part. The first peak refers to the peak that is closest to the start of the profile line and is dependent on the direction of traverse. The figure indicates that the ratio of the peaks provides a useful estimate of the dip of steeply dipping bodies (> 50°) but is less sensitive to the dip for bodies that are more horizontal (i.e. < 40°). Figure 4.4(b) shows the corresponding plot of the quadrature part. While this plot does show a strong dependence on dip angle, the quadrature part of the SLR peak ratio is not practical for dip estimation since a particular peak ratio can be indicative of two different dip angles. Also, in some cases, the shape of the profile does not resemble a trough and two peaks (at 880 Hz in this example) and so a ratio of peak amplitudes is not possible.

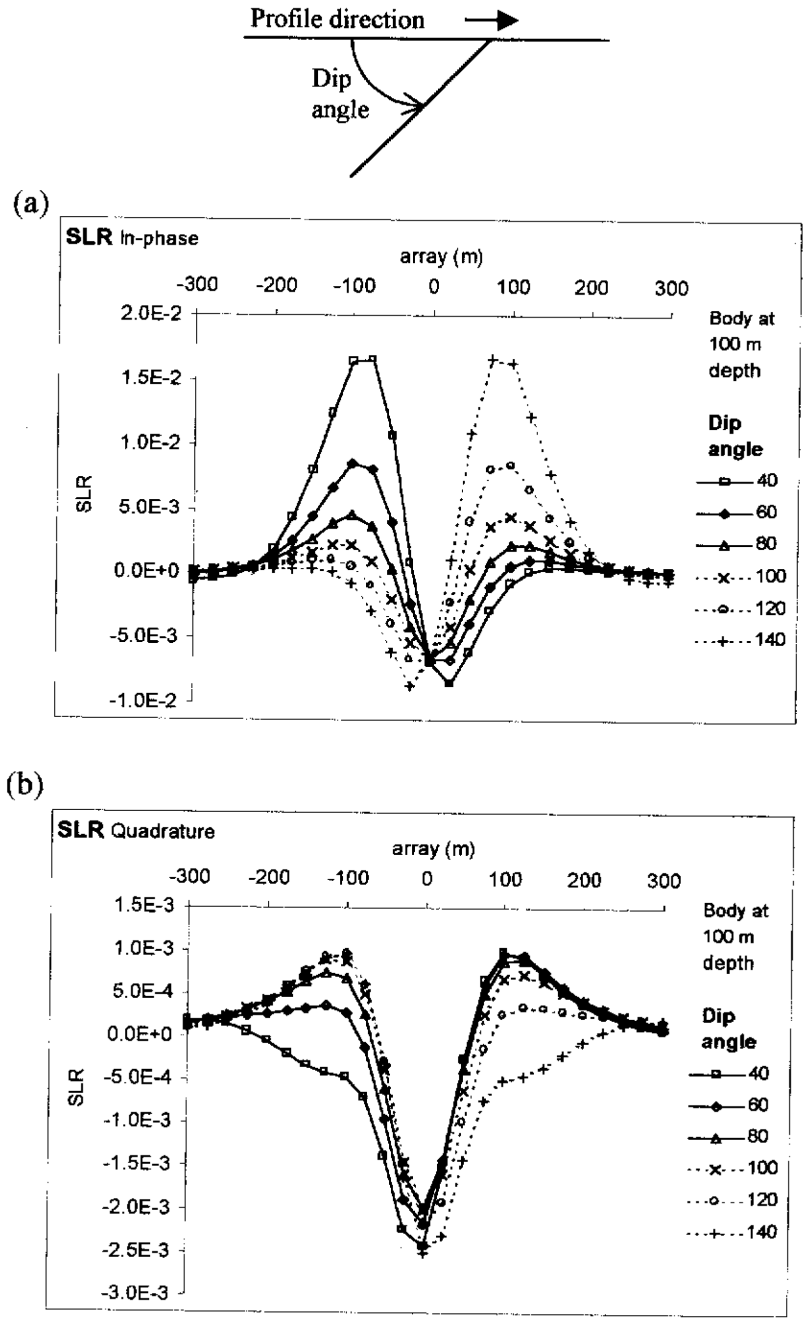

Figure 4.3 The effect of dip angle on the SLR profiles. SLR profile responses for a conductive plate in a half-space at 440 Hz for a range of dip angles. **(a)** The in-phase response is very sensitive to dip whereas in **(b)** the quadrature response is relatively insensitive to dip.

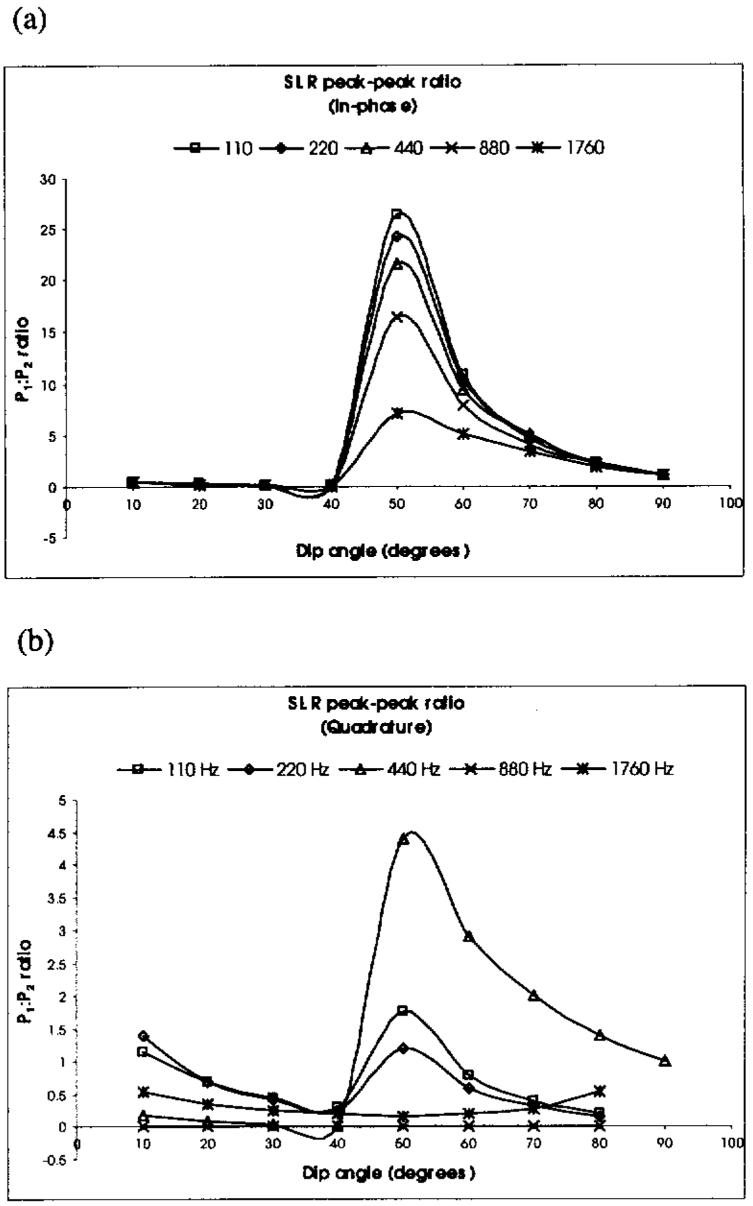

Figure 4.4 Interpretation of dip angle using the SLR peak to peak ratio. **(a)** ratio of the peak-peak in-phase amplitudes for a range of frequencies provides a good estimate of dip for steeply dipping targets (> 40^0) **(b)** ratio of quadrature peak-peak amplitudes. The quadrature responses do not provide a useable means of dip estimation. The peak-peak ratio is not useful for small dip angles.

An alternate method that can be used to estimate the dip of a target is to examine the ratio of the peak to trough amplitudes. Figure 4.5(a) shows a plot of the *first* peak to trough ratios obtained for a range of dip angles. Figure 4.5(b) shows the corresponding quadrature plot. It is apparent in these figures that the ratio of peak to trough amplitudes can be used for steeply dipping targets but is of little use for gently sloping targets. Figure 4.6(a) shows a plot of the *second* (i.e. down profile) peak to trough ratio for a range of dip angles and Figure 4.6(b) the corresponding quadrature plot. In this case, there is a noticeable change in the in-phase ratios obtained for dip angles less than 45°. Therefore, this ratio would be useful for estimating the dip of gently sloping targets.

Although these crude methods of dip estimation do not replace the need for thorough analysis using computer modelling, they do provide a simple and effective indication of the dip of the target which is important in field operations.

4.3.3 Strike of the target

The strike of a target is defined as the direction of intersection of a surface and a horizontal plane (Sheriff, 1994) and is usually determined by comparing the location of anomalies on adjacent profile lines. The strike direction has particular significance in EM prospecting because it also corresponds to the preferred orientation of currents induced in tabular bodies. Knowledge of the strike of a target enables the geophysicist to modify the design of follow-up surveys to ensure the maximum excitation of the target body by the field from the transmitter. For large 3-D prismatic bodies the strike may be difficult to define and there may not be a preferred direction for the current flow.

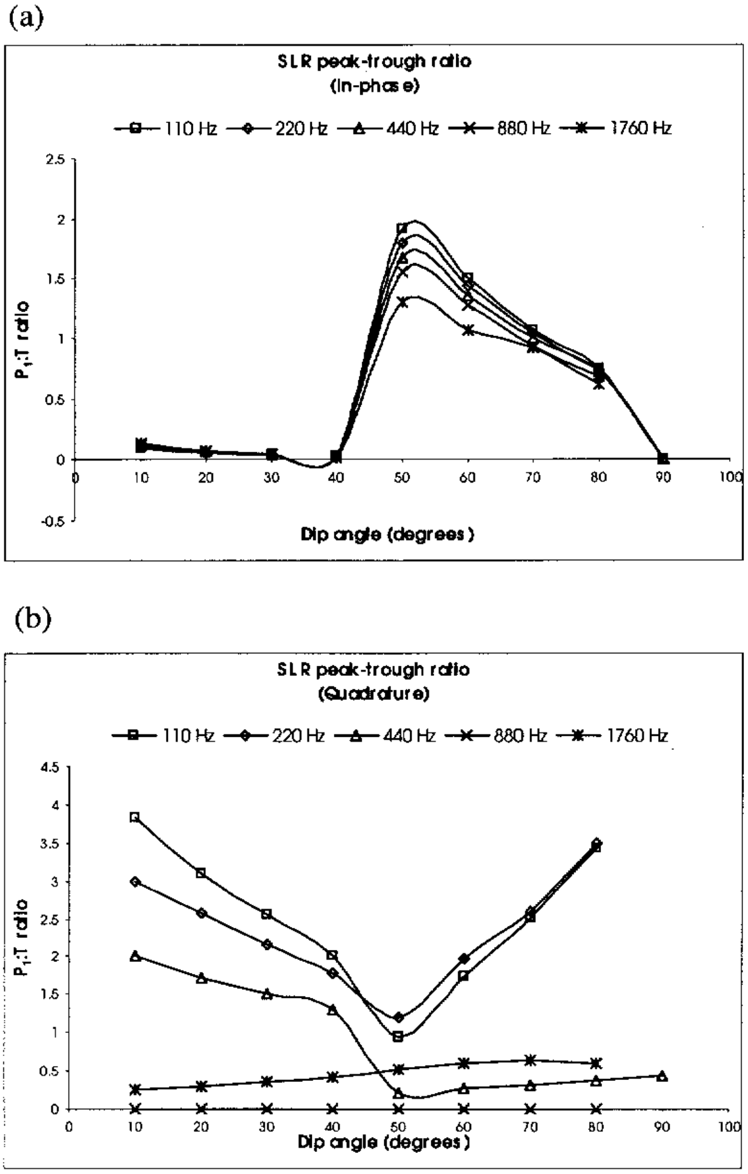

Figure 4.5 Interpretation of dip angle using the first SLR peak to trough ratio **(a)** The in-phase part is insensitive to small dip angles but provides a good measure for steep dips. **(b)** the quadrature part is ambiguous and does not provide reliable information about the dip.

(a)

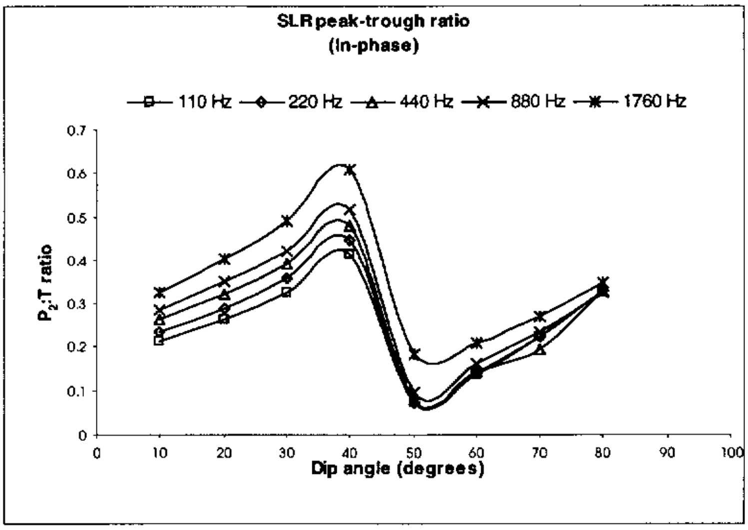

(b)

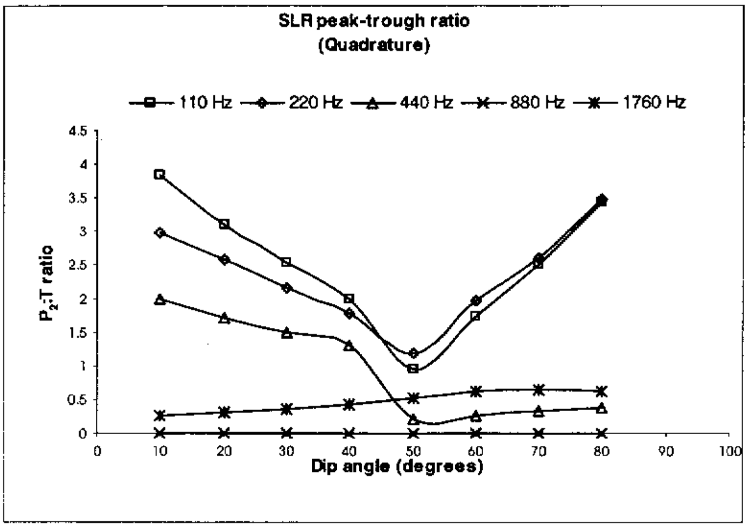

Figure 4.6 Interpretation of dip angle using the second SLR peak to trough ratio. The non-uniqueness of the ratio in both the in-phase **(a)** and quadrature **(b)** parts means that it is not a reliable indicator of the dip.

Such targets do not conform to the simple interpretative rules applicable to thin sheets and dykes and produce profile responses that require more thorough analysis for interpretation using numerical modelling. The HCP configuration is relatively insensitive to off-profile features and cannot be used to determine the strike of a target from one profile alone. The SLR, being a combination of three orthogonal configurations has the potential to be more responsive to off-profile variations and may provide information about the strike of a target from one profile alone.

For the purpose of modelling the effect of strike direction on the SLR, the same thin plate as above was modelled at 100 m depth with a dip of 90° and the angle between the strike of the target and the profile line was varied from 0° to 180°. The strike angle is measured in the anti-clockwise sense when viewed from above with zero degrees representing the 'along profile' direction. Figures 4.7(a) shows the quadrature SLR at 440 Hz for the range of strike angles shown in the figure when the target is centred on the profile line. The symmetry of the model gives rise to a symmetric response that is characterised only by reduced amplitudes associated with the reduced coupling due to the strike angle. For near-perpendicular strike angles the profiles exhibit characteristic shapes that enable an estimate of depth and dip of the target to be made. For targets that strike at less than 45° from the profile direction, the profile shape becomes very broad and cannot used for depth and dip estimation. Broad SLR profiles may therefore be indicative of a target that is far from perpendicular to the profile line. Figure 4.7(b) presents the quadrature response for the case of the target centred 50 m off-profile. The asymmetry introduced by the positioning of the target produces responses that are very sensitive to the strike angle.

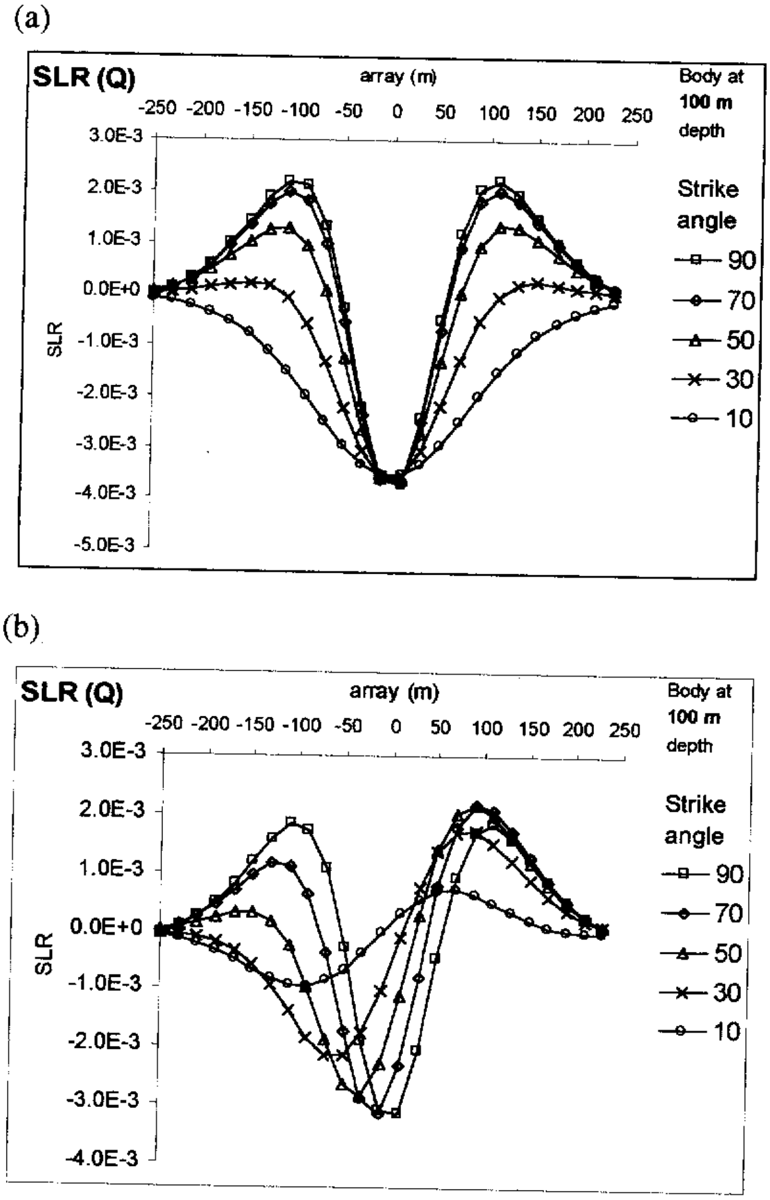

Figure 4.7 The effect of strike direction on the SLR. In **(a)** the target is centred on the profile line, in **(b)** the target centre is 50 m to one side of the profile line. A non-perpendicular strike broadens the response and may make depth estimation unreliable.

In this case the trough, which is usually centred directly above the target, is seen to be displaced from its true position (at x = 0 m), and the peak amplitudes are different on opposite sides of the target. As before, the peak to peak distance increases as the strike angle decreases, which may lead to an inaccurate depth estimate. The shape of the profile responses may enable only a qualitative estimate of strike angle to be made, i.e. near-perpendicular or not near-perpendicular. The fact that the target is not centred on the profile line and is not perpendicular to strike makes interpretation more difficult.

4.4 Time domain LLR

The shape of the LLR profile response will vary according to the survey configuration being used. In this section, some simple interpretative guidelines are described that can be applied for the moving-loop configurations.

4.4.1 In-loop configuration

4.4.1.1 Location of the target

It is seen in Figure 3.23(b) that for vertical, tabular bodies with strike perpendicular to the profile direction, the cross-over of the residual from positive to negative amplitudes occurs directly over the target. This provides a clear indication of the location of the target.

4.4.1.2 Depth of the target

Using the same plate model as above, Figure 4.8 presents the in-loop profile responses for a 400 S target placed at various depths in a 100 Ω.m half-space. The gradual broadening of the profile response is related to the depth of the target and enables an estimate of depth to be made.

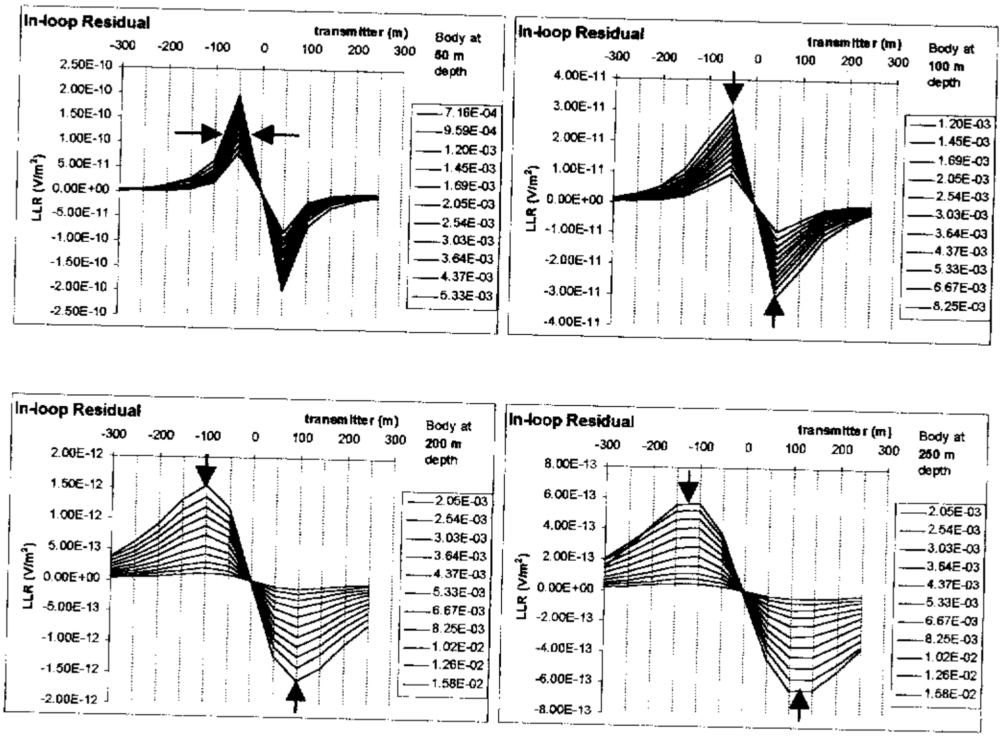

Figure 4.8 Using the in-loop LLR profile response to estimate the depth of burial. Depth of burial is indicated in the figure. The arrows indicate the points at which the estimates are made. Note the minimum peak to trough distance is equal to the transmitter length L.

The relative amplitudes of the peak and trough remain constant at the different depths but the separation between them increases as the depth of burial increases. For targets that are buried deeper than the transmitter length L (see Figure 4.8), the depth of a target is approximately equal to the distance between the maximum amplitude on either side of the cross-over.

The minimum distance between the peak and trough is equal to the transmitter length L since the peak is observed when the leading edge of the transmitter is directly over the target and the trough is produced when the trailing edge of the transmitter is over the target. For shallow targets (depth < L) the depth is approximately equal to the width of the leading peak at half its maximum amplitude (full-width, half-maximum).

4.4.1.3 Dip of the target

The dip angle can be estimated by the relative amplitudes of the peak and trough on either side of the cross-over. In Figure 4.9 the LLR profiles are shown for targets having dip angles ranging from 10° to 170°. For this figure, the 400 S plate was placed at a depth of 150 m in a uniform half-space of resistivity 100 Ω.m. The LLR is very sensitive to the dip of the target and the asymmetry of the profile response provides a good estimate of the dip angle to be made. The ratio of the peak to trough amplitudes is unity for a vertical target (90° dip) and increases as the dip angle becomes more horizontal.

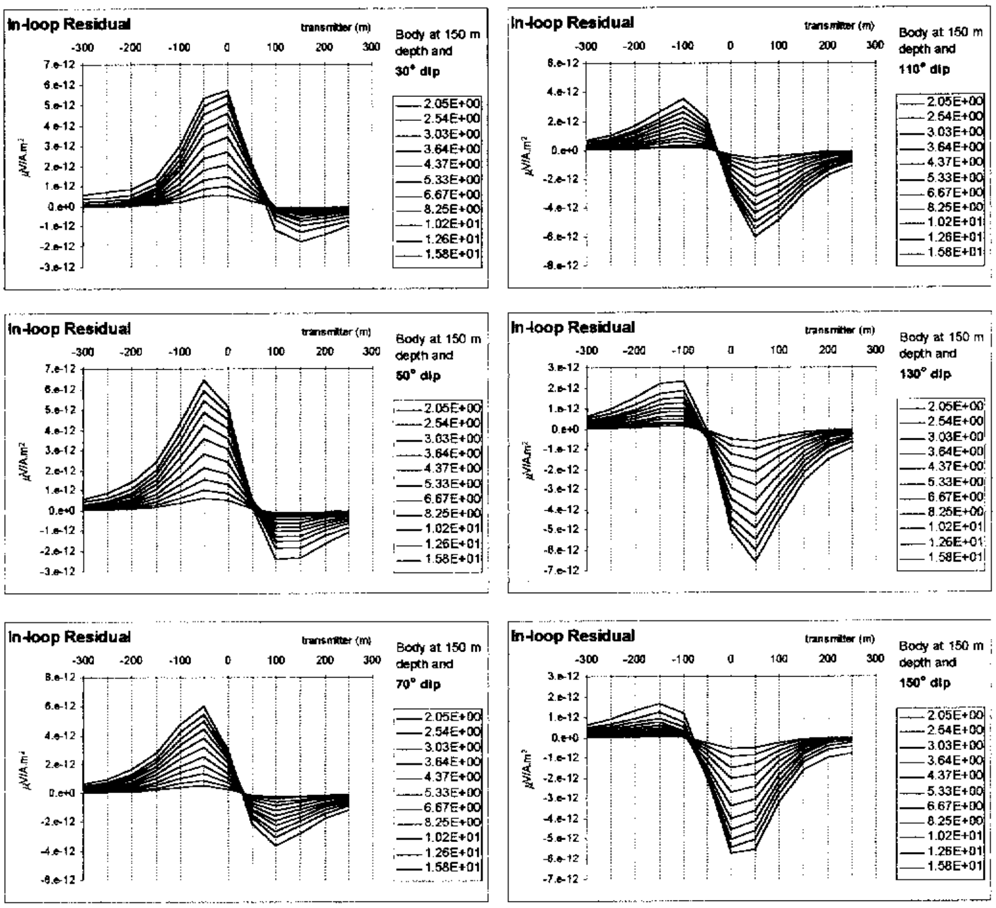

Figure 4.9 The effect of target dip angle on the in-loop LLR. The ratio of the peak to trough amplitude provides a measure of the dip angle. Note also the effect of dip angle on the displacement of the cross-over from its true location at x = 0m.

4.4.1.4 Strike of the target

The effect of a non-perpendicular strike direction can be seen in Figure 4.10 to affect the amplitude of the peak response. In that figure, the symmetric target is centred on the profile line from which the strike direction is measured. The larger amplitude associated with a more perpendicular strike is due to the greater coupling of the transmitter with the target. The shape of the LLR profile response however does not enable its use as an indication of strike direction.

4.4.2 Slingram configuration

The same thin plate target and half-space model as before was used to compute the LLR responses for the slingram configuration to aid interpretation.

4.4.2.1 Location of the target

In slingram surveys it is customary to plot the dB_z/dt responses at the mid-point between the transmitter and receiver. In that way the trough is directly over the target. The slingram LLR indicates the location of the target by the cross-over from positive amplitudes to negative amplitudes when plotted relative to the *transmitter* location.

4.4.2.2 Depth of the target

The variation of the slingram LLR profiles with depth of burial of the target is shown in Figure 4.11. The steepness of the leading peak decreases as the depth of burial increases. For targets deeper than the transmitter-receiver separation, the width of the leading peak at half of its maximum height gives a good estimate of the depth of burial. The estimation becomes less accurate as the depth increases.

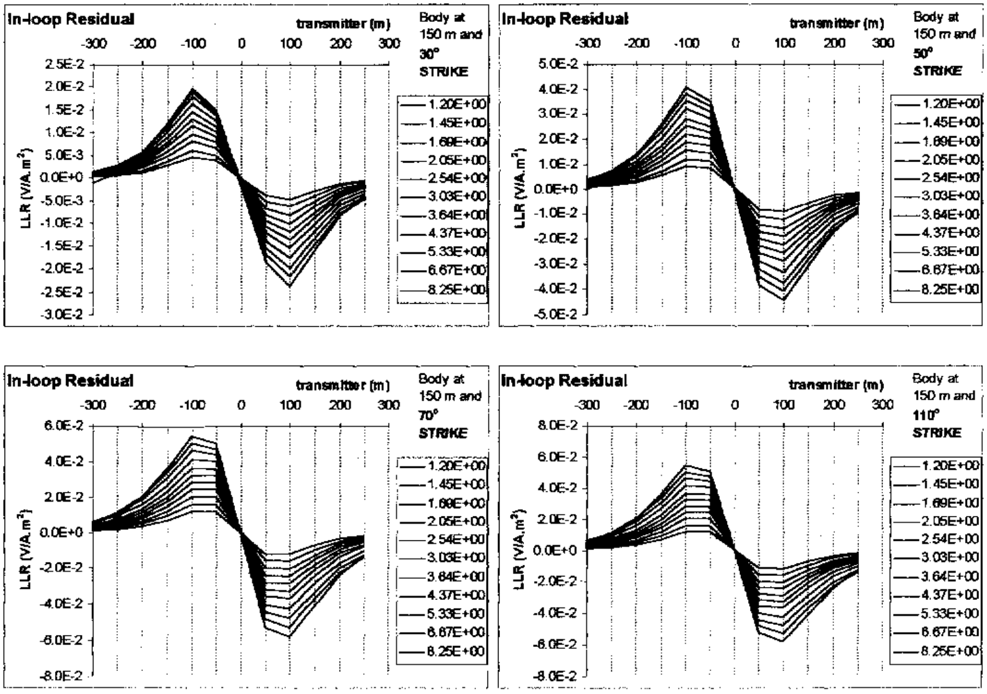

Figure 4.10 The effect of strike direction on the in-loop LLR. The profile responses give little indication of the strike of a target.

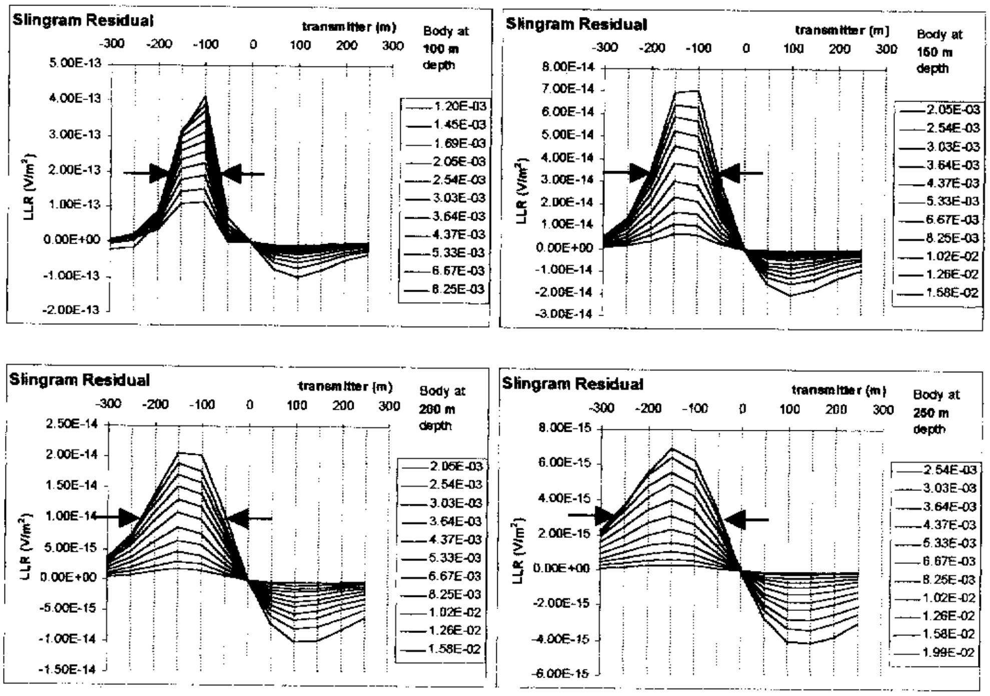

Figure 4.11 Estimation of depth of burial from the slingram LLR profile response. The half-width of the leading peak provides a useful indication of the depth of burial. Actual depths are indicated in the figure.

For targets that are shallower than the Tx-Rx separation the leading peak becomes a peak-trough pair. The separation between the peak and trough is roughly equal to the depth of burial.

4.4.2.3 Dip of the target

The dip of the target has a significant effect on the slingram LLR profiles. Figure 4.12 shows the profile responses of the 400 S plate at 150 m depth for different angles of dip. The most noticeable feature in the profiles is the gradual change in relative magnitudes of the leading peak and following trough. For a target that is dipping toward the on-coming survey configuration, the peak to trough ratio is between 4 and 10. For a vertical target the ratio is approximately 3.5 and for a target that is dipping away from the on-coming configuration, the ratio is between 2.5 and 0.5. The variation of the peak to trough amplitude ratio is almost linear for targets dipping ± 45° either side of vertical, but changes rapidly beyond that range. The shape of the slingram LLR profile responses can be used to provide a useful semi-quantitative estimation of the dip of a target.

4.4.2.4 Strike of the target

Like the in-loop configuration, the slingram profiles responses are affected by the strike of a target. However, as seen in Figure 4.13, the shapes of the responses are very similar for all strike angles which prevents an estimate of strike being made. Like the in-loop case, quantitative estimation of the strike is not possible from one profile line alone.

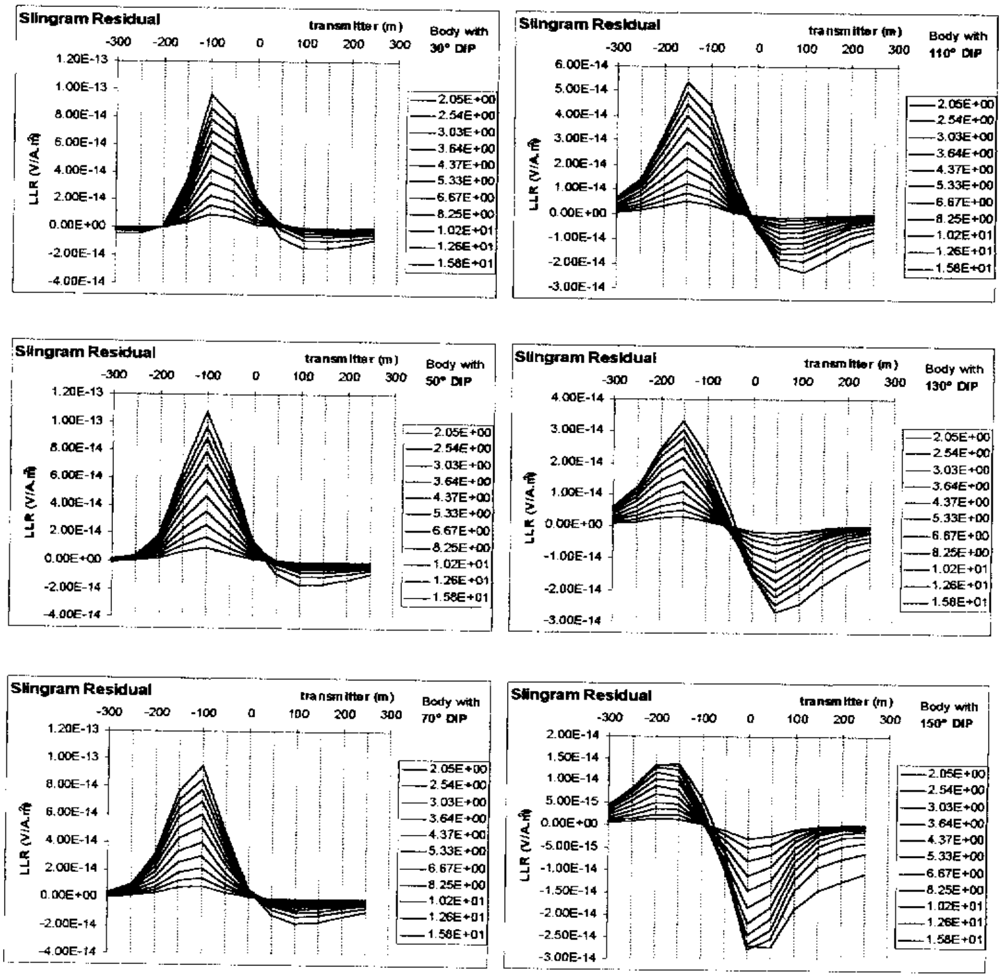

Figure 4.12 The effect of target dip angle on the slingram LLR. Slingram LLR profile responses for a conductive plate in a half-space at a range of dip angles. Note the lack of change in the relative amplitude of the peak and trough for angles less than 90°. The slingram LLR is not sensitive to up-dip targets. However, note the change in the relative amplitude of the peak and trough for angles greater than 90°. The slingram LLR is very sensitive to down-dip targets.

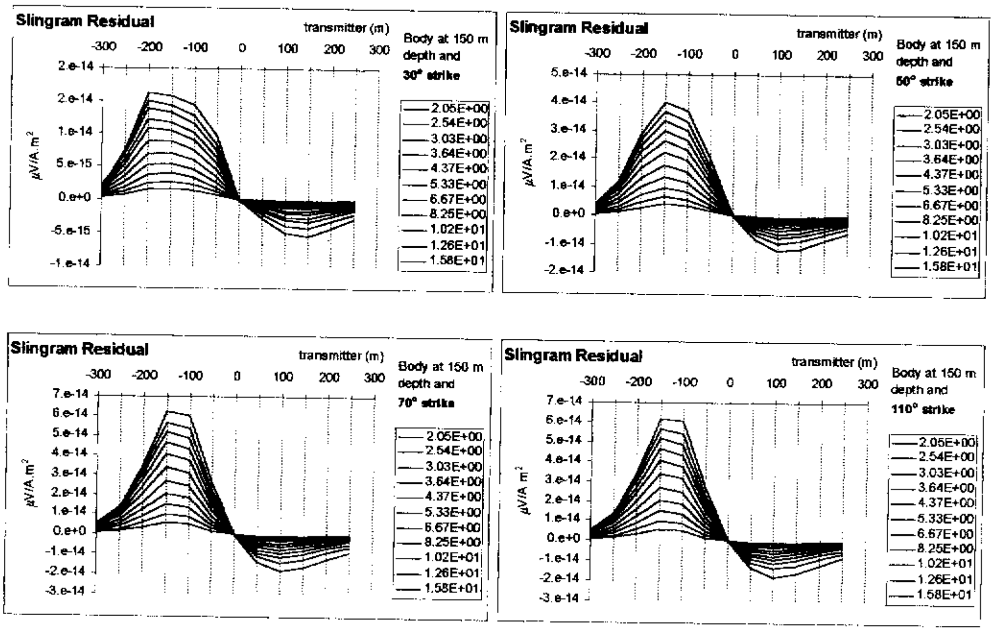

Figure 4.13 The effect of target strike angle on the slingram LLR. The profile shape does not provide an indication of strike direction.

4.4.2.5 Conductance of the target

The time domain LLR also enables an estimate of the conductance of the target to be made. In Figure 4.14(a) the profile responses are presented for the vertical plate located at 100 m depth. Each plot corresponds to a different target conductance in the range of 10 S to 400 S. The profiles all exhibit the same general shape and do not provide a means of determining the conductance of the target. Figure 4.14(b) shows the corresponding LLR decay curves for each station along the profiles for the target. It is apparent in Figure 4.14(b) that station $x = -100$ m exhibits the slowest decay, regardless of the conductance of the target. A plot of the decay constant τ measured at this station, against target conductance is shown in Figure 4.15. The linearity of the trend allows a reliable estimate of target conductance to be made from the measured decay constants.

4.5 Concluding remarks

Interpretation of EM signatures is a difficult proposition in many instances and is best achieved with the assistance of sophisticated numerical modelling. This chapter has presented some results of simple numerical modelling to assist in the development of simple interpretative guidelines for the SLR and LLR. The shape of the profile response may provide information regarding the depth, dip and strike of the target. The decay time constant of the LLR can be used to estimate the conductance of a plate-like conductor.

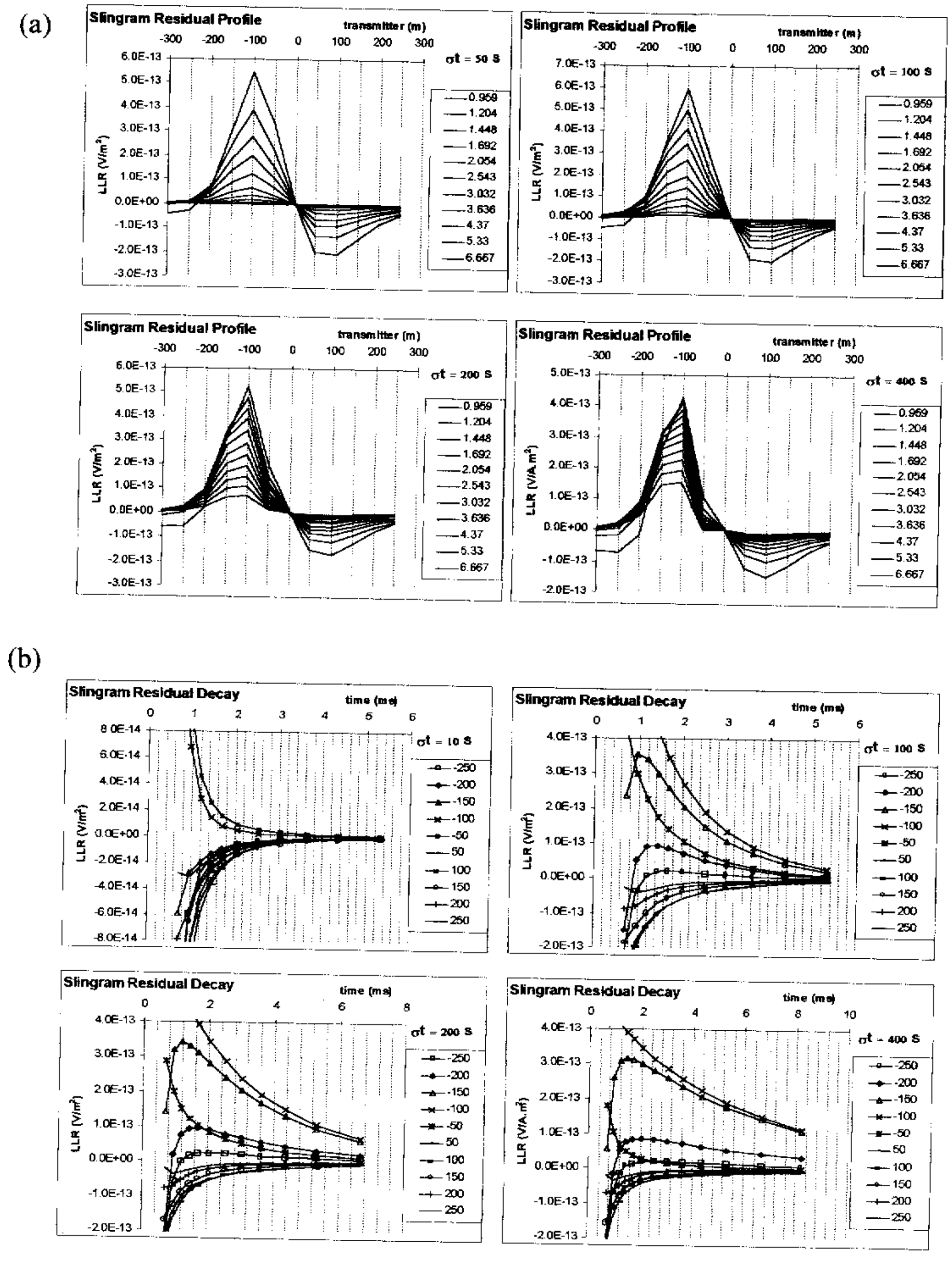

Figure 4.14 The effect of target conductance on the slingram LLR. **(a)** Slingram LLR responses for a vertical conductive plate of conductance 50 S, 100 S, 200 S and 400 S respectively located at 100 m depth in a 100 Ω.m half-space. The profile responses do not allow an estimate of conductance to be made. **(b)** the corresponding slingram LLR decay curves. Station x = –100 m provides the most obvious response from the target.

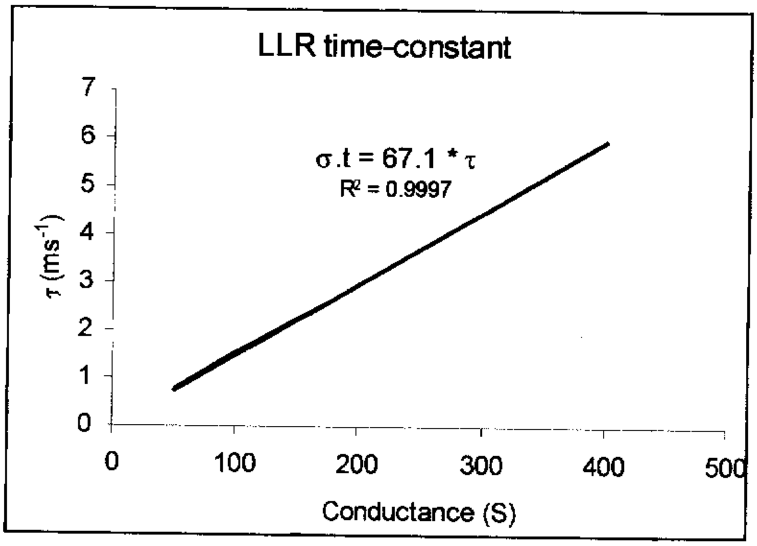

Figure 4.15 Plot of LLR time constant versus target conductance. Time constants are taken from the decays in Figure 4.14(b) at x = -100 m. The linearity of the plot enables an accurate estimate of target conductance to be made using the LLR decay.

CHAPTER 5

ENHANCEMENT OF GEOPHYSICAL MAPS USING THE RADON TRANSFORM

5.1 Introduction

In the previous chapters the profile signature of a conductive target was enhanced by the combination of data measured by different survey configurations. A natural extension of this is the combination of adjacent profiles to produce a two–dimensional map of the entire survey area. This is a common procedure that can be applied to any type of data set. In this chapter, data processing techniques are developed that can be applied to geophysical data to improve the quality of map presentation. The Radon transform is applied here to synthetic data to investigate its usefulness for reducing flight line related artefacts in airborne electromagnetic maps with a view to enhancing the quality of the map. In addition to this, the inherent directional quality of the Radon transform provides the potential for selectively enhancing particular features for display on a map. This capability is also investigated in this chapter.

5.1.1 Background

There are a number of processing techniques available to the geophysicist to improve the quality of data presentation. With magnetic data for example, raw field measurements can be processed to produce a vertical derivative to display more clearly the gradients within the map and help distinguish between deep and shallow bodies. Upward and downward continuation of the potential field is often used to highlight particular features in a map, or to reduce the contribution of unwanted features as well as helping to determine the depth of burial. Such processing enables more useful information to be extracted from the same survey measurements. In seismic exploration, for example, the raw data is processed to such a large degree that it can often be quite difficult to reconcile the end product with the raw data.

In addition to the data processing that can be performed, modern visualisation software enables the production of multi-layered images to enhance the character of a display. Different types of data (magnetic intensity and topography for example) can be merged to produce a more detailed composite map of a survey area. Artificial illumination techniques can also be used to highlight amplitude changes and thereby improve the visual clarity of a map.

In many cases, the end product of an EM survey is a two-dimensional map displaying the measured amplitude distribution across the survey area, or some other quantity derived from those measurements. The quantity most commonly used for data presentation of EM data is apparent resistivity or apparent conductivity. Apart from the derivation of a suitable quantity to display, there is currently very little other processing done on EM data to improve the data presentation or enhance the features of interest. It is an unfortunate reality that the nature of the data acquisition systems used in *airborne* surveys may result in artefacts being present in the maps that are related to the direction of flight. For example, Figure 5.1 shows an apparent conductivity map derived from AEM data which is affected by flight related artefacts. This form of signal distortion (noise), referred to as the herringbone effect, makes the task of identifying conductor boundaries very difficult and severely detracts from the quality of the map.

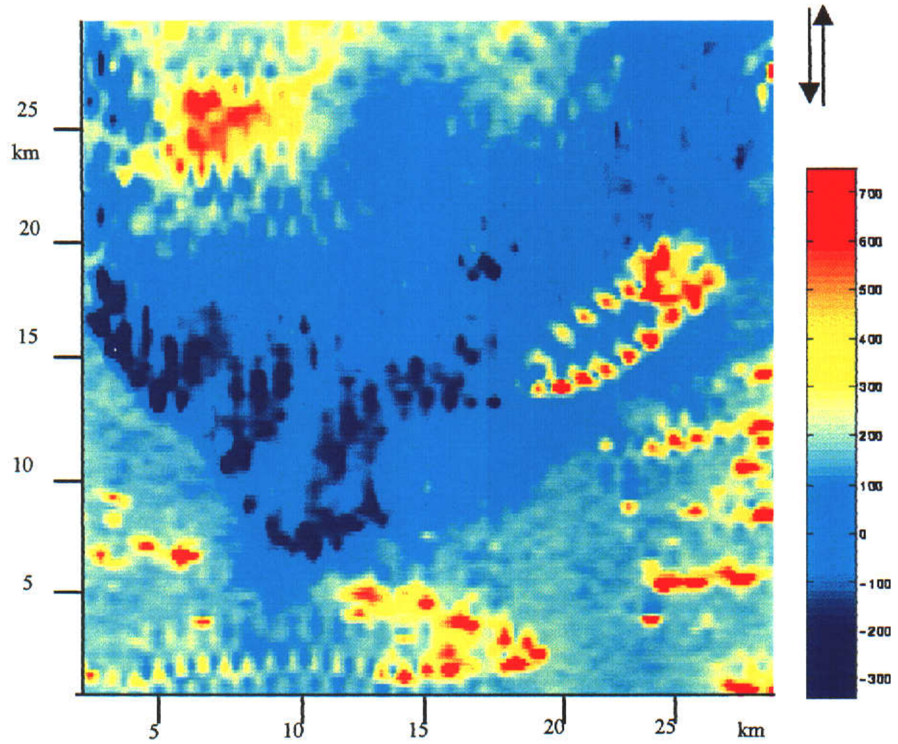

Figure 5.1 Herringbones in an AEM map. dB_x/dt component at 0.2 ms using a GEOTEM® system. The alternating flight-line direction (indicated by the arrows) results in 'herringbones' in the map making boundary definition more difficult.

5.1.2 What's important?

In order to make worthwhile improvements to the way data are presented, it is necessary to know what is important in the final product. Regardless of the ultimate purpose of the exploration program, the maps produced using EM data are usually used in conjunction with other geological and geophysical information to develop a model of the geological structure beneath the survey area. Presently, airborne electromagnetic (AEM) surveys are used primarily for reconaissance i.e. as a first pass look at an area. Regions of interest are identified and follow-up ground surveys are conducted to more thoroughly investigate prospective targets near the AEM anomalies. Although the physical significance of the measured AEM amplitudes (or other quantities derived from them) are useful in terms of the quality of a conductor, the most important knowledge to be gained from the initial AEM survey is the *location* of conductors and *changes* in basement features. As such, the principal function of an AEM survey is to locate sub-surface conductors and delineate their boundaries. The task facing the AEM geophysicist is to produce a map that most clearly and accurately displays the boundaries between regions of conductivity contrast. This may be quite difficult where the herringbone effect is prominent.

5.2 Herringbones in AEM data maps

The herringbone effect appears in AEM maps as a sequence of alternating distortions of a boundary along the direction of the flight-line (see Figure 5.1). It can be seen from this figure that the true locations of the boundaries are difficult to identify due to the presence of the herringbones. It should be noted here that although most interpreters prefer to see the edges of conductors correctly placed in a map, some do prefer to see the herringbones in a map because of the benefits of easy pattern recognition. The characteristic pattern draws immediate attention to the area. Also, herringbones may enable inferences to be made about the dip of a conductor since the herringbones are more pronounced when flying up-dip than down-dip. However, it remains that the herringbones are an artefact of the measuring system and do not reflect the true geological structure. For fixed-wing towed-bird AEM systems the herringbones are more likely to be observed in the horizontal component data (dB_x/dt) than the vertical component (dB_z/dt).

5.2.1 Cause of the herringbone effect

The lack of information in the literature about the herringbone effect indicates that very little attention has been given to understanding the cause, and methods of removal of herringbones in AEM maps. The coupling of the transmitter with a conductive unit in the Earth is a function of their relative position and orientation. A better coupling will induce a larger current in the body. Similarly, the greater the coupling between the body and the survey receiver, the greater the measured response. The different coupling obtained when flying in opposite directions across a conductive unit gives rise to a profile response that is direction dependent. Herringbones arise as a direct result of placing the profile responses from oppositely directed flight-lines side by side in a map. If all flight-lines were flown in the same direction, herringbones simply would not be produced, although the resulting map may be displaced along the flight direction. Simple economics dictates that alternate traverses are in opposite directions.

5.2.2 Simulation of Herringbones

Smith (1994) simulated the herringbone effect using a horizontal, semi-infinite conductive plate in free-space, and acquisition parameters representing a fixed-wing, towed-bird Geotem survey (Annan and Lockwood, 1991). In this work I use a conductive sheet of finite dimensions embedded in a uniformly conducting half-space, and use a similar acquisition system. Figure 5.2(a) shows a map of the dB_x/dt responses computed at 0.2 ms for the AEM system flying off the edge of a flat conductor, to the right. Figure 5.2(b) presents the corresponding map produced by flying onto the conductor, to the left. In each case the receiver location is used as the plotting point. The anomaly pattern is remarkably smooth in both cases and allows easy identification of the edge of the conductor. It is noticed, however, that the apparent location of the edge of the conductor is displaced from its true position when flying off the conductor. This is due to the transmitter-receiver separation which needs to be taken into account. Figure 5.2(c) presents the same data arranged as though alternate lines were flown in opposite directions to simulate a real survey. Plotting the profile responses side-by-side in this way produces herringbones in the map and the edge of the conductor is difficult to resolve. The herringbones are centred near the edge of the conductor but definition of the boundary is very difficult due to the distortion of the contours. The extra cost of flying all profile lines in the same direction to prevent herringbones from affecting the maps is prohibitive and so it is necessary to seek an effective means of removing herringbones from the maps.

5.2.3 Complicating factors

Based on the simple example given above, one might be tempted to shift the profiles in opposite directions to compensate for the different Tx–Rx positions along adjacent profiles. Such a practice is in effect a geologically dependent adjustment. Generally speaking, the geology is irregular and unknown. Therefore, such an adjustment is not recommended.

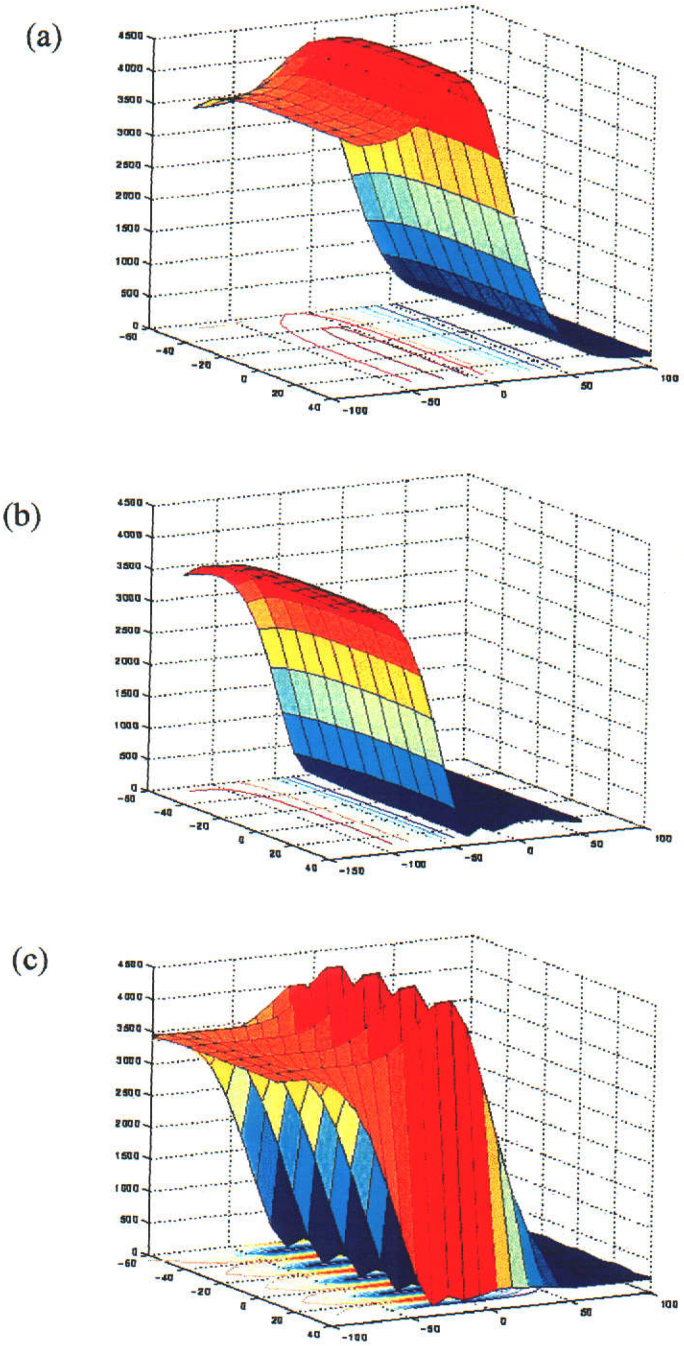

Figure 5.2 Synthetic AEM maps of the edge of a conductor. **(a)** AEM dB_x/dt amplitude map at 0.2 ms for the aircraft flying on to the flat-lying conductor at x = 0m. The maximum amplitude occurs as the *receiver* passes over the edge. **(b)** aircraft flying off the conductor. Note that the maximum amplitude occurs when the *transmitter* passes over the edge. **(c)** the profile lines flown in alternate directions leads to the production of herringbones.

The response measured over a vertical conductor is intrinsically different from that over a horizontal one and in an EM survey both cases are likely to be encountered. The most suitable method of data display is governed by the nature of the intended target and should be chosen accordingly. See section 5.2.3.1.

5.2.3.1 Plotting point

Herringbones are the result of asymmetry in the system. The asymmetry displayed in a map can be reduced to some degree by selecting the appropriate plotting point for the data. When using a vertical magnetic dipole source (the norm for fixed-wing airborne EM surveys) the x component dB_x/dt profile response is asymmetric for vertical (or steeply dipping) bodies. This component has a large amplitude response when the receiver is located directly over the body. For this reason the receiver location is usually used as the plotting point for the x component. However, the vertical component dB_z/dt produces a more symmetric response over a vertical body than the x component, with peaks on either side of the body and a trough over the centre of the body. For this reason, the mid-point between transmitter and receiver is selected as the plotting point for the z component. For a symmetric body, the y component dB_y/dt is zero. The y component produces a small but asymmetric response over a vertical tabular body that is displaced from the profile line, so the receiver position is also selected for displaying this component. For the case of a flat-lying target, the x and z components are both asymmetric, while the y component is again very small.

Figure 5.3 shows the effect of plotting point choice on the airborne data map generated using a finite *vertical* plate model.

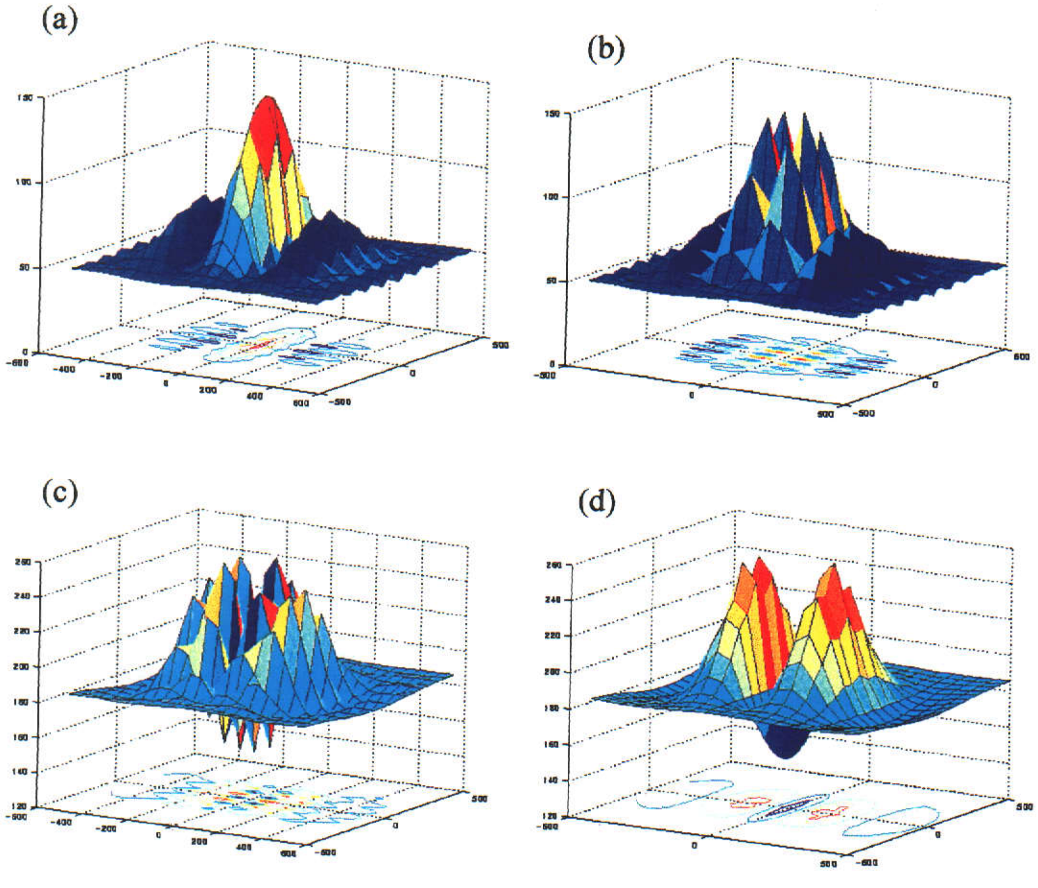

Figure 5.3 The effect of plotting point on the AEM map of a *vertical* conductor in a conductive half-space. In **(a)** the dB_x/dt component is plotted at the receiver location and in **(b)** the mid point of the T-R array is used. The herringbones are more severe when the mid-point is used as the plotting point. In **(c)** the dB_z/dt responses are plotted at the receiver and in **(d)** the mid-point is used. The herringbones are much more severe when using the receiver location as the plotting point. Different components require different plotting points.

It is seen in Figure 5.3 that the map of the dB_x/dt component response is grossly distorted when using the mid point as the plotting point but more coherent when the receiver location is used. In contrast, the z component data is very coherent when using the mid point and less so when using the receiver location. Figure 5.4 shows the effect of plotting point choice on the map produced over the edge of a *flat-lying* conductor. In this case, using the mid point as the plotting point for the x component data is seen to produce less severe herringboning than the case where the receiver location is used. The edge of the conductor is sharper and more well-defined. The z component data is more symmetric and therefore relatively insensitive to the choice of plotting point for flat lying conductors than the x component. Either of the receiver location or the mid-point can be used.

It is clear from this very simple analysis that the choice of plotting point has a significant impact on the production of herringbones in AEM maps and should be selected with the survey objectives in mind. Regardless of which plotting point is chosen it is likely that the map will still contain some herringbones due to the inherent asymmetry of the variety of geological structures likely to be encountered in the survey.

5.2.3.2 Dip and strike angle

In the numerical examples in Figures 5.3 and 5.4, the profile line is perpendicular to the strike of the vertical or horizontal conductor. In a real survey, the strike and dip of the conductors may be unknown, and will almost certainly be variable. The asymmetry associated with an angled and dipping target contributes to the production of herringbones. Figure 5.5 shows the x component map produced using a conductive plate oriented at 60° to the profile and dipping at 60° to the horizontal.

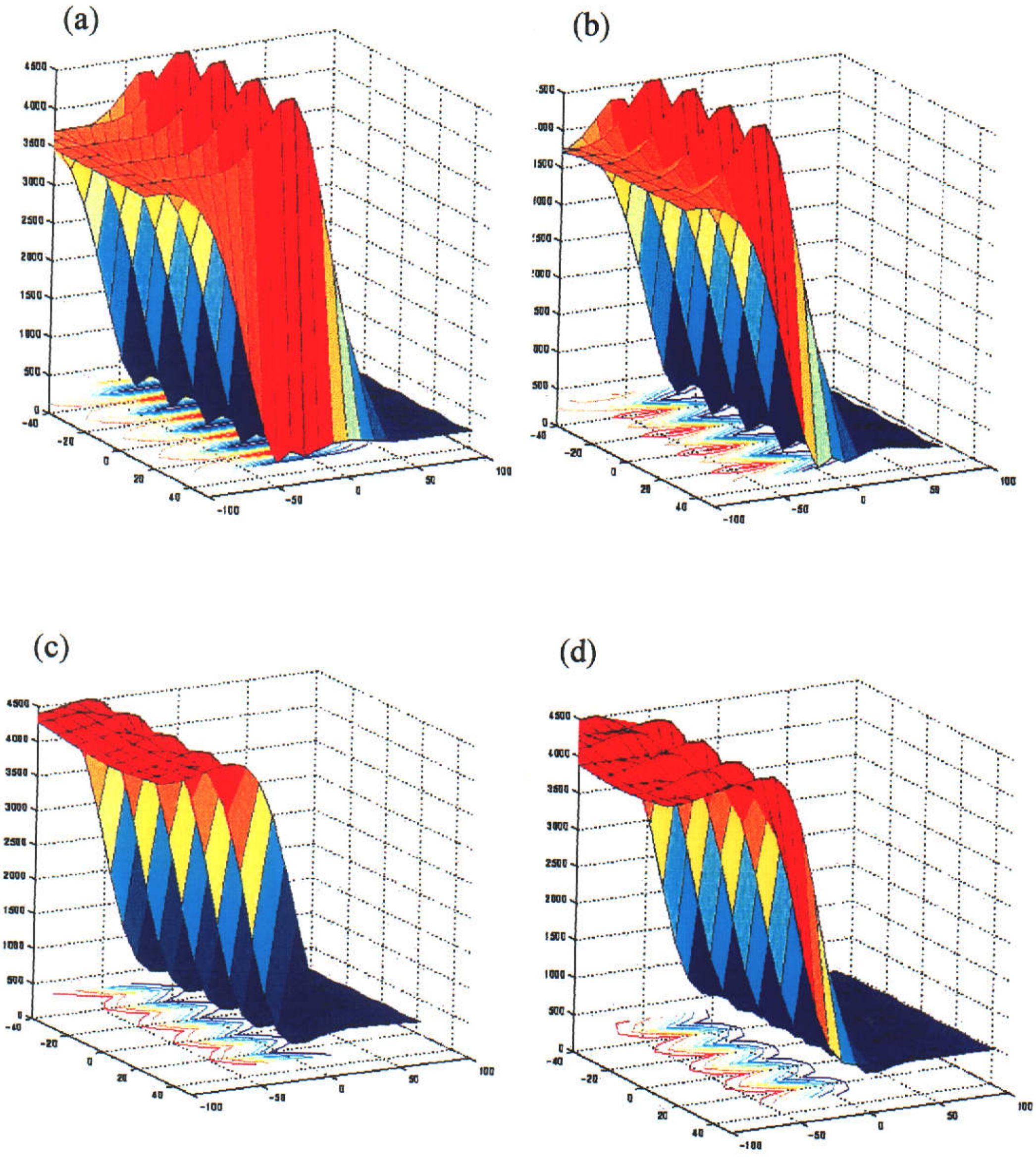

Figure 5.4 The effect of plotting point on the AEM map of a *flat-lying* conductor in a conductive half-space. In **(a)** the dB$_x$/dt response is plotted at the receiver location and in **(b)** the mid point of the T-R array is used. The herringbones are more severe when the *receiver* location is used as the plotting point. In **(c)** the dB$_z$/dt responses are plotted at the receiver location and in **(d)** the mid-point is used. There is very little difference between the two maps for this component.

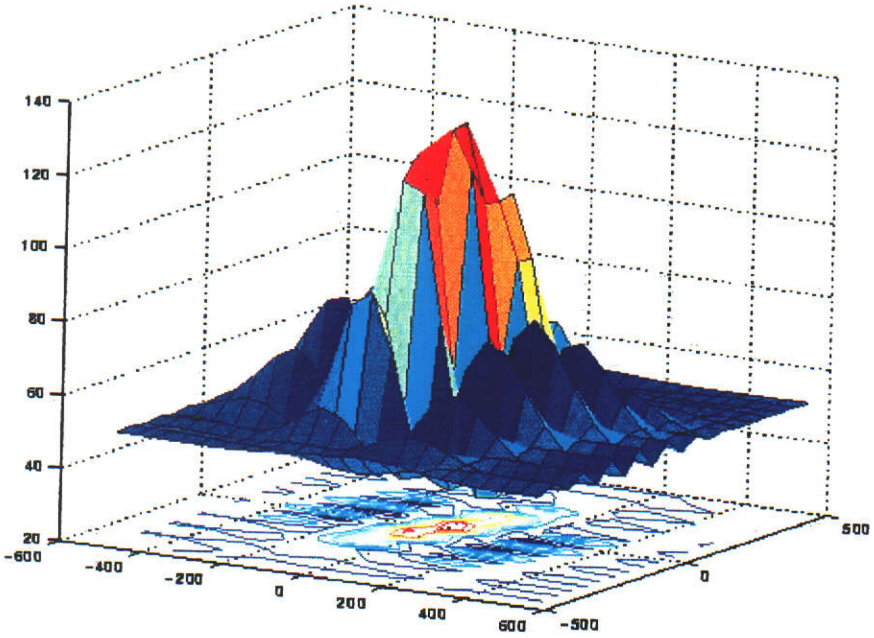

Figure 5.5 AEM map over a conductive plate oriented at an angle of 60° to the flight-line and dipping at 60°. The extra asymmetry introduced by the dip and the angled strike direction exaggerates the herringbone effect.

Even in the case where the asymmetry due to the towed-bird is absent, i.e. the transmitter and receiver are at the same altitude, the map will exhibit herringbones.

5.2.4 Removal of herringbones from data maps – current practice

The task of removing the herringbones from EM maps can be approached in a number of ways. To help reduce the asymmetry observed in the profile responses, Smith and Keating (1995) combined the component responses into a quantity referred to as the energy envelope EE,

$$\mathrm{EE} = \sqrt{\mathrm{V_x}\overline{\mathrm{V}}_\mathrm{x} + \mathrm{V_y}\overline{\mathrm{V}}_\mathrm{y} + \mathrm{V_z}\overline{\mathrm{V}}_\mathrm{z}}\,, \tag{5.1}$$

where V represents the measured responses in the x, y or z direction and $\overline{\mathrm{V}}$ the corresponding Hilbert transform of the responses. The energy envelope derived from the computed responses displays a more symmetric profile response than the measured data making it a more suitable parameter for display. Any remaining herringbone features can be removed by a micro-levelling procedure (Minty, 1991).

Probably the most simple and widely used method of herringbone removal is to produce two maps by processing the data as two separate surveys: one map derived from the flight lines in one direction and the second map derived from the flight lines in the opposite direction. The two maps are then merged into a single map comprising both flight line directions. Figure 5.6(a) shows the map produced by separately gridding the profiles used in Figure 5.1 and then merging the two maps. Most noticeable in this figure is blurred and diffuse nature of the features compared to Figure 5.1 resulting from the separate gridding.

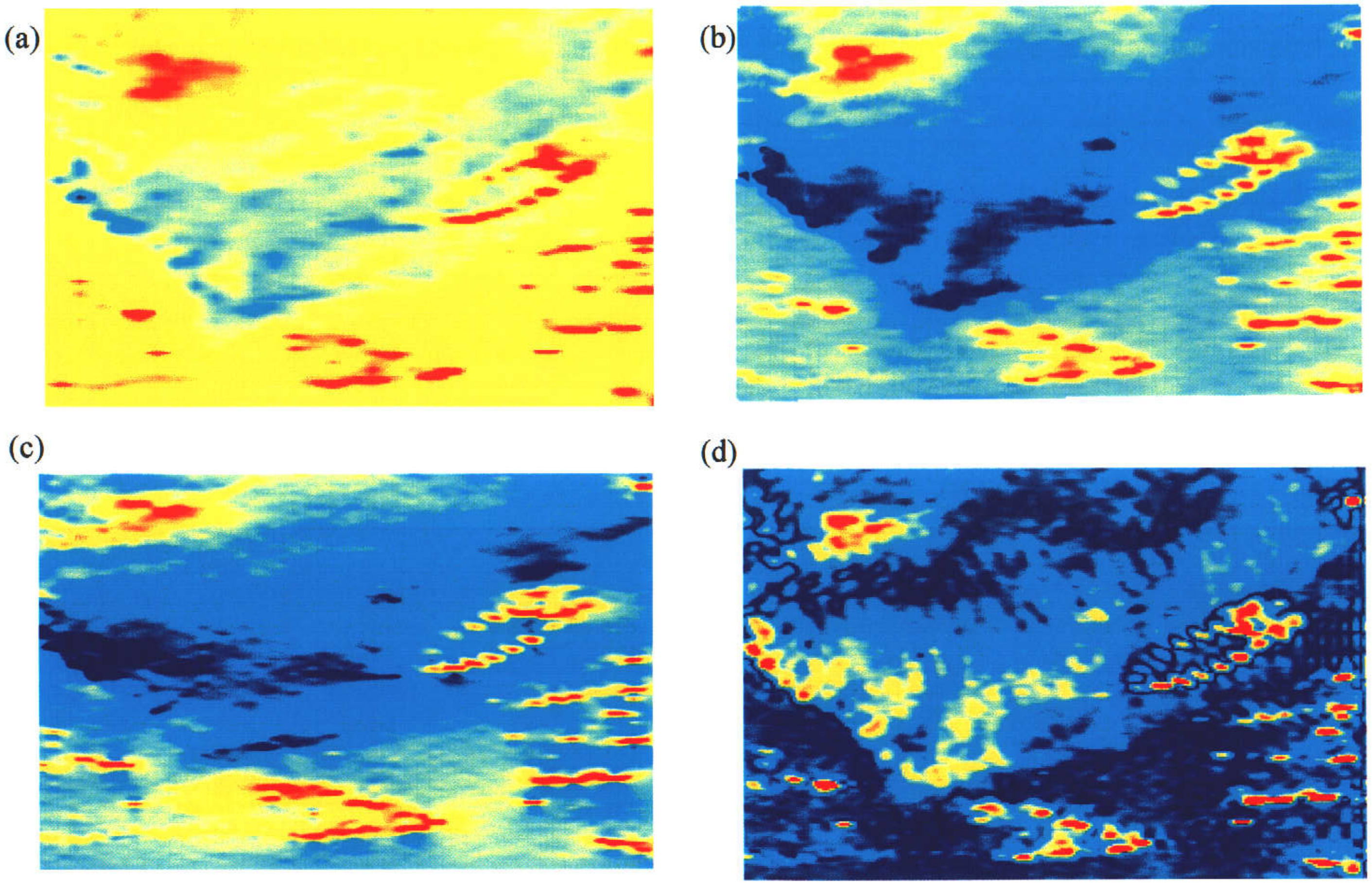

Figure 5.6 Comparison of herringbone removal techniques using space domain and Fourier domain processing. **(a)** separate gridding, **(b)** space domain median filter, **(c)** Fourier domain directional filter, **(d)** Fourier domain attenuation. Fourier domain processing causes severe distortion of the features in the map.

By using alternate flight-lines to generate each grid separately, the interpolations required in the gridding algorithm must be performed over a distance of two times the flight-line spacing (400m in this case) causing the features to appear broader than would otherwise have been the case.

A recently developed method of herringbone removal (O'Connell et al., 1998) involves the use of a two dimensional median filter window. The filter is applied directly to the space domain data and replaces the central data point with the median value of the window. Essentially, the filter smears out the herringbones and produces 'cleaner' map. A nine point filter was applied to the data in Figure 5.1 to produce the map in Figure 5.6(b). The herringbones have been removed and the features displayed in the map exhibit less broadening than in the case of separate gridding and conductor boundaries are much more clearly defined.

I now investigate some new methods for removing, or at least reducing, herringbones from AEM maps.

5.2.4.1 The Fourier transform

The Fourier transform is a well known and well utilised tool in signal processing (Peters, 1949; Grant and West, 1965; Bracewell, 1978). It is used extensively in seismic processing for noise reduction as well as other processes such as seismic migration. In magnetic and gravity surveys it is used as a means of field continuation and directional filtering. The Fourier transform displays data in terms of its temporal or spatial variations and as such it may be of some use in the removal of herringbones. The directional nature of the herringbones suggest that a directional rejection filter may be useful in removing them from the map. Also, the herringbones, by virtue of the way they are produced, will have a spatial frequency (wavenumber) in the cross-profile direction equal to twice the flight-line spacing. It is conceivable that if this spatial frequency were attenuated then the herringbones would be reduced or possibly removed altogether. Both of these ideas are tested using the synthetic map of Figure 5.3(a).

5.2.4.2 Cosine rejection filter

The data in Figure 5.3(a) were transformed to the Fourier domain using the Intrepid processing package and a cosine tapered, rejection filter was applied. The filter, which was centred on the flight line direction, has the effect of removing all features having that particular orientation. The map produced after inverse Fourier transform is seen in Figure 5.7(b) to be free of herringbones. However, the filtering has also distorted the shape of the feature by making it somewhat elongated in the strike direction and narrower in width.

5.2.4.3 Spectral attenuation

Herringbones have a wavelength equal to two times the flightline spacing and will therefore contribute to the spectral domain near the Nyquist wave-number pertinent to that direction. To test this idea the synthetic data used to produce Figure 5.3(a) were transformed using the standard 2-D fast Fourier transform algorithm of Matlab v 5.5. A plot of the Fourier domain data for a selected k_y value is shown in Figure 5.8(b) to exhibit elevated amplitudes corresponding to the x coordinate wavenumber near $2\Delta x$. These elevated amplitudes are not found in the Fourier domain data of maps without herringbones. This leads to the conclusion that the high frequency components in the k_x coordinate spectral data are, indeed, due to the herringbone features in the space domain map.

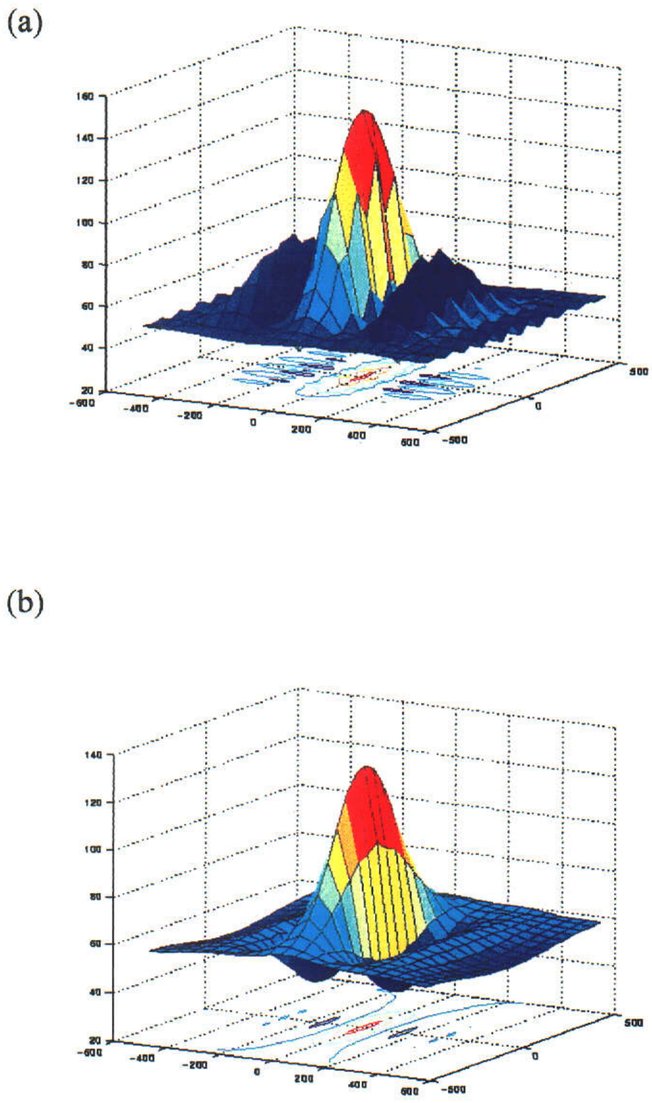

Figure 5.7 Fourier domain direction filtering to remove herringbones. **(a)** original dB_x/dt map with herringbones **(b)** new map produced after removal of the flightline direction using a cosine tapered rejection filter in the Fourier domain. The herringbones have been removed and a smooth anomaly is produced. The anomaly has been significantly elongated and narrowed by the application of the filter.

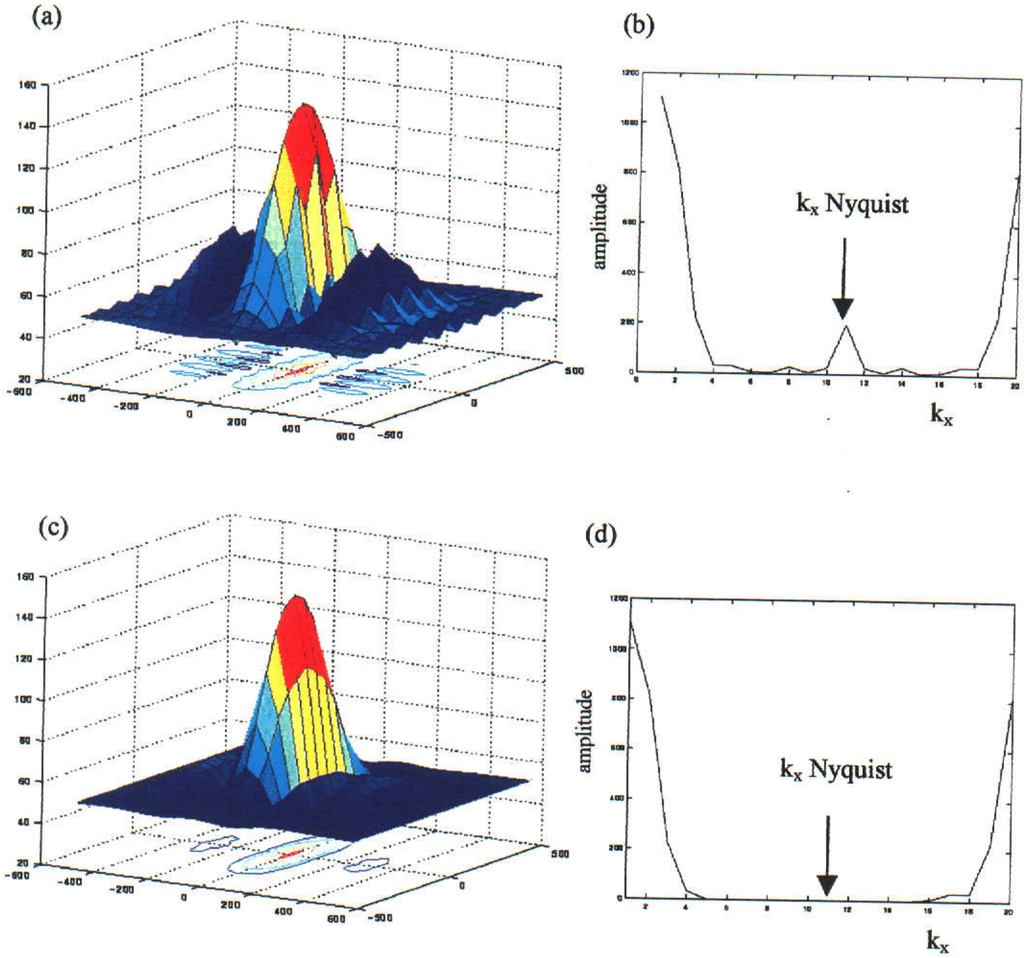

Figure 5.8 Fourier domain attenuation to remove herringbones. **(a)** original map and **(b)** Fourier domain line (constant k_y)showing elevated amplitudes at the wavenumbers near the Nyquist limit. **(c)** new map without herringbones after the elevated amplitudes were reduced prior to inverse Fourier transform. **(d)** spectral line with large k_x amplitudes attenuated.

Reducing the amplitudes in this portion of the spectral domain might be expected to reduce the severity of the herringbones in the space domain map after inverse transformation. With this in mind, the portion of the spectral data near the k_x Nyquist wavenumber was reduced to the estimated background level prior to inversion [see Fig. 5.8(d)]. Selection of the filter limits was made by inspection of the spectral domain data on a line-by-line basis. The space domain map recovered from the filtered spectral data shown in Figure 5.8(c) is void of the herringbones and displays a smoothly varying anomaly that accurately reflects the location of the conductor.

Application of the directional filter and spectral attenuation methods to the 'real' map shown in Figure 5.1 produced the maps in Figure 5.6(c) and 5.6(d) respectively. The directional filter method has removed the herringbones but has also distorted many of the features in the map. The spectral attenuation method was less successful due to the difficulty in determining the filter limits needed to remove the herringbones. The filter dimensions were adjusted until a noticeable reduction of the herringbones was observed in the recovered map. Figure 5.6(d) shows the best result obtained using this method. There has been a severe distortion of the amplitude distribution of the map caused by the filtering required to remove the herringbones.

5.3 The Radon Transform

The Radon transform is a numerical process that is useful for analysing lineaments in a 2-D map. It is an integration procedure that, in its most general form, maps a shape in the space domain into a single pixel in the spectral (transform) domain. The most common type of Radon transform operates along straight lines and has application to many areas including Physics, Medical imaging, Astronomy and Geophysics (Deans, 1983). In seismic processing a type of Radon transform, commonly known as the slant stack, has been used for the generation of synthetic seismograms (Chapman, 1978), multiple suppression (Taner, 1980), ground roll removal and separation of refractions on seismic records (Stoffa et al., 1981). Although the theory of the Radon transform is well established and is used extensively in seismic data processing (Duranni and Bisset, 1984; Brysk and McCowan, 1986; Beylkin, 1987), and many other fields (Deans, 1983), there are a number of variations in the way it can be defined. Therefore, I include a brief description of the 1-D Radon transform which I use in this thesis.

The slant stack RT operates along straight lines which are defined by their slope p and intercept τ as shown in Figure 5.9(a). Off-end seismic shot records lead to this natural choice of line parameters since, in these records, there exists an obvious choice of origin at $x = 0$, $t = 0$ and a preferred direction of events that limits the range of τ and p. However, the slant-stack is limited in its ability to transform steeply sloping events (Toft, 1996) and vertical lines cannot be transformed. To avoid this limitation, it is usual practice to define two transform domains: one relative to the x-axis, and the other relative to the t-axis. In potential field and electromagnetic maps the features of interest strike in any direction. To accommodate the full range of possible strike directions the 'normal' RT is preferred. In this form, the origin can be chosen as the centre of the map and the lines defined by their 'normal' slope (θ) and offset (ρ) parameters [Figure 5.9(b)]. Integration of the map amplitudes along each line (S lines in Figure 5.9) provides the amplitude of the Radon domain point located at (ρ,θ). It should be noted that the normal RT and the slant-stack RT are very closely related and may perform the same function equally well.

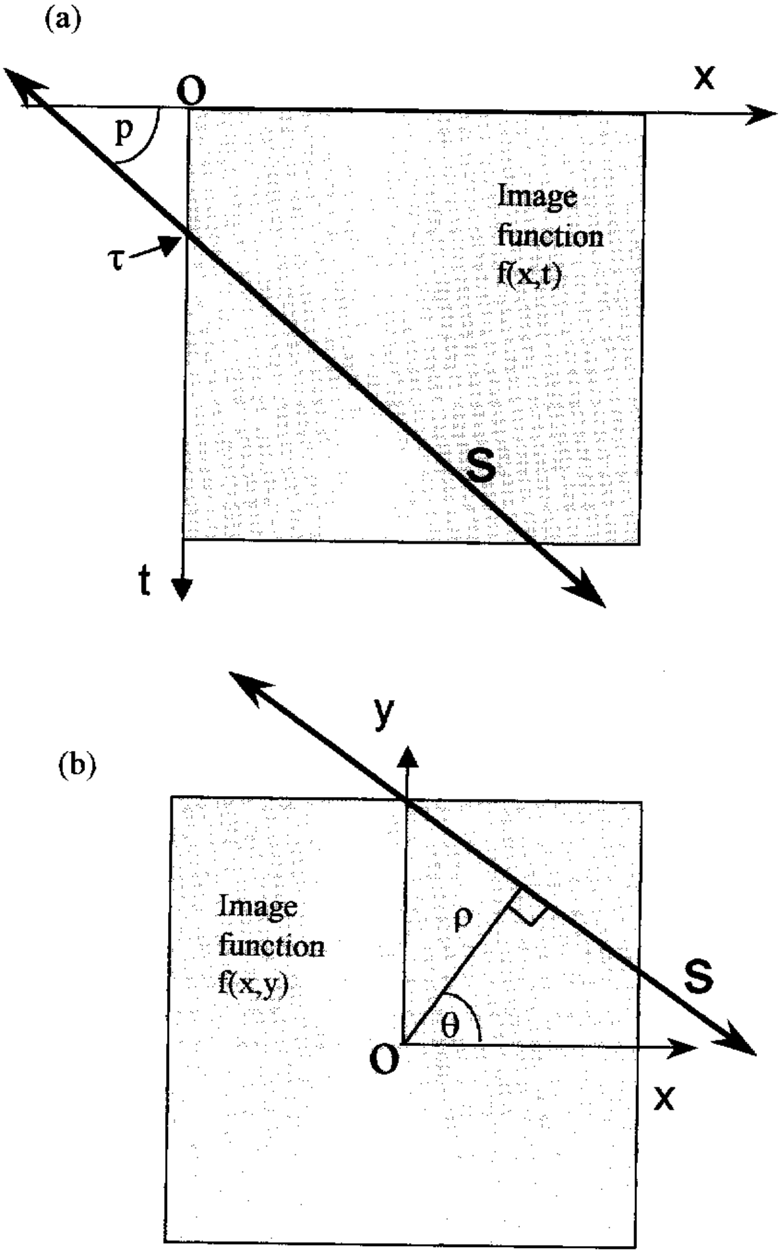

Figure 5.9 Schematic comparison of slant-stacking and the Normal definitions of the Radon transform. **(a)** slant stacking integrates along S lines defined in terms of the slope p and t axis intercept τ. **(b)** the Normal form integrates along S lines defined by their slope θ and normal offset distance ρ.

Mathematically, the Radon transform domain function F(ρ,θ) is obtained by applying the normal RT to the space domain function f(x,y) with the help of the following equation:

$$F(\rho,\theta) = \int_{-\infty}^{\infty}\int_{-\infty}^{\infty} f(x, y)\delta(\rho - x\cos\theta - y\sin\theta)dxdy\ , \qquad (5.2)$$

where δ is the Dirac delta function. The delta function ensures that only points that lie on the line S contribute to the transform domain. The RT maps linear features with significant strike length as high amplitude points at the appropriate location in the Radon domain. A unique correspondence exists between space domain linear features and Radon domain high spots (Robinson, 1982). Thus, the analysis of the linear features in a 2-D map can be carried out by examining the amplitude distribution of the transform domain function. Also, the amplitudes in the transform domain can be selectively amplified or attenuated to produce a corresponding enhancement or suppression of specific linear events in the space domain.

Inversion of the 'normal' Radon domain function F(ρ,θ) to f(x,y) is achieved via the filtered back-projection method (Toft, 1996) defined as

$$f(x,y) = \int_{0}^{\pi}\int_{-\infty}^{\infty}|\nu|\left(\int_{-\infty}^{\infty}F(\rho,\theta)e^{-i2\pi\rho\nu}d\rho\right)e^{i2\pi\nu(x\cos\theta+y\sin\theta)}d\nu d\theta\ , \qquad (5.3)$$

where ν is a wavenumber vector used for filtering in the Fourier domain.

An advantage of working in the Radon domain compared to the Fourier domain is that the Radon domain data are real numbers. This makes data manipulation much more simple and reliable. The complex numbers of the Fourier domain can be scaled accurately but cannot be averaged or interpolated accurately (Lamontagne, 1975). In many cases it is advantageous (or necessary) to find the average of, or interpolate between, a number of transform domain data points.

5.3.1 The Radon transform of synthetic data

Numerical implementation of the Radon transform is not an exact process and its inverse will not always recover the original amplitudes accurately. To establish the Radon transform as the basis of a valid processing tool, I make use of artificial maps to which the Radon transform processing can be applied. The artificial maps have the advantage of being computed on a regular grid to avoid the need for data interpolation.

Radon transform algorithms involve the summation of data amplitudes along straight lines of various slopes and offsets. The discrete nature of the transform requires that the number of 'S' lines and the sampling rate along those lines be selected to ensure sufficient accuracy. In order to achieve an exact transform an infinite number of lines would be required (Deans, 1983). The trade-off between accuracy and CPU time is a matter for consideration. The optimum sampling parameters required for the desired accuracy will also depend on the nature of the data being transformed. It would be advantageous to make use of a variable sampling rate to reflect the complexity and variability of the space domain data. In this work, however, a simple technique that can be easily applied as routine processing, without the need for complicated analyses is the objective. In view of this, a constant gradient increment (between S lines) across the whole space domain data is used.

5.3.2 Transform integrity

A well known feature (Deans, 1983) of the discrete implementation of the inverse Radon transform is that the mean value of the recovered data will always be set to zero, i.e. the DC amplitude is zero. This arises from the use of a wavenumber scaling factor $|v|$ which is equal to zero for the DC component. This apparent flaw can be avoided by converting the original data to a zero mean set prior to performing the

Radon transform. The DC component can then be added to the recovered data after inverse transformation.

Figure 5.10(a) presents a very simple test pattern comprised of vertical and horizontal lines and Figure 5.10(b) presents its Radon transform. The linear features are clearly distinguishable in the Radon domain as high amplitude peaks whose locations are determined by the corresponding line parameters (ρ,θ). The amplitudes of the Radon domain peaks are related to the strike length and amplitude of the lineament as well as the sampling rate used in the transform. Note that each horizontal line produces two peaks in the transform domain, one at either extreme of the θ values. This is due to the fact that the forward Radon transform integrates along lines of gradient (θ values) ranging from $-\pi/2$ to $+\pi/2$, both of which represent a horizontal line in the space domain. This double sampling of horizontal features could be avoided by restricting the range of θ values used in the forward RT, but is considered unnecessary. Parallel linear events in the space domain are transformed as high amplitude peaks at different locations in the Radon domain due to their different offset from the origin. This separation in the Radon domain enables linear features in the space domain to be processed separately.

Figure 5.10(c) shows the map produced by application of the forward and inverse RT transform pair to Figure 5.10(a) and Figure 5.10(d) shows a contour map of the amplitude differences between the two maps. In most parts of the recovered map, the amplitude differences are less than 2% of the original amplitudes. The largest difference represents less than 20% change.

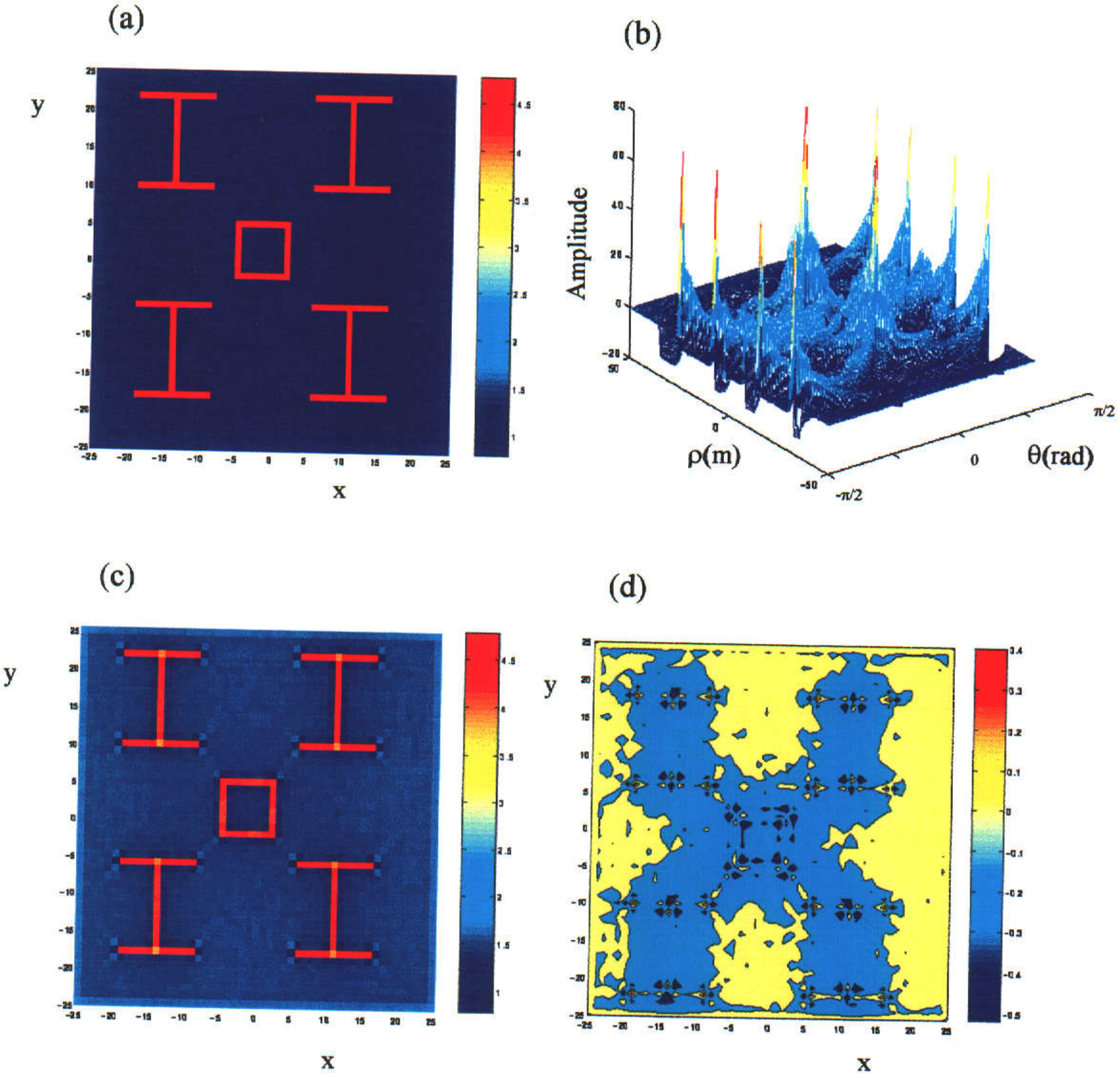

Figure 5.10 Integrity of the forward and inverse Radon transformations on a synthetic test pattern. **(a)** Synthetic test pattern showing linear horizontal and vertical features. **(b)** Radon transform of the test pattern showing a separate peak corresponding to each line segment. **(c)** recovered pattern after application of the forward and inverse Radon transforms. **(d)** contour plot of the difference between the two patterns. Amplitudes are recovered within 2% for most of the data but differences can be as high as 20% near sharp edges.

The test pattern used in this example represents a difficult image to process due to the very sharp boundaries. The contours that represent high percentage changes occur where there are small differences in the low amplitudes near steep edges. In most geophysical maps, the amplitude gradients are less severe and will therefore not suffer the same level of variation. In terms of visual appearance, the two maps are very similar.

This provides confidence that the RT can be used for image processing without creating excessive distortion of the original image.

It is fortuitous that sharp boundary edges are not usually found in geophysical data maps. Even if there is an abrupt change in the geological structure, e.g. a fault, dyke or other such feature, the geophysical signature of this change is not so abrupt, particularly when measurements are taken above the ground. The edges in a map are usually gradual. To simulate a geophysical data map more closely, a map of a sloping edge was produced. Figure 5.11 shows the original map together with the map produced by application of the forward and inverse Radon transforms. The amplitudes in the recovered map are not exactly the same as the original amplitudes and exhibit small, localised variations but the two maps are quite similar. Small amplitude differences can be tolerated since the maps are to be used for visual interpretation and comparisons.

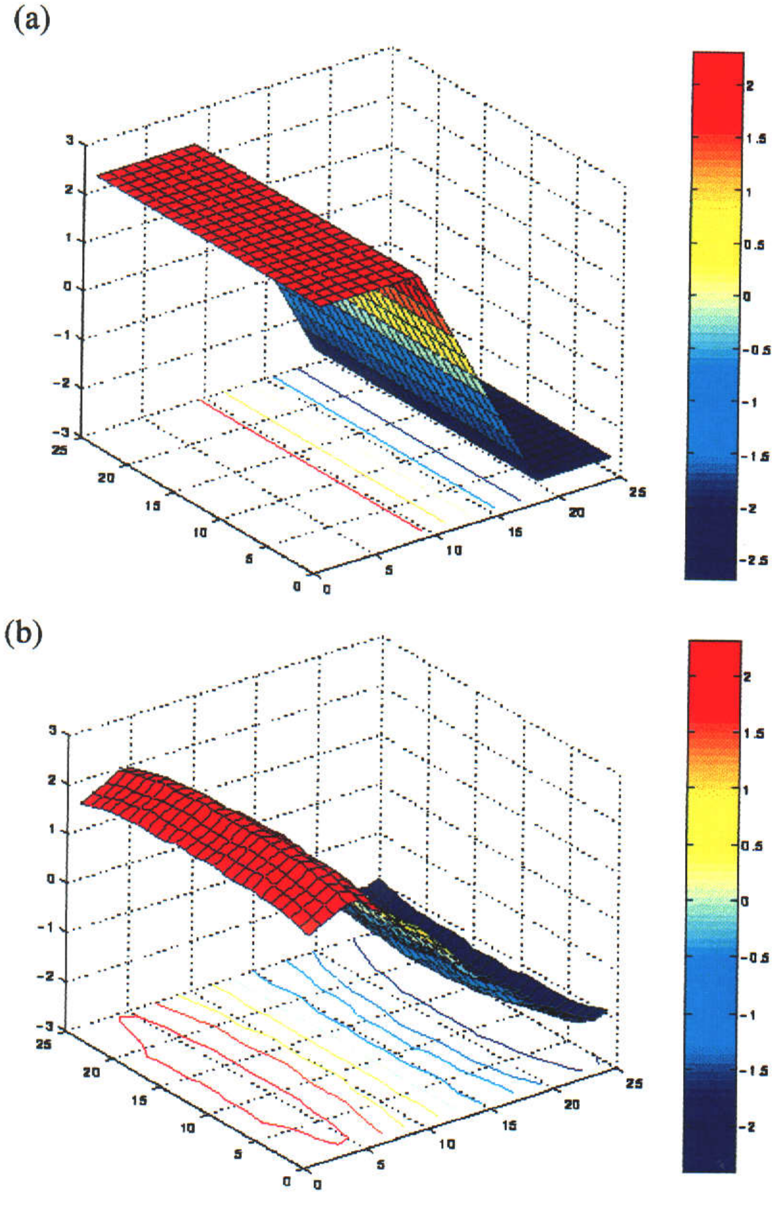

Figure 5.11 The effect of the forward and inverse Radon transformations on a sloping edge. **(a)** A simulated geophysical map of a conductive edge. **(b)** the map produced by application of the forward and inverse Radon transform. A feature of the transform is a broadening of the feature and an inability to recover the exact amplitudes. In this figure the minimum sampling rate suggested by Toft (1996) was used.

5.3.3 Radon domain processing

Having established that the forward and inverse Radon transform algorithms can be applied to synthetic data with good results I now examine the use of filtering in the Radon domain as a means of map enhancement. Yunxuan (1992) successfully applied a slant-stacking algorithm to airborne gravimetric data and developed a gridding algorithm and a continuation algorithm. Pawlowski (1997) applied the Radon transform to magnetic data and showed that direction specific events could be removed from maps by appropriate blanking (muting) of sections of the transform domain. I build on these ideas to develop a processing technique for the removal of flight-line related artefacts as well as the enhancement and removal of specific lineaments in geophysical maps.

5.3.4 Radon filtering for herringbone removal

Application of the Radon transform to the data of Figure 5.3(a) produces the Radon domain map of Figure 5.12. The Radon domain data show a centrally located peak corresponding to the linear feature present, as well as two irregular peaks located at the edges of the domain. These jagged features in the Radon domain are located in the region that corresponds to the flight-line direction. A comparison of the Radon domain data from a map containing herringbones and the Radon domain data from a similar map without herringbones provides the key to the approach. In the Radon domain data, the herringbones show as rapid amplitude variations along portions of lines of constant θ values that correspond to space domain lines parallel to the flight-line direction. These rapid variations, which are restricted to a small section of the Radon domain, are not found in the Radon domain of the herringbone-free data.

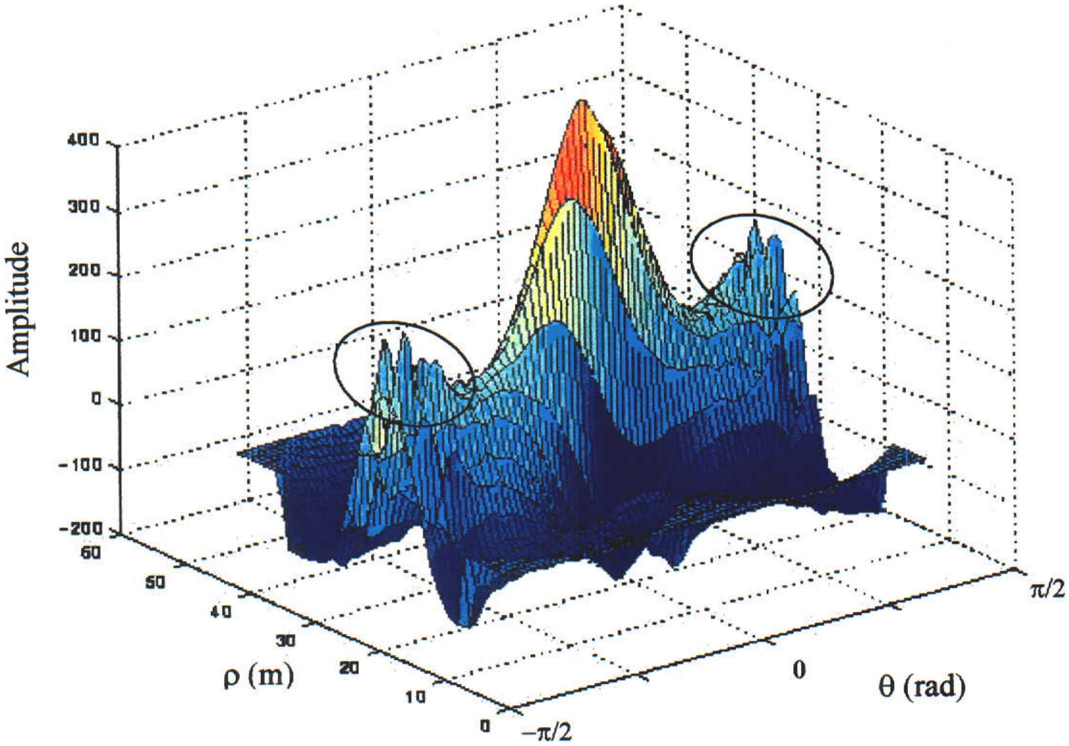

Figure 5.12 Radon transform domain of a herringbone affected map. The Radon transform of the map in Figure 5.3(c) showing a large, regular shaped central peak due to the anomaly and two irregular secondary peaks at $\theta = \pi/2$ and $\theta = -\pi/2$. These jagged features (circled) correspond to the herringbones in the space domain map.

In the case of a space domain map that is free of herringbones, a line of constant θ in the Radon domain displays a smoothly varying amplitude. One might expect that if the rapid variations along the Radon domain lines were removed, the space domain map recovered by the inverse Radon transform would not display the herringbones.

5.3.5 Radon domain smoothing

The most simple way of removing the herringbone related amplitude variations from the Radon domain data is to zero the data points along the lines corresponding to the flight-line direction. This approach was successfully applied to the data in Figure 5.12 to produce the herringbone-free map shown in Figure 5.13(b).

In his work on gravity anomalies, Yunxuan (1992) recommends that the Radon domain data be replaced with average value of the entire Radon domain to reduce processing artefacts.

The effect of replacing the affected lines with the mean value of the Radon domain data is shown in Figure 5.13(c). Although there are differences between the two maps, both methods have been effective in reducing the herringbones. Although effective in this case, the total removal of portions of data is undesirable in principle and may have deleterious effects on the overall map quality. Because of this, alternative methods of Radon domain smoothing were tested. The portion of the Radon domain that requires smoothing cannot be determined accurately without examining each θ line and assessing the degree to which the herringbone effects are noticeable. Naturally, those lines corresponding to the flight line direction are where the effects are most noticeable, but it is not possible to predict with certainty where the effects cease to be significant. Also, examination of the θ lines enables a better choice of filtering method to be employed. In some cases, depending on the data being used, the rapid variations are superimposed on a linear background and can be adequately suppressed by linear interpolation. In other cases they may be superimposed on a more complicated background and cannot be adequately treated by a simple linear interpolation. The issue of interpolation techniques is considered in sections 5.3.5.1 to 5.3.5.3.

5.3.5.1 Method 1. Linear interpolation

In regions of the Radon domain where the rapid variations appear to be superimposed on a straight line it is expedient to simply interpolate between the end points of the perceived line. Such a procedure is valid since the Radon domain data are all real numbers and can be reliably interpolated, unlike the Fourier domain where interpolation of complex numbers is unreliable. Although this method has been successful on synthetic data (Sykes and Das, 1998) it is unlikely that such data will be encountered in a real survey and so it is not presented here.

5.3.5.2 Method 2. Averaging filter

An advantage of working with real numbers in the Radon domain is the ability to find the average value of a set of data. In the complex Fourier domain, averaging of data values is unreliable. A simple 3 point running average filter was applied to the selected Radon domain data in the region where rapid variation were considered to be significant. Filter weights of 0.25, 0.5 and 0.25 were selected and applied to the Radon domain lines of constant θ once only. Repeated averaging may be performed to improve the results.

An alternative method of smoothing data is by the use of polynomial curves to represent short segments of the data sequence. Convolution of the polynomial curves with the data sequence can be achieved using a simple algebraic filter (Savitzky and

Golay, 1964). A commonly used filter is Shepard's five point moving average filter (Davis, 1986) described by the equation

$$\overline{E}_i = \tfrac{1}{35}\left[17E_i + 12(E_{i+1} + E_{i-1}) - 3(E_{i+2} + E_{i-2})\right]. \qquad (5.4)$$

In this method the central point within the filter window is replaced by a value determined from the two adjacent values on either side of the centre. Again, repeated application of the filter may be performed if required.

5.3.5.3 Method 3. Spectral scaling

In this method, a 1-D FFT was applied in turn to each affected Radon domain line of constant θ. The FFT produced a spectrum having high amplitudes at the larger wavenumbers resulting from the rapid amplitude variations along the line. This portion of the spectrum was attenuated using an appropriate scaling factor determined by inspection, prior to the inverse FFT being performed.

A comparison of the different methods of smoothing is made in Figure 5.13. Each method of Radon domain smoothing produces slight differences in the appearance of the new maps. However, in each case the main objective to remove the herringbones and produce a well-defined anomaly has been achieved, confirming the general effectiveness of the Radon domain approach.

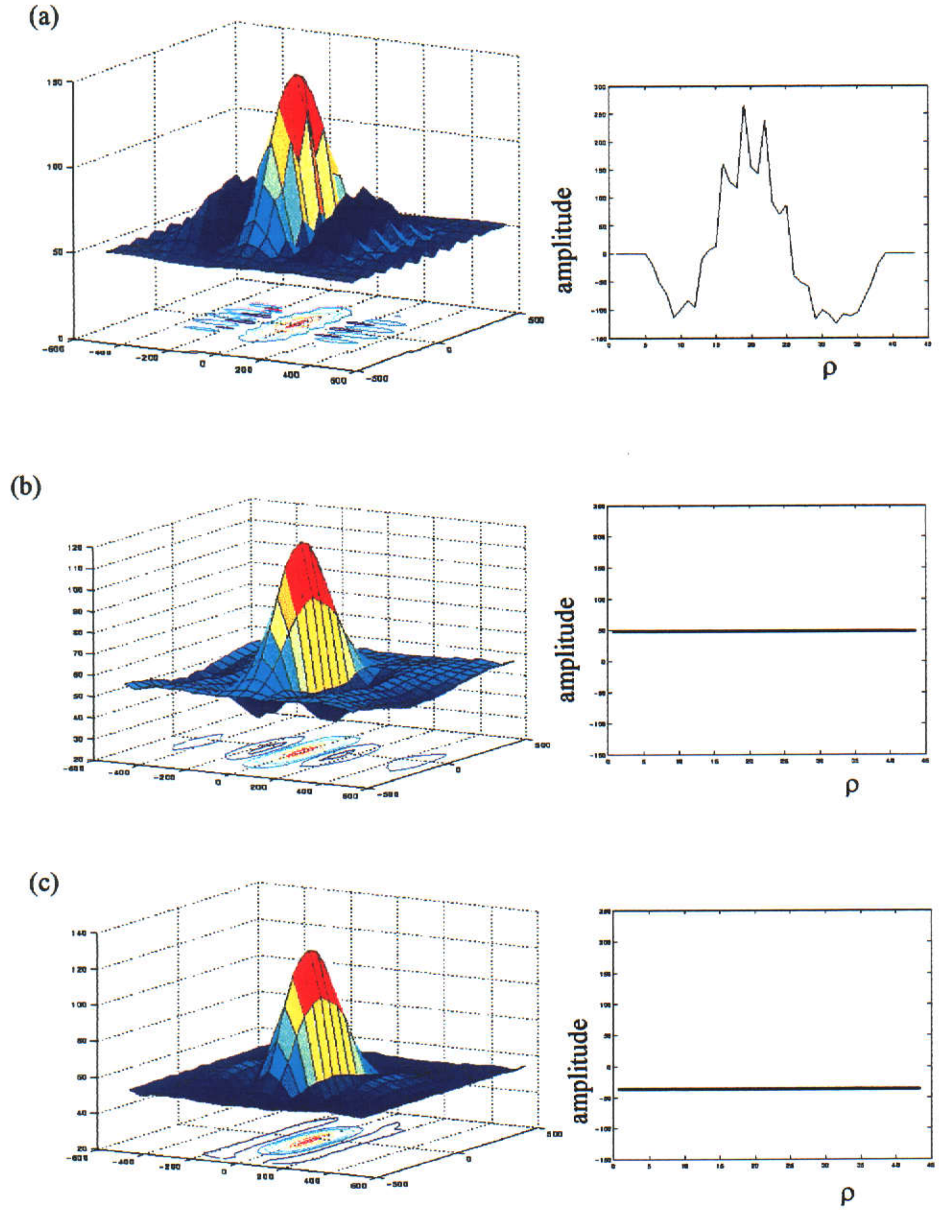

Figure 5.13 Comparison of Radon domain processing methods of herringbone removal. **(a)** Original map containing severe herringbones and a Radon domain spectral line showing the rapid amplitude variations. **(b)** Map produced by zeroing the affected spectral lines. **(c)** Map produced by replacing the lines with the mean value of the transform data.

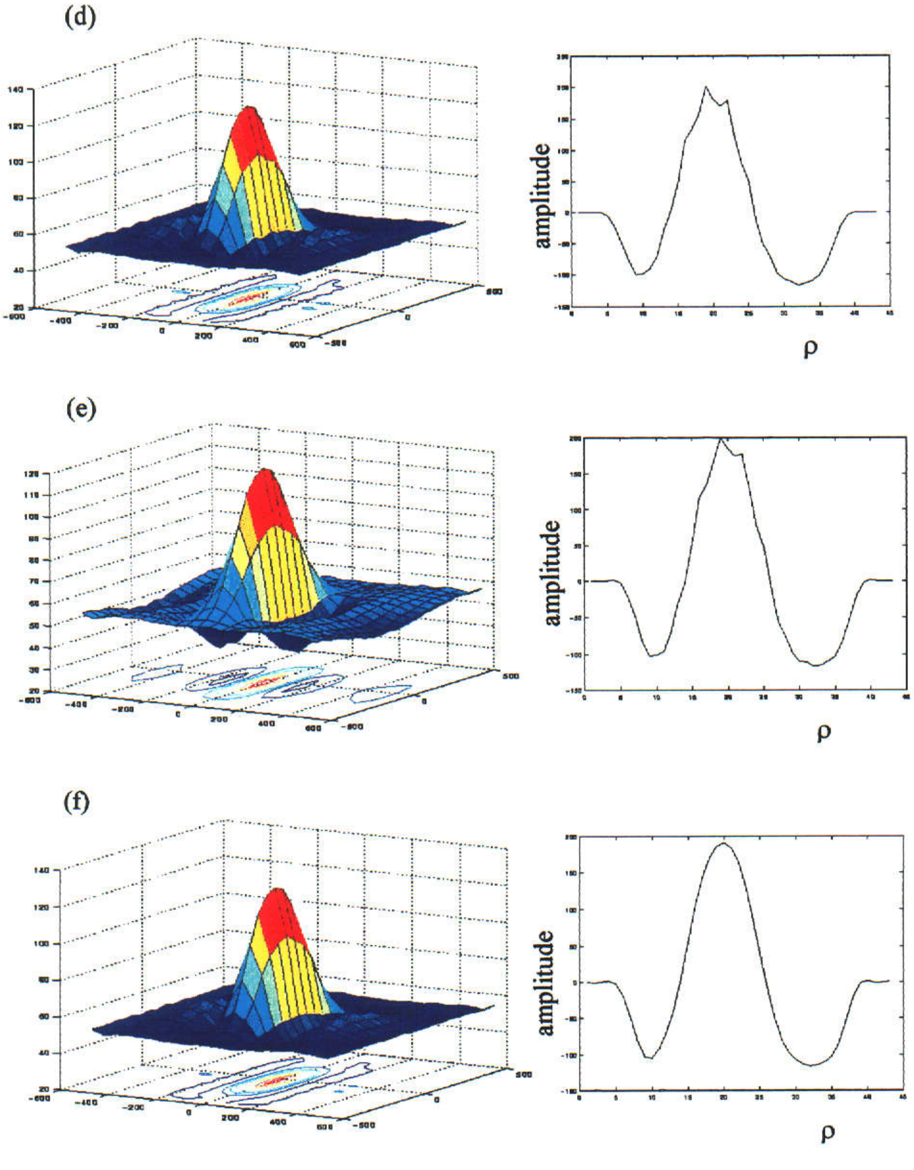

Figure 5.13 *continued* **(d)** spectral line smoothing using a 3 point averaging filter. **(e)** smoothing filter with Shepard's coefficients **(f)** smoothing by high frequency spectral attenuation of the affected Radon domain lines. In all cases the new map has significantly less herringboning than the original.

5.3.6 Radon domain lineament enhancement

The ability of the Radon transform to decompose a 2-D map into 1-D line integrals provides the opportunity to selectively manipulate individual lineaments with minimal effect on the rest of the data. Features in the space domain having a significant strike length appear in the Radon domain as high amplitude peaks. In this section, I investigate the use of the Radon transform to selectively enhance or suppress particular linear features in a geophysical map with the aim of improving the interpretability of the map. Yunxuan (1992) and Pavlowski (1997) have already shown that the Radon transform can be used to remove strike-specific features from a data map by the appropriate blanking of a section of the spectral domain data prior to inversion. I extend this idea by applying transform domain scaling to selectively enhance or attenuate specific linear features displayed in a 2-D geophysical map as well as developing a more general noise reduction procedure.

5.3.6.1 Lineaments in noisy data

Figure 5.14(a) shows a very noisy synthetic map containing a diagonal North-West to South-East linear feature whose amplitude is equal to the maximum noise level. The linear feature is very difficult to resolve in the space domain due to the noisy background. In real situations such a signal to noise ratio is unacceptably small but it is used here to demonstrate the power of the Radon domain approach. Application of the forward RT to this data produces the Radon transform distribution shown in Figure 5.14(b).

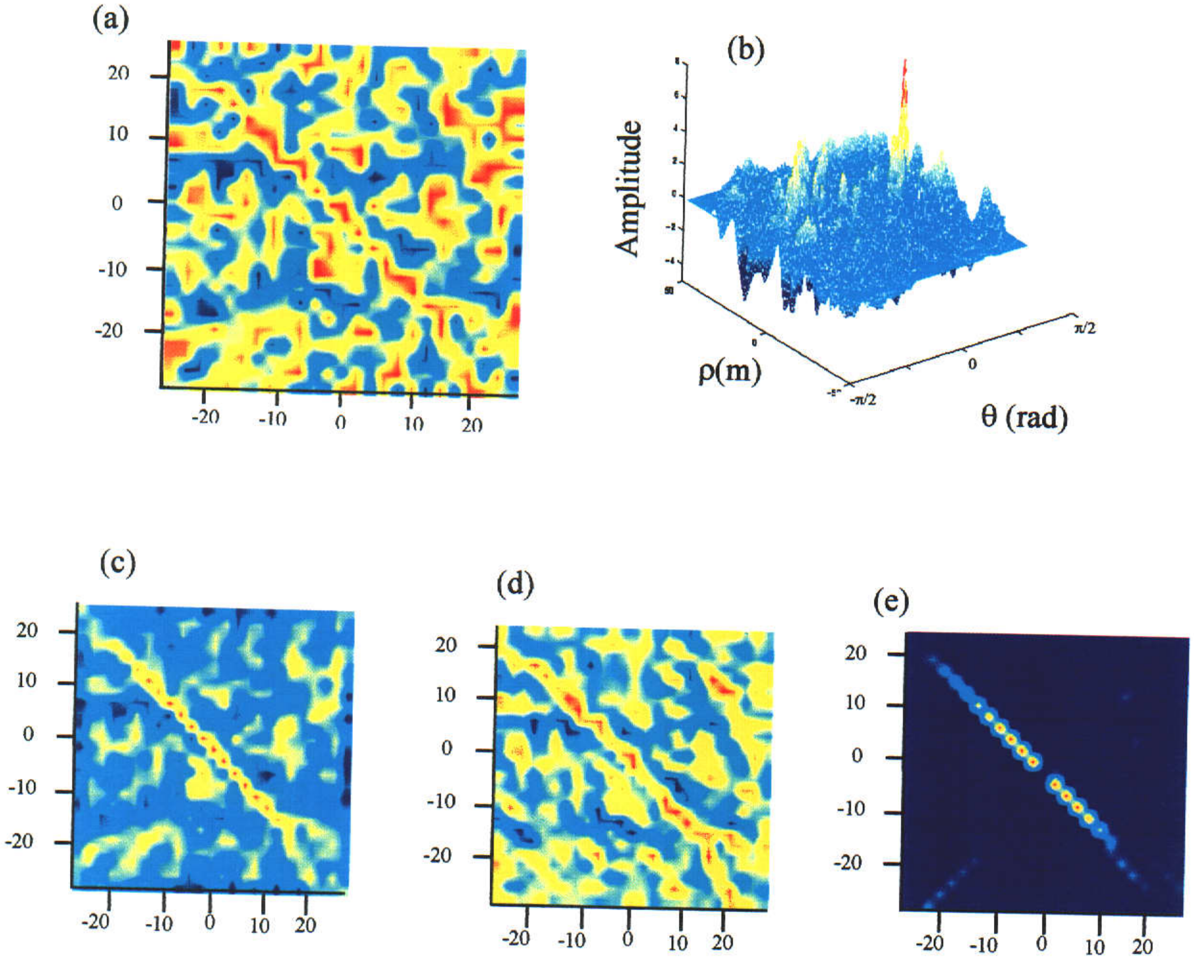

Figure 5.14 Enhancement of a linear feature using the Radon transform technique. **(a)** The lineament is barely visible in a noisy map. **(b)** The Radon transform of the noisy map showing a lineament peak **(c)** map produced by amplifying the peak prior to inverse transformation. **(d)** directional filtering in the Fourier domain to enhance the feature for comparison. **(e)** map produced by attenuating the non-linear features in the Radon domain.

The linear feature is now quite recognisable as a peak in the transform domain. To enhance the appearance of the linear feature in the new map, the Radon transform data was scaled to enhance the peak prior to the inverse transformation to the space domain. This was achieved by selecting a threshold value equal to the approximate background level in the Radon domain. Data points having a value larger than the threshold were amplified. The degree of amplification was varied until a satisfactory result was achieved. To produce the map of Figure 5.14(c), the Radon domain peak was amplified by a factor of two prior to inverse transformation. The linear feature is much more apparent in the new map than it was in the original map.

For comparison, a Fourier directional cosine-pass filter, in the direction of the lineament, was used to produce the image in Figure 5.14(d). In this case the directional filtering has enhanced the lineament. However, the processing filter has also created small linear features in parts of the map where there are no lineaments. The lineament is not as well defined as it is in Figure 5.14(c). Also, directional filtering in the Fourier domain could not be used as effectively if the map contained two features having different strike directions. In such a case, one of the features would be removed from the map altogether. The Radon domain filtering does not suffer from this restriction.

5.3.6.2 Noise reduction technique

The lineament enhancement method described above can be applied in reverse to reduce the influence of unwanted non-linear events. Instead of amplifying the peaks in the Radon domain to enhance the lineament, it is equally valid to attenuate the Radon domain data that do not contribute to a lineament peak. In this way the noisy background signals that do not contribute to a lineament are reduced and the linear features of interest are thereby enhanced relative to the noise. The attenuation parameters need to be determined according to the nature of the data being processed and are best determined by trial and adjustment until a satisfactory result is obtained. In this investigation, the selected data were either replaced with the mean value, zeroed or scaled down by a common factor. This idea was applied to the noisy map of Figure 5.14(a). Attenuation of the Radon domain data was applied to any point having an amplitude less than 25% of the amplitude of the lineament peak. After inverse transformation of the attenuated Radon domain data, the linear feature in the space domain map is more clearly displayed. In Figure 5.14(e), the random noise which had previously obscured the linear feature is greatly reduced and the lineament is now much more apparent. Attenuation of such a large proportion of the Radon domain data has however, resulted in the new map being less coherent than desired. The removal of information (by muting or attenuation) will always affect the quality of the recovered map and a balance must be sought so that the most important information is presented as clearly as possible. Also, a minor North-East trending feature near the lower corner of the map is now visible in Figure 5.14(e). This feature is a result of noisy data points in Figure 5.14(a) being aligned to a sufficient degree that they form a small peak in the Radon domain and avoid being attenuated. With the rest of the noise removed, the 'accidental' lineament has become noticeable.

5.3.7 Lineament filtering

Figure 5.15(a) presents a simple map containing three distinct anomalies that intersect at a common point. Under transformation to the Radon domain, each lineament maps into a separate high amplitude peak in the spectral domain located at a position that is determined by its strike direction and position in the space domain map.

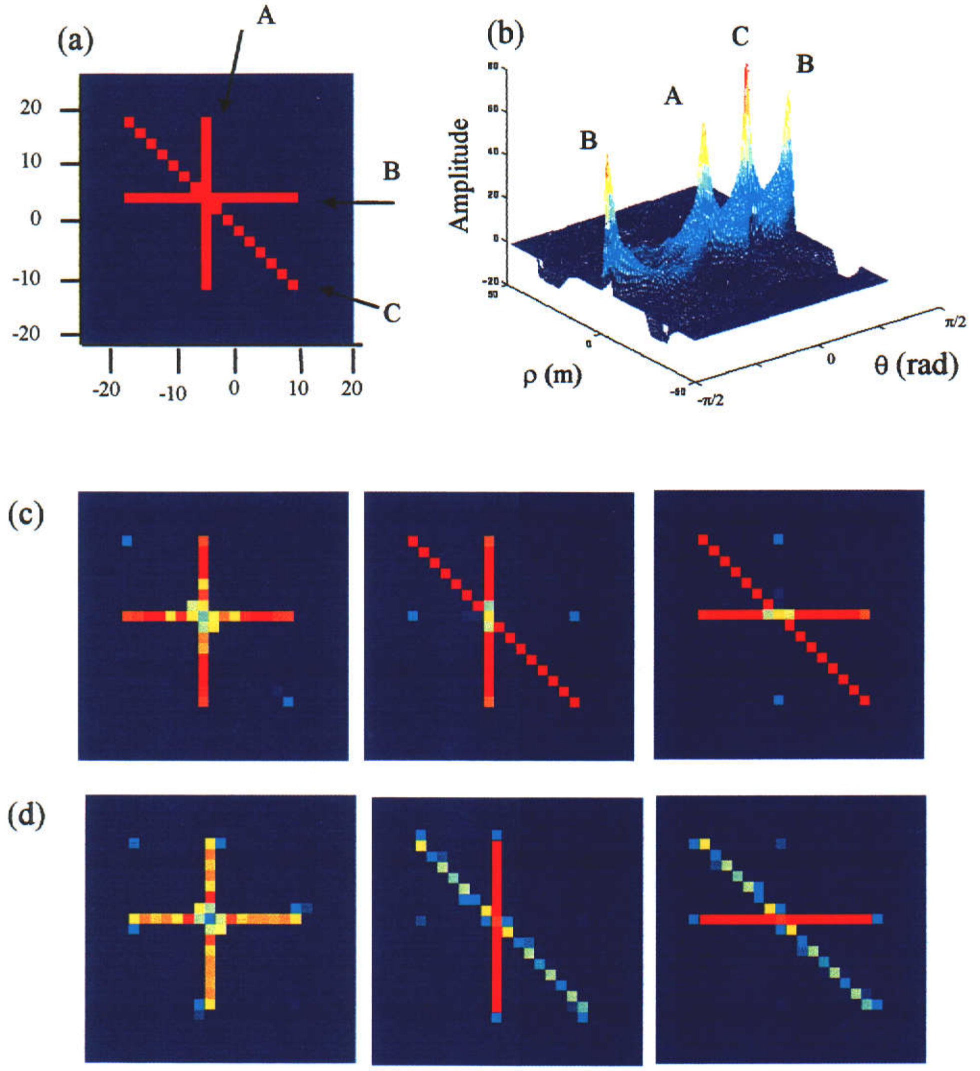

Figure 5.15 Comparison of Radon and Fourier domain directional filtering methods for selective removal of intersecting linear features. **(a)** synthetic map showing intersecting anomalies. **(b)** Radon transform of the map showing each lineament distinct from the others. **(c)** selective removal of linear features by filtering in the Radon domain prior to inverse transformation. **(d)** selective removal of linear features using Fourier domain directional filtering for comparison. Note that the Radon technique removes the feature without affecting the other features. The Fourier filtering has quite a severe effect on the other features.

It should be noted in Figure 5.15(b) that the peaks in the Radon domain are well separated from each other despite the fact that the space domain lineaments intersect. The ability of the Radon transform to separate the lineaments provides the opportunity to process each lineament separately and is the key to its usefulness as a processing tool. Each lineament peak was in turn removed from the Radon domain data by replacing the large amplitudes with the mean value of the transform data. Application of the inverse Radon transform produces a space domain map that has the particular feature removed. In Figure 5.15(c) and 5.15(d) a comparison is made between lineament filtering using the Radon transform method and lineament filtering using the Fourier transform directional filtering method. Both methods are effective at removing the intended feature but the Radon domain method is seen to be more event specific. The intended feature is removed with very little effect on the other features whereas the Fourier method is seen to affect the amplitudes of the other features to a much greater degree.

A further advantage of the Radon transform method is that it can be used to filter specific lineaments of a particular strike direction *without affecting other features which have the same strike direction*. This is impossible to do using Fourier domain techniques. Using the test pattern of Figure 5.10(a) and replacing the Radon domain peaks with the average value of the data prior to inverse transformation, specific lineaments can be removed from the map. This is shown in Figure 5.16. By muting out specific sections of the Radon domain, the linear features can be removed. In 5.16(a) *all* horizontal lineaments have been removed and in 5.16(b) *all* vertical lineaments have been removed. In Figure 5.16(c) *only the left-side* vertical features have been removed while the right-side features remain largely unaffected.

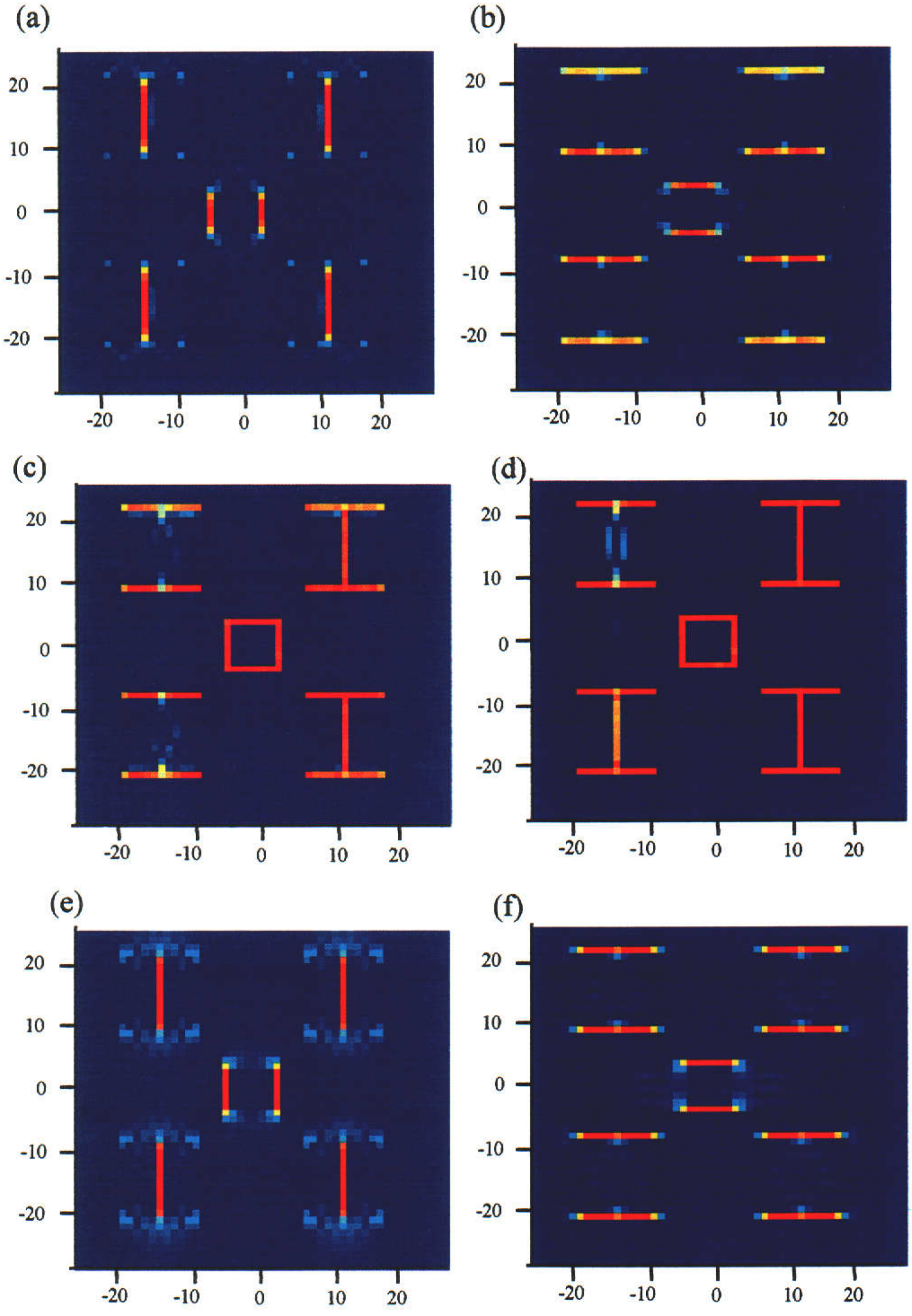

Figure 5.16 Removal of linear features by transform domain filtering. **(a)** horizontal features removed by Radon domain filtering. **(b)** vertical features removed by Radon domain filtering **(c)** *left-side* vertical features removed by Radon domain filtering **(d)** *individual* vertical feature removed by Radon domain filtering **(e)** horizontal features removed by Fourier domain directional filtering **(f)** vertical features removed by Fourier domain directional filtering.

In Figure 5.16(d) the filtering in the Radon domain has been restricted so that *only the upper lineament* on the left-side has been removed. The filtering in this case is not complete but demonstrates the ability of the method to process specific features without adversely affecting the entire map. As before, the corresponding Fourier domain processing is shown for comparison. In Figure 5.16(e) a horizontal directional filter has been used and in Figure 5.16(f) a vertical directional filter was used. Both filters used a cosine taper to restrict the production of artefacts but as can be seen in the figure, the Fourier domain filtering has resulted in the generation of a significant amount of 'ringing'. Also, the Fourier directional filters are non-discriminatory and cannot be used to remove specific features. *All* lineaments having the selected strike direction are removed by the Fourier domain filters.

5.4 Concluding remarks

It is evident from this investigation that the presence of flight-line related artefacts in airborne geophysical maps may be concentrated in a particular region of the Radon domain. The removal of flight-line related and other artefacts can be achieved by processing only a very small portion of the total Radon domain data, thereby minimising the effect on the data as a whole. The quality of the maps produced using the Radon transform method to remove herringbones appears to be relatively independent of the smoothing technique used in the Radon domain. The method to be used in any particular instance is a matter of personal choice and convenience, provided the rapid amplitude variation along the θ lines can be adequately removed. In addition to this, the Radon transform has been shown to be useful for the enhancement of linear features in noisy maps as well as being a versatile tool for the removal of individual lineaments. In the examples shown in this chapter, the Radon domain processing has been more useful and produced less processing artefacts than the Fourier domain directional filtering method.

CHAPTER 6

APPLICATION TO FIELD DATA

The previous chapters have presented the theoretical basis and numerical models that demonstrate the usefulness of the new processing techniques developed in this thesis. Any new technology must be seen to be effective in a real setting if it is to be accepted by the exploration industry. The type of data acquisition required for the application of the EM residual concept is not commonly performed in practice. Due to the scarcity of readily accessible, appropriate data the results of three specially conducted experimental field trials that were performed in 1998 and 1999 are presented. The Radon transform processing methods presented in Chapter 5 are very general and can be applied to any two-dimensional map. Later in this chapter, AEM and radiometric maps are used to demonstrate their application.

6.1 Frequency domain Small Loop Residual

A frequency domain survey was performed along a profile line over a region exhibiting a North-West trending magnetic anomaly shown in Figure 6.1(a). The line is part of a survey of the Rutabygget area in Sweden conducted by North Exploration Limited. A Max-Min II system utilising a Tx-Rx separation of 100 m was used and data were recorded for the VCA, VCP and HCP configurations at 25 m intervals using ten frequencies ranging from 110 Hz to 14080 Hz. The ground surface was not level so the measured data were corrected for loop alignment variations using the method described in Appendix C, before being used to compute the SLR.

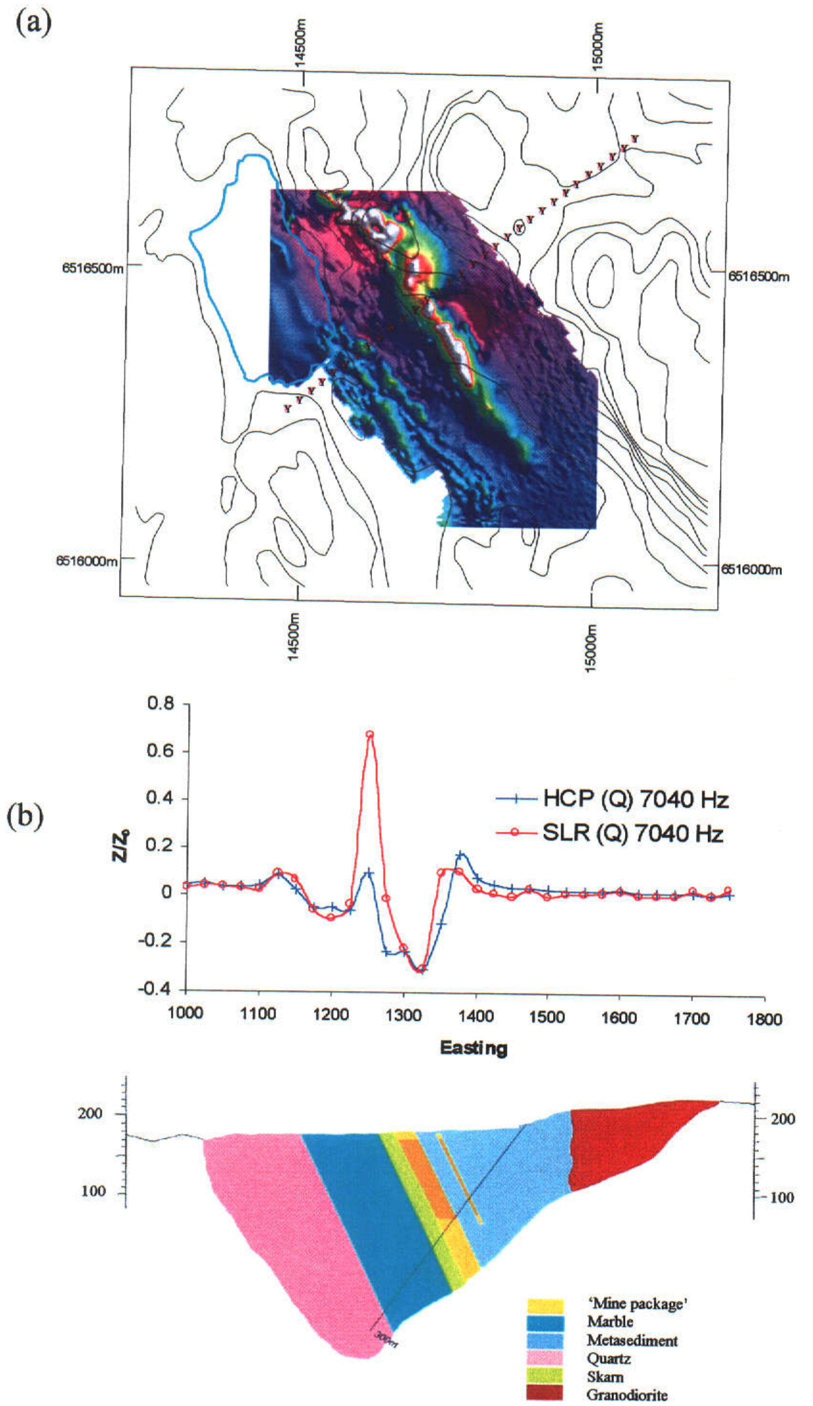

Figure 6.1 Frequency domain SLR field test. **(a)** Total magnetic intensity map showing a north-west trending magnetic high. The Max-Min survey line is indicated by the dots. **(b)** simple geologic section of the survey area upon which is imposed the HCP and SLR quadrature profiles for 7040 Hz. The SLR provides a greatly enhanced signature of the conductive units.

Very little geological information is available for the survey area other than the simple geological cross-section shown in Figure 6.1(b). As can be seen from this cross-section, the subsurface contains igneous, crystalline rocks that typically have resistivities of the order of 10^4 Ω.m. In such a resistive environment the host response will be very small and even a moderate conductor will provide a readily detected EM target. Imposed above the section are the HCP and SLR quadrature profiles at 7040 Hz which both show a signature of the conductive zone. The SLR response provides a much larger signal than the HCP.

6.1.1 In-phase response

Figure 6.2 presents a comparison of the in-phase responses measured using the three loop configurations and the SLR at all eight frequencies along the profile line shown in Figure 6.1(a). All profiles have been plotted at the same scale to provide a more accurate comparison. With the exception of the HCP configuration, the in-phase responses do not provide a very good indication of the presence of a conductor other than at the maximum frequency. The VCA and VCP in-phase responses contain a number of small bumps that may be a signal from a conductive target but are not clearly distinguishable from the topographical variation along the profile. The HCP in-phase data set also contains a number of small bumps but provides a clear indication of a conductor near station 1300 E for the frequencies above 880 Hz. The SLR profile contains larger variations than displayed by the individual configurations but does not provide a signature of a conductor except at the two highest frequencies. The amplitude variations along the SLR profile are noticeably larger than those displayed in the VCA, VCP and HCP profiles and are consistent across the different frequencies.

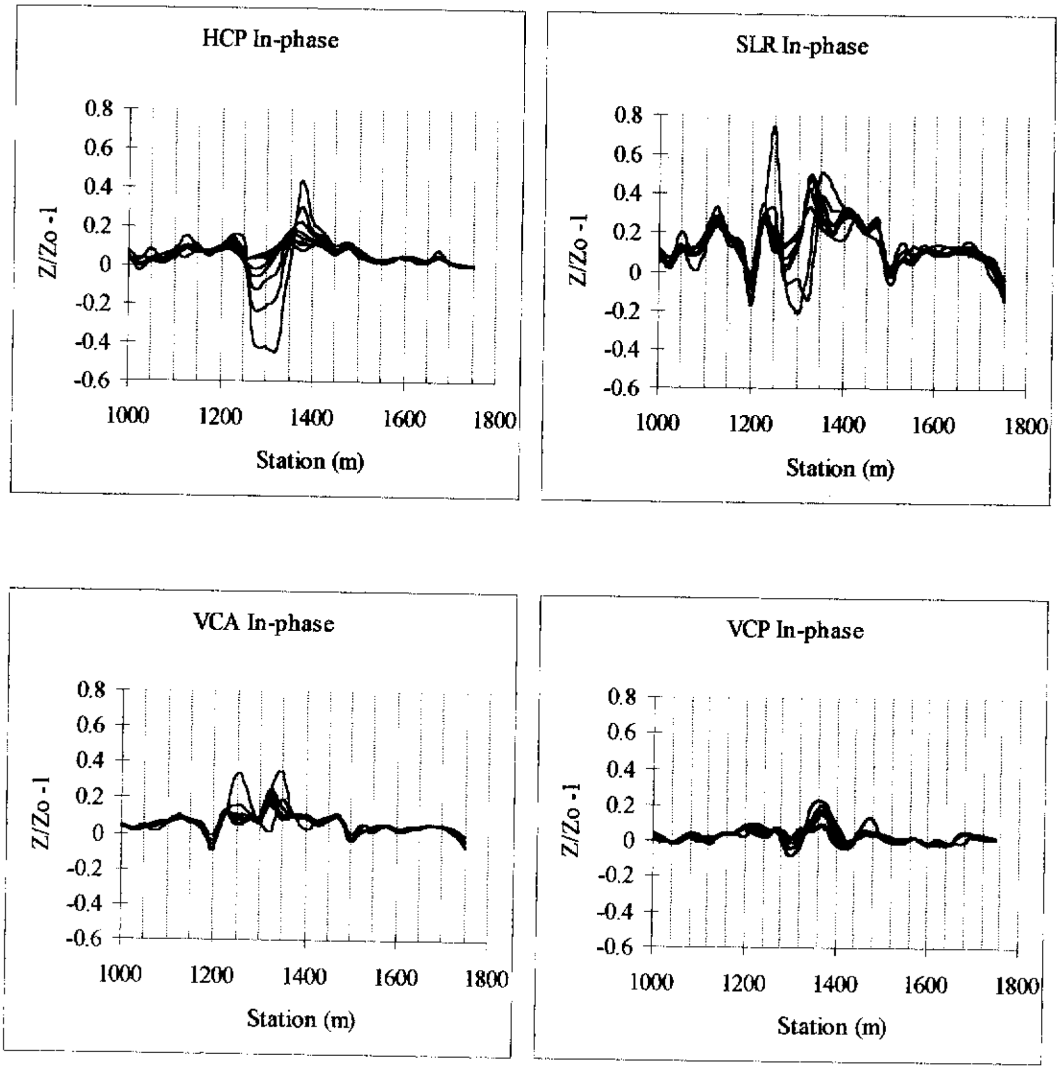

Figure 6.2 Profile responses for the in-phase measurement using HCP, VCP and VCA configurations and the SLR derived from them. The HCP provides a very good indication of the target at frequencies above 880 Hz. The VCA and VCP do not provide a good indication of the target. The SLR appears to be more sensitive to topography than the target except at the higher frequencies.

This suggests that the in-phase SLR may be more sensitive to surface topography and loop mis-alignment than the sub-surface conductivity, but without the benefit of other information it is difficult to determine the exact cause of the variations. It is only at the higher frequencies (7040 Hz and 14080 Hz) that a definite signature of a conductor can be seen in the SLR near station 1300 E. In this survey, the in-phase SLR does not appear to have been particularly advantageous in providing more information about the target despite significantly increasing the amplitude of the signature.

6.1.2 Quadrature responses

Figure 6.3 presents the quadrature profile response for the same survey together with the SLR derived from them. Again, the plots are all on the same scale for a better comparison. The quadrature responses from all three configurations provide a clear indication of a conductive zone near station 1300 E. The VCP response is very small and consists of a trough centred on 1300 E. The asymmetry of the peaks is consistent at different frequencies and indicates that the conductor may be displaced from the profile line or plunging to one side. The VCA profiles consist of two peaks of different amplitude separated by a trough at station 1300 E. Although not evident in Figure 6.3, the asymmetry of the VCA peaks varies with frequency and shows a progressive change in the relative amplitudes of the peaks to the extent that the asymmetry is reversed at lower frequencies. The variation of the relative amplitudes of the peaks indicates that there may be two bodies of different conductivities that dominate the response at different frequencies. One located at 1250 E and the other at 1350 E.

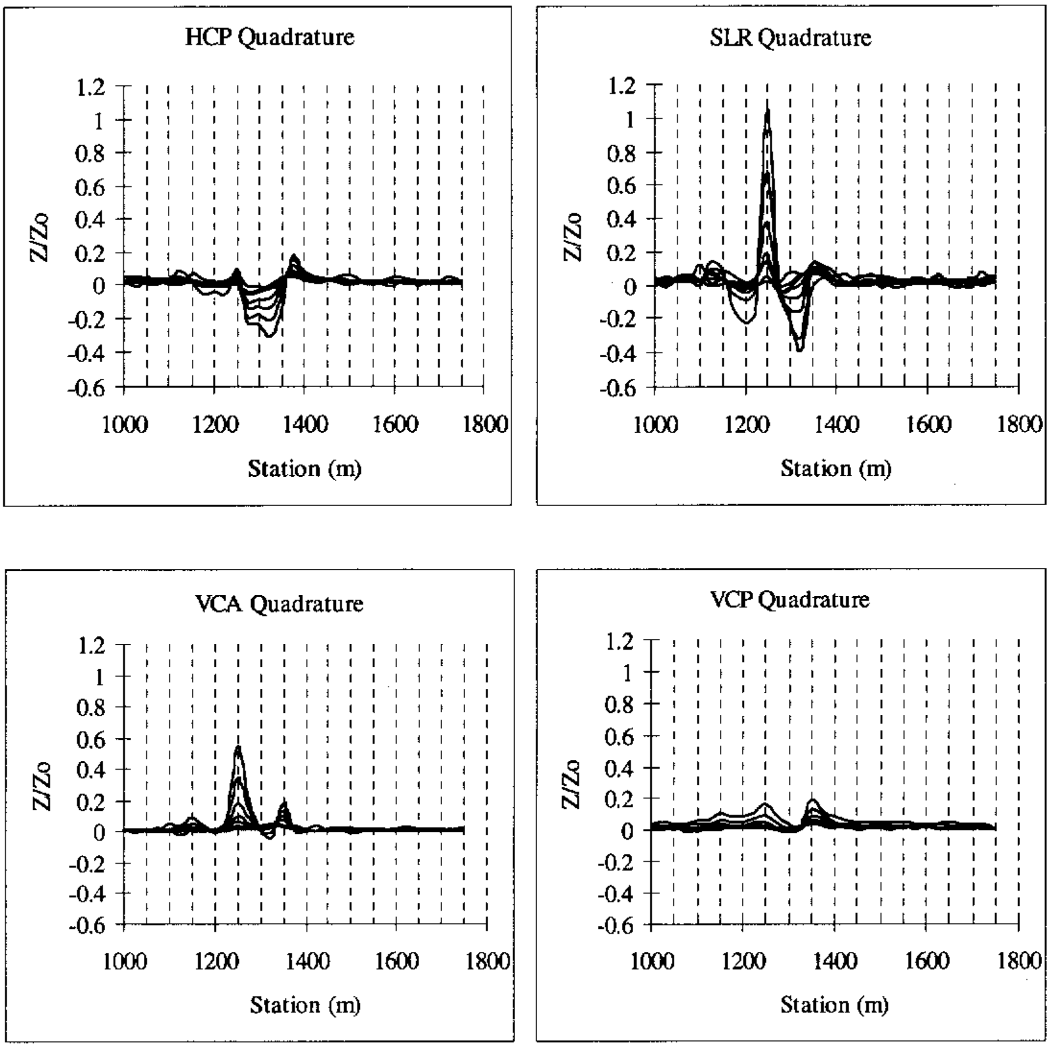

Figure 6.3 Profile responses for the quadrature measurement using HCP, VCP and VCA configurations and the SLR derived from them. The HCP provides a good indication of the target but the signal is greatly enhanced by the SLR combination. The VCA and VCP also show a small signal caused by the target.

The HCP quadrature response shown in Figure 6.3 provides a very clear signal of a conductive target that can be modelled as a dipping plate. The modelling shown in Figure 6.4 (courtesy of North Exploration Ltd.) was performed using software designed specifically for MaxMin data and shows both the in-phase and quadrature responses for the field data and model data. Although the simple plate model matches the quadrature field data at the lower frequencies quite well, there is a definite mis-match at the higher frequencies, indicating that the geology is more complicated than the model suggests. It is possible that there is a second conductive zone near 1200 E.

The scale used in Figure 6.3 makes small changes difficult to resolve, but at the lower frequencies (220 Hz - 880 Hz) the HCP field data exhibits a small trough centred on 1275 E and indicates a dip to the East. As the frequency increases the trough develops a second lobe at 1325 E which could indicate the presence a second conductor or be an indication of the other edge of the same conductor. At the two highest frequencies (7040 Hz and 14080 Hz) the HCP quadrature response has a vastly different character. At these frequencies the profiles contain two deep troughs at 1200 E and 1300 E separated by a small peak at 1250 E. The changing nature of the responses makes accurate interpretation more difficult.

The quadrature SLR shown in Figure 6.3 consists of a very sharp peak at 1250 E with small, broad trough at 1200 E and a larger, sharper trough near 1320 E. The quadrature SLR profile provides a greatly amplified signature of a conductive target in comparison to the individual configurations. Insufficient drilling has been carried out on this line to define the geology more closely.

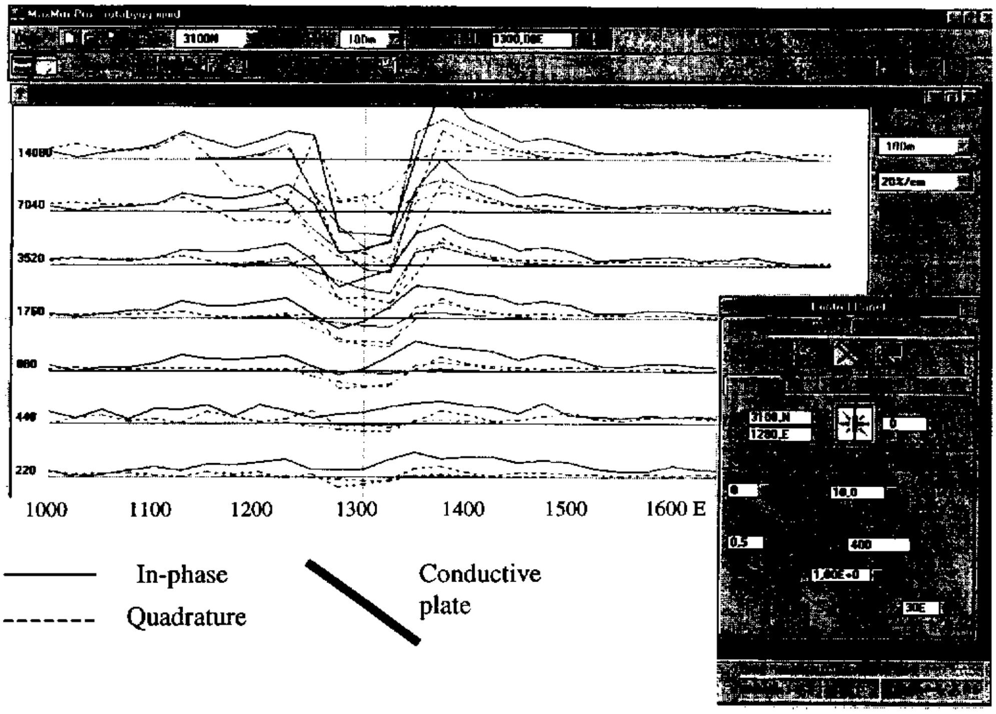

Figure 6.4 Interpretation of the MaxMin HCP data using a dipping plate model. The high frequency quadrature responses measured in the field indicate a more complicated situation than a single plate-like conductor. (supplied by North Exploration Ltd.)

Without extra geological information it is difficult to correctly reconcile the features displayed in the residual but it is obvious that the SLR combination has produced a significant enhancement of the signal.

As mentioned previously, the very resistive environment in which the survey was performed provides a relatively 'easy' exploration setting. The resistive Earth materials do not contribute very much to the measurements and, therefore, little is to be gained by reducing that portion using the SLR concept. The conventional survey configuration (HCP) is sufficient to identify the conductive zone even though the high frequency profiles are a little inconsistent. Despite not having such a large effect on reducing the Earth response, the quadrature part of the SLR has been very effective in producing an enhanced signature of the conductive zone.

6.2 Time domain large loop residual

6.2.1 Fixed loop survey

A fixed loop survey was performed near Kalgoorlie, Western Australia as follow-up to a commercial in-loop survey that had recorded a late time anomaly. The late-time anomaly was centred on 9950 E and believed to be due to the black shales at a depth of about 50 m. The survey area is in close proximity to an existing gold mine and is centred on a substantial magnetic anomaly. Drill-hole data from the vicinity were used to construct the simple geological section shown in Figure 6.5. It should be noted that the drill hole information does not extend along the entire length of the test survey line. The overburden is very conductive and non-uniform and represents a very difficult exploration setting. The parameters for the fixed-loop test survey are listed in Table 6.1.

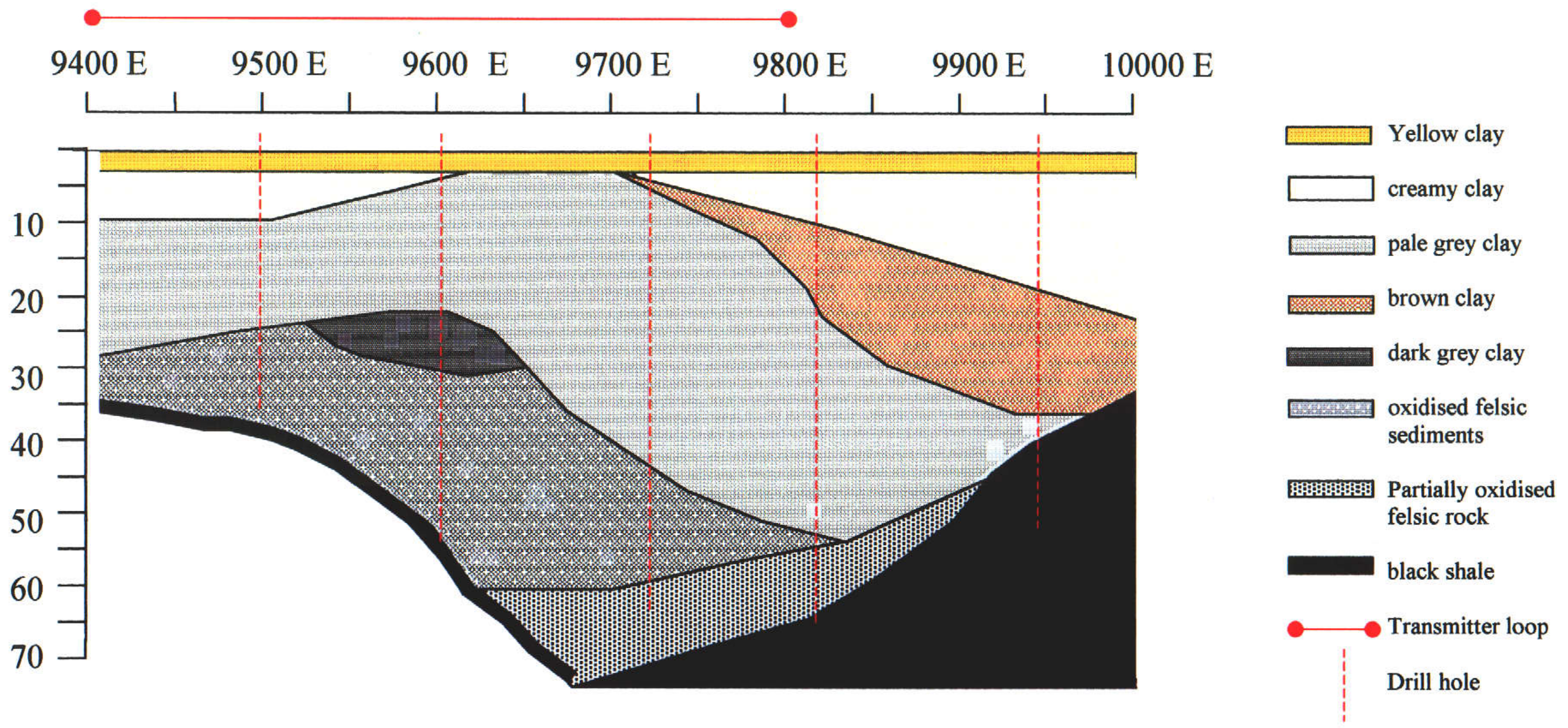

Figure 6.5 Geological cross-section of the fixed-loop survey area constructed from drill-hole logs. The anomaly noticed at 9950 E may be due to the black shale. The large anomaly near 10200 E is beyond the limit of the drill hole information.

Location	Kalgoorlie, W. Australia
Loop size	400 m x 400 m
Loop centre	5050 N 9600 E (local grid)
Transmitter	Zonge GGT-30
Current	15 A
Waveform	Bipolar step turn-off
Ramp time	0.128 ms
Base frequency	0.5 Hz
No. of cycles	128
Data logger	Zonge GDP-16
No. channels	31
Measurement range	0.47 – 388 ms
Electric field sensor	Porous pots
Magnetic field sensor	Air-core coil (10^4 m^2)

Table 6.1 Survey parameters for the fixed-loop survey at Kalgoorlie, WA.

6.2.1.1 Profiles

Figure 6.6 shows the dB_z/dt profiles in groupings of 10 ms duration. The early channels (< 10 ms) are dominated by the transmitter wire (at 9800 E) and the characteristic cross-over is observed to move away from the loop as the 'smoke-ring' diffuses into the Earth. In the 10 - 20 ms channels the cross-overs appear to remain almost stationary near 9920 E indicating that the currents are concentrated at that location. This is indicative of a conductive body and approximately corresponds to the location of the late-time anomaly noted in the previous in-loop survey. At times later than 20 ms the crossover appears to move out again and the dB_z/dt response becomes very small. At these times the profile does not contain much useful information.

The electric field measurements are shown in Figure 6.7. At early times (< 10 ms), the electric field measurements are also dominated by the large amplitudes near the transmitter wire. Of particular interest in the electric field measurements is the early-time migration of the cross-over. On a uniform Earth, the electric field would cross-over at the centre of the transmitter loop. It is seen in the profiles that the change of sign occurs away from the centre of the transmitter and moves about 100 m to the East in the first 2 ms. The sign change then remains at that location (9700 E) for the remainder of the measurement time. The migration of the current centre is probably an indication of the deepening of the overburden to the East of the transmitter. The deeper overburden offers less resistance to the flow of charge, resulting in the circulation of induced current around the deepest point. The most striking feature of electric field measurements in the 10 - 20 ms range is the elevated amplitudes near station 10200 E.

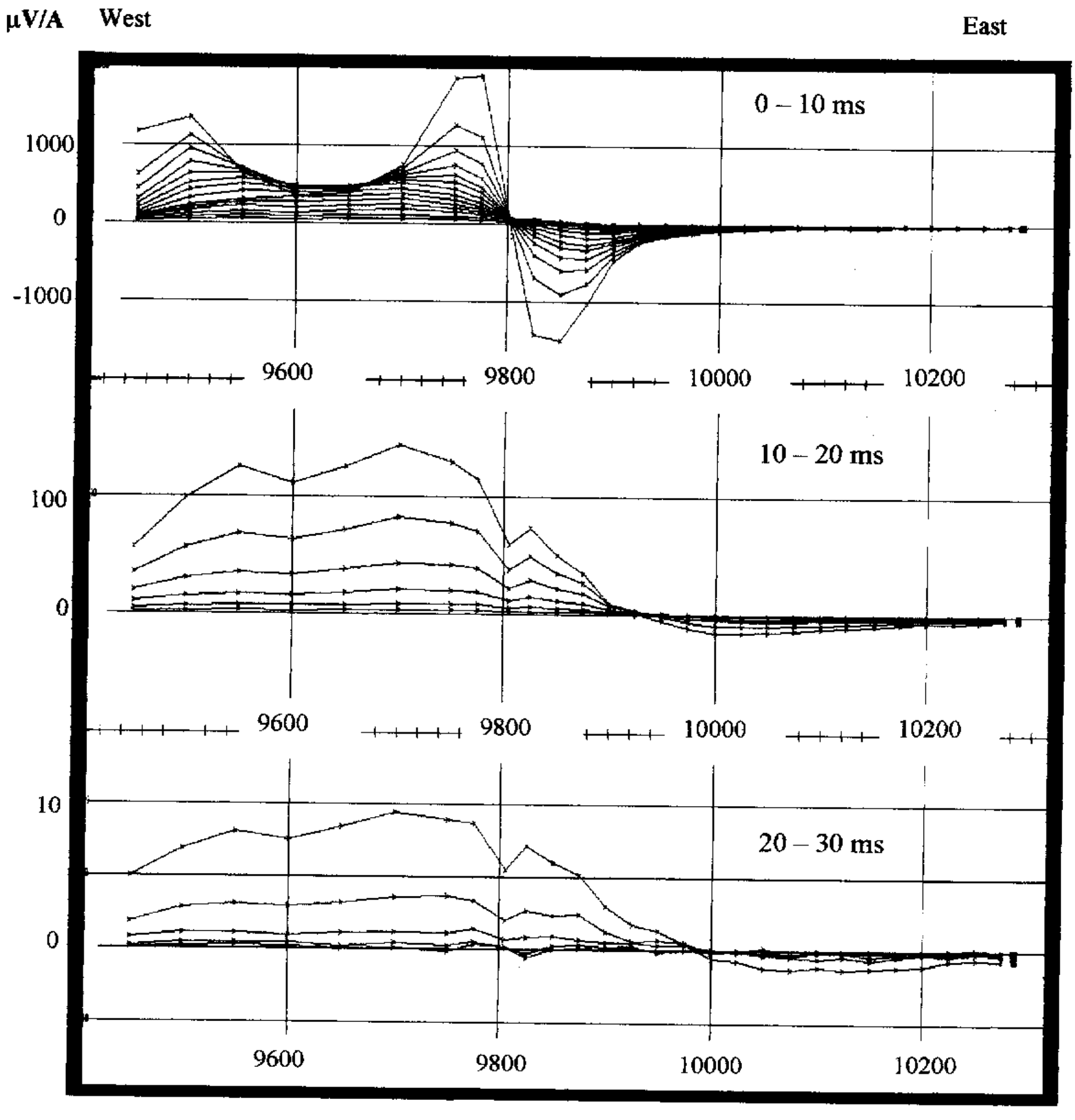

Station (Easting)

Figure 6.6 Fixed-loop dB_z/dt profiles for the Kalgoorlie test survey. The cross-over at 9920 E in the 10 - 20 ms range may indicate the presence of a conductive zone.

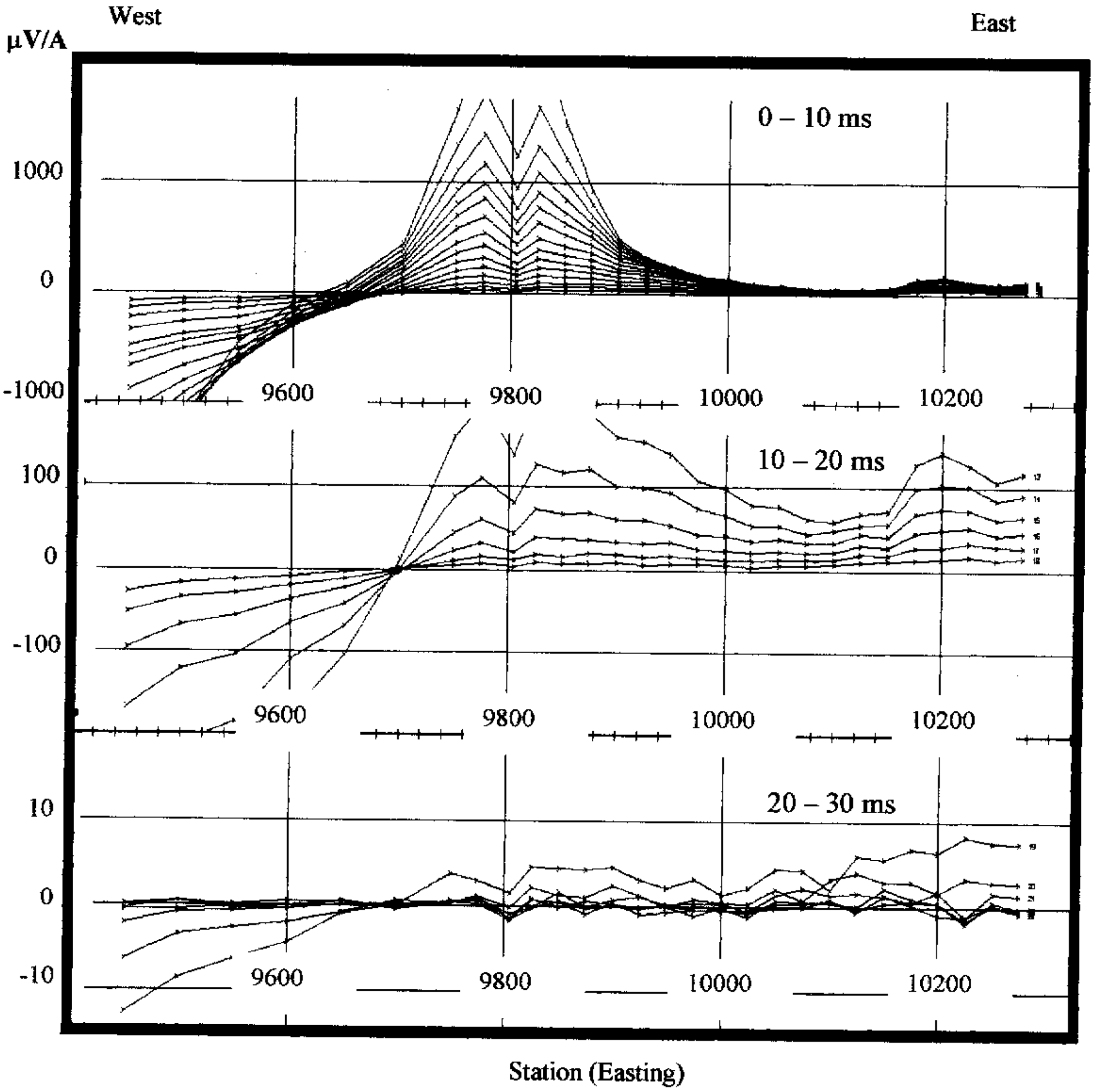

Figure 6.7 Fixed loop E_ϕ profiles for Kalgoorlie test survey. The profiles exhibit an early time migration of the central loop cross-over from 9600 E to 9700 E which may be indicative of a deepening overburden layer. The elevated amplitudes near 10200 E may be due to the channelling of current to the surface by the uplifting basement. There is no indication of a conductive zone near 9920 E.

These elevated amplitudes are also present in the earlier time channels but are less apparent due to the relative magnitude of the response near the transmitter wire.

It is unlikely that these large responses are due to the presence of a conductor because the dB_z/dt measurements do not show a similar anomaly. The elevated electric field amplitudes suggest an increased current density near 10200 E caused (possibly) by the rapid shallowing of the overburden. The currents would be 'channelled' closer to the surface by the non-conductive basement rock. At times greater than 20 ms the profiles do not contain any useful features other than the cross over at 9700 E. There are no obvious features in the profiles to suggest a conductive unit near 9920 E.

The LLR was computed using the dB_z/dt and E_ϕ measurements. A cubic polynomial fit was applied to the E_ϕ data to compute $dE_\phi/d\rho$ after an abrupt change in the electric field near the transmitter wire was smoothed out by interpolation. The profiles are shown in Figure 6.8. Most striking in the LLR profiles is the absence of the characteristic response associated with the transmitter loop. In the measured data the loop dominates the response in early times and is still evident as late as 20 ms. The LLR profiles are centred on the zero line which indicates that the layered Earth response has been greatly reduced by the LLR transformation and only anomalous signals are displayed. In the LLR early-time profiles ($<$ 10 ms) two features are apparent. The trough-peak feature centred on 9680 E and the peak-trough feature centred on 10200 E. These two features are probably indicative of the deepening of the overburden at 9700 E and a shallowing of the overburden at 10200 E. Without the benefit of additional drill holes near 10200 E it is uncertain whether such an interpretation is correct.

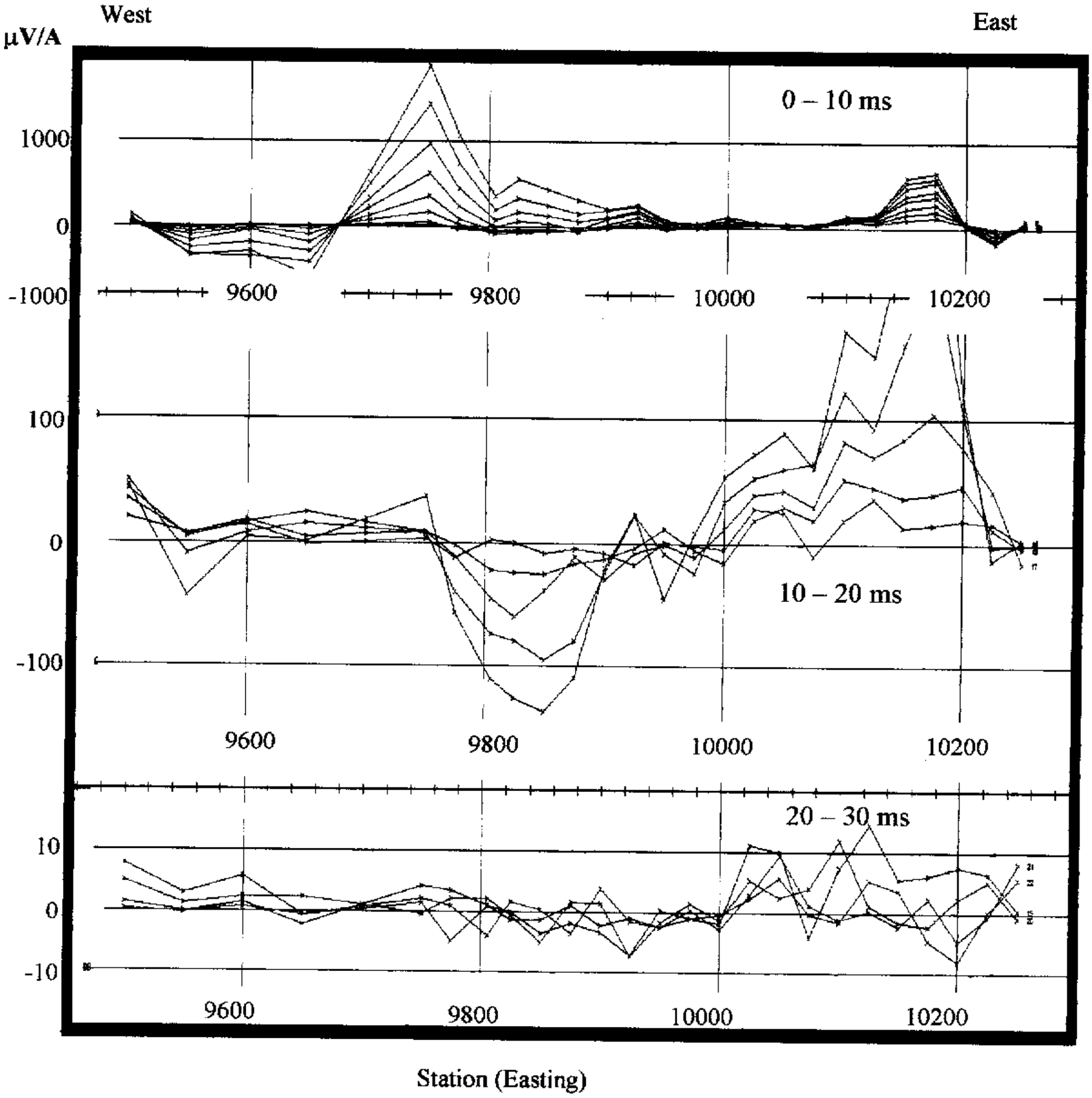

Figure 6.8 Fixed loop LLR profiles for the Kalgoorlie test survey. The LLR is centred on the zero line and shows two distinct anomalies at 9680 E and 10200 E, as well as a possible anomaly near 9950 E. The mid time channels contain a large trough-peak anomaly centred on 9920 E. The late time channels do not contain useful information. The LLR profiles contain more information than the dB_z/dt and E_ϕ profiles.

The mid-time channels (10 - 20 ms) show a peak-trough feature centred near 9950 E and coincides with the location of the anomaly noted in the previous survey. The signature is affected by the anomalous response at 10200 E and is quite erratic. The feature at 9680 E is not apparent in these profiles which indicates that it is probably an overburden effect. The anomaly at 10200 E is still apparent in these profiles indicating that either a very conductive zone is causing the currents to persist for a long period of time, or the residual current from the conductive target is being channelled toward the surface by the basement rock. The late time (> 20 ms) profiles are much more erratic than the dB_z/dt and E_ϕ profiles and do not provide any useful information.

6.2.1.2 Decay curves

The time domain measurements provide an extra dimension to the interpretation by enabling a measure of the decay of the transient fields. The nature of the decay provides information about the conductivity of the Earth rocks. A power-law decay is indicative of a layered Earth environment whereas an exponential decay is indicative of a confined conductor. The decay of the dB_z/dt, E_ϕ and LLR amplitudes for selected stations are shown in Figure 6.9 on log-log scales. The decay curves are very similar for all of the stations and are characteristic of a uniform host rock with a power-law type decay. At station 9950 E the dB_z/dt decay shows a sign reversal followed by an exponential decay with a late-time decay constant of 9 ms [Figure 6.9(a)]. The electric field decay curves [Figure 6.9(b)] are very similar for all stations and do not provide any indication of the conductor at 9950 E.

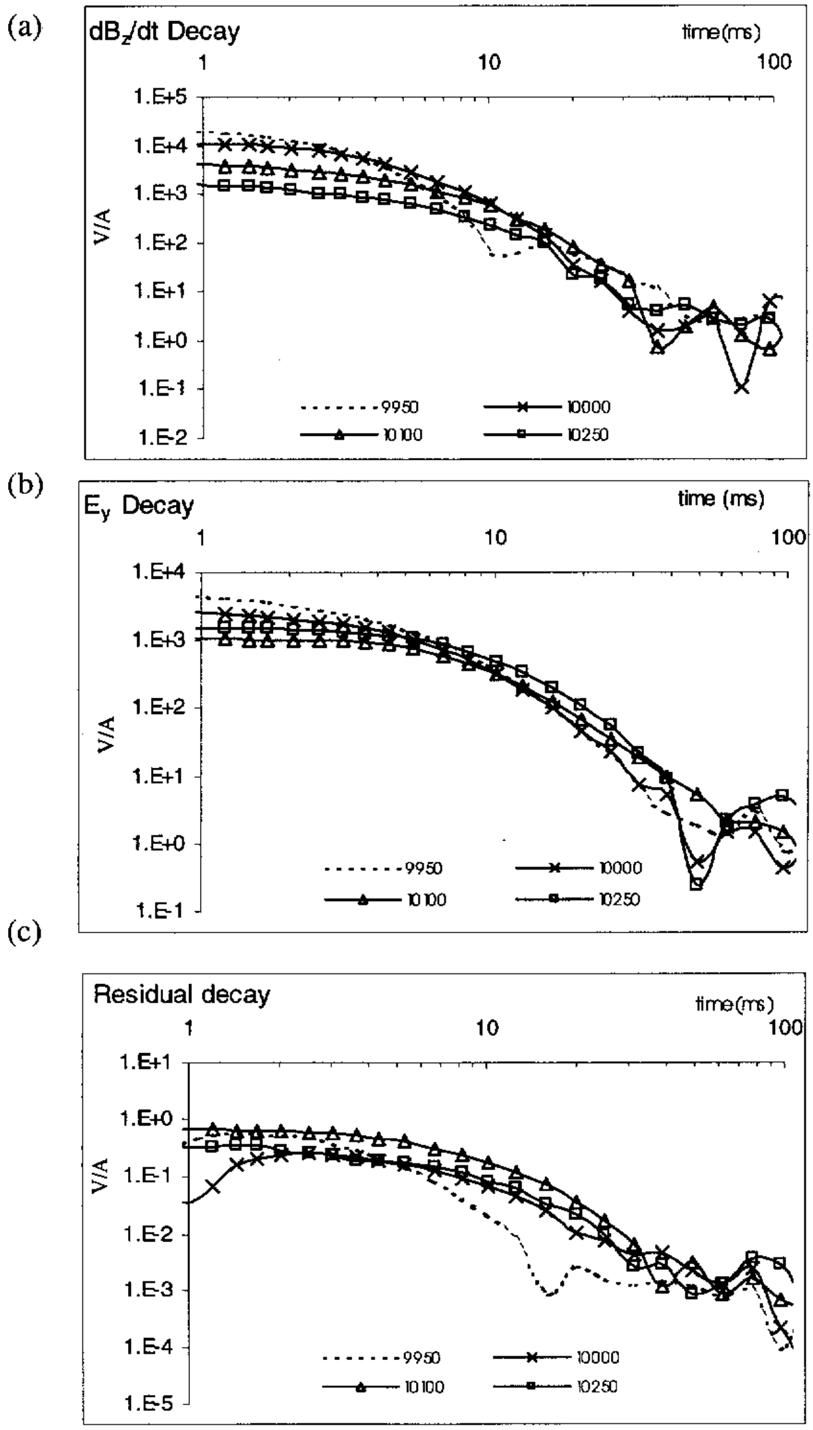

Figure 6.9 Fixed loop decay curves for selected stations plotted on a logarithmic time scale. **(a)** dB_z/dt decay showing an anomalous decay at 9950 E. **(b)** E_ϕ decay showing no anomalous decays **(c)** LLR showing a greatly enhanced anomalous decay at 9950 E indicating the presence of a conductive zone.

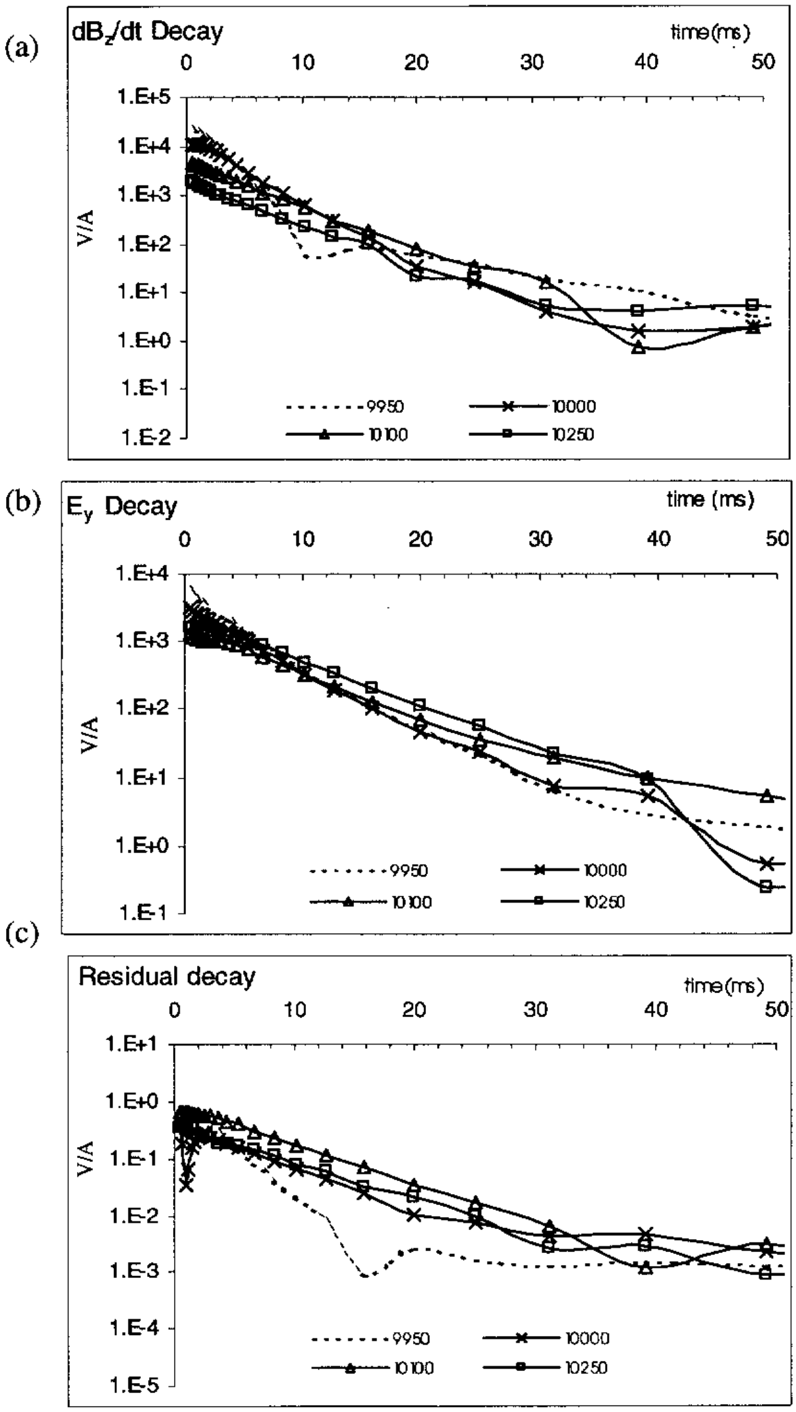

Figure 6.10 Fixed loop decay curves for selected stations plotted on a linear time scale. **(a)** dB_z/dt decay showing an anomalous decay at 9950 E. **(b)** E_ϕ decay showing no anomalous decays **(c)** LLR showing a greatly enhanced anomalous decay at 9950 E indicating the presence of a conductive zone.

The decay of the electric field in the vicinity of the large anomaly at 10200 E is not indicative of a good conductor suggesting that the anomaly is probably due to the changing overburden depth.

The decay of the LLR displays a marked change at station 9950 E between 10 and 20 ms compared to the other stations [Figure 6.9(c)]. This time interval corresponds to the noticeable anomaly in the profile responses at 9950 E. The nature of the decay at this station clearly indicates that presence of an inhomogeneity of some kind at that location. The difference in the decay at 9950 E is made more noticeable by plotting the decay on log-linear scale in Figure 6.10. The indication of an inhomogeneity is greatly enhanced in the LLR suggesting that the procedure has been successful.

6.2.2 Moving Loop survey

A moving loop survey was conducted in the Forrestania region of Western Australia that forms part of the Yilgarn craton. The region has detailed geological information obtained from previous drilling. The simplified geological section of the area shown in Figure 6.11 shows three features of interest. The very conductive overburden (< 10 Ω.m) is seen to increase in depth from 50 m to about 80 m towards the West. Two conductive units are the objects of the survey. The large vertical conductor near 33000 E is part of an extensive belt of black shales at a depth of 50 - 80 m that extends North–South for 1 - 2 km. The second feature of interest is the East dipping massive sulfide deposit (referred to as the 'Newmorning' ore body) located near 32650 E at a depth of approximately 100 m. Analysis of the drill samples shows the deposit contains in excess of 80% sulfides. A recent EM survey of the area detected the shale belt but was not able to detect the sulfide deposit.

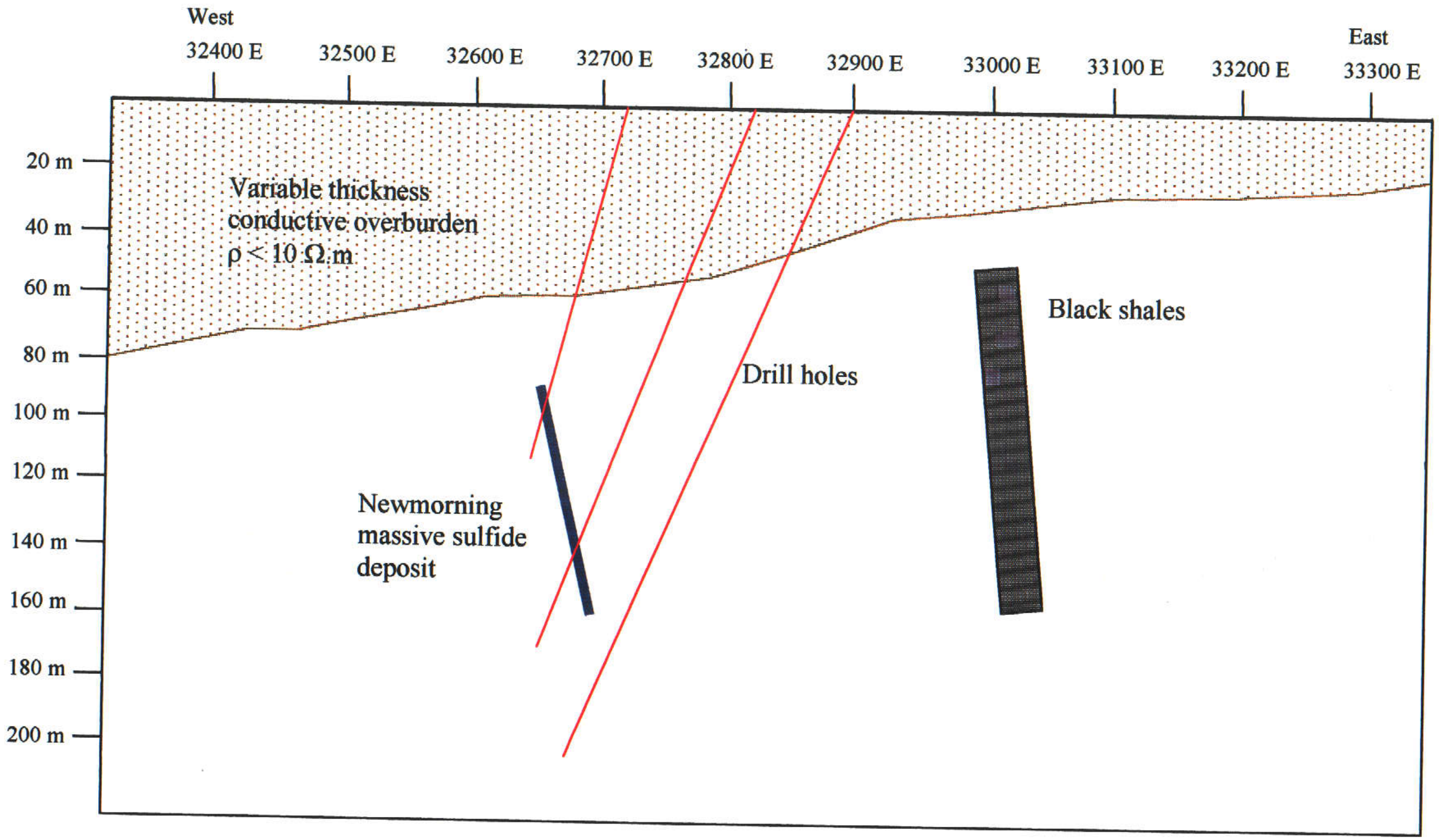

Figure 6.11 Simplified geological section of the Newmorning survey area. The small sulfide deposit beneath the conductive overburden has not been detected using conventional EM surveys.

Two surveys, in-loop and slingram, were conducted simultaneously to measure the dB_z/dt and E_ϕ components needed for the LLR concept. In addition the horizontal magnetic field (dB_x/dt) component was also measured. The survey parameters are shown in Table 6.2.

6.2.3 In-loop configuration

6.2.3.1 Profiles

The dB_z/dt profiles are shown in Figure 6.12(a) plotted on log-linear scale. The profiles are dominated in the early channels by the overburden response that is seen to increase to the West of the line. This indicates a deepening of the overburden in that direction. Evident in the later channels (5-30 ms) is a very obvious signature of a steeply dipping conductor centred on 33000 E. The signature coincides with the location of the black shales. There is also a very noticeable trough in the dB_z/dt profiles at location 32820 E. This coincides with a sulfidic ultramafic sequence at about 80 m depth but it is uncertain if the trough is caused by that sequence. There is no indication of the massive sulfide deposit at location 32640 E in the dB_z/dt profiles. This EM survey, like those before it has failed to detect the known ore body beneath the conductive overburden.

The LLR was computed using the dB_z/dt and E_ϕ measurements as described in Chapter 3. The early time (0.5 – 3 ms) LLR profiles shown in Figure 6.12(b) show that the LLR is centred on the zero line as most of the Earth response has been removed. The cross-over at 32640 E corresponds to the location of the massive sulfide deposit and gives a clear indication of its presence.

Location	Forrestania, W. Australia
Loop size	120 m x 120 m (2 turns)
Loop move-up	60 m
Transmitter	Zonge GGT-20
Current	25 A
Waveform	Bipolar step turn-off
Ramp time	0.128 ms
Base frequency	1.25 Hz
No. of cycles	128
Data logger	SMARTem
No. channels	35
Measurement range	0.08 – 136 ms
Electric field sensor	Porous pots
Magnetic field sensor	Ferrite-core coil (10^4 m^2)

Table 6.2 Survey parameters for the moving–loop survey at Forrestania, WA.

Also noticeable in these channels is a small peak at 32940 E which is the initial stages of the signature of the black shale belt at 32980 E. In the later time channels (3 – 30 ms) the LLR profiles shown in Figure 6.12(c) show a clear signature of the shale belt with the cross-over near 32980 E. The signature of the sulfide body at 32640 E is no longer evident in the LLR at later times. The significance of the cross-over at 33200 E is uncertain at this stage and further investigation will be necessary to elucidate this.

6.2.3.2 Decay curves

The decay curves for the dB_z/dt component are shown in Figure 6.13(a). Station 32940 E displays an exponential decay in the 10 – 20 ms channels with a time constant of 9.0 ms, which indicates the presence of a significant conductor. The LLR decay curves are shown in Figure 6.13(b) for the 0.5 – 3 ms range and in Figure 6.13(c) for the 3 – 30 ms range. In these figures, the decays are plotted on linear scales to emphasise the sign change on opposite sides of the conductor. Figure 6.13(b) indicates the presence of a conductor at 32640 E (i.e. the massive sulfide body) and the later channels indicate a conductor at 33000 E (i.e. the black shales). The LLR amplitude decays exponentially with a time constant of 1.0 ms at location 32640 E and 8.29 ms at location 33000 E. The small time constant at location 32640 E suggests that the massive sulfide body is not very conductive and helps to explain why it has not been detected by conventional EM surveys.

(a) **dB_z/dt** IN-LOOP 0.5 – 30 ms East

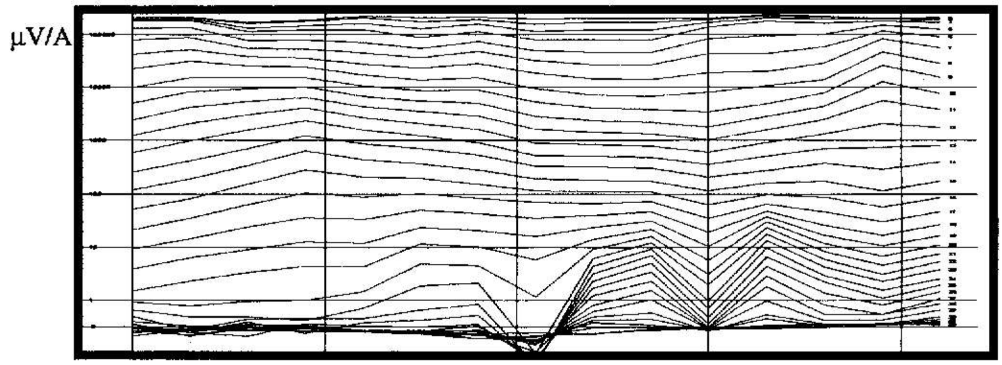

(b) **LLR** IN-LOOP 0.5 – 3 ms

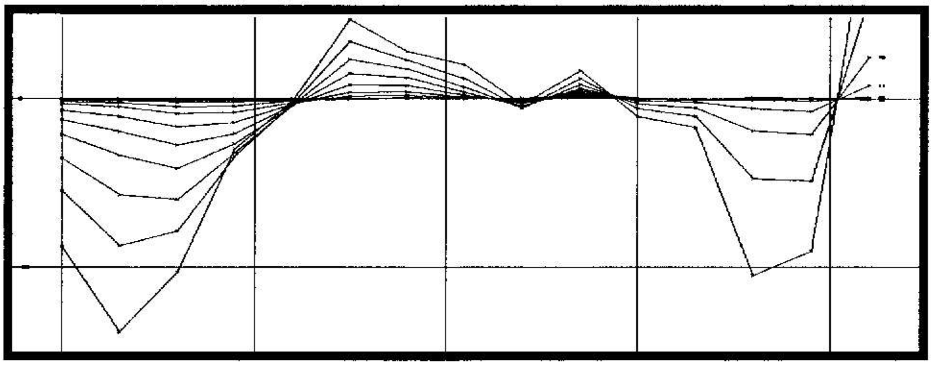

(c) **LLR** IN-LOOP 3 – 30 ms

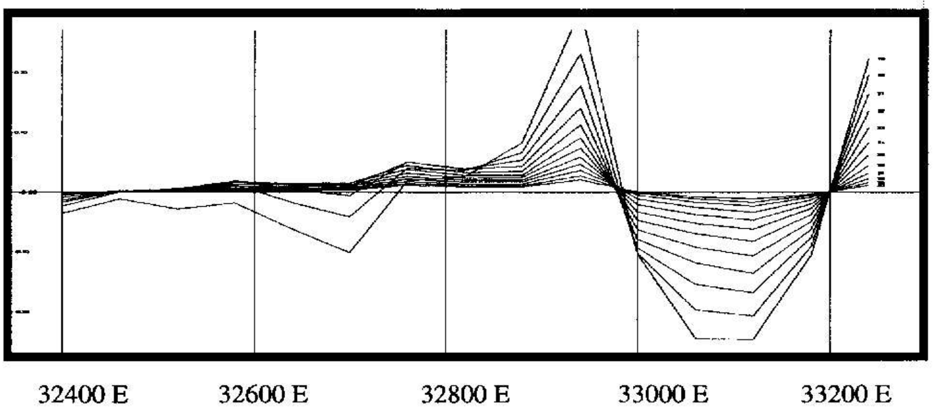

Figure 6.12 In-loop dB_z/dt and LLR profiles plotted against transmitter location. **(a)** The dB_z/dt response is dominated by the layered Earth response at early times but provides a clear indication of a conductor near 33000 E in the later channels. **(b)** the in-loop LLR for the early time channels, centred on the zero line and displaying a cross-over at 32640 E. **(c)** LLR profiles for the late times showing the signature of the conductive black shales at 32980 E.

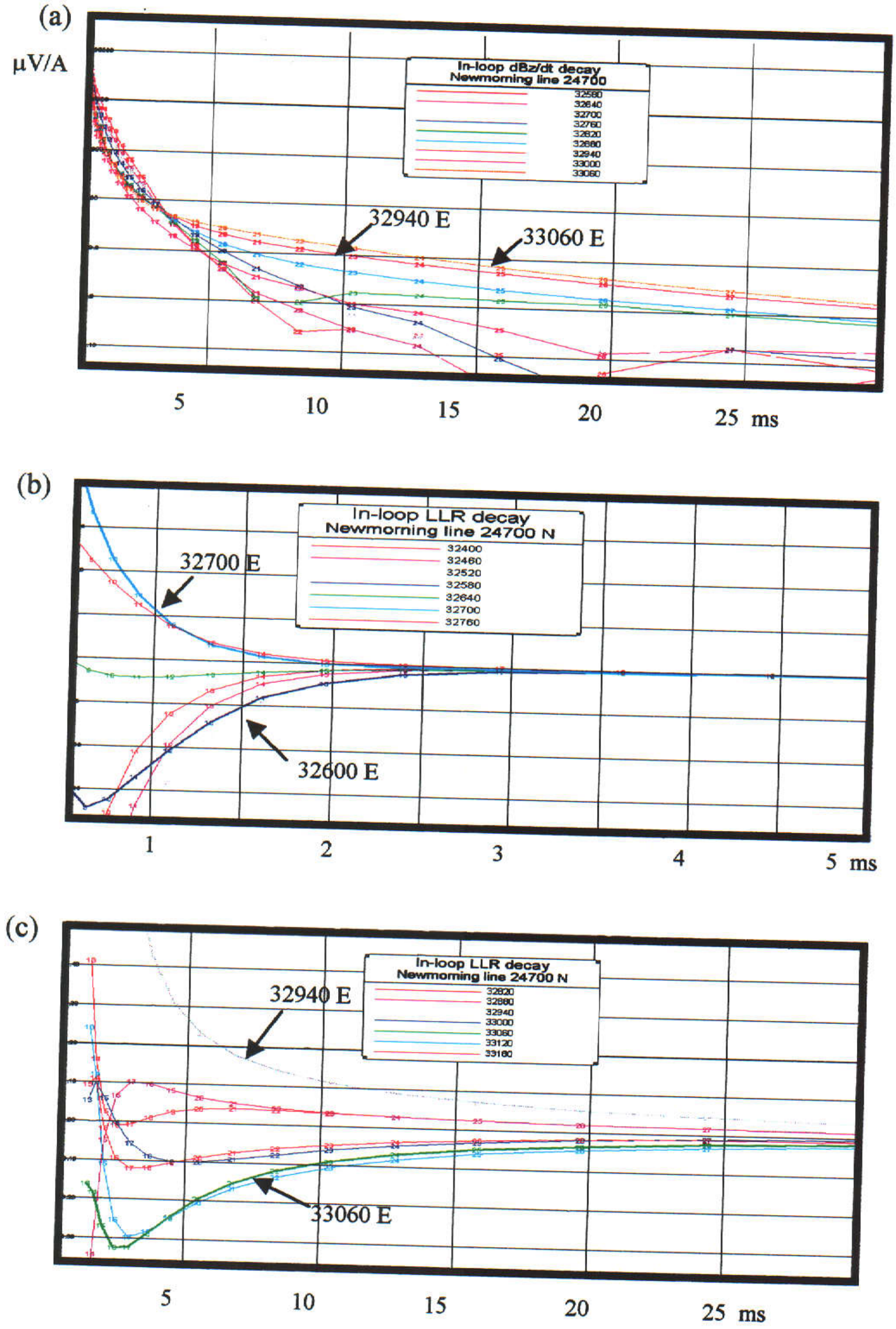

Figure 6.13 In-loop dB_z/dt and LLR decay curves. **(a)** The dB_z/dt decays indicate a good conductor at 33000 E. **(b)** The early time in-loop LLR decay curves indicate a conductor at 32640 E **(c)** the late time LLR decays indicate a good conductor at 33000 E.

6.2.4 Slingram configuration

6.2.4.1 Profiles

The slingram survey was performed concurrently with the in-loop survey using a Tx-Rx separation of 120 m. The dB_z/dt profiles are shown in Figure 6.14(a) and the LLR profiles in Figure 6.14(b). The transmitter location is used as the plotting point so that the LLR cross-overs indicate the location of the conductor. Consequently, the dB_z/dt trough associated with a conductor's signature will be displaced by 60 m to the East of the conductor. The dB_z/dt profiles are dominated by the overburden response at early times but contain a strong late time feature near 33060 E corresponding to the black shales. There is also a possible signature at 32700 E that may reflect the known sulfide deposit at 32640 E.

The early time (0.5 – 3 ms) LLR profiles displayed in Figure 6.14(b) contain a migrating cross-over that starts near 32660 E and moves toward the East. This indicates conductor with a dip toward the East and is consistent with the known sulfide deposit. The small positive peak near 33100 E is probably due to the black shales. The LLR is again centred on the zero line indicating that most of the layered Earth response has been removed. The late time (3 – 30 ms) LLR profiles are shown in Figure 6.14(c). These profiles display a definite cross-over at 32980 E corresponding to the black shales. There is also a cross-over near 32500 E which cannot be verified as the drill hole information does not extend far enough to the West.

6.2.4.2 Decay curves

The dB_z/dt decay curves shown in Figure 6.15(a) exhibit exponential decays at stations 32940 E and 33060 E, and indicate the presence of a very strong conductor. There is no indication of the massive sulfide body near 32640 E.

(a) **dB_z/dt** SLINGRAM 0.5 – 30 ms East

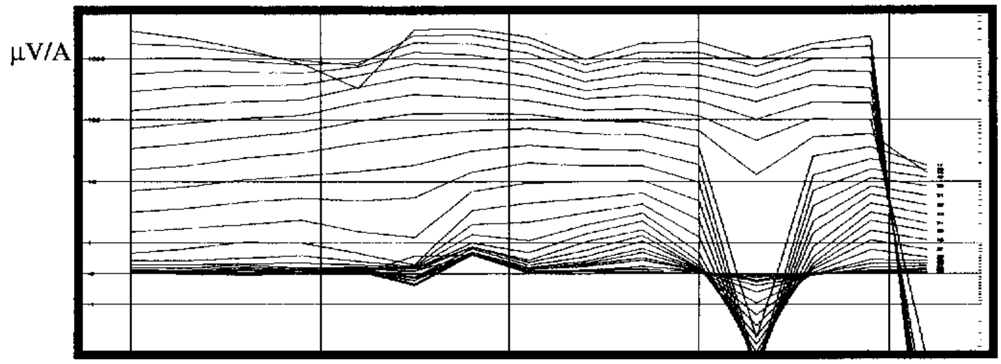

(b) **LLR** SLINGRAM 0.5 – 3 ms

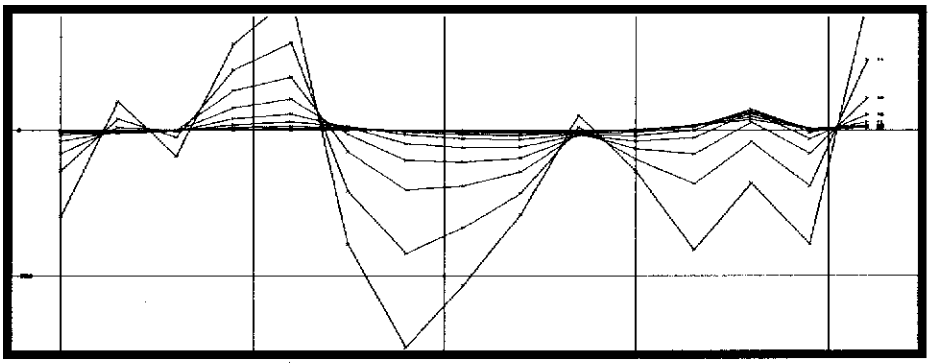

(c) **LLR** SLINGRAM 3 – 30 ms

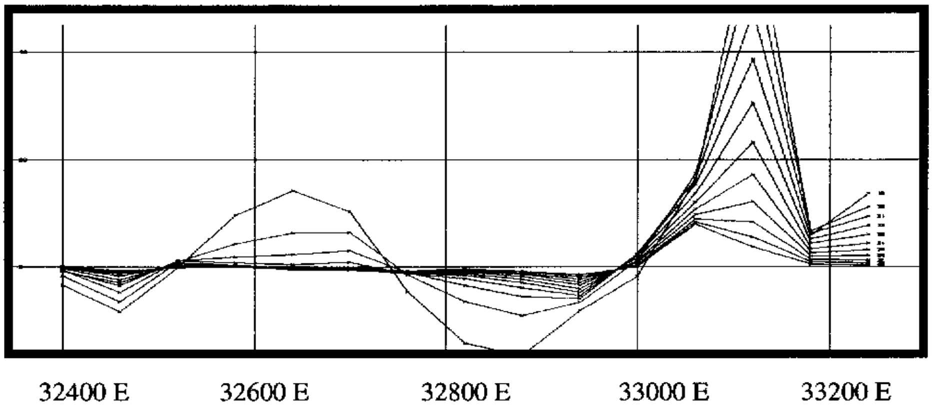

Figure 6.14 Slingram dB_z/dt and LLR profiles plotted against transmitter location. **(a)** dB_z/dt The response is dominated by the layered Earth response in the early times but provides a clear indication of a conductor near 33000 E at later times. **(b)** the slingram LLR for the early time channels, centred on the zero line and displaying a migrating cross-over near at 32660 E indicating a dipping conductor. **(c)** LLR profiles for the late times showing the signature of the conductive black shales at with the cross-over at 32990 E.

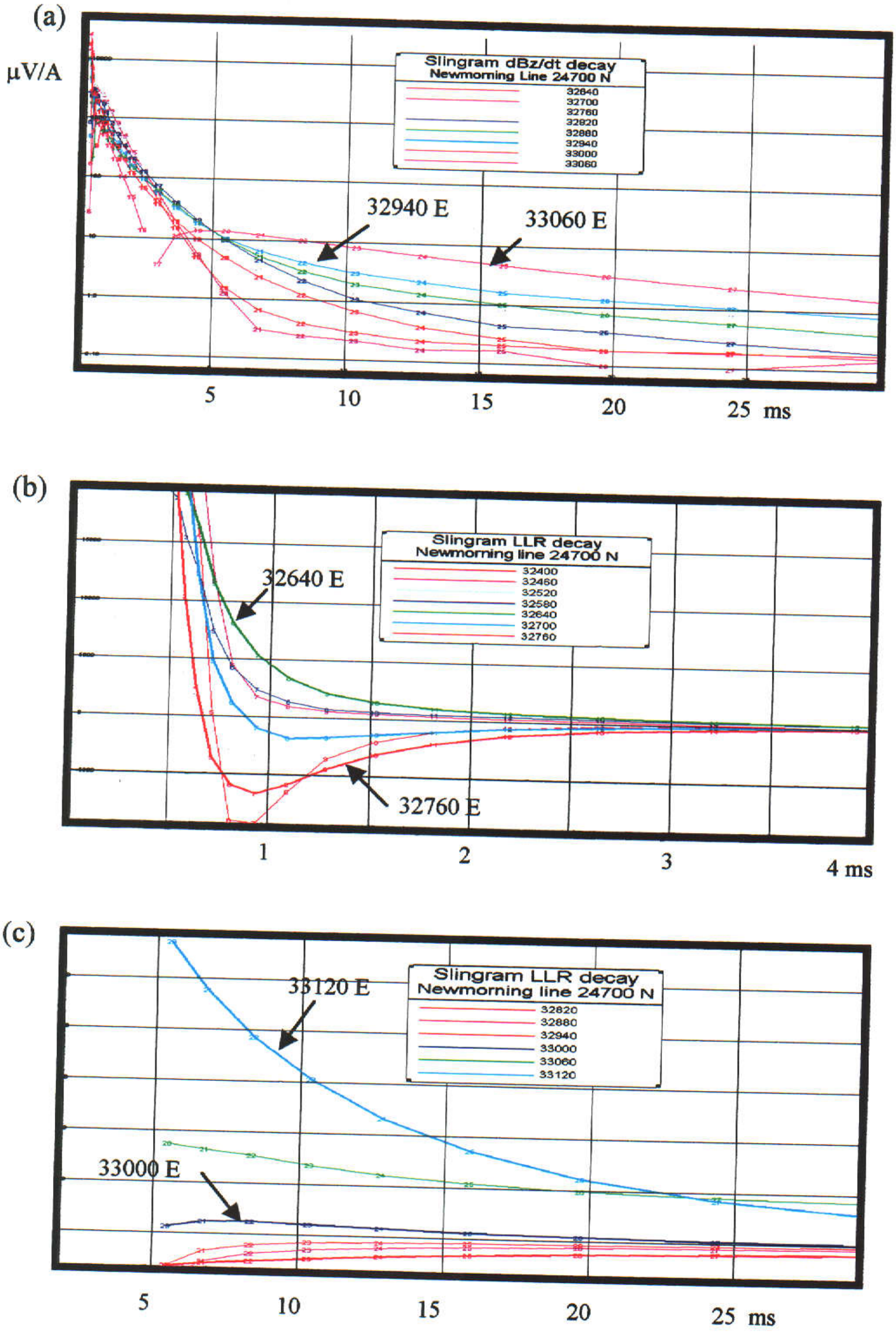

Figure 6.15 Slingram dB_z/dt and LLR decay curves. **(a)** The dB_z/dt decays indicate a very good conductor at 33000 E. **(b)** The early time slingram LLR decay curves indicate a conductor at 32700 E that coincides with the dipping sulfide body. **(c)** the late time LLR decays indicate a good conductor at 33000 E.

All decays along the profile display positive voltages. In contrast, the early time (0.5 – 4 ms) LLR decays shown in Figure 6.15(b) exhibit both positive and negative exponential decays. The decays indicate that the conductor is located near 32700 E and has a time constant of approximately 1.2 ms. The late time (5 – 30 ms) decays are shown in Figure 6.15(c). These channels indicate a conductor at 33000 E with a time constant of 8.9 ms. These results are consistent with those obtained by the in-loop survey. The slingram LLR has provided a signature of both conductors and has also correctly indicated the dipping nature of the massive sulfide deposit.

6.3 Enhancement of geophysical maps

The Radon transform method of data enhancement described in Chapter 5 was applied to three field data maps. In the first example, the Radon transform was used to enhance the lineaments in a map of radiometric data. The map shown in Figure 6.16(a) represents the total radiometric count i.e. K, Th, U and the data were not processed in any way prior to the production of the map. The Radon transform of the map is shown in Figure 6.16(b). The Radon domain contains a number of peaks corresponding to lineaments in the space domain map. To enhance the lineaments, the peaks in the Radon domain data were amplified relative to a selected threshold level as described in Chapter 3. The 'processed' map recovered after inverse Radon transform is shown in Figure 6.16(c). In this map, the linear features are more coherent than in the original map and provide a better view of the possible sub-surface structure. As a comparison, Figures 6.16(d) and 6.16(e) show the maps produced by using the traditional Fourier domain direction filtering in the North-East and North-West directions respectively.

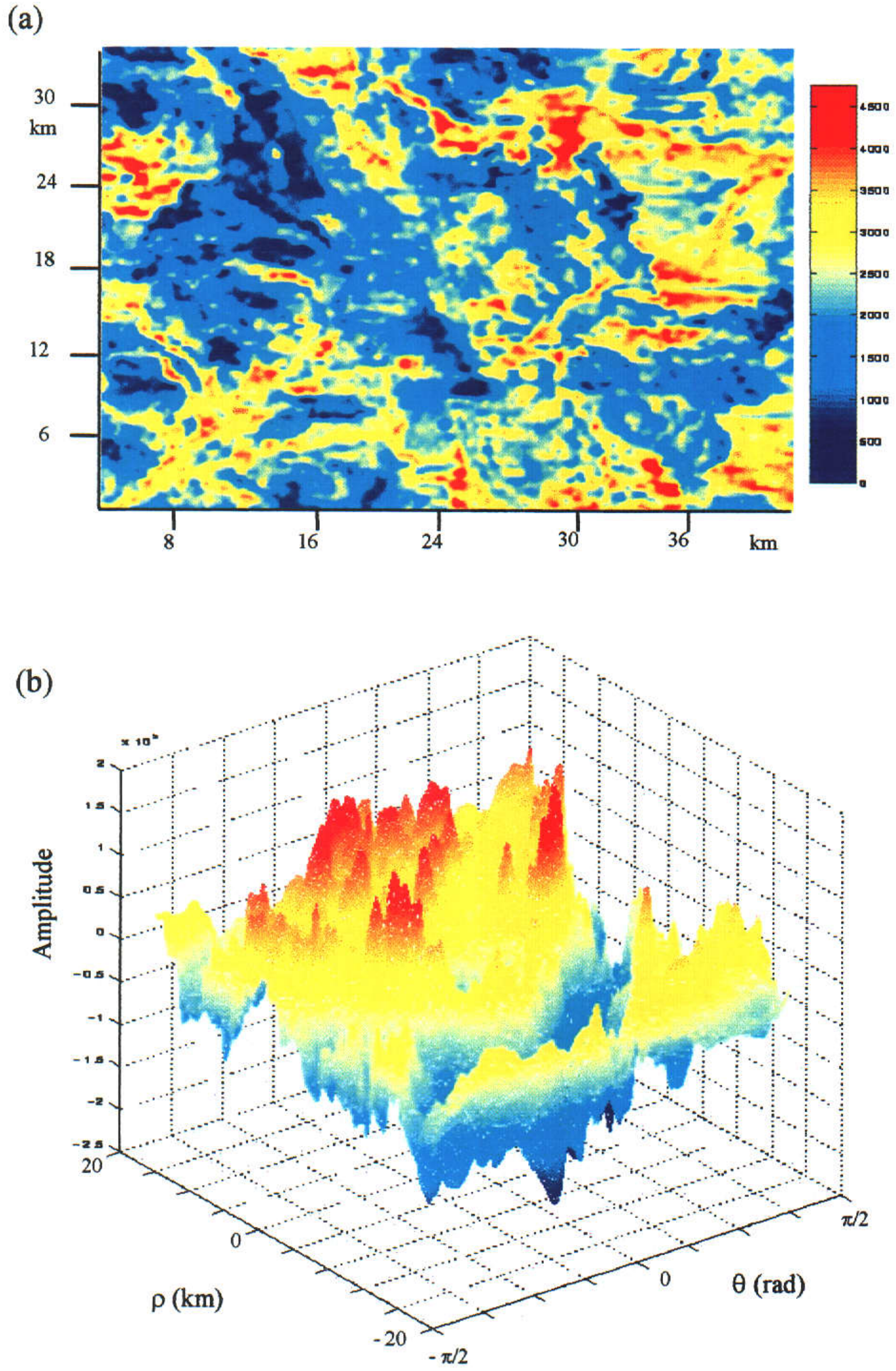

Figure 6.16 Enhancement of radiometric lineaments using the Radon transform. **(a)** Map of the total radiometric count near Newcastle, Australia showing diffuse lineaments **(b)** Radon domain spectral data of the map in (a). The peaks correspond to lineaments in the space domain map.

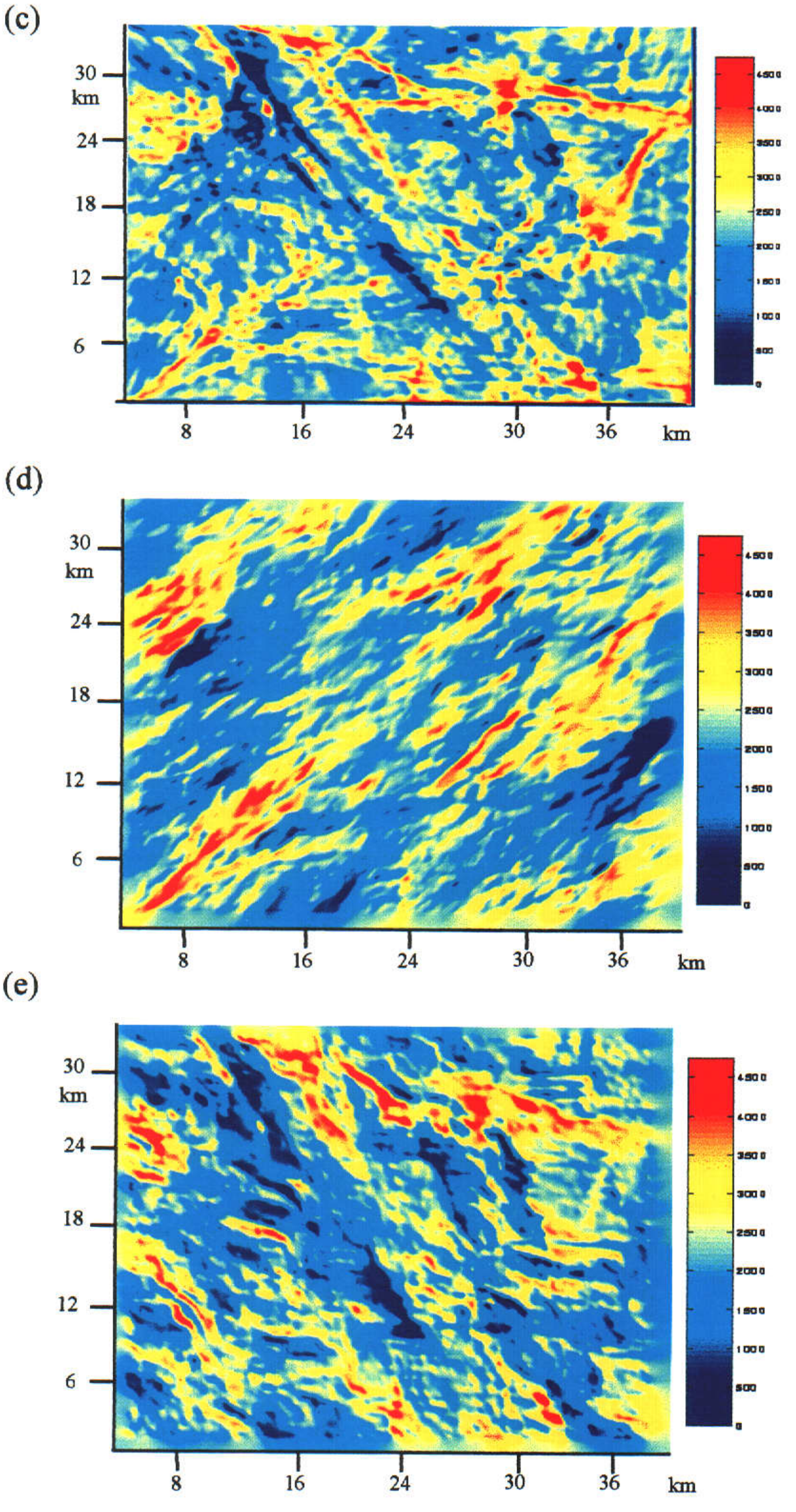

Figure 6.16 *continued* **(c)** Radiometric lineaments enhanced by Radon domain scaling. **(d)** Fourier domain directional filtering to enhance the North-East lineaments **(e)** Fourier directional filtering to enhance the North-West lineaments.

The Fourier method is not capable of enhancing lineaments of all strike directions at the same time and produces maps that are very different from the original. The Radon method has the benefit of enhancing all the lineaments regardless of their particular strike direction.

The Radon domain processing enhances the lineaments in a map without removing direction dependent information. This results in the resolution of the Radon processed map being far greater than that obtained using the Fourier domain processing.

6.3.1 Lineament filtering

The map shown in Figure 6.17(a) is represents the dB_z/dt component of a fixed-wing AEM survey conducted in Western Australia. The map contains a dominant linear feature in the direction of the flight-lines in the North-West region of the map. It was believed that this feature was caused by instrument malfunction and was not a real signal. The lineament is clearly visible in the Radon domain as a peak located in the region corresponding to the flight line direction. The peak was muted by zeroing the appropriate section of the Radon domain prior to inverse transformation. Figure 6.17(b) shows the processed map with the large lineament removed. For comparison, the traditional method of lineament removal by Fourier transform direction filtering is shown in Figure 6.17(c). The feature has been removed, but the Fourier transform filter has severely degraded the other features displayed in the map.

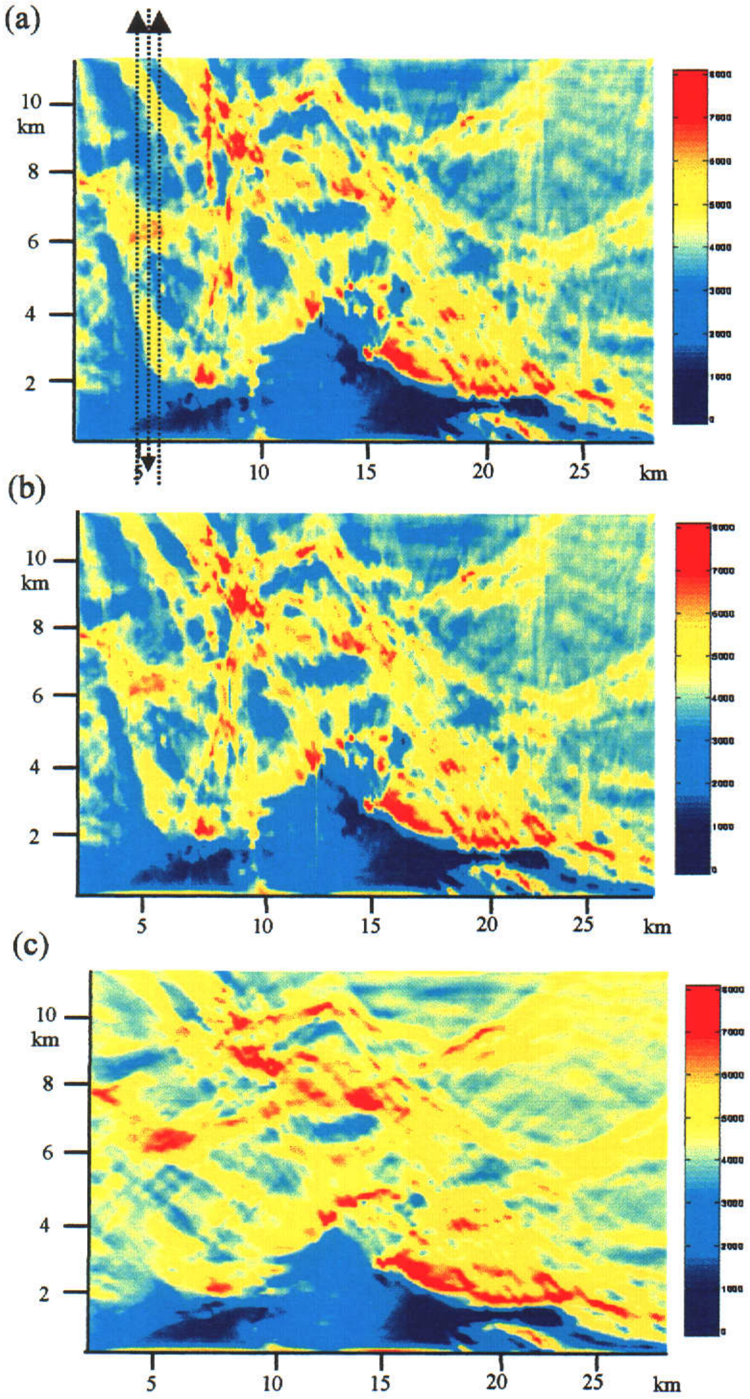

Figure 6.17 Removal of linear features by Radon and Fourier domain filtering. **(a)** Original map containing a large vertical feature believed to be fictitious. **(b)** Feature removed by filtering a portion of the Radon domain. **(c)** Feature removed using Fourier domain directional filtering. The Radon method has had very little effect on the rest of the map whereas the Fourier method has severely altered the entire map. Arrows indicate the flight-line direction.

6.3.2 Herringbone removal

The AEM map of Figure 5.1 was processed as described in Chapter 5 to remove the herringbones. Figure 5.1 is reproduced in Figure 6.18(a) for easy comparison. In this case, a five point smoothing filter was applied to the affected Radon domain spectral lines prior to inverse transformation. In this case, it was difficult to determine the optimum filtering limits to apply in the Radon domain because of the natural variability of 'real' data compared to the synthetic models. It is possible that the data were filtered more than necessary.

However, the processed map shown in Figure 6.18(b) indicates that the processing technique has been very successful. The map does not contain herringbones and the other features in the map have been relatively unaffected by the processing when compared to the Fourier processing methods used to produce Figures 5.6(c) and 5.6(d). There is a slight broadening of the features due to the inexact nature of the Radon transform but the boundaries between different zones are much more well-defined. The features in the processed map are more coherent than those displayed in the original map. The large NE trending feature on the right-hand side of the map remains somewhat dis-jointed after the processing since this feature was not adequately sampled at the time of acquisition. The reason for this is unknown but emphasises that the processing cannot compensate for inadequate data acquisition.

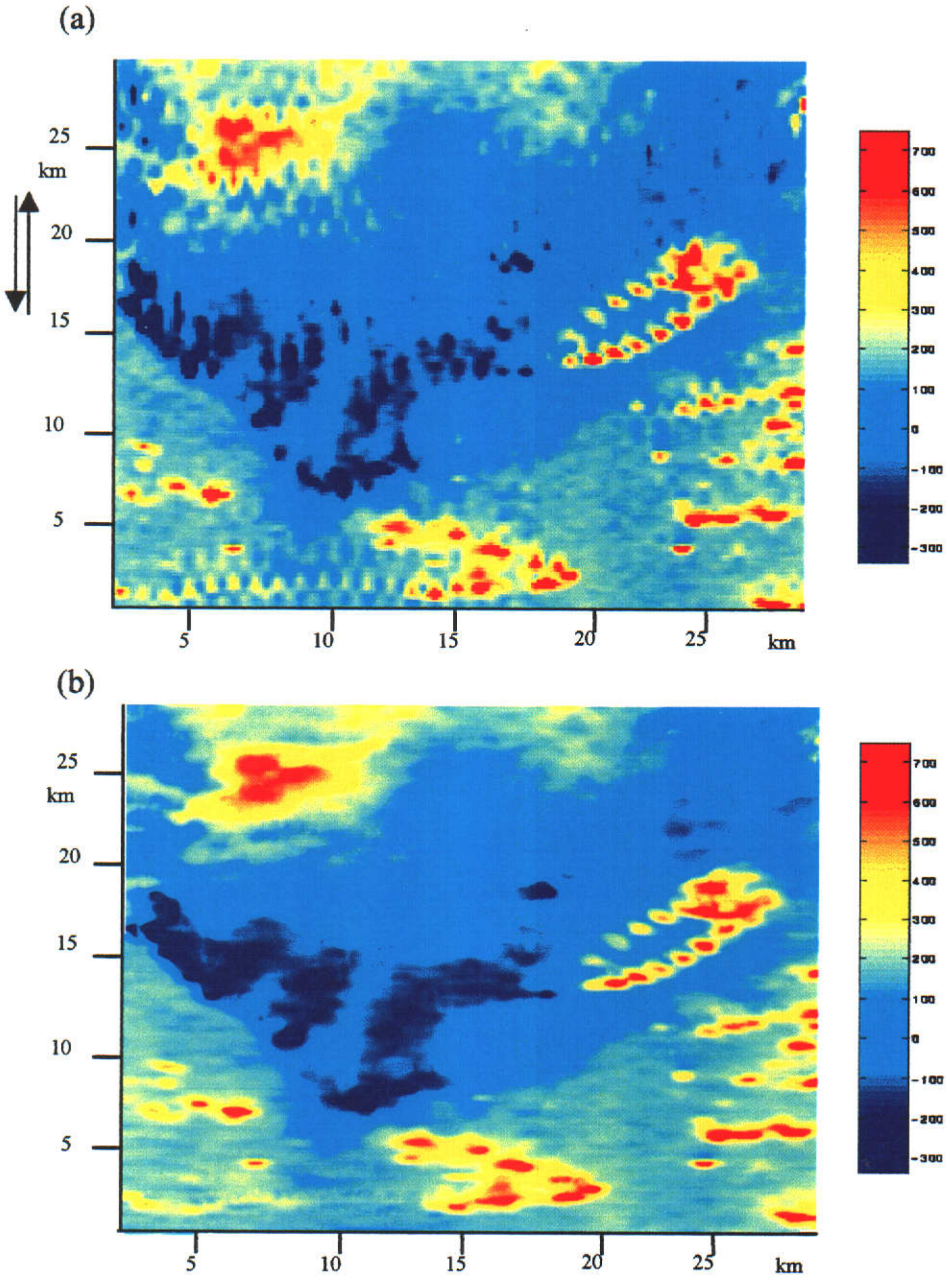

Figure 6.18 Herringbone removal using the Radon transform method. **(a)** herringbone affected AEM map. **(b)** herringbones removed using the Radon transform method. Spectral lines in the Radon domain were smoothed using a five-point filter with Shepard's coefficients. The slight difference in amplitudes due to the transformation is insignificant in view of the improvement in map quality.

The information must be present in the data at the time of measurement. The overall appearance of the map has been greatly enhanced.

6.4 Concluding remarks

The processing methods described in Chapters 3 and 5 have been applied to 'real' data with success. The SLR and LLR concepts were tested on field data and have in each case provided an enhanced indication of the presence of a conductive target. The Radon transform methods were useful in selectively enhancing the lineaments and removing unwanted features in AEM maps.

REFERENCES

Abramowitz, M. and Stegun, I.A., 1970, Handbook of mathematical functions: National Bureau of Standards Applied Mathematics Series.

Anderson, W.L., 1975, Improved digital filters for evaluating Fourier and Hankel transform integrals: Nat. Tech. Inf. Serv. Rep. PB-242-800.

Anderson, W.L., 1979, Numerical integration of related Hankel transforms of order 0 and 1 by adaptive digital filtering: Geophysics, 44, 1287-1305.

Annan, A.P., and Lockwood, R., 1991, An application of airborne GEOTEM in Australian conditions: Explor. Geophys., 22, 5-11.

Asten, M.W., 1992, Interpretation of ground TEM data from conductive terrains: Explor. Geophys. 23, 9-16.

Avdeev. D.B., Kuvshinov, A.V., Pankratov, O.V., and Newman, G.A., 1998, Three-dimensional frequency-domain modelling of airborne electromagnetic responses: Explor. Geophys., 29, 111-119.

Banos, A., 1966, Dipole radiation in the presence of a conducting half-space: Permagon Press, Inc.

Benson, A.K., Payne, K.L., and Stubben, M.A., 1997, Mapping groundwater contamination using dc resistivity and VLF geophysical methods - A case study: Geophysics, 62, 80-86.

Best, M.E., Duncan, P., Jacobs, F.J., and Scheen, W.L., 1985, Numerical modeling of the electromagnetic response of three-dimensional conductors in a layered earth: Geophysics, 50, 665-676.

Beylkin, G., 1987, Discrete Radon transform: IEEE Transactions on Acoustics, Speech and Signal processing, ASSP-35, 162-172.

Bostick, F.X., 1977, A simple almost exact method of MT analysis: Workshop on electrical methods in geothermal exploration, U.S. Geol. Surv., contract no. 14080001-8-359.

Bracewell, R.N., 1978, The Fourier transform and its applications: McGraw-Hill.

Brescianini, R.F., Asten, M.W., and McLean, N., 1992, Geophysical characteristics of the Eloise Cu-Au deposit North-West Queensland: Explor. Geophys., 23, 33-42.

Brysk, H., and McCowan, D.W., 1986, A slant-stack procedure for point-source data: Geophysics, 51, 1370-1386.

Buselli, G., Barber, C., Davis, G.B., and Salama, R.B., 1990, Detection of groundwater contamination near waste disposal sites with transient electromagnetic and electrical methods, *in* Ward, S.H., Ed., Geotechnical and environmental geophysics: Soc. Explor. Geophys., 2, 27-38.

Buselli, G., Pik, J.P., and Hwang, H.S., 1998, AEM noise reduction with remote referencing: Explor. Geophys., 29, 71-76.

Chapman, C.H., 1978, A new method for computing synthetic seismograms: Geophys. J. Roy. Astr. Soc., 54, 482-518.

Christensen, N.B., 1990, Optimized fast Hankel transform filters: Geophys. Prosp., 38, 545-568.

Coggon, J.H., 1971, Electromagnetic and electrical modelling by the finite element method: Geophysics, 36, 132-155.

Das, U.C., and Verma, S.K., 1982, Electromagnetic response of an arbitrarily shaped three-dimensional conductor in a layered earth-numerical results: Geophys. J. Roy. Astr. Soc., 68, 55-56

Davis, J.C., 1986, Statistics and data analysis in geology, 2nd ed.: John Wiley and Sons, New York.

Deans, S.R., 1983, Radon transform and some of its applications: John Wiley and Sons, Inc.

Doll, W.E., Skibicky, T.V., and Clay, C.S., 1984, Enhancement of transient electromagnetic soundings: A metallic study: Geophysics, 49, 895-901.

Durrani, T.S., and Bisset, D., 1984, The Radon transform and its properties: Geophysics, 49, 1180-1187.

Eadie, E.T., Silic, J., and Jack, D.J., 1985, The application of geophysics to the discovery of the Hellyer ore deposit, Tasmania: Explor. Geophys., 16, 207-209.

Eaton, P.A., and Hohmann, G.W., 1987, An evaluation of electromagnetic methods in the presence of geologic noise: Geophysics, 52, 1106-1126.

Erdelyi, A., 1954, Tables of integral transforms: McGraw-Hill Book Co.

Ferneyhough, A.B., 1985, The quantitative interpretation of airborne electromagnetic data: Rsch. Appl. Geophysics, 34, Univ. Toronto.

Fountain, D., 1998, Airborne electromagnetic systems - 50 years of development: Explor. Geophys., 29, 1-11.

Fraser, D.C., 1979, The multicoil II airborne electromagnetic system: Geophysics, 44, 1367-1394.

Frischknecht, F.C., Labson, V.F., Spies, B.R. and Anderson, W.L., 1991, Profiling methods using small sources, *in* Nabighian, M.N., Ed., Electromagnetic methods in applied geophysics: Soc. Explor. Geophys. 2, 105-270.

Frohlich, R.K., Urich, D.W., Fuller, J., and O'Reilly, M., 1994, Use of geoelectrical methods in groundwater pollution surveys in a coastal environment: Applied Geophysics, 32, 139-154.

Fullar, J.A., and Wait, J.R., 1976, A pulsed dipole in the Earth, *in* Felsen, L.B., Ed., Transient electromagnetic fields: Springer-Verlang.

Ghosh, D.P., 1971, The application of linear digital filter theory to the direct interpretation of geoelectrical resistivity sounding measurements: Geophys. Prosp., 19, 192-217.

Gomez-Trevino, E., 1987, A simple sensitivity analysis of time-domain and frequency-domain electromagnetic measurements: Geophysics, 52, 1418-1423.

Grant, F.S., and West, G.F., 1965, Interpretational theory in applied geophysics: McGraw-Hill Book Co.

Green, A., 1998, Altitude correction of time domain AEM data for image display and geological mapping using the Apparent Dipole Depth (ADD) method: Explor. Geophys., 29, 87-91.

Guptasarma, D., and Singh, B., 1997, New digital linear filters for Hankel J_0 and J_1 transforms: Geophys. Prosp., 45, 745-762.

Harrington, R.F., 1961, Time-harmonic electromagnetic fields: McGraw-Hill Book Co.

Hohmann, G.W., 1983, Three dimensional EM modeling: Geophysics Surv., 6, 27-83.

Hohmann, G.W., 1975, Three dimensional induced polarisation and electromagnetic modeling: Geophysics, 40, 309-324.

Johansen, H.K., and Sorensen, K., 1979, Fast Hankel transforms: Geophys. Prosp., 27, 876-901.

Kaufman, A.A., 1978a, Frequency and transient responses of electromagnetic fields created by currents in confined conductors: Geophysics, 43, 1001-1010.

Kaufman, A.A., 1978b, Resolving capabilities of inductive methods of electroprospecting: Geophysics, 43, 1392-1398.

Kaufman, A.A., 1989, A paradox in geo-electromagnetism and its resolution, demonstrating the equivalence of frequency and transient domain methods: Geoexpl., 25, 287-317.

Kaufman, A.A., and Keller, G.V., 1983, Frequency and transient soundings: Elsevier.

Keller, G.V., 1991, Rock and mineral properties, *in* Nabighian, M.N., Ed., Electromagnetic methods in applied geophysics: Soc. Explor. Geophys., 1, 13-51.

Knight, J.H., and Raiche, A.P., 1982, Transient electromagnetic calculations using the Gaver-Stehfest inverse Laplace transform method: Geophysics, 47, 47-50.

Koefoed, O., 1972, A note on the linear filter method of interpreting resistivity sounding data: Geophys. Prosp., 20, 403-405.

Kumar, R., 1974, Direct interpretation of two-electrode resistivity soundings: Geophys. Prosp., 22, 224-237.

Lajoie, J.J., and West, G.F., 1976, The electromagnetic response of a conductive inhomogeneity in a layered Earth: Geophysics, 42, 655-660.

Lamontagne, Y., 1975, Applications of wideband time-domain electromagnetic measurements in mineral exploration: PhD Thesis, Univ. of Toronto.

Lee, K.H., Pridmore, D.F., and Morrison, H.F., 1981, A hybrid three-dimensional electromagnetic modeling scheme: Geophysics, 46, 769-805.

Macnae, J.C., 1981, Geophysical prospecting with electric fields from an inductive source: Research in Applied Geophysics, 18, Univ. of Toronto.

Macnae, J.C., Lamontagne, Y., and West, G.F., 1984, Noise processing techniques for time-domain EM systems: Geophysics, 49, 934-948.

Mahmoud, S.F., Botros, A.Z., and Wait, J.R., 1979, Transient electromagnetic fields of a vertical magnetic dipole on a two-layer Earth: Proc. IEEE, 67, 1022-1029.

McCracken, K.G., Hohmann, G.W., and Oristaglio, M.L., 1986(a), A comparison of electromagnetic exploration systems: Geophysics, 51, 810-818.

McCracken, K.G., Hohmann, G.W., and Oristaglio, M.L., 1986(b), The minimization of noise in electromagnetic exploration systems: Geophysics, 51, 819-832.

Meyer, W.H., 1976, Computer modelling of electromagnetic prospecting methods: Ph.D. thesis, Univ. of California, Berkeley.

Minty, B.R.S., 1991, Simple micro-levelling for aeromagnetic data: Explor. Geophys., 22, 591-592.

Mohsen, A.A., and Hashish, E.A., 1994, The fast Hankel transform: Geophys. Prosp., 42, 131-139.

Mooney, H.M., 1980, Handbook of engineering geophysics: Bison instruments, Inc.

Morrison, H.F., Becker, A., and Hoversten, G.M., 1998, Physics of airborne EM systems: Explor. Geophys., 29, 97-102.

Mundry, E., and Blohm, E.K., 1987, Frequency electromagnetic sounding using a vertical magnetic dipole: Geophys. Prosp., 35,110-123.

Nabighian, M.N., 1972, The analytical signal of two-dimensional magnetic bodies with polygonal cross-section – Its properties and use for automated anomaly interpretation: Geophysics, 37, 507-517.

Nabighian, M.N., and Macnae, J.C., 1991, Time domain electromagnetic prospecting methods, *in* Nabighian, M.N., Ed., Electromagnetic methods in applied geophysics: Soc. Explor. Geophys., 2, 427-520.

Newman, G.A., Hohmann, G.W., and Anderson, W.L., 1986, Transient electromagnetic response of a three-dimensional body in a layered earth: Geophysics 51,1608-1627.

O'Connell, M.D., Lemieux, J., and Thurston, J., 1998, New methods for processing and displaying GEOTEM electromagnetic and magnetic data: Proc. Intl. AEM conf., Sydney, Poster 2.P3.

Olm, M.C., 1981, Electromagnetic scale model study of the dual frequency differencing technique: M.Sc. thesis, Colorado School of Mines.

Oristaglio, M.L., and Hohmann, G.W., 1984, Diffusion of electromagnetic fields in a two-dimensional earth: A finite-difference approach: Geophysics, 49, 870-894.

Palacky, G.J., 1975, Interpretation of Input AEM measurements in areas of conductive overburden: Geophysics, 40, 490-502.

Palacky, G.J., 1991, Resistivity characteristics of geologic targets, *in* Nabighian, M.N., Ed., Electromagnetic methods in applied geophysics: Soc. Expl. Geophys. 1, 53-129.

Palacky, G.J., and West, G.F., 1991, Airborne electromagnetic methods, *in* Nabighian, M.N., Ed., Electromagnetic methods in applied geophysics: Soc. Explor. Geophys., 2, 811-879.

Patra, H.P., and Mallick, K., 1980, Geosounding Principles: Elsevier Science Publ. Co., Inc.

Pawlowski, R.S., 1997, Use of slant stack for geologic or geophysical map lineament analysis: Geophysics, 62, 1774-1778.

Peltoniemi, M., 1998, Depth of penetration of frequency-domain airborne electromagnetics in resistive terrains: Explor. Geophys., 29, 12-15.

Peters, L.J., 1949, The direct approach to magnetic interpretation and its practical application: Geophysics, 14, 290-320.

Poddar, M., 1982, A rectangular loop source of current on a two-layered Earth: Geophys. Prosp., 30, 101-114.

Press, W.H., Teukolsky, S.A., Vetterling, W.T., and Flannery, B.P., 1992, Numerical recipes in FORTRAN, The art of scientific computing: Cambridge University Press.

Pridmore, D.F., Hohmann, G.W., Ward, S.H., and Sill, W.R., 1981, An investigation of finite-element modelling for electrical and electromagnetic data in three dimensions: Geophysics, 46, 1009-1024.

Raiche, A.P. and Gallagher, R.G., 1985, Apparent resistivity and diffusion velocity: Geophysics, 50, 1628-1633.

Raiche, A.P., 1974, An integral equation approach to three dimensional modeling: Geophys. J. Astr. Soc., 36, 363-376.

Raiche, A.P., 1978, Green's functions for modeling the electromagnetic response of a target near a dipping contact: Geophys. J. Roy. Astr. Soc., 55, 507-511.

Raiche, A.P., and Coggon, J.H., 1975, Analytic Green's tensors for integral equation modelling: Geophys. J. Roy. Astr. Soc., 42, 1035-1038.

Raiche, A.P., Jupp, D.L.B., Rutter, H., and Vozoff, K., 1985, The joint use of coincident loop transient electromagnetic and Schlumberger sounding to resolve layered structures: Geophysics, 50, 1618-1627.

Rainville, E.D., and Bedient, P.E., 1974, Elementary differential equations: Macmillan Publishing Co.

Robinson, E.A., 1982, Spectral approach to geophysical inversion by Lorentz, Fourier and Radon transforms: Proc. Inst. Electr. and Electron. Eng., 70, 1039-1053.

Savitzky, A. and Golay, M.J.E., 1964, Smoothing and differentiation of data by simplified least squares procedures: Analytical Chemistry, 36, 1627-1639.

Scheen, W.L., 1978, EMMMA, a computer program for three-dimensional modeling of airborne electromagnetic surveys: Proc., workshop on modeling of electrical and electromagnetic methods, LBL-7053, 53.

Scott, W.J., and Fraser, D.C., 1973, Drilling of EM anomalies caused by overburden: Bull. Can. Inst. Min. Metallurg. 66, 72-77.

Sheriff R.E., 1994, Encylopedic dictionary of exploration geophysics: Soc. Explor. Geophys.

Sinha, A.K., 1979, Maxiprobe EMR-16: A new wideband multifrequency EM system: Current research, Part B., Geol. Surv. Canada, Paper 79-1B, 23-26.

Slob, E.C., and Van den Berg, P.M., 1995, A new integral equation method for solving transient diffusive electromagnetic scattering problems: Int. Symp. on 3-D electromagnetism, 63-75.

Smith, R.S., 1994, Flat-lying conductor responses: A guide to interpreting asymmetric GEOTEM responses associated with overburden edges: Geoterrex internal report, unpublished.

Smith, R.S., and Keating, P., 1995, The usefulness of multicomponent time-domain airborne electromagnetic measurements: Geophysics, 61, 74-81.

Smith, R.S., and West, G.F., 1987, Electromagnetic induction in an inhomogeneous conductive thin sheet: Geophysics, 52, 1677-1688.

Spiegel, M.R., 1968, Mathematical handbook of formulas and tables. Mcgraw-Hill.

Spies, B.R. and Eggers, D.E., 1986, The use and misuse of apparent resistivity in electromagnetic methods: Geophysics, 51, 1462-1471.

Spies, B.R., 1980, Interpretation and design of time-domain EM surveys in areas of conductive overburden, *in* Emerson, D.W., Ed., Geophysics of the Elura orebody, Cobar, New South Wales: Aust. Soc. Explor. Geophys., 130-139.

Spies, B.R., 1989, Depth of investigation in electromagnetic sounding methods: Geophysics, 54, 872-888.

Spies, B.R., and Frischknecht, F.C., 1991, Electromagnetic sounding, *in* Nabighian, M.N., Ed., Electromagnetic methods in applied geophysics: Soc. Expl. Geophys., 2, 285-425.

Stephan, A., and Strack, K.M., 1991, A simple approach to improve the S/N ratio for TEM data using multiple receivers: Geophysics, 56, 863-869.

Stoffa, P.L., Buhl, P., Diebold, J.B., and Wenzel, F., 1981, Direct mapping of seismic data to the domain of intercept time and ray parameter- A plane-wave decomposition: Geophysics, 46, 255-267.

Stoyer, C.H., 1977, Electromagnetic fields of dipoles in stratified media: IEEE Trans. Antennas Propagat., 7, 547-552.

Strack, K.M., Hanstein, T.H., and Eilenz, H.N., 1989, LOTEM data processing for areas with high cultural noise levels: Physics of the Earth and Planetary interiors, 53, 261-269:

Stratton, J., 1941, Electromagnetic Theory: McGraw-Hill, New York.

Sykes, M.P., and Das, U.C., 1998, Removal of herringbone effects from AEM data maps using the Radon transform: Explor. Geophys., 29, 92-95.

Taner, M.T., Koehler, F., and Sheriff, R.E., 1979, Complex trace analysis: Geophysics, 44, 1041-1063.

Taner, M.T., 1980, Long-period sea-floor multiples and their suppression: Geophys. Prosp., 28, 30-48.

Toft, P.A., 1996, The Radon transform - theory and implementation: PhD thesis, Technical University of Denmark.

Uren, N.F., and Leiss, E.L., 1989, Interpolation in a complex spectrum: Fast versus slow Fourier transforms: 59th Ann. Internat. Mtg., Soc. Expl. Geophys., Expanded Abstracts, 99-101.

Villigas-Garcia, C.J., and West, G.F., 1983, Recognition of electromagnetic overburden anomalies with horizontal loop electromagnetic survey data: Geophysics, 48, 42-51.

Vogelsang, D., 1995, Environmental geophysics: Springer-Verlag.

Vozoff, K., 1991, The magnetotelluric method, *in* Nabighian, M.N., Ed., Electromagnetic methods in applied geophysics: Soc. Explor. Geophys: 2, 641-711.

Wait, J.R., 1982, Geo-electromagnetism: Academic Press Inc.

Wang, T., and Hohmann, G.W., 1993, A finite-difference, time-domain solution for three-dimensional electromagnetic modelling: Geophysics, 58, 797-809.

Wangsness, R.K., 1979, Electromagnetic fields: John Wiley and Sons.

Wannamaker, P.E., Hohmann, G.W., and SanFilipo, W.A., 1984, Electromagnetic modeling of three-dimensional bodies in layered earths using integral equations: Geophysics, 49, 60-74.

Ward, S.H., 1990, Resistivity and induced polarisation methods, *in* Ward, S.H., ed., Geotechnical and environmental geophysics: Soc. Explor. Geophys., 1, 147-189.

Ward, S.H., and Hohmann, G.W., 1991, Electromagnetic theory for geophysical applications, *in* Nabighian, M.N., Ed., Electromagnetic methods in applied geophysics: Soc. Expl. Geophys., 1, 131-311.

Ward, S.H., Ryu, J., Glenn, W.E., Hohmann, G.W., Dey, A., and Smith, B.D., 1974, Electromagnetic methods in conductive terranes: Geoexploration, 12, 121-183.

Weidelt, P., 1975, Electromagnetic induction in three dimensional structures: Geophys. J. Roy. Astr. Soc., 41, 85-109.

West, G.F., Macnae, J.C., and Lamontagne, Y., 1984, A time-domain electromagnetic system measuring the step response of the ground: Geophysics, 49, 1010-1026.

West, G.F., and Macnae, J.C., 1991, Physics of the electromagnetic induction exploration method, *in* Nabighian, M.N., Ed., Electromagnetic methods in applied geophysics: Soc. Explor. Geophys., 2, 5-45.

Wilt, M., and Stark, M., 1982, A simple method for calculating apparent resistivity from electromagnetic data: Geophysics, 47,1100-11-5.

Yunxuan, Z., 1992, Application of the Radon transform to the processing of airborne geophysical data: PhD thesis, International Institute for Aerospace Survey and Earth Sciences (ITC), The Netherlands.

Zonge, K.L., and Hughes, L.J., 1991, Controlled source audio-frequency magnetotellurics, *in* Nabighian, M.N., Ed., Electromagnetic methods in applied geophysics: Soc. Explor. Geophys., 2, 713-809.

APPENDIX A

Analytical expressions for EM fields

In order to derive the analytical expressions for the integrals shown in equations (2.64) to (2.66) I make use of the derivative of Bessel functions relations

$$\partial_\rho J_0(\rho\lambda) = -\lambda J_1(\rho\lambda) \tag{A-1}$$

and

$$\partial_\rho J_1(\rho\lambda) = \lambda J_0(\rho\lambda) - \frac{J_1(\rho\lambda)}{\rho}, \tag{A-2}$$

and apply successive differential operations with respect to ρ and z to the Sommerfeld and Foster's integrals of equation (2.67) and (2.68).

H_x component

Consider firstly the H_x component given in equation (2.64) as

$$H_x = \frac{mx}{2\pi k^2 \rho}\int_0^\infty p_2\lambda^2(p_1 - p_2)e^{-p_2 z}J_1 d\lambda. \tag{A-3}$$

Invoking the quasi-static approximation by replacing p_1 with λ enables equation (A-3) to be written as

$$H_x = \frac{mx}{2\pi k^2 \rho}\left[\int_0^\infty p_2\lambda^3 e^{-p_2 z}J_1 d\lambda - \int_0^\infty p_2^2\lambda^2 e^{-p_2 z}J_1 d\lambda\right]. \tag{A-4}$$

Making use of equation (A-1) and differentiating the Sommerfeld integral in equation (2.68) with respect to ρ yields

$$S_\rho = \int_0^\infty -\frac{\lambda^2}{p_2}e^{-p_2 z}J_1(\rho\lambda)d\lambda. \tag{A-5}$$

Differentiating (A-5) with respect to z three times gives an equivalent expression of the second integral in (A-4) i.e.

$$S_{\rho zzz} = \int_0^\infty p_2 \lambda^2 e^{-p_2 z} J_1(\rho\lambda) d\lambda \tag{A-6}$$

The first integral in (A-4) can be obtained by successive differentiation of the Foster integral of equation (2.67) with respect to ρ and z. Differentiating with respect to z and ρ once only, leads to

$$F_{\rho z} = \int_0^\infty \lambda e^{-p_2 z} J_1(\rho\lambda) d\lambda . \tag{A-7}$$

Using equation (A-2) and differentiating equation (A-7) with respect to ρ leads to

$$F_{\rho\rho z} = \int_0^\infty \lambda^2 e^{-p_2 z} J_0(\rho\lambda) d\lambda - \tfrac{1}{\rho} \int_0^\infty \lambda e^{-p_2 z} J_1(\rho\lambda) d\lambda \tag{A-8}$$

which using (A-7) can be written as

$$F_{\rho\rho z} + \tfrac{1}{\rho} F_{\rho z} = \int_0^\infty \lambda^2 e^{-p_2 z} J_0(\rho\lambda) d\lambda . \tag{A-9}$$

Differentiating (A-8) again with respect to ρ leads to

$$F_{\rho\rho\rho z} = \int_0^\infty - \lambda^3 e^{-p_2 z} J_1(\rho\lambda) d\lambda - \tfrac{1}{\rho} \int_0^\infty \lambda^2 e^{-p_2 z} J_0(\rho\lambda) d\lambda , \tag{A-10}$$

which using (A-9) is re-written as

$$F_{\rho\rho\rho z} = \int_0^\infty - \lambda^3 e^{-p_2 z} J_1(\rho\lambda) d\lambda - \tfrac{1}{\rho} \left[F_{\rho\rho z} + \tfrac{1}{\rho} F_{\rho z} \right]. \tag{A-11}$$

Finally, differentiating (A-11) with respect to z produces

$$F_{\rho\rho\rho zz} = \int_0^\infty p_2 \lambda^3 e^{-p_2 z} J_1(\rho\lambda) d\lambda - \tfrac{1}{\rho} \left[F_{\rho\rho zz} - \tfrac{1}{\rho} F_{\rho zz} \right], \tag{A-12}$$

or

$$\int_0^\infty p_2 \lambda^3 e^{-p_2 z} J_1(\rho\lambda) d\lambda = F_{\rho\rho\rho zz} + \tfrac{1}{\rho} \left[F_{\rho\rho zz} - \tfrac{1}{\rho} F_{\rho zz} \right]. \tag{A-13}$$

Substituting (A-6) and (A-13) into (A-4) produces an alternate method of computing the H_x component.

$$H_x = \frac{mx}{2\pi k^2\rho}\left(F_{\rho\rho\rho zz} + \frac{1}{\rho}F_{\rho\rho zz} - \frac{1}{\rho^2}F_{\rho zz} - S_{\rho zzz}\right) \tag{A-14}$$

E_ϕ component

The E_ϕ component is given in equation (2.65) as

$$E_\phi = \frac{mx}{2\pi\sigma\rho}\int_0^\infty \lambda^2(p_1 - p_2)e^{-p_2 z}J_1 d\lambda\,. \tag{A-15}$$

By setting $p_1=\lambda$ the equation becomes

$$E_\phi = \frac{mx}{2\pi\sigma\rho}\left\{\int_0^\infty \lambda^3 e^{-p_2 z}J_1 d\lambda - \int_0^\infty \lambda^2 p_2 e^{-p_2 z}J_1 d\lambda\right\}. \tag{A-16}$$

Now, differentiating (A-5) twice with respect to z provides the second integral in (A-16).

$$S_{\rho zz} = \int_0^\infty - \lambda^2 p_2 e^{-p_2 z}J_1 \partial\lambda\,, \tag{A-17}$$

and the first integral in (A-16) is obtained directly from (A-11)

$$\int_0^\infty \lambda^3 e^{-p_2 z}J_1(\rho\lambda)d\lambda = -F_{\rho\rho\rho z} - \frac{1}{\rho}\left[F_{\rho\rho z} - \frac{1}{\rho}F_{\rho z}\right]. \tag{A-18}$$

Combining equation (A-17) with (A-18) in (A-16) provides the analytical equivalent for the E_ϕ component

$$E_\phi = \frac{mx}{2\pi\sigma\rho}\left\{-F_{\rho\rho\rho z} - \frac{1}{\rho}\left[F_{\rho\rho z} - \frac{1}{\rho}F_{\rho z}\right] + S_{\rho zz}\right\} \tag{A-19}$$

H_z component

The H_z component is given in equation (2.66) as

$$H_z = \frac{m}{2\pi}\int_0^\infty \lambda(p_1 - p_2)e^{-p_2 z}J_0 d\lambda - \frac{m}{2\pi k^2}\int_0^\infty p_2^2\lambda(p_1 - p_2)e^{-p_2 z}J_0 d\lambda . \qquad \text{(A-20)}$$

Invoking the quasi-static approximation and setting $p_1=\lambda$ the equation becomes

$$H_z = \frac{m}{2\pi}\left[\int_0^\infty \lambda^2 e^{-p_2 z}J_0 d\lambda - \int_0^\infty \lambda p_2 e^{-p_2 z}J_0 d\lambda\right] -$$

$$\frac{m}{2\pi k^2}\left[\int_0^\infty p_2^2\lambda^2 e^{-p_2 z}J_0 d\lambda - \int_0^\infty p_2^3\lambda e^{-p_2 z}J_0 d\lambda\right] \qquad \text{(A-21)}$$

The first integral in (A-21) is found in (A-9) and the second integral is found by differentiating the Sommerfeld integral twice with respect to z i.e.

$$S_{zz} = \int_0^\infty p_2\lambda e^{-p_2 z}J_0(\rho\lambda)d\lambda . \qquad \text{(A-22)}$$

The third and fourth integrals in (A-21) are simply the second derivative with respect to z of the first and second integrals respectively, so the vertical magnetic field component can be computed using

$$H_z = \tfrac{m}{2\pi}(F_{\rho\rho z} + \tfrac{1}{\rho}F_{\rho z} - S_{zz}) + \tfrac{m}{2\pi k^2}(F_{\rho\rho zzz} + \tfrac{1}{\rho}F_{\rho zzz} - S_{zzzz}) . \qquad \text{(A-23)}$$

The H_y and E_x components can be found using the H_x and E_y expressions by replacing y for x in equations (A-14) and (A-19).

Computation of the field components requires the derivatives of the analytical expressions for the Sommerfeld and Foster integral to be evaluated. This involves lengthy algebraic procedures that are summarised in Appendix B.

APPENDIX B

Derivatives of the Sommerfeld integral

Consider first the Sommerfeld integral in equation (2.68),

$$S = \int_0^\infty \frac{\lambda}{p_2} e^{-p_2 z} J_0(\rho\lambda) d\lambda = \frac{e^{-ikr}}{r}, \tag{B-1}$$

repeated differentiation with respect to the depth variable z yields

$$S_z = \int_0^\infty -\lambda e^{-p_2 z} J_0(\rho\lambda) d\lambda = \left[-\frac{z}{r^3} - \frac{ikz}{r^2} \right] e^{-ikr} \tag{B-2}$$

$$S_{zz} = \int_0^\infty p_2 \lambda e^{-p_2 z} J_0(\rho\lambda) d\lambda = \left[\frac{3ikz^2}{r^4} + \frac{3z^2}{r^5} - \frac{k^2 z^2 + 1}{r^3} - \frac{ik}{r^2} \right] e^{-ikr} \tag{B-3}$$

$$S_{zzz} = \int_0^\infty - p_2^2 \lambda e^{-p_2 z} J_0(\rho\lambda) d\lambda = \left[\frac{3k^2 z}{r^3} + \frac{9ikz + ik^3 z^3}{r^4} + \right.$$

$$\left. \frac{9z + 6k^2 z^3}{r^5} - \frac{15ikz^3}{r^6} - \frac{15z^3}{r^7} \right] e^{-ikr} \tag{B-4}$$

$$S_{zzzz} = \int_0^\infty p_2^3 \lambda e^{-p_2 z} J_0(\rho\lambda) d\lambda = \left[-\frac{3k^2}{r^3} + \frac{9ik + 6ik^3 z^2}{r^4} + \frac{9 + 36k^2 z^2 + k^4 z^4}{r^5} - \right.$$

$$\left. \frac{90ikz^2 + 10ik^3 z^4}{r^6} - \frac{90z^2 + 45k^2 z^4}{r^7} + \frac{105ikz^4}{r^8} + \frac{105z^4}{r^9} \right] e^{-ikr} \tag{B-5}$$

Using the relation in equation (A-1) the Sommerfeld integral can be differentiated with respect to ρ as follows:

$$S_\rho = \int_0^\infty -\frac{\lambda^2}{p_2} e^{-p_2 z} J_1(\rho\lambda) d\lambda = \left[-\frac{\rho}{r^3} - \frac{ik\rho}{r^2} \right] e^{-ikr}. \tag{B-6}$$

Further derivatives with respect to ρ are not necessary for the computation of EM fields but derivatives with respect to z are needed for both the H_x and E_ϕ components. So, taking the derivative of equation (B-6) with respect to z gives

$$S_{\rho z} = \int_0^\infty \lambda^2 e^{-p_2 z} J_1(\rho\lambda)d\lambda = \left[-\frac{k^2\rho z}{r^3} + \frac{3ik\rho z}{r^4} + \frac{3\rho z}{r^5} \right] e^{-ikr}, \tag{B-7}$$

which can be repeated to produce

$$S_{\rho zz} = \int_0^\infty - p_2 \lambda^2 e^{-p_2 z} J_1(\rho\lambda)d\lambda = \left[-\frac{k^2\rho}{r^3} + \frac{ik^3\rho z^2 + 3ik\rho}{r^4} + \frac{3\rho + 6k^2\rho z^2}{r^5} - \frac{15ik\rho z^2}{r^6} - \frac{15\rho z^2}{r^7} \right] e^{-ikr}, \tag{B-8}$$

and once more to give

$$S_{\rho zzz} = \int_0^\infty p_2^2 \lambda^2 e^{-p_2 z} J_1(\rho\lambda)d\lambda = \left[\frac{3ik^3\rho z}{r^4} + \frac{k^4\rho z^3 + 18k^2\rho z}{r^5} - \frac{45ik\rho z + 10ik^3\rho z^{32}}{r^6} - \frac{45k^2\rho z^3 + 45\rho z}{r^7} + \frac{105ik\rho z^3}{r^8} + \frac{105\rho z^3}{r^9} \right] e^{-ikr}. \tag{B-9}$$

Derivatives of the Foster integral

The derivatives of the Foster integral are a little more complicated due to the presence of the modified Bessel functions. The derivatives of modified Bessel functions are found by making use of the following identities:

$$\tfrac{\partial}{\partial\rho} I_0[\tfrac{ik}{2}(r-z)] = I_1[\tfrac{ik}{2}(r-z)]\tfrac{ik\rho}{2r}, \tag{B-10}$$

$$\tfrac{\partial}{\partial\rho} K_0[\tfrac{ik}{2}(r+z)] = -K_1[\tfrac{ik}{2}(r+z)]\tfrac{ik\rho}{2r}, \tag{B-11}$$

$$\tfrac{\partial}{\partial\rho} I_1[\tfrac{ik}{2}(r-z)] = \left\{ I_0[\tfrac{ik}{2}(r-z)] - \frac{I_1[\tfrac{ik}{2}(r-z)]}{\tfrac{ik}{2}(r-z)} \right\} \tfrac{ik\rho}{2r}, \tag{B-12}$$

$$\tfrac{\partial}{\partial\rho} K_1[\tfrac{ik}{2}(r+z)] = \left\{ -K_0[\tfrac{ik}{2}(r+z)] - \frac{K_1[\tfrac{ik}{2}(r+z)]}{\tfrac{ik}{2}(r+z)} \right\} \tfrac{ik\rho}{2r}, \tag{B-13}$$

$$\tfrac{\partial}{\partial z} I_0[\tfrac{ik}{2}(r-z)] = I_1[\tfrac{ik}{2}(r-z)]\tfrac{ik(z-r)}{2r}, \tag{B-14}$$

$$\tfrac{\partial}{\partial z}K_0[\tfrac{ik}{2}(r+z)] = -K_1[\tfrac{ik}{2}(r+z)]\tfrac{ik(z+r)}{2r}, \tag{B-15}$$

$$\tfrac{\partial}{\partial z}I_1[\tfrac{ik}{2}(r-z)] = \left\{ I_0[\tfrac{ik}{2}(r-z)] - \frac{I_1[\tfrac{ik}{2}(r-z)]}{\tfrac{ik}{2}(r-z)} \right\} \tfrac{ik(z-r)}{2r}, \tag{B-16}$$

$$\tfrac{\partial}{\partial z}K_1[\tfrac{ik}{2}(r+z)] = \left\{ -K_0[\tfrac{ik}{2}(r+z)] - \frac{K_1[\tfrac{ik}{2}(r+z)]}{\tfrac{ik}{2}(r+z)} \right\} \tfrac{ik(z+r)}{2r}. \tag{B-17}$$

So, starting with the Foster integral of equation (2.67)

$$F = \int_0^\infty \frac{e^{-p_2 z}}{p_2} J_0(\rho\lambda)d\lambda = I_0[\tfrac{ik}{2}(r-z)].K_0[\tfrac{ik}{2}(r+z)], \tag{B-18}$$

the derivatives are found by making use of equations (B-10) to (B-17). In the following equations the argument of the modified Bessel functions $[\tfrac{ik}{2}(r-z)]$ and $[\tfrac{ik}{2}(r+z)]$ are omitted for simplicity and $\tfrac{ik}{2}$ is replaced by γ.

Taking the derivative of equation (B-18) with respect to ρ leads to

$$F_\rho = \int_0^\infty -\frac{\lambda}{p_2} e^{-p_2 z} J_1(\rho\lambda)d\lambda = \frac{\gamma\rho}{r}\left[I_1K_0 - I_0K_1\right], \tag{B-19}$$

which is differentiated with respect to z to give

$$F_{\rho z} = \int_0^\infty \lambda e^{-p_2 z} J_1(\rho\lambda)d\lambda = \frac{\gamma\rho}{r^3}\left[2\gamma zr(I_0K_0 - I_1K_1) + (r+z)I_0K_1 + (r-z)I_1K_0\right]. \tag{B-20}$$

Differentiating again with respect to z produces

$$\begin{aligned} F_{\rho zz} = \int_0^\infty -p_2\lambda e^{-p_2 z} J_1(\rho\lambda)d\lambda = {} & \frac{-6\gamma^2\rho z^2}{r^4} I_0K_0 + \left[\frac{6\gamma^2\rho z^2}{r^4} - \frac{4\gamma^2\rho}{r^2}\right] I_1K_1 + \Biggl[\frac{-4\gamma^3\rho z^2}{r^3} \\ & - \frac{3\gamma\rho z}{r^4} - \frac{3\gamma\rho z^2}{r^5}\Biggr] I_0K_1 + \left[\frac{4\gamma^3\rho z^2}{r^3} - \frac{3\gamma\rho z^2}{r^4} + \frac{3\gamma\rho z^2}{r^5}\right] I_1K_0 \end{aligned} \tag{B-21}$$

and another derivative with respect to ρ yields

$$F_{\rho\rho zz} = \int_0^\infty -\lambda^2 p_1 e^{-p_2 z} J_0(\rho\lambda) d\lambda + \tfrac{1}{\rho}\int_0^\infty \lambda p_1 e^{-p_2 z} J_1(\rho\lambda) d\lambda =$$

$$\frac{\gamma\rho}{r}\left[\frac{4\gamma^3\rho z^2}{r^3} - \frac{3\gamma\rho z}{r^4} + \frac{3\gamma\rho z^2}{r^5}\right]\left[I_0K_0 - I_1K_1 - \frac{I_1K_0}{\gamma(r-z)}\right] +$$

$$\left[\frac{4\gamma^3 z^2}{r^3} + \frac{3\gamma z^2 - 12\gamma^3\rho^2 z^2}{r^5} + \frac{12\gamma\rho z^2}{r^6} - \frac{15\gamma\rho^2 z^2}{r^7}\right] I_1K_0 \qquad \text{(B-22)}$$

Further derivatives of the Sommerfeld and Foster integrals with respect to z and ρ can be obtained as necessary to evaluate the required Hankel transforms. These expressions require a significant amount of algebra and become unweildy so are not presented here.

APPENDIX C

Topographical correction of MaxMin data.

MaxMin data must be corrected for errors introduced by not keeping the coils separated by the nominal distance due to surface topography. In such instances the actual horizontal coil separation is less than the nominal distance and consequently, the free-space field (used as a normalising constant) is larger than it should be.

The correction formulae are given by Lindholm (1998) as

$$(z/z_0)^{R*} = [(z/z_0)^{R} + 100*K] - 100 + 300\sin^2\alpha \qquad \text{(C-1)}$$

and

$$(z/z_0)^{Q*} = (z/z_0)^{Q} * K. \qquad \text{(C-2)}$$

In equations (C-1) and (C-2),

$$K = (r^A/r_N)^3 \qquad \text{(C-3)}$$

where

r^A is the actual loop separation and r^N is the nominal separation. $(z/z_0)^{R*}$ and $(z/z_0)^{Q*}$ are the corrected in-phase and quadrature measurements and α is the angle between the transmitter and receiver loop.

Since the ratio r^A/r_N is equivalent to $\cos\alpha$ the corrections are dependent only on the angle between the loops and not the separation.